



HAL
open science

Numerical study of electron transport in Hall thrusters

Thomas Charoy

► **To cite this version:**

Thomas Charoy. Numerical study of electron transport in Hall thrusters. Plasma Physics [physics.plasm-ph]. Institut Polytechnique de Paris, 2020. English. NNT: 2020IPPAX046 . tel-02982367

HAL Id: tel-02982367

<https://theses.hal.science/tel-02982367>

Submitted on 28 Oct 2020

HAL is a multi-disciplinary open access archive for the deposit and dissemination of scientific research documents, whether they are published or not. The documents may come from teaching and research institutions in France or abroad, or from public or private research centers.

L'archive ouverte pluridisciplinaire **HAL**, est destinée au dépôt et à la diffusion de documents scientifiques de niveau recherche, publiés ou non, émanant des établissements d'enseignement et de recherche français ou étrangers, des laboratoires publics ou privés.



INSTITUT
POLYTECHNIQUE
DE PARIS

NNT : 2020IPPAX046

Thèse de doctorat



Numerical study of electron transport in Hall Thrusters

Thèse de doctorat de l'Institut Polytechnique de Paris
préparée à École polytechnique

École doctorale n°626 Institut Polytechnique de Paris (IPP)
Spécialité de doctorat : Physique des Plasmas

Thèse présentée et soutenue à Palaiseau, le 30/09/2020, par

THOMAS CHAROY

Composition du Jury :

Jean-Pierre Boeuf Directeur de recherche, CNRS, LAPLACE (Université Paul Sabatier)	Président
Eduardo Ahedo Professeur, Université Carlos III, Madrid	Rapporteur
Francesco Taccogna Chercheur, IMIP/CNR	Rapporteur
Nicolas Plihon Chargé de recherche, CNRS, Laboratoire de Physique (ENS de Lyon)	Examineur
Andrei Smolyakov Professeur, University of Saskatchewan	Examineur
Anne Bourdon Directeur de Recherche, CNRS, LPP, École polytechnique	Directrice de thèse
Pascal Chabert Directeur de Recherche, CNRS, LPP, École polytechnique	Co-directeur de thèse
Olivier Duchemin Ingénieur, Safran Aircraft Engines	Invité

Ad astra per aspera

Résumé

Ces dernières années, le nombre de satellites en orbite autour de la Terre a augmenté de manière exponentielle. Grâce à leur faible consommation en carburant, de plus en plus de propulseurs électriques sont utilisés à bord de ces satellites, notamment le propulseur de Hall qui est l'un des plus efficaces. De la diversité des applications découle le besoin d'avoir des propulseurs de taille et puissance variables, pouvant être utilisés sur une large gamme de fonctionnement, avec une durée de vie accrue. Cependant, la physique des propulseurs de Hall est encore méconnue et les nouveaux designs se font de manière empirique, avec un développement long et coûteux, pour un résultat final limité. Pour pallier ce problème, des codes de simulation peuvent être utilisés mais une meilleure compréhension des phénomènes clés est alors nécessaire, plus particulièrement du transport anormal des électrons qui doit être pris en compte de manière auto-consistante pour pouvoir capturer totalement le comportement de la décharge.

Ce transport étant relié à l'instabilité azimuthale de dérive électronique, un code 2D particulière existant a été amélioré pour pouvoir simuler cette direction azimuthale mais aussi la direction axiale, dans laquelle les ions sont accélérés, produisant la poussée. Avant d'analyser le comportement de la décharge, ce code a été vérifié sur un cas de benchmark, avec 6 autres codes particuliers développés par différents groupes de recherches internationaux. Ce cas simplifié a été ensuite utilisé pour vérifier de manière intensive un développement analytique pour estimer la force de friction électron-ion, qui est le témoin de la contribution des instabilités azimuthales sur le transport anormal. Puis, la dynamique des neutres a été rajoutée pour capturer de manière auto-consistante le comportement de la décharge. Une technique artificielle de loi d'échelle a été adoptée, avec une augmentation de la permittivité du vide, pour alléger les contraintes de stabilité du code particulière et accélérer les simulations. Grâce à une parallélisation du code efficace, ce facteur artificiel a été réduit de manière significative, se rapprochant ainsi d'un cas proche de la réalité. La force de friction électron-ion a été observée comme étant celle qui contribuait le plus au transport anormal durant les oscillation basse-fréquence du mode de respiration. De plus, deux zones ont pu être distinguées pour les instabilités azimuthales, en fonction du caractère sonique des ions. En amont du point sonique, l'instabilité de dérive électronique est forte et le transport anormal peut être correctement estimé grâce à la théorie quasi-linéaire déjà mentionnée. Cependant, quand les ions deviennent super-soniques, une autre instabilité croît et se propage dans la direction axiale : l'instabilité de

transit des ions. Elle interagit avec l'instabilité de dérive électronique, causant la formation de structures azimuthales à grande longueur d'onde, associées à un plus grand transport anormal.

Abstract

In the last decade, the number of satellites orbiting around Earth has grown exponentially. Thanks to their low propellant consumption, more and more electric thrusters are now used aboard these satellites, with the Hall thrusters being one of the most efficient. From the diversity of applications stems the need of widening the thruster power capabilities. However, due to a lack of knowledge on Hall thruster physics, this scaling is currently done empirically, which limits the efficiency of the newly developed thrusters and increases the development time and cost. To overcome this issue, numerical models can be used but a deeper understanding on key phenomena is still needed, more specifically on the electron anomalous transport which should be self-consistently accounted for to properly capture the discharge behaviour.

As this transport is related to the azimuthal electron drift instability, an existing 2D Particle-In-Cell code was further developed to simulate this azimuthal direction along with the axial direction in which the ions are accelerated, producing the thrust. Prior to analyse the discharge behaviour, this code has been verified on a benchmark case, with 6 other PIC codes developed in different international research groups. This simplified case was later used to stress-test previous analytical developments to approximate the instability-enhanced electron-ion friction force which represents the contribution of the azimuthal instabilities to the anomalous transport. Then, the neutral dynamics has been included to capture the full self-consistent behaviour of the discharge. We used an artificial scaling technique, increasing the vacuum permittivity, to relax the PIC stability constraints and speed-up the simulations. Thanks to an efficient code parallelisation, we managed to reduce this scaling factor to a small value, hence simulating a case close to reality. The electron-ion friction force was found to be the main contributor to the anomalous transport throughout the whole low-frequency breathing mode oscillations. Moreover, we found that we could distinguish two zones for the azimuthal instabilities, depending on the sonic behaviour of the ions. Upstream of the ion sonic point, the electron drift instability is strong and the anomalous electron transport can be well approximated by the aforementioned quasi-linear kinetic theory. However, when the ions become supersonic, another instability is growing and propagating axially: the ion transit-time instability. It interacts with the electron drift instability, hence causing the formation of long-wavelength azimuthal structures associated with an enhanced anomalous transport.

Acknowledgements

A PhD is an adventure, and for an adventure to be successful, one needs colourful characters. Throughout these last three (and a half) years, I had the chance to spend time with many of them that I would like to thank.

First, a young engineering student needs mentors to guide him through the complex world of plasma physics. Anne Bourdon and Pascal Chabert played this role to perfection and gave me the opportunity to work on a fascinating subject and interact with a dynamic team. Thank you for your countless advices, your availability and your passion for physics and research in general. I really liked interacting with you, about science or else, and I am convinced that I was very lucky to have you two as supervisors. This list of mentors would be incomplete without my colleague Antoine Tavant who took me under his wing when I first started as an intern and along whom I enjoyed working during my PhD. You taught me not only how to code properly but also the importance of scientific rigour, so many thanks Antoine.

Of course, this work could have not been done without the help of the LP-Propulsion team. Thank you Vivien Croes for building from scratch this very useful tool LPPic. Thank you Romain Lucken for your passion for physics and your hard work on both the code and your start-up, it was very inspiring. Thank you Trevor Lafleur for your many insightful advices and your enthusiasm, you gave me the impulse I needed and made my work more valuable. Thank you Roberto Martorelli, for the same reasons as for Trevor, and many more, your friendship inside and outside the lab was precious to me. Thank you Alejandro Alvarez Laguna, not for your dedication to the football team (sorry), but for your expertise in numerical methods and the good mood you constantly bring to the team. Thank you Florian Marmuse for your commitment to the lab social life and for communicating your endless passion for space, you prevented mine to extinguish too fast. Thank you Sergey Shcherbanev for initiating me to the mysteries of experimental diagnostics and thank you Victor Desangles for taking over, it was a pleasure to learn from you two and be able to later monitor motivated students (Noé Clément and Pablo Richard). Théo Courtois, it is too bad you had to stop your PhD, but I am sure you will become a great pilot. I would also like to acknowledge the newcomers, Federico Petronio, Benjamin Esteves, Tarek Ben Slimane, Louis Reboul and Lui Habl, to whom I wish to enjoy at the fullest their PhD, and I know they will. Finally, I would like to thank David Tordeux, Denis Werth, Guillaume Bogopolsky and Clarence Deltel for their valuable help

during their respective internships.

During a battle, fighters are not enough, you also need back-ups. I would like to thank the PhDarium fellows who made this big office warmer: Abhyuday Chatterjee, Ana Sofia Morillo Candas, Marlous Hofmans and later Edmond Baratte. Beers, barbecues and conference trips are now indelible memories; Constance Duchesne, Gautier Nguyen, Olivier Guaitella, Elmar Slikboer, Audrey Chatain, Polina Oglobina, Xianjie Wang, Pedro Viegas, Victor Montagud, Ralph Kutra, Mhedine Alicherif, the DocUnion team; I had a great time with you all, I could keep writing about it but I am sure it is already in your mind. These days, many people have a bad image of football but I think they should remember its main power: bring people together. Thank you coach Abhyuday for assembling the team, it gave me (and others I think) the opportunity to interact with many people in the lab in a very friendly atmosphere, and I know it played a big role in improving the lab social life. A big thanks to everyone who played with us (including our fellows at LOA and Exotrail), I am sure the next team will be able to finally win the tournament. I would also like to thank the administrative and technical teams, who were always available to help, and the numerous organizations who financed and supported this project: *Agence Nationale pour la recherche*, in partnership with Safran Aircraft Engines (POSEIDON project), the HPC resources of CINES (under Allocation Nos. A0060510439 and A0040510092 made by GENCI) and of CERFACS at Toulouse.

When travelling to reach a goal, you encounter many protagonists. First, the team at CERFACS (Valentin Jonquieres, Francois Pechereau and Willca Villafana), at VKI (Stefano Boccelli and Thierry Magin), Zdenek Bonaventura and Tasman Powis, it was a pleasure to work with you and interact during your visits. Among the many people I had the opportunity to meet at conferences, special thanks to Kerstin and Tim, I hope we could have again some wine tasting soon. I would also like to acknowledge the colleagues who were part of the benchmark, you did a great job and I have learned a lot by collaborating with you. In general, I should say that the ExB community is very dynamic and open-minded and I would like to thank my PhD committee for their valuable insights and questions. As there is always a flashback in a good story, I would like to thank Roderick Boswell, Christine Charles and the SP3 group at the ANU who warmly welcomed me five years ago for an internship, you made me discover the joy of plasma physics and space propulsion and I will always be grateful for that.

Lastly, I would like to end this long list of acknowledgements with my personal friends and my family, and especially my beloved archaeologist, Eva Noyer, who was always there to support me throughout these three years. She was the best partner I can dream of, reminding me of a famous quote: 'I can't carry it for you, but I can carry you'.

List of publications

Journal articles

- T. Charoy, JP. Boeuf, A. Bourdon, J.A. Carlsson, P. Chabert, B. Cuenot, D. Eremin, L. Garrigues, K. Hara, I.D. Kaganovich, A.T. Powis, A. Smolyakov, D. Sydorenko, A. Tavant, O. Vermorel, and W. Villafana. "*2D axial-azimuthal particle-in-cell benchmark for low-temperature partially magnetized plasmas*". [Plasma Sources Sci. Technol.](#), **28(10):105010**, 2019.
- T. Charoy, T. Lafleur, A. Tavant, P. Chabert, and A. Bourdon. "*A comparison between kinetic theory and particle-in-cell simulations of anomalous electron transport in $E \times B$ plasma discharges*". [Phys. Plasmas](#), **27(6):063510**, 2020.
- S. Boccelli, T. Charoy, A. Alvarez Laguna, P. Chabert, A. Bourdon, and T. E. Magin. "*Collisionless ion modeling in hall thrusters: Analytical axial velocity distribution function and heat flux closures*". [Phys. Plasmas](#), **27(7):073506**, 2020.
- V. Désangles, S. Shcherbanev, T. Charoy, N. Clément, C. Deltel, P. Richard, S. Vincent, P. Chabert, and A. Bourdon. "*A fast camera analysis of plasma instabilities in hall effect thrusters using a POD method under different operating regimes*". [Atmosphere](#), **11:518**, 2020.

Conference proceedings

- T. Charoy, T. Lafleur, A. Tavant, A. Bourdon, and P. Chabert. "*Oscillation analysis in hall thrusters with 2D (axial-azimuthal) particle-in-cell simulations*". In 36th International Electric Propulsion Conference, Vienna. [Paper A487](#), 2019.

Contents

Résumé	V
Abstract	VII
Acknowledgements	IX
List of publications	XI
List of Figures	XXVIII
List of Tables	XXIX
1 Introduction	1
1.1 A new age for spacecraft propulsion	1
1.1.1 Electric propulsion	5
1.1.2 A broad range of needs	7
1.1.3 Working principles of the two main electric thrusters	8
1.2 Hall thrusters - General concepts	12
1.2.1 Basic concepts of Hall thruster plasma physics	13
1.2.2 Hall thruster instabilities	16
1.2.3 Why do we keep studying Hall thrusters?	23
1.3 Hall thrusters - Modeling	25
1.3.1 Multi-fluid models	27
1.3.2 Particle-In-Cell models	28
1.3.3 Hybrid and Direct-Kinetic models	29
1.4 Scope and outline of the thesis	29
2 Code development: from radial-azimuthal to axial-azimuthal geometry	31
2.1 A quick overview of <i>LPPic</i> , a 2D PIC-MCC code	32
2.1.1 Code main structure	32
2.1.2 A powerful numerical tool	36
2.2 Preliminary modifications towards axial-azimuthal simulations	38
2.2.1 Magnetic field	38
2.2.2 Ionization process	39

2.2.3	Code optimization	40
2.3	Neutral dynamics	43
2.3.1	Context	43
2.3.2	Model description	44
2.3.3	Solver verification and validation	48
2.4	Cathode model	49
2.4.1	Current Equality condition	51
2.4.2	Quasi-neutrality condition	52
2.4.3	Setting positions and energies	52
2.4.4	Which model should we choose?	53
2.5	Further improvements of the model	53
2.5.1	Fake radial dimension	54
2.5.2	Doubly-charged xenon ions	54
2.6	Conclusion	55
3	Code verification: 2D axial-azimuthal benchmark	57
3.1	Why do we need this benchmark?	58
3.2	Description of the model	59
3.2.1	Simulation domain	60
3.2.2	Imposed axial profiles	61
3.2.3	Boundary conditions	61
3.3	Code specificities	63
3.4	Results	64
3.4.1	Main plasma parameters	67
3.4.2	Azimuthal instabilities	68
3.5	Discussion	72
3.5.1	Numerical convergence	72
3.5.2	Case sensitivity	75
3.6	A tool to challenge numerical models - Example of the cathode injection	77
3.6.1	Studied cathode models	79
3.6.2	Main plasma parameters	80
3.6.3	Azimuthal instabilities	82
3.7	Conclusion	83
4	Instability-enhanced electron transport	85
4.1	Context	86
4.2	Theoretical models for enhanced electron transport	87
4.2.1	Electron-ion friction force	87
4.2.2	Theoretical models	89
4.2.3	Comparison with the nominal simulation case	95
4.3	2D PIC simulations	97
4.3.1	Model & Parametric studies	97
4.3.2	Comparison with parametric PIC results of the friction force derivation accounting for non-Maxwellian electrons	105

4.3.3	Ion-electron friction force	108
4.4	Influence of ion-neutral collisions	108
4.5	Discussion and Conclusion	112
5	Towards self-consistent simulations of Hall thrusters	115
5.1	Motivation	116
5.2	Numerical model	117
5.2.1	Case description	117
5.2.2	Importance of neutral dynamics and anode ion recombination	121
5.2.3	Cathode model	121
5.3	Axial electron transport during a breathing mode oscillation . . .	123
5.3.1	Case closer to reality ($\alpha_e = 4$)	123
5.3.2	Influence of vacuum permittivity scaling factor	126
5.3.3	VDF and plasma fluctuations	131
5.3.4	Azimuthal instabilities	138
5.4	Conclusion	141
6	Instabilities in Hall thrusters	143
6.1	Ion transit-time instabilities	144
6.1.1	Current understanding	144
6.1.2	Analysis of ITT: "1D axial" simulations	145
6.1.3	Origin of the ITTI?	149
6.1.4	Evidence of ITTI in the self-consistent axial-azimuthal sim- ulations	150
6.2	Influence of the azimuthal domain length L_y	155
6.2.1	Axial electron transport	155
6.2.2	Azimuthal instabilities	158
6.3	Interaction between ITTI & EDI	165
6.3.1	Preliminary analysis on the self-consistent simulations . . .	165
6.3.2	Insights from the simplified benchmark case	168
6.4	Conclusion	171
7	Conclusion	173
7.1	Summary of the thesis	173
7.1.1	Importance of code verification	174
7.1.2	Origin of electron anomalous transport	175
7.2	Recommendations and prospects	176
7.2.1	Improvements of <i>LPPic</i>	176
7.2.2	Code validation with experiments	177
7.2.3	Towards an engineering tool?	178
A	Sod test case	179
	Bibliography	181

List of Figures

1.1	From [3]: Ratio of the propellant mass to the initial mass as a function of the exhaust velocity v_{ex} for two values of the velocity increment Δv . The dashed area corresponds to the domain of chemical propulsion with v_{ex} below $5.5 \text{ km} \cdot \text{s}^{-1}$	4
1.2	Artist view of <i>SMART 1</i> (propelled by a Hall thruster) entering lunar orbit. Credit: David A. Hardy, Futures: 50 years in space, Science Photo Library	6
1.3	From [8]: Schematic showing the three main components of an electric thruster (plume neutralizer not shown).	6
1.4	From [13]: Classification of the main types of electric thrusters in the power-specific impulse coordinates. Insets illustrate the principal schematics of each device type.	8
1.5	From [3]: Schematic diagram of a DC electron bombardment Gridded Ion-Thruster.	9
1.6	Example of HT: <i>PPS[®]1350</i> operating with xenon. Credit: Safran Aircraft Engines.	10
1.7	From [22]: Schematic of a Hall thruster.	10
1.8	Axial profiles of the main parameters of an HT discharge (from the self-consistent case of chapter 5)). (a) Ionization source term S_{iz} (red) and axial electric field E_x (blue), with the normalized radial magnetic field B_z (dashed black) and the exit plane position (vertical dashed line). The red arrows delimit the ionization zone while the blue ones delimit the acceleration zone. (b) Ion density n_i (red) and ion axial velocity v_{ix} (blue).	12
1.9	From [40]: Illustrations of convective and absolute instabilities for a perturbed quantity $\delta\tilde{\phi}$ evolving at successive times t_i	18
1.10	From [59]: Effects of the transit-time oscillations on discharge properties through five moments of the oscillation period. On the left: electric potential lines spaced by 30 V for 300 V applied voltage and plasma density (gray scale, $3 \times 10^{18} \text{ m}^{-3}$). On the right: phase-space diagram of ion axial velocities regardless of their radial positions/velocities.	21

1.11	From [122]: Plasma modeling techniques for HT discharge plasmas. The numerical techniques are approximations to the actual physics in which individual atoms and molecules move and collide with each other. Note that the blue arrows denote the particle velocities and the velocity distribution function (VDF) results from the ensemble of particles in the direct kinetic (DK) method. . . .	26
2.1	Schematic of the typical Cartesian mesh used in this work	33
2.2	Particle-In-Cell loop executed every time step.	35
2.3	From [151]: Null collision method.	35
2.4	HLLC approximate Riemann solver. Solution in the intermediate region consists of two constant states separated from each other by a middle wave of speed S^*	46
2.5	Axial profiles of neutral density (top left), velocity (top right) and temperature (bottom left) for a given ionization profile (bottom right) when using a 1 st order Euler scheme (red line) or a 2 nd order Runge-Kutta scheme (orange line). 100 cells are considered, with a CFL of 0.5 and a coefficient of relaxation $\tau=10^{-8}$	50
2.6	Currents in a HT. I_d : discharge current. I_{ae} and I_{ai} : electron and ion anode currents, respectively. I_{cd} and I_{cp} : cathode electron currents in the plume and in the discharge, respectively. I_{az} and I_{bi} : electron and ion currents leaving the domain through the right axial boundary, respectively.	51
3.1	Simulation domain. x is the axial direction, y the (periodic) azimuthal direction. Black pointed dashed line ($x_{B_{max}} = 0.75$ cm): position of maximum radial magnetic field. Green dashed line ($x_e = 2.4$ cm): plane from which electrons are emitted uniformly along the azimuthal direction. The azimuthally averaged fluxes are represented. Γ_{ea} and Γ_{ia} : respectively electron and ion fluxes through the left boundary. Γ_{ec1} : electron flux from the emission plane going into the discharge. Γ_{ec2} and Γ_{ic} : respectively electron and ion fluxes through the right boundary.	60
3.2	Axial profiles of the imposed radial magnetic field and ionization rate. Dashed line corresponds to the position of maximum magnetic field.	62
3.3	(a) : Time evolution of $\frac{J_{ec1}}{J_M}$ for Case 1 for all the codes. Brown dashed line: beginning of time averaging interval (until 20 μ s). (b): Time evolution of $\frac{J_{ec1}}{J_M}$ for Case 1 with code LPP . (c): Corresponding Fast-Fourier-Transform taken from data between 12 and 20 μ s.	66
3.4	2D axial-azimuthal snapshots of the azimuthal electric field (top) and ion density (bottom) obtained with code LPP at $t = 20$ μ s. Dashed line corresponds to the position of maximum magnetic field that separates zone (I) and zone (II).	67

3.5	Case 1 : Azimuthally and time (between 16 and 20 μs) averaged axial profiles of axial electric field (a), ion density (b) and electron temperature (c). Dashed line corresponds to the position of maximum magnetic field.	69
3.6	Case 2 : Azimuthally and time (between 16 and 20 μs) averaged axial profiles of axial electric field (a), ion density (b) and electron temperature (c). Dashed line corresponds to the position of maximum magnetic field.	70
3.7	Case 3 : Azimuthally and time (between 16 and 20 μs) averaged axial profiles of axial electric field (a), ion density (b) and electron temperature (c). Dashed line corresponds to the position of maximum magnetic field.	71
3.8	2D FFT of the azimuthal electric field at $x=0.3$ cm (a) and $x=1.5$ cm (b), obtained with code LPP . Solid white line: ion acoustic dispersion relation. Green dashed lines: wavelength and frequency of the dominant mode.	72
3.9	Case 1 : Axial evolution of dominant mode characteristics for azimuthal electric field (azimuthal instabilities). (a) Wavelength. (b) Frequency. (c) Debye length. (d) Ion plasma frequency. Dashed line corresponds to the position of maximum magnetic field.	73
3.10	Case 2 : Axial evolution of dominant mode characteristics for azimuthal electric field (azimuthal instabilities). (a) Wavelength. (b) Frequency. (c) Debye length. (d) Ion plasma frequency. Dashed line corresponds to the position of maximum magnetic field.	73
3.11	Case 3 : Axial evolution of dominant mode characteristics for azimuthal electric field (azimuthal instabilities). (a) Wavelength. (b) Frequency. (c) Debye length. (d) Ion plasma frequency. Dashed line corresponds to the position of maximum magnetic field.	74
3.12	Azimuthally and time (between 16 and 20 μs) averaged axial profiles of axial electric field and ion density for different number of macroparticles per cell at initialisation $N_{ppc,ini}$. Results obtained with code LPP	75
3.13	Mean value (between 12 and 20 μs) of $\frac{J_{ec1}}{J_M}$ depending on $N_{ppc,final}$ in normal scale (a) and semi-log scale (b). The three benchmark cases correspond to $N_{ppc,final} = 550$ (Case 1), $N_{ppc,final} = 275$ (Case 2) and $N_{ppc,final} = 1100$ (Case 3).	76
3.14	Comparison of 3 simulations with the same code (LPP) for the same input parameters (Case 2). (a): Time evolution $\frac{J_{ec1}}{J_M}$. (b): Azimuthally and time (between 11 and 15 μs as shown on (a)) averaged axial profiles of ion density (blue) and axial electric field (red).	78
3.15	Time evolution of $\frac{J_{ec1}}{J_M}$ for 2 simulations with the same code (LPP) for the same input parameters (Case 2), and the same seed for their RNG.	79

- 3.16 For different cathode models: (a) Time evolution of $\frac{J_{ec,1}}{J_M}$. (b) Time evolution of the total number of macroparticles. Axial profiles (averaged in time and azimuthally) of (c) ion density (solid lines) and axial electric field (dashed lines), (d) axial electron (solid lines) and ion (dashed lines) currents, (e) axial (solid lines) and azimuthal (dashed lines) electron temperatures, (f) axial (solid lines) and azimuthal (dashed lines) ion temperatures. The black horizontal line corresponds to the position of maximum magnetic field. . . . 81
- 3.17 (Left column) 2D maps of azimuthal electric field at $t = 26 \mu s$. The green and red vertical dashed lines indicates the position of the FFT. The black vertical dashed line corresponds to the position of maximum magnetic field. (Middle column) Corresponding 2D FFT at $x=0.4$ cm. (Right column) Corresponding 2D FFT at $x=1.5$ cm. White thick line: ion-acoustic dispersion relation. Red dashed line: ion-acoustic growth rate rescaled by a constant factor to fit the image. The spectrum has been zoomed to focus on the zone of interest. Each row corresponds to a different cathode model: (a) BM - $T_{e,inj} = 0.1$ eV. (b) BM - $T_{e,inj} = 10$ eV. (c) QN - $T_{e,inj} = 0.1$ eV. (d) QN - $T_{e,inj} = 10$ eV. 82
- 4.1 Electron momentum force density terms for the nominal case ($B = 100$ G and $J = 400 \text{ A} \cdot \text{m}^{-2}$) in the azimuthal direction (a) and the axial direction (b). The curves labelled "RHS" represent the sum of all of the individual terms on the right-hand side of equations 4.1 and 4.2. The vertical black dashed lines correspond to the position of the maximum magnetic field. 90
- 4.2 Comparison of the anomalous force approximations with the PIC simulation results for the nominal case. Blue dotted line: $R_{ei,empirical}$ from equation 4.9. Purple line: $R_{ei,saturated}$ from equation 4.10. Orange dotted line: $R_{ei,maxwellian}$ from equation 4.26. Red dotted line: $R_{ei,quasi-linear}$ from equation 4.24. The vertical black dashed line corresponds to the position of the maximum magnetic field. 96
- 4.3 Electron Velocity Distribution Functions in the axial (a) and azimuthal (b) directions for the nominal simulation case at different axial positions. The vertical black dashed line splits the negative and positive velocities. 96
- 4.4 Ratio of the time-averaged wave energy density to the electron thermal energy density as a function of axial position for different magnetic fields strengths with $J = 400 \text{ A} \cdot \text{m}^{-2}$ (a), and discharge current densities with $B = 100$ G (b). The horizontal grey dot-dashed line corresponds to the ion-wave trapping saturation limit. The vertical black dashed lines correspond to the position of the maximum magnetic field. 98

4.5	2D maps of the azimuthal electric field (left column) and ion density (right column) at $t = 15 \mu\text{s}$ for different magnetic field strengths . The vertical black dashed lines correspond to the position of the maximum magnetic field.	101
4.6	Axial profiles (azimuthally and time averaged over the last $10 \mu\text{s}$) of: (a) Magnetic field and ionization source term, (b) Ion (thick line) and electron (dashed line) densities, (c) Axial electric field, (d) Azimuthal electric field, (e) Plasma potential, (f) Total axial current; for different magnetic field strengths . The vertical black dashed lines correspond to the position of the maximum magnetic field.	102
4.7	2D maps of the azimuthal electric field (left column) and ion density (right column) at $t = 15 \mu\text{s}$ for different discharge current densities . The vertical black dashed lines correspond to the position of the maximum magnetic field.	103
4.8	Axial profiles (azimuthally and time averaged over the last $10 \mu\text{s}$) of: (a) Magnetic field and ionization source term, (b) Ion (thick line) and electron (dashed line) densities, (c) Axial electric field, (d) Azimuthal electric field, (e) Plasma potential, (f) Total axial current; for different discharge current densities . The vertical black dashed lines correspond to the position of the maximum magnetic field.	104
4.9	Azimuthal electron momentum terms for different magnetic fields with $J = 400 \text{ A} \cdot \text{m}^{-2}$ (left column) and current densities with $B = 100 \text{ G}$ (right column). The nominal case, shown in figure 4.1(a), corresponds to $B = 100 \text{ G}$ and $J = 400 \text{ A} \cdot \text{m}^{-2}$. The vertical black dashed lines correspond to the position of the maximum magnetic field. The force terms $F_{t,y}$, $F_{E,y}$ and $F_{en,y}$ are not shown for the sake of clarity but are still included in the curve labelled "RHS" that represent the sum of all of the individual terms on the right-hand side of equations 4.2.	106
4.10	Friction force as a function of axial position for different magnetic field strengths (left column) and discharge current densities (right column). The blue thick line corresponds to the PIC results, while the green dashed line corresponds to the Non-Maxwellian approximation. The vertical black dashed lines correspond to the position of the maximum magnetic field.	107
4.11	Comparison between the azimuthal electron-ion and ion-electron force density terms for all of the simulation cases tested. The vertical black dashed lines correspond to the position of the maximum magnetic field.	109
4.12	Axial profile of the imposed neutral density for the cases in section 4.4.	110

4.13	Friction force approximation if: no collisions (i.e. nominal case) (a), only ion/neutral isotropic collisions (b) only ion/neutral charge-exchange collisions (c) all collisions electron/neutral and ion/neutral (d). Vertical black dashed lines correspond to the position of the maximum magnetic field. R_{en} correspond to the electron-neutral momentum collisional drag force term.	111
5.1	Simulation domain. x is the axial direction, y the (periodic) azimuthal direction. Black pointed dashed line ($x_{B_{max}}=2.5$ cm): position of maximum radial magnetic field. Xenon atoms are injected at the anode and electrons are emitted from the cathode.	118
5.2	Axial profiles of the imposed radial magnetic field and initial neutral density. Dashed line corresponds to the position of maximum radial magnetic field.	119
5.3	Time evolution (from 100 μ s) of the effective anode mass flow rate Q for different values of the vacuum permittivity scaling factor α_ϵ . The dashed lines corresponds to the averages. Q_{ini} has been set to $\dot{m}=5$ mg \cdot s $^{-1}$	122
5.4	Time evolution of discharge current for two different cathode models, with $\alpha_\epsilon=64$ (and no anode ion recombination). The dashed horizontal lines (overlapped here) correspond to the mean value at steady state.	122
5.5	$\alpha_\epsilon = 4$: Time evolution of discharge current. Red rectangle corresponds to the BM oscillation analysed in this section.	124
5.6	$\alpha_\epsilon = 4$: Azimuthal terms of electron momentum conservation equation 4.2 for four moments of a breathing mode oscillation: minimum (a), increase (b), maximum (c) and decrease (d). The red line corresponds to the magnetic force term $F_{B,y} = -qn_e B v_{e,x}$ related to the axial electron transport. The cyan $F_{ei,y}$ line corresponds to the instability-enhanced drag force on the electrons. The magenta line corresponds to the electron-neutral collision term $F_{en,y}$. Inset: Time evolution of discharge current, red dot indicating the corresponding time.	124
5.7	$\alpha_\epsilon = 4$: Friction force approximation at different breathing mode moments: (a) minimum, (b) increase, (c) maximum and (d) decrease. PIC values (green) are compared with the Maxwellian approximation (yellow) and the non-maxwellian approximation with the dominant mode from the ion-acoustic approximation (red) or directly from the FFT (cyan). Inset: Time evolution of discharge current, red dot indicating the corresponding time.	127
5.8	Time evolution of discharge current for 4 values of α_ϵ . The dashed horizontal lines correspond to the mean value at steady state.	128

- 5.9 Azimuthal terms of electron momentum conservation equation when the discharge current is minimum (right column) or maximum (left column), for $\alpha_\epsilon=16$ (top row) or $\alpha_\epsilon = 64$ (bottom row). Only the dominant terms contributing to $F_{B,y}$ related to the electron axial transport are displayed: instability-enhanced drag force on the electrons $F_{ei,y}$ (cyan) and electron-neutral collisions force $F_{en,y}$ (magenta). Inset: Time evolution of discharge current, red dot indicating the corresponding time. Vertical black dashed line corresponds to the position of maximum radial magnetic field. 128
- 5.10 Axial profiles of electron-ion friction force averaged over several breathing mode cycles, for different values of α_ϵ . Vertical black dashed line corresponds to the position of maximum radial magnetic field. 130
- 5.11 Axial profiles of some plasma parameters (averaged over several BM oscillations and azimuthally) for $\alpha_\epsilon= 4$ (solid line), $\alpha_\epsilon= 16$ (dashed line) and $\alpha_\epsilon= 64$ (dotted line). (a): Axial electric field (blue) and electron density (red). (b): electron (blue) and ion (red) axial current densities. (c): axial (blue), azimuthal (green) and total (red) electron temperatures. (d): axial (blue), azimuthal (green) and total (red) ion temperatures. 130
- 5.12 Azimuthal electron momentum terms averaged over several BM oscillations, for different values of α_ϵ . The red line corresponds to $F_{B,y} = -qn_e Bv_{e,x}$, related to the axial electron transport. The cyan $F_{ei,y}$ line corresponds to the instability-enhanced drag force on the electrons. The magenta line corresponds to the electron-neutral collision term $F_{en,y}$ 131
- 5.13 Axial (blue) and azimuthal (orange) EVDF for 3 axial positions (rows) and for 4 values of α_ϵ (columns) when I_d increases. On the top left, the value of the azimuthal EVDF derivative at null-velocity (named A) is displayed. Careful, the x-axis range has been adapted for the best display. 133
- 5.14 Axial (blue) and azimuthal (orange) EVDF for 3 axial positions (rows) and for 4 values of α_ϵ (columns) when I_d decreases. On the top left, the value of the azimuthal EVDF derivative at null-velocity (named A) is displayed. Careful, the x-axis range has been adapted for the best display. 133
- 5.15 Axial (blue) and azimuthal (orange) IVDF for 3 axial positions (rows) and for 4 values of α_ϵ (columns) when I_d increases. Top row: $x = 1$ cm, middle row: $x = 2$ cm and bottom row: $x = 3$ cm. Careful, the x-axis range has been adapted and the azimuthal IVDF y-axis has been put in log-scale for the best display. 134

- 5.16 Axial (blue) and azimuthal (orange) IVDF for 3 axial positions (rows) and for 4 values of α_ϵ (columns) when I_d decreases. Top row: $x = 1$ cm, middle row: $x = 2$ cm and bottom row: $x = 3$ cm. Careful, the x-axis range has been adapted and the azimuthal IVDF y-axis has been put in log-scale for the best display. 134
- 5.17 $\alpha_\epsilon = 4$: Time and axial evolution during one BM oscillation of: (a) axial electric field, (b) azimuthal electric field, (c) normalized electron density and (d) normalized plasma potential fluctuations. Green vertical curve: axial position of null ion axial velocity. Red vertical curve: axial position of ion sonic point ($v_{ix} = c_s$). Horizontal white dashed lines: moments used to compute figure 5.18 (I_d maximum at $t=120\mu s$). Vertical black dashed lines: axial position of maximum magnetic field. 136
- 5.18 $\alpha_\epsilon = 4$: Axial profiles of the azimuthal electric field (divided by 4×10^4), normalized electron density and normalized plasma potential fluctuations for different moments of a BM oscillation (same as the ones in figure 5.7). Vertical green dashed lines: axial position of null ion axial velocity. Vertical red dashed lines: axial position of ion sonic point ($v_{ix} = c_s$). Vertical black dashed lines: axial position of maximum magnetic field. Horizontal black dashed lines: expected amplitude for a fully-saturated ion-acoustic instability i.e. $\frac{1}{6\sqrt{2}}$. Inset: Time evolution of discharge current, red dot indicating the corresponding time. 137
- 5.19 2D maps of azimuthal electric field for different α_ϵ , when I_d increases. Red dashed lines: axial position of ion sonic point ($v_{ix} = c_s$). White dashed lines: axial position of FFTs (figure 5.20). Black dashed line: position of maximum magnetic field. 139
- 5.20 Corresponding FFT for $x=1$ cm (left column) and $x=3$ cm (right column), when I_d increases. White thick line: ion-acoustic dispersion relation. Red dashed line: ion-acoustic growth rate rescaled by a constant factor to fit the image. The spectrum has been zoomed to focus on the zone of interest. 139
- 5.21 2D maps of azimuthal electric field for different α_ϵ , when I_d decreases. Red dashed lines: axial position of ion sonic point ($v_{ix} = c_s$). White dashed lines: axial position of FFTs (figure 5.22). Black dashed line: position of maximum magnetic field. 140
- 5.22 Corresponding FFT for $x=1$ cm (left column) and $x=3$ cm (right column), when I_d decreases. White thick line: ion-acoustic dispersion relation. Red dashed line: ion-acoustic growth rate rescaled by a constant factor to fit the image. The spectrum has been zoomed to focus on the zone of interest. 140

- 6.1 **$\alpha_\epsilon=16$** : Time evolution of the discharge current for the nominal case and the case with EDI suppressed (by averaging azimuthally). Dashed horizontal lines: mean value at steady state. 146
- 6.2 **$\alpha_\epsilon=16$ - EDI suppressed**: Time and axial evolution of (a) axial electric field and (b) ion density. Green vertical curve: axial position of null ion axial velocity. Red vertical curve: axial position of ion sonic point ($v_{ix} = c_s$). The white dashed lines have been used to compute the wave velocity. 146
- 6.3 **$\alpha_\epsilon=16$ - EDI suppressed**: 4 different moments of an ion transit-time oscillation. Top: Axial ion phase-space with $v_{i,max}$ given by the horizontal red dashed line and in inset, time evolution of discharge current with the green dot indicating the corresponding time. The yellow zones indicate the ions that will form the low-velocity group in the plume. Bottom: Corresponding profiles of ion density (blue line), axial electric field (solid red line) and electric potential (dashed red line, normalized). 148
- 6.4 **$\alpha_\epsilon=16$ - EDI suppressed**: Time evolution at $x = 1.5$ cm of: (a) ion density, neutral density (dashed blue) and axial electric field - (b) Axial ion and electron velocity and ion sound speed (dashed red) - (c) Electron and ion (dashed blue) temperatures and ionization source term. The vertical black dashed lines correspond to the time where the ions become supersonic ($v_{ix} > c_s$). 149
- 6.5 **EDI suppressed**: For different α_ϵ , (a) time evolution of the discharge current (the dashed horizontal lines correspond to the mean value at steady state) and (b) corresponding FFT. 151
- 6.6 **$\alpha_\epsilon=64$ - EDI suppressed - Frozen neutrals**: Time evolution of discharge current and neutral density at the exit plane. The neutrals have been frozen at the time indicated by the vertical black dashed line. 151
- 6.7 **$\alpha_\epsilon=16$, nominal**: 4 different moments of an ion transit-time oscillation. Top: Axial ion phase-space with $v_{i,max}$ given by the horizontal red dashed line and in inset, time evolution of discharge current with the green dot indicating the corresponding time. The yellow zones indicate the ions that will form the low-velocity group in the plume. Bottom: Corresponding profiles of ion density (blue line), axial electric field (solid red line) and electric potential (dashed red line, normalized). 153

- 6.8 **$\alpha_\epsilon=64$, nominal**: 4 different moments of an ion transit-time oscillation. Top: Axial ion phase-space with $v_{i,max}$ given by the horizontal red dashed line and in inset, time evolution of discharge current with the green dot indicating the corresponding time. The yellow zones indicate the ions that will form the low-velocity group in the plume. Bottom: Corresponding profiles of ion density (blue line), axial electric field (solid red line) and electric potential (dashed red line, normalized). 154
- 6.9 **$\alpha_\epsilon = 64$** : Time evolution of discharge current for 4 values of azimuthal length L_y . The dashed horizontal lines correspond to the mean value at steady state. 156
- 6.10 **$\alpha_\epsilon = 64$** : Azimuthal electron momentum terms averaged over several BM oscillations, for different values of L_y . The red line corresponds to $F_{B,y} = -qn_e Bv_{e,x}$, related to the axial electron transport. The cyan $F_{ei,y}$ line corresponds to the instability-enhanced drag force on the electrons. The magenta line corresponds to the electron-neutral collision term $F_{en,y}$ 156
- 6.11 **$\alpha_\epsilon = 64$** : Averaged profiles over several BM oscillations (and azimuthally), for different L_y , of: (a) Electron-ion friction force. (b) Ratio of the wave energy density to the electron thermal energy density. Horizontal grey dot-dashed line: ion-wave trapping saturation limit (Eq. 4.29). Vertical coloured dashed lines: axial position of ion sonic point ($v_{ix} = c_s$). Black dashed line: position of maximum magnetic field. 157
- 6.12 **$\alpha_\epsilon = 64, L_y = 8$** : Time and axial evolution during one BM oscillation of: (a) axial electric field, (b) azimuthal electric field, (c) normalized electron density and (d) normalized plasma potential fluctuations. Green vertical curve: axial position of null ion axial velocity. Red vertical curve: axial position of ion sonic point ($v_{ix} = c_s$). Horizontal white dashed line: moments used to compute figure 6.13 (I_d maximum at $t=266\mu s$). Vertical black dashed lines: axial position of maximum magnetic field. 159
- 6.13 **$\alpha_\epsilon = 64, L_y = 8$** : Axial profiles of the azimuthal electric field (divided by 5×10^3), normalized electron density and normalized plasma potential fluctuations for different moments of a BM oscillation. Vertical green dashed lines: axial position of null ion axial velocity. Vertical red dashed lines: axial position of ion sonic point ($v_{ix} = c_s$). Vertical black dashed lines: Axial position of maximum magnetic field. Horizontal black dashed lines: expected amplitude for a fully-saturated ion-acoustic instability i.e. $\frac{1}{6\sqrt{2}}$. Inset: Time evolution of discharge current, red dot indicating the corresponding time. 160

- 6.14 $\alpha_\epsilon = 64$: Axial (blue) and azimuthal (orange) IVDF for 3 axial positions (rows) and for 4 values of L_y (columns) when I_d decreases. Careful, the azimuthal IVDF y-axis has been put in log-scale for the best display. 160
- 6.15 $\alpha_\epsilon = 64$: 2D maps of azimuthal electric field for different L_y , when I_d increases. Red dashed lines:axial position of ion sonic point ($v_{ix} = c_s$). White dashed lines: axial position of FFTs (figure 6.16). Black dashed line: position of maximum magnetic field. . . 162
- 6.16 $\alpha_\epsilon = 64$: Corresponding FFT for $x=1$ cm (left column) and $x=3$ cm (right column), when I_d increases. White thick line: ion-acoustic dispersion relation. Red dashed lines: ion-acoustic growth rate rescaled by a constant factor to fit the image. The spectrum has been zoomed to focus on the zone of interest. 162
- 6.17 $\alpha_\epsilon = 64$: 2D maps of azimuthal electric field for different L_y , when I_d decreases. Red dashed lines: axial position of ion sonic point ($v_{ix} = c_s$). White dashed lines: axial position of FFTs (figure 6.18). Black dashed line: position of maximum magnetic field. . . 163
- 6.18 $\alpha_\epsilon = 64$: Corresponding FFT for $x=1$ cm (left column) and $x=3$ cm (right column), when I_d decreases. White thick line: ion-acoustic dispersion relation. Red dashed line: ion-acoustic growth rate rescaled by a constant factor to fit the image. The spectrum has been zoomed to focus on the zone of interest. 163
- 6.19 $\alpha_\epsilon = 64, L_y = 8$ cm: PSD of azimuthal electric field at (a) $x = 1$ cm, (b) $x = 2$ cm and (c) $x = 3$ cm. The white vertical dashed lines correspond to moments when the discharge current is maximum. 164
- 6.20 $\alpha_\epsilon=64, L_y = 4$ cm: Dynamical Mode Decomposition at a specific time. Mode 1 corresponds to the sum of the modes between 100 and 500 kHz, Mode 2 between 500 kHz and 1 MHz, Mode 3 between 1 and 2 MHz, Mode 4 between 2 and 4 MHz. The sum of all these modes is compared with the original signal on the bottom row. All the images have the same colorbar range. 166
- 6.21 $L_y = 1$ cm: Power Spectral Density of ion density fluctuations normalized by the ion density for different values of α_ϵ , at different axial positions. 167
- 6.22 $\alpha_\epsilon=64$: Power Spectral Density of ion density fluctuations normalized by the ion density for different values of L_y , at different axial positions. 169

6.23	Benchmark case with $L_y=10$ cm: (a) 2D maps of azimuthal electric field at $t = 26 \mu\text{s}$. The green and red vertical dashed lines indicates the position of the FFT. The black vertical dashed line corresponds to the position of maximum magnetic field. (b) Corresponding 2D FFT at $x=0.5$ cm. (c) Corresponding 2D FFT at $x=1.5$ cm. White thick line: local ion-acoustic dispersion relation. White dashed line: ion-acoustic dispersion relation convected from $x=0.5$ cm. Red dashed line: ion-acoustic growth rate rescaled by a constant factor to fit the image. The spectrum has been zoomed to focus on the zone of interest.	170
A.1	Initial conditions of Sod test case, with left state 1 (ρ_1, u_1, P_1) and right state 2 (ρ_2, u_2, P_2) . The absciss is in centimeters.	179
A.2	Results of Sod test case for $\Delta z = 2 \times 10^{-3}$ cm and $t=0.8$ ms. Dashed black line: analytical solution. Blue line: LPPic solver. Diaphragm was originally at $z=0.5$ cm. Adapted from [176]. . . .	180

List of Tables

2.1	Nominal input parameters for the simplified benchmark case (chapters 3 and 4) and the self-consistent simulations (chapters 5 and 6).	38
3.1	Main codes specificities.	64
3.2	Three benchmark cases. N_{ppc} is the number of macroparticles per cell. The nominal case is Case 1.	65
3.3	Cathode models simulated. The case in bold (case 2) represents the nominal case.	80
4.1	Simulation cases. Case 0 represents the nominal case.	99
5.1	Typical computational requirements to simulate 150 μs of physical time. The total simulated time is indicated in the last column. . .	120

List of acronyms

1D, 2D, 3D	One-dimensional, Two-dimensional, Three-dimensional
BM	Breathing Mode
CE	Current-Equality (cathode model)
CFL	Courant-Friedrichs-Lewy condition
CIC	Cloud-In-Cell
CPU	Central Processing Unit
DMD	Dynamic Mode Decomposition
DR	Dispersion Relation
EDI	Electron Drift Instability
EP	Electric Propulsion
FFT	Fast Fourier Transform
GIT	Gridded-Ion-Thruster
HDF5	Hierarchical Data Format 5
HLLC	Harten-Lax-van Leer Contact solver
HT	Hall Thruster
IAI	Ion-Acoustic Instability
ITT	Ion Transit-Time
LANDMARK	Low temperAture magNetized plasMA benchmaRKs
LHS	Left Hand Side
LPP	Laboratoire de Physique des Plasmas
MCC	Monte Carlo Collisions
MPI	Message Passing Interface
ND	Neutral Dynamics
PIC	Particle-In-cell
PSD	Power Spectral Density
QN	Quasi-Neutral (cathode model)
RHS	Right Hand Side
RMS	Root Mean Square
RNG	Random Number Generator
VDF	Velocity Distribution Function
Xe	Xenon

Chapter 1

Introduction

Contents

1.1 A new age for spacecraft propulsion	1
1.1.1 Electric propulsion	5
1.1.2 A broad range of needs	7
1.1.3 Working principles of the two main electric thrusters	8
1.2 Hall thrusters - General concepts	12
1.2.1 Basic concepts of Hall thruster plasma physics	13
1.2.2 Hall thruster instabilities	16
1.2.3 Why do we keep studying Hall thrusters?	23
1.3 Hall thrusters - Modeling	25
1.3.1 Multi-fluid models	27
1.3.2 Particle-In-Cell models	28
1.3.3 Hybrid and Direct-Kinetic models	29
1.4 Scope and outline of the thesis	29

1.1 A new age for spacecraft propulsion

Based on current archaeological evidence, modern humans have existed for roughly 200,000-300,000 years. Over these many years, people have constantly contemplate the stars, wondering what was hidden behind this bright immensity. While gods and spirits were for a long time closely related to the sky observation (astrology and astronomy were hardly distinguishable up to the Middle Age), the Copernican revolution during the Renaissance period was a turning point. Copernicus in 1543 (heliocentric system), Galileo in 1610 (first telescope), Kepler in 1619 (three laws of planetary motion) and Newton in 1687 (law of universal gravitation) were the pioneers of modern astronomy.

But seeing was not enough.

In 1903, Konstantin Tsiolkovsky proposed to use rockets to enable human spaceflight [1]. On the other side of the Earth, two decades later, Robert Goddard designed and launched the first liquid-fueled rocket in 1926. In the 20th

century, war became the main fuel for rocket science. The German V2 missile, developed during World War II, was the first artificial object to travel into space by crossing the Karman line (1944). During the Cold War, instead of fighting on the ground, the United States and the Soviet Union decided to take part in the so-called Space Race. From the first satellite in orbit around Earth (*Sputnik 1* in 1957) to the first man on the Moon (*Apollo 11* in 1969), in merely twelve years, thousands of rockets were launched into space, writing the first page of human space exploration history.

These first decades were characterized by human-centered exploration that inspired most of the scientists and fed the imagination of people who needed to recover from the horrors of World War II. When private companies, such as *Intelsat* in 1965, appeared in the satellite market, the near-Earth orbit grew in interest: the broad range of applications for satellites (telecommunications, Earth observation, localisation services, etc.) was a bonanza. The post Cold War period marked a loss of impetus for space innovation, driven mainly by the development of always larger satellites to meet the increasing bandwidth requirements. In the early XXIst century, newcomers such as *Space X* or *Rocket Lab* gave a breath of fresh air: they demonstrate the capability of launching rockets and putting satellites in orbit, which was previously only achievable by governmental space agencies. Their fast success paved the way to the creation of numerous start-ups and small companies for which *Agile* development and cost/time efficiency were at the center of their business model. This current framework, often called the *New Space industry*, represents a healthy environment to encourage space innovation and breakthroughs. The current Mars Space Race is a good example of how these new private companies gave a boost to governmental space agencies.

However, the increasing number of satellites in orbit (around 2000 currently) should be put into perspective with the need to keep control of their trajectories. The recent collision avoidance manoeuvre (between a *Space X* and an *ESA* satellite) shed the light on the importance of space debris removal, while strengthening the paramount need of on-board propulsion systems for satellites. These thrusters have often two main objectives: compensate the atmospheric drag that inescapably make the satellites lose altitude (station-keeping), but also place the satellite in a defined orbit (orbit raising). While most satellites are still using chemical thrusters, the increasing demand for lighter satellites has made Electric Propulsion (EP) significantly more popular: between 2012 and 2016, roughly 25 percent of the 106 satellites ordered were using EP, according to Northern Sky Research [2].

But, why this growing interest towards EP?

If we consider a satellite of mass m subject to external forces \mathbf{F}_{ext} , its motion is determined by the second law of Newton

$$m \frac{d\mathbf{v}}{dt} = \mathbf{F}_{ext} - \frac{d(m_p \mathbf{v}_{ex})}{dt}, \quad (1.1)$$

with \mathbf{v} its velocity and m_p the mass of propellant ejected at the exhaust veloc-

ity \mathbf{v}_{ex} . The last term corresponds to the time rate of change of the propellant momentum, i.e. the matter ejected at high velocity that will propel the satellite. This is an important parameter for space propulsion, called the thrust \mathbf{T} . Assuming a constant exhaust velocity, it can be expressed as

$$\mathbf{T} = \frac{d(m_p \mathbf{v}_{ex})}{dt} = \frac{dm_p}{dt} \mathbf{v}_{ex} = \dot{m} \mathbf{v}_{ex}, \quad (1.2)$$

with \dot{m} the propellant mass flow rate. If we integrate equation 1.1 between an initial time 0 and a final time f , neglecting all external forces, we can obtain the increment in velocity Δv

$$\Delta v = v_f - v_0 = v_{ex} \ln \left(\frac{m_0}{m_f} \right) = v_{ex} \ln \left(1 + \frac{m_p}{m_f} \right). \quad (1.3)$$

This equation is often referred as the Rocket equation, or the Tsiolkovsky equation [1]. One can notice that the initial mass m_0 is the sum of the final mass m_f (often called the "dry" mass) and the propellant mass m_p . The increment of velocity Δv is a crucial parameter that characterized any space missions: it lies between $9.4 \text{ km} \cdot \text{s}^{-1}$ (Low-Earth Orbit) and $13.3 \text{ km} \cdot \text{s}^{-1}$ (Geostationary Orbit) for near-Earth missions and can be way higher for deep-space exploration. To obtain a given Δv , one can increase the amount of propellant (which will decrease the available payload mass) or, more efficiently, use a thruster with a high exhaust velocity.

The Rocket equation can be rewritten to express the amount of propellant needed to obtain a fixed increment of velocity

$$m_p = m_0 \left[1 - \exp \left(-\frac{\Delta v}{v_{ex}} \right) \right]. \quad (1.4)$$

Hence, to decrease m_p and allow for more payload mass, a thruster with a sufficient exhaust velocity (at least higher than the Δv needed) is required. However, in chemical thrusters, the exhaust velocity is limited by the energy per unit of mass stored in the propellant. For example, the maximum exhaust velocity obtained with the current most efficient chemical reaction (the oxygen-hydrogen combustion, used in the Vulcain engine of the last *Ariane 6*) is only $5.5 \text{ km} \cdot \text{s}^{-1}$. We can see in figure 1.1 that even for a mission with a small Δv of $5 \text{ km} \cdot \text{s}^{-1}$, the mass of propellant needed with a chemical thruster is close to the initial mass ($\frac{m_p}{m_0} \approx 0.6$ for the Vulcain engine) and hence, it drastically limits the available mass for the satellite payload. On the contrary, in an electrical thruster, the energy conversion mechanism is different (an external energy source is used to energize and accelerate the propellant) which removes the maximum limit for the exhaust velocity and makes EP a suitable option for high- Δv missions.

A common parameter is used to quantify the thruster efficiency regarding the propellant consumption, the so-called specific impulse I_{sp} . It corresponds to the time during which a given quantity of propellant can provide a thrust equivalent

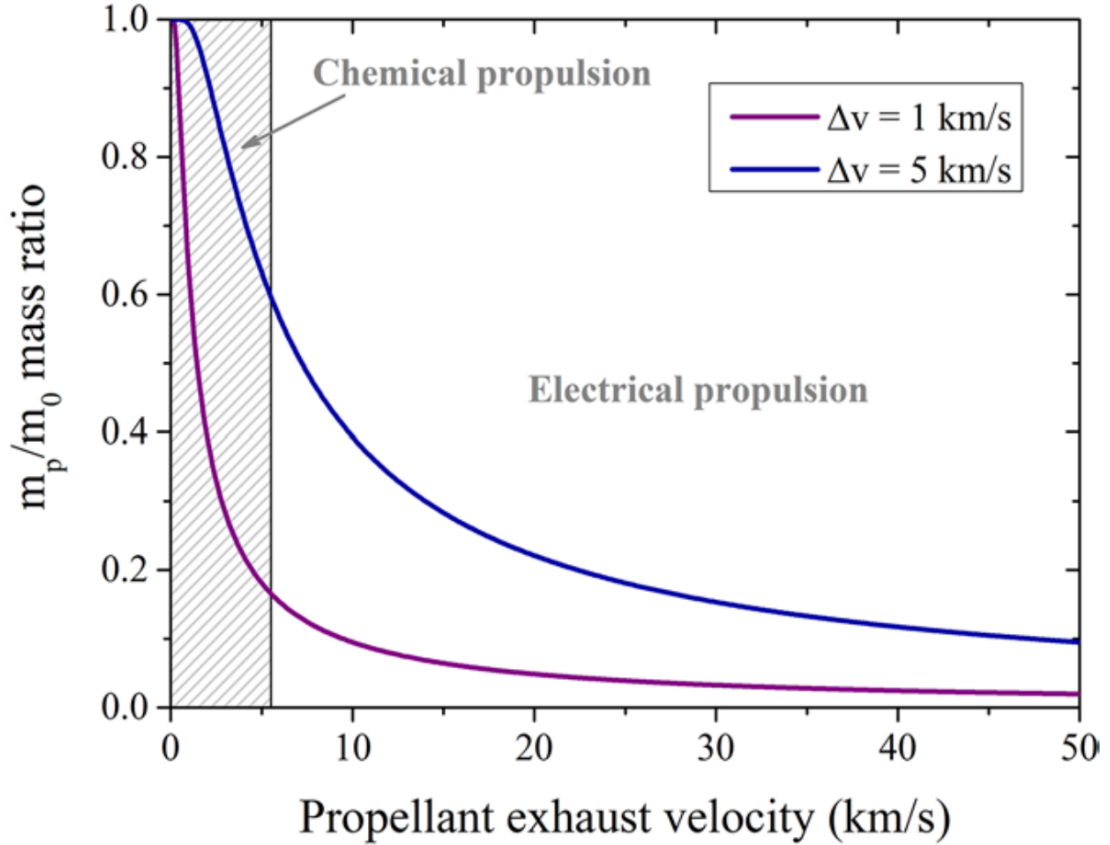


Figure 1.1 – From [3]: Ratio of the propellant mass to the initial mass as a function of the exhaust velocity v_{ex} for two values of the velocity increment Δv . The dashed area corresponds to the domain of chemical propulsion with v_{ex} below $5.5 \text{ km} \cdot \text{s}^{-1}$.

to its weight at sea-level and it can be expressed (if the thrust is considered constant) as the ratio between the exhaust velocity v_{ex} and the gravitational acceleration $g=9.81 \text{ m} \cdot \text{s}^{-2}$

$$I_{sp} = \frac{T}{\frac{dm_p}{dt}g} = \frac{v_{ex}}{g}. \quad (1.5)$$

The specific impulse is expressed in unit of time (often seconds): the higher I_{sp} , the more efficient will the propellant be.

Finally, a last important parameter needs to be taken into account, namely the thrust-to-power ratio. Basically, the thrust efficiency η is given by

$$\eta = \frac{\frac{1}{2}\dot{m}v_{ex}^2}{P}. \quad (1.6)$$

The thrust-to-power ratio T/P can be expressed as

$$\frac{T}{P} = \frac{2\eta}{v_{ex}}. \quad (1.7)$$

We can see that if we want to increase v_{ex} , even at optimum efficiency of $\eta=1$, the thrust to power ratio will decrease, i.e. the power needed will be more important. Hence, the attainable exhaust velocity is capped by the power available on the satellite. Even though nuclear reactors can be used on satellites and will be needed for deep-space missions [4] (with the final objective of using fusion reactors instead of fission ones), the power often comes from solar panels which can produce from several to thousands Watts, depending on their size, efficiency and orientation with respect to the Sun.

Despite the specific impulse of electric thrusters being higher than chemical thrusters (around 5000 s compared to around 500 s), they deliver a thrust orders of magnitude lower (around 100 mN compared to around 1 MN). Hence, chemical propulsion remains the only viable way of launching rockets. However, electric propulsion appears to be the most suitable option for in-space thrusters.

1.1.1 Electric propulsion

The history of EP starts with the same pioneers than for chemical propulsion (Tsiolkovsky, Goddard, Oberth), over one century ago. But at that moment, the relevant scientific fields (plasma physics, electrical engineering, etc.) were not mature enough and their brilliant ideas have not been applied to build thrusters [5]. It was many decades later, in 1964, that the first electric thruster was fired in space, aboard the SERT-1 spacecraft. This Gridded Ion Thruster (GIT) was later followed by a Hall thruster (HT) in 1972, aboard the *Meteor 18* satellite. While these two types of electric thrusters were both studied independently in the US and in USSR, the former decided to use mainly the GIT while the latter focused on the HT development, lead by Morozov [6]. The situation changed in 1991 when the Cold War ended and the HT Russian design plans were made available. It is interesting to note that the French spatial agency (CNES) decided to focus its EP research work on this particular thruster technology and, in collaboration with Safran Aircraft Engines (SAE), they successfully equipped the *SMART-I* satellite (that reached the moon orbit in 2003) with Hall Thrusters (*PPS[®]1350*). Since then, almost 600 spacecraft have been launched, with various types of electric thrusters. For a more detailed history of EP, the reader may refer to the review of Choueiri [5] for the first 50 years, or the more recent review of Lev *et al.* [7].

As mentioned earlier, what distinguishes an electric thruster from a chemical one is the decoupling between energization (a plasma is produced by adding energy to a gas) and acceleration (thrust is produced by accelerating the plasma charged particles). Hence, an electric thruster is usually decomposed in three separate zones: the region where the plasma is created (plasma coupling region), the one where it is accelerated (ion extraction/acceleration region) and the thruster plume (ion beam neutralization/detachment region), as seen in figure 1.3. The thruster plume needs to be neutral because charged particles could interact with other subsystems of the satellite and perturb their operation. Moreover, plume neutralization is necessary to avoid space charge region that can be a barrier for



Figure 1.2 – Artist view of *SMART 1* (propelled by a Hall thruster) entering lunar orbit. Credit: David A. Hardy, *Futures: 50 years in space*, Science Photo Library

Ion extraction & acceleration

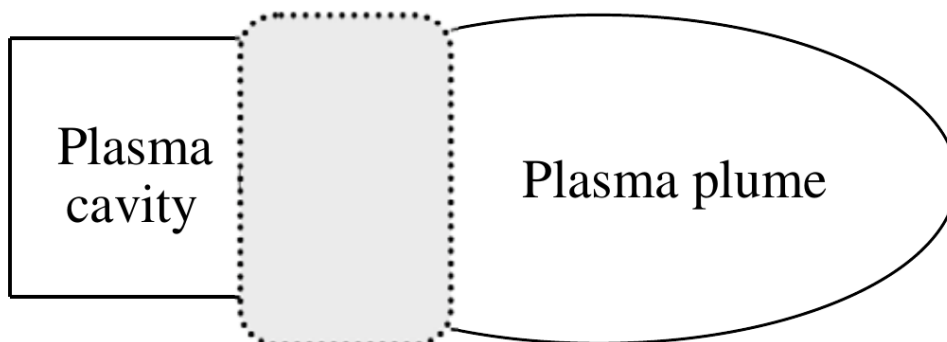


Figure 1.3 – From [8]: Schematic showing the three main components of an electric thruster (plume neutralizer not shown).

the following ions.

Electric thrusters are usually distinguished by the acceleration method used to produce the thrust. Hence, we can list three main categories:

- **Electrothermal thrusters:** the propellant is heated electrically (by a resistive heater for *resistojets* or with a high current arc for *arcjets*) and this thermal energy is then converted in kinetic energy by a nozzle. The propellant can also be heated by a radio-frequency source [9].
- **Electrostatic thrusters:** the propellant is accelerated by a static electric field, created by a potential difference applied between two close parallel grids (for GIT) or between an anode and a cathode at each end of the thruster (for HT).
- **Electromagnetic thrusters:** the propellant is accelerated by a combination of magnetic and electric fields (i.e. by the Lorentz force). One can mention the Helicon Double Layer Thruster [10], along with the very promising VASIMR technology [11].

1.1.2 A broad range of needs

From the diversity of space missions stems the need of widening the thruster power capabilities. The specific impulse and power ranges of the main types of electric thrusters are given in figure 1.4. In the last decade, mainly for constellation purposes (like OneWeb), the number of small satellites (micro and nano-satellites) has grown exponentially, and with them, the need of low-power thrusters (10-500 W). Many companies have already developed these smaller thrusters, such as ThrustMe (iodine gridded thruster) and ExoTrail (HT) in France. Moreover, high-power thrusters (5-25 kW) are needed for deep-space missions [12] and manned flight, to the Moon, Mars, or even beyond.

However, this scaling is often done empirically (trial and error method), which limits the efficiency of the newly developed thrusters and increases the development time and cost. Innovative spacecraft technologies are also under-development [14] to meet these new needs and, as mentioned before, alternative propellants must be found to overcome the xenon problematic [15, 16]. The reader can refer to the review of Levchenko *et al.* [13] for more insights on the future of plasma propulsion.

The working principles of the two most commonly used thrusters (GIT and HT) are described in the following. For more general informations on electric propulsion devices, the reader may refer to detailed textbooks [17, 18] or review articles [19, 8, 3].

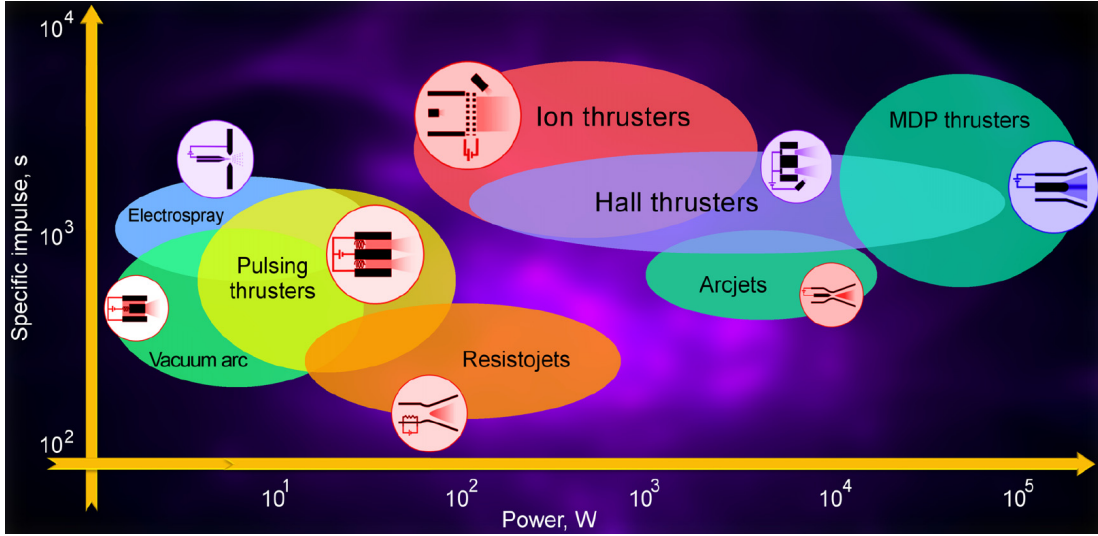


Figure 1.4 – From [13]: Classification of the main types of electric thrusters in the power-specific impulse coordinates. Insets illustrate the principal schematics of each device type.

1.1.3 Working principles of the two main electric thrusters

Gridded Ion Thrusters (GIT)

Whereas GIT can differ by the way the plasma is created (Direct-Current (DC) heating or radio-frequency (RF) heating), the thrust is always produced by ions extracted and accelerated by a multi-aperture grid assembly, commonly two parallel grids, as seen in figure 1.5. Each grid is biased, and the potential difference induces an electric field which accelerates the ions produced upstream. A source of electrons is then needed to neutralize the ion beam of the plume.

The main characteristic of GIT is that the thrust is directly proportional to the ion current density. However, this extracted ion current density J_i is limited by space-charge saturation. Its maximum value is a function of the discharge voltage V and the distance between the grids d , given by the Child-Langmuir law

$$J_{max} = \frac{4\epsilon_0}{9} \sqrt{\frac{2e}{M}} \frac{V^{3/2}}{d^2}, \quad (1.8)$$

with ϵ_0 the vacuum permittivity, e the elementary charge and M the ion mass. Hence, while GIT have the advantage of a well-focused ion beam (no divergence), this fundamental limitation is a drawback for the maximum achievable thrust.

No more details on GIT will be given here, as these thrusters are out of scope of this manuscript, and the reader can refer to [20] for the history of GIT or [21] for an example of GIT global model.

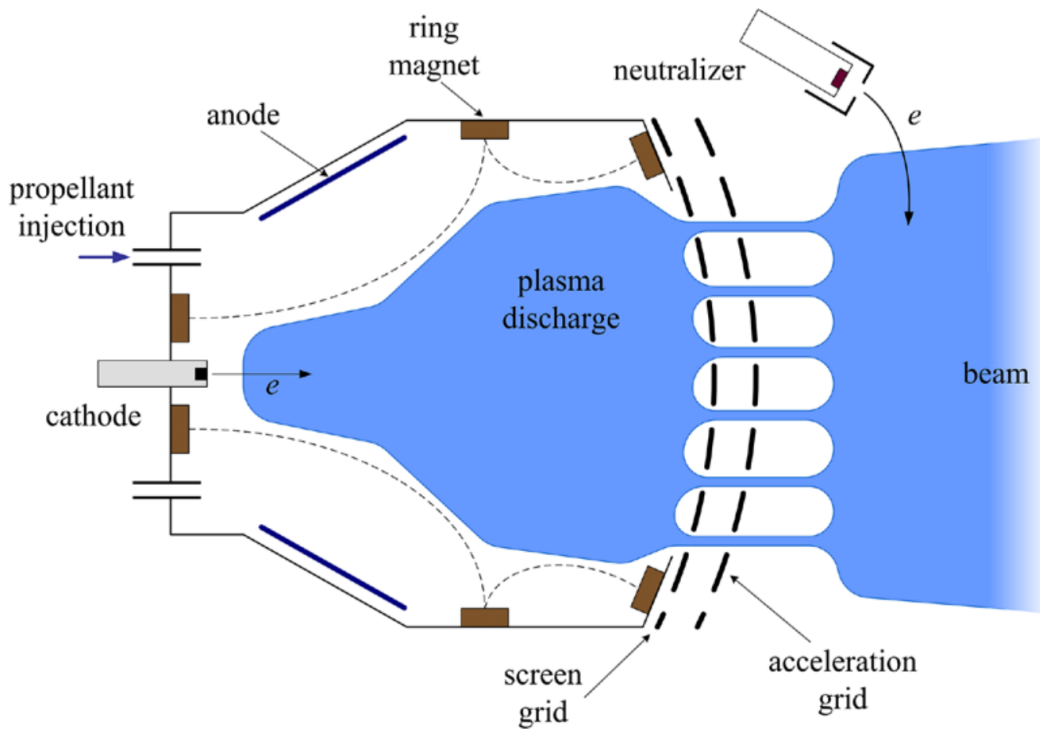


Figure 1.5 – From [3]: Schematic diagram of a DC electron bombardment Gridded Ion-Thruster.

Hall thrusters (HT)

Since their original development in the mid-1960s, mainly in the Soviet Union at the instigation of Morozov, many experimental, numerical and theoretical work have been undergone to better understand the Stationary Plasma Thrusters (SPT), or Hall thrusters (HT), that have now been propelling many satellites.

The Hall thruster working principle will be detailed more extensively compared to the GIT. However, for additional insights, the reader can refer to the initial work of Morozov *et al.* [23, 6] or various topical reviews [24, 25, 22], including one focused on the French research [19]. Other closed-drift thrusters are often associated with HT, such as the Thruster Anode Layer (TAL) with a shorter acceleration region and conducting walls instead of dielectric ones [26]. Even though most of the results that will be presented in this work can be applied to them, the study will be focused on typical SPT thrusters such as the *SPT-100* or the *PPS[®]1350*.

A side and front view of a Hall thruster are displayed in figure 1.7. Their working principle is rather simple:

1. Neutral gas is injected through an anode at one end of the discharge channel. At the other end, electrons are emitted from a cathode. However, the gas pressure is very low and without an imposed magnetic field, the ionization mean free path is orders of magnitude longer than the thruster size and

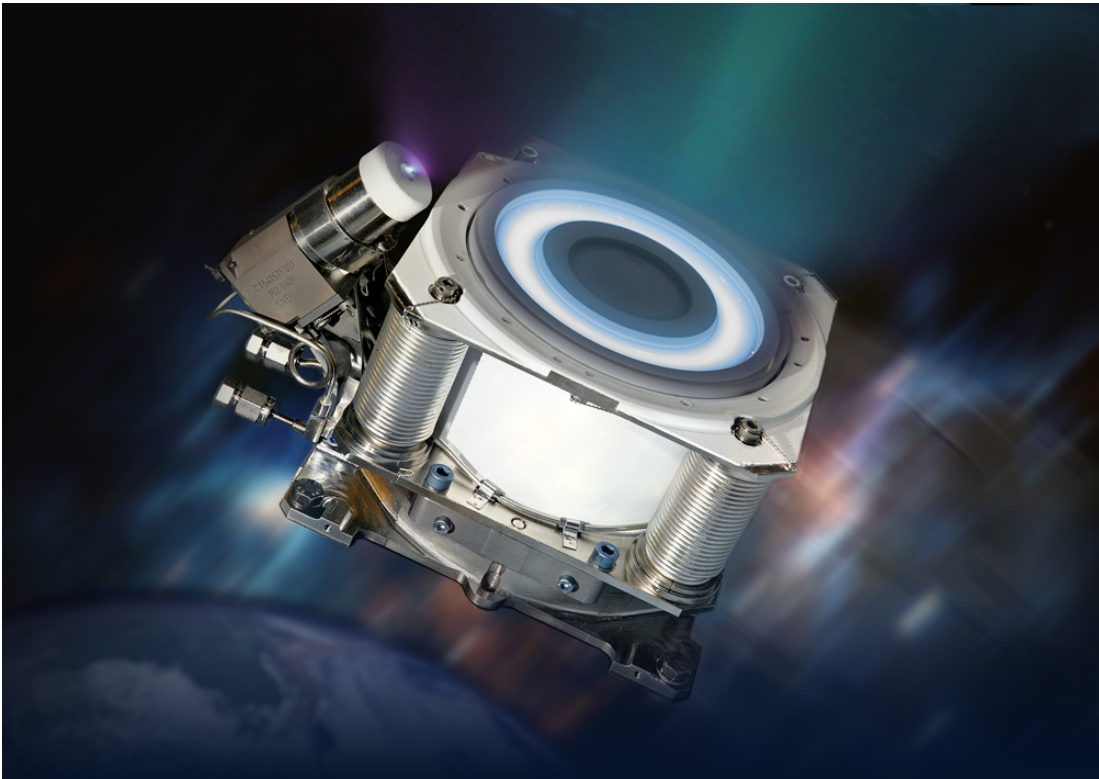


Figure 1.6 – Example of HT: *PPS® 1350* operating with xenon. Credit: Safran Aircraft Engines.

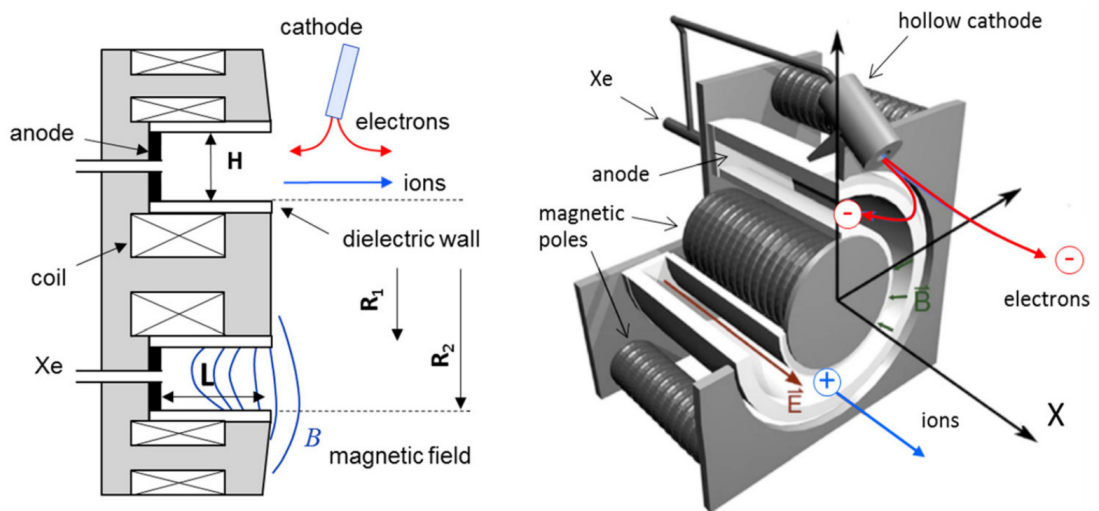


Figure 1.7 – From [22]: Schematic of a Hall thruster.

hence, the ionization efficiency (mass flow rate of output ions over the one of input neutrals) is low.

2. For this reason, coils are added to the thruster (often 5 coils, with one central and four on the corners) in order to create a radial magnetic field which acts to confine the electrons: when they enter the channel from the cathode, they are trapped by this magnetic field and due to the $\mathbf{E} \times \mathbf{B}$ configuration, they drift in the azimuthal direction. Hence, the ionization efficiency will be greatly increased (they will encounter more neutrals to ionize), up to 95%.
3. Due to the potential difference imposed between the anode and the cathode, an axial electric field will form and accelerate the ions created inside the channel, to produce the thrust. Also, a part of the electrons emitted by the cathode are meant to neutralize this ion plume.

To better understand this working principle, the averaged axial profiles of the main parameters of interest in a HT have been displayed in figure 1.8. First, it highlights a fundamental feature of HT: the presence of two different zones, an upstream one (near $x = 1.5$ cm) where the ions are created, called the **ionization zone**, and a downstream one (near $x = 2.5$ cm) characterized by a strong axial electric field, called the **acceleration zone**. The HT performance depends on how these two zones will overlap: if they are too far, the ions will not experience any electric field and hence will stay immobile after being created. If the overlap is too important, some ions will only experience a small electric field and hence, reach lower axial velocities. We can relate the position of the axial electric field peak to the one of the maximum of radial magnetic field (with B_{max} often set to 150-200 G): the electric field is forming where the electron mobility is lower due to the magnetic trapping. In most of the HT, this position corresponds to the exit plane of the discharge channel. Finally, we can see that the ions reach axial velocities of the order of $15 \text{ km} \cdot \text{s}^{-1}$.

Despite the apparent simplicity of these thrusters, many questions can be raised during their development phase:

- Which **neutral gas** should we choose? Xenon is almost always used because of its low ionization energy $E_i=12.1$ eV and its high molar mass $M=131\text{u}$, but its high and fluctuating cost will probably be a major issue in the next years [27].
- Which **material** do we choose for the channel walls? Initially made of alumine Al_2O_3 , dielectric walls of BNSiO_2 are now commonly used because they exhibit an excellent combination of fabricability, performance [28, 29] and lifetime. The erosion of the walls should also be taken into account as it affects the thruster performance and lifetime.
- Which **magnetic topology** should we use? Recently, Magnetically-Shielded (MS) HT have been used to shift the acceleration zone and limit the wall erosion. [30, 31].

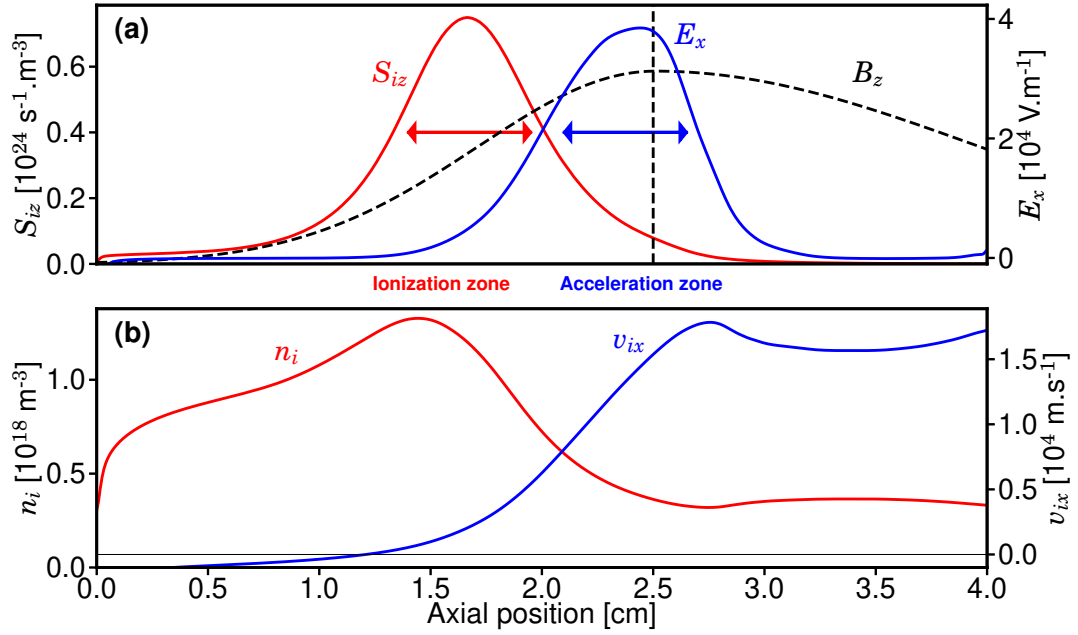


Figure 1.8 – Axial profiles of the main parameters of an HT discharge (from the self-consistent case of chapter 5). (a) Ionization source term S_{iz} (red) and axial electric field E_x (blue), with the normalized radial magnetic field B_z (dashed black) and the exit plane position (vertical dashed line). The red arrows delimit the ionization zone while the blue ones delimit the acceleration zone. (b) Ion density n_i (red) and ion axial velocity v_{ix} (blue).

- Where to **position the cathode**? The inherent asymmetry of having an exterior cathode might be an issue and work have been done to use instead a cathode at the center of the discharge channel [32, 33].

All these features affect the performance of HT and should be optimized [34]. Keeping in mind the never-ending human dream of conquering the stars, these many challenges needs to be overcome by studying these complex systems.

1.2 Hall thrusters - General concepts

At the heart of this work lies the concept of plasmas. Often referred as the fourth state of matter, plasma is constituted of ions and electrons, and while the bulk plasma is electrically neutral (**quasi-neutrality**), a charge difference can appear at the walls (**sheaths**) due to the lower mass of electrons (higher velocity) compared to ions. This mass difference between these two species is the main driver of the collective phenomena in plasmas and is hence responsible for their complexity.

Plasmas can be found in diverse systems, from solar wind to tokamaks, by way of Earth's ionosphere and magnetosphere or neon lamps. They are often

classified using their density and temperature: HT plasmas are belonging to the category of "low-temperature plasmas" (LTP). In these weakly ionized plasmas, there is no thermal equilibrium between the electrons and the ions/gas i.e. the electron temperature is often way higher than the ion temperature (which is close to the gas temperature): $T_e \gg T_i \approx T_g$.

To understand the HT plasma physics, some fundamental concepts will be introduced in this section. The reader can refer to various textbooks for extensive details on general plasma physics [35, 36] or plasma instabilities [37].

1.2.1 Basic concepts of Hall thruster plasma physics

The two important parameters characterizing a plasma are the Debye length λ_d and the electron plasma frequency ω_{pe} . The first one corresponds to the typical screening distance between charged particles, i.e. if two particles are separated by a distance lower than λ_d , they can act on each other via Coulomb interaction and a static polarisation can appear. For distances higher than λ_d , this force is screened and the plasma can be considered quasi-neutral. This Debye length is defined as

$$\lambda_d = \sqrt{\frac{\epsilon_0 k_B T_e}{n_e e^2}}, \quad (1.9)$$

with k_B the Boltzmann constant and n_e, T_e the electron density and temperature respectively.

When there is a small electronic perturbation in the plasma, it will naturally relax towards quasi-neutrality. The electron plasma frequency defines the corresponding characteristic time and is also the most fundamental plasma oscillation (Langmuir wave). It is defined as

$$\omega_{pe} = \sqrt{\frac{n_e e^2}{m \epsilon_0}}, \quad (1.10)$$

with m the electron mass.

Typically in HT, the plasma density can vary between 10^{17} and 10^{18} m^{-3} with electron temperatures between 5 and 50 eV. It gives Debye lengths in the range of 50 μm and plasma frequencies around 10^9 s^{-1} for electrons and 10^7 s^{-1} for ions.

Low-temperature plasmas

To understand the concept of temperature, a glimpse of plasma kinetic theory needs to be given. If we consider N particles with a random distribution of positions \mathbf{r} and velocities \mathbf{v} , the number of particles being at a given time t inside the elementary volume of phase space ($d^3\mathbf{r} \times d^3\mathbf{v}$) is given by the velocity distribution function $f(\mathbf{r}, \mathbf{v}, t)$. The plasma dynamic is then characterized by the Boltzmann equation, which describes particle motion in phase-space

$$\frac{\partial f}{\partial t} + \mathbf{v} \cdot \nabla_{\mathbf{r}} f + \frac{\mathbf{F}}{m} \cdot \nabla_{\mathbf{v}} f = \frac{\partial f}{\partial t} \Big|_c, \quad (1.11)$$

with ∇_r and ∇_v the gradients in position and velocity respectively, $\mathbf{F} = e(\mathbf{E} + \mathbf{v} \times \mathbf{B})$ the Lorentz force acting on charged particles, \mathbf{E} the electric field \mathbf{B} the magnetic field and $\left. \frac{\delta f}{\delta t} \right|_c$ representing the collision processes.

When the collision operator is neglected, we obtained the so-called Vlasov equation. The distribution function can be integrated over the velocity space to obtain the density n , the fluid velocity \mathbf{u} and the temperature T (first moments of Vlasov equation)

$$n = \iiint_{\mathbf{v}} f d^3v, \quad (1.12)$$

$$\mathbf{u} = \frac{1}{n} \iiint_{\mathbf{v}} \mathbf{v} f d^3v, \quad (1.13)$$

$$T = \frac{m}{3k_B n} \iiint_{\mathbf{v}} (\mathbf{v} - \mathbf{u})^2 f d^3v. \quad (1.14)$$

In a stationary case and considering only elastic collision, the Vlasov equation can be solved to obtain the so-called Maxwellian distribution function [35]

$$f(\mathbf{v}) = n \left(\frac{m}{2\pi k_B T} \right)^{3/2} \exp \left(-\frac{mv^2}{2k_B T} \right), \quad (1.15)$$

a fundamental type of distribution function that can also be expressed in term of energy

$$f_\epsilon(\epsilon) = \frac{2n}{\sqrt{\pi}} \left(\frac{1}{k_B T} \right)^{3/2} \sqrt{\epsilon} \exp \left(-\frac{\epsilon}{k_B T} \right), \quad (1.16)$$

with the particle energy $\epsilon = \frac{1}{2}mv^2$. Whereas normally the temperature should be expressed in K (Kelvin), often in plasma physics the unit of eV (electron-volt) is used. The conversion is made using

$$eT[\text{eV}] = k_B T[\text{K}]. \quad (1.17)$$

It is important to mention that, similarly to many LTP, the VDF is often not Maxwellian in HT discharges. Hence, in this work, the temperature will be calculated using its kinetic definition, given by equation 1.14.

Partially magnetized plasmas

The HT plasma can be called "partially magnetized", which means that the magnetic field acts on the electrons but not on the ions. To understand why, we need to introduce an important notion: the Larmor radius.

In a magnetized plasma, charged particles tend to spiral around magnetic field lines, with a frequency given by

$$\omega_c = \frac{qB}{m}, \quad (1.18)$$

with B the intensity of the magnetic field, q and m the charge and mass of the particle, respectively. ω_c is called the cyclotron frequency. The particle gyration radius, called the Larmor radius ρ_L , is defined by

$$\rho_L = \frac{v_{\perp}}{\omega_{ce}} = \frac{mv_{\perp}}{eB}, \quad (1.19)$$

with v_{\perp} the particle velocity vector in the plane perpendicular to the magnetic field.

We can see that the Larmor radius is directly proportional to the mass of the particle. Hence, as the electrons are way lighter than the ions (by a factor of $\approx 10^5$ for Xenon), we have $\rho_{L,e} \ll \rho_{L,i}$. The interesting feature of a HT is that typically, $\rho_{L,e} \approx 10^{-4}$ - 10^{-3} m while $\rho_{L,i} \approx 1$ m (for xenon). Hence, as the channel length is of the order of 4 cm, we get

$$\begin{cases} \rho_{L,e} \ll L_{system} \\ \rho_{L,i} \geq L_{system} \end{cases} \quad (1.20)$$

which means that the electrons are magnetized while the ions are not.

Moreover, if we add an electric field \mathbf{E} perpendicular (in the axial direction x) to the magnetic field \mathbf{B} (in the radial direction z), the Lorentz force $\mathbf{F} = q(\mathbf{E} + \mathbf{v} \times \mathbf{B})$ will act on the charged particles and make them drift in the $\mathbf{E} \times \mathbf{B}$ (azimuthal direction y) direction with the velocity

$$\mathbf{v}_{\mathbf{E} \times \mathbf{B}} = \frac{\mathbf{E} \times \mathbf{B}}{B^2}. \quad (1.21)$$

This mechanism is at the core of HT operation: as electrons are magnetized, they will be trapped by the magnetic field and drift azimuthally while circling around the magnetic field lines (helix motion). In the mean time, the ions are just accelerated out of the thruster by the electric field. Hence, the ionization is enhanced without reducing the thrust.

Collisional plasmas

The ideal situation would be to have electrons which drift forever in the azimuthal direction, to get a maximum ionization efficiency. However, several mechanisms will act to "free" the electrons from the magnetic field influence and make them drift towards the anode. The base mechanism is the classical collisions between electrons and heavier particles. It can be explained by writing the steady state electron momentum equation for a uniform plasma

$$-\frac{e}{m}[\mathbf{E} + \mathbf{v}_e \times \mathbf{B}] - \nu_m \mathbf{v}_e = 0, \quad (1.22)$$

with ν_m the total electron collision frequency. As \mathbf{E} is in the axial (x) direction and \mathbf{B} in the radial (z) direction, it gives us (y being the azimuthal direction)

[22]

$$\begin{cases} v_{e,x} = -\frac{eE}{m\nu_m} \frac{1}{1+h^2} \\ v_{e,y} = \frac{eE}{m\nu_m} \frac{h}{1+h^2} \end{cases} \quad (1.23)$$

with h the hall parameter given by

$$h = \frac{\omega_{ce}}{\nu_m}. \quad (1.24)$$

In the acceleration region of HT (where most of the electrons are trapped by the magnetic field), $\omega_{ce} \gg \nu_m$ and hence

$$\begin{cases} v_{e,x} \approx -\frac{1}{hB}E \\ v_{e,y} \approx \frac{E}{B} \end{cases} \quad (1.25)$$

Hence, we see that the velocity in the azimuthal direction $v_{e,y}$ corresponds to the $\mathbf{E} \times \mathbf{B}$ drift velocity. The axial velocity $v_{e,x}$ can also be expressed in term of mobility μ_e , such that $v_{e,x} = \mu_e E$. Here, the electron mobility is

$$\mu_e = \frac{1}{hB} = \frac{\nu_m m}{eB^2}. \quad (1.26)$$

This concept of mobility is crucial in this work. We can notice that the magnetic field B reduces this mobility, while the classical collisions (via ν_m) make the electrons move towards the anode. However, HT plasma are weakly collisional in the acceleration region (the electron mean free path is orders of magnitude larger than the channel length) and hence, axial electron transport should not be important. However, we will see in the next section that in reality, other mechanisms such as instabilities or wall effects, can greatly enhanced this axial electron transport, which is then termed as "anomalous".

1.2.2 Hall thruster instabilities

Despite their apparent simplicity, Hall thrusters are very complex systems because of the presence of gradients in many directions. Multiple instabilities can grow and interact together, in a broad range of frequencies. Here, the three main instabilities that will be observed and studied in this work are described: the low-frequency (kHz) Breathing Mode (BM), the intermediate frequency (hundreds of kHz) Ion Transit-Time instability (ITTI) and the high-frequency (MHz) Electron Drift Instability (EDI). A brief description of some other instabilities that will be encountered is also given, but the reader can refer to the review of Choueiri [38] and the more recent work of Smolyakov *et al.* [39] for extensive details.

To study plasma waves, a linear analysis is often made by using the hypothesis of small perturbations which assumes that a quantity Φ can be splitted in a

equilibrium term Φ_0 and a small perturbation $\tilde{\Phi}$: $\Phi(\mathbf{x}, t) = \Phi_0(\mathbf{x}) + \tilde{\Phi}(\mathbf{x}, t)$, such that $\Phi_0 \gg \tilde{\Phi}$. For the perturbed value, a monochromatic mode with a frequency ω and a wave vector \mathbf{k} is often assumed

$$\tilde{\Phi}(\mathbf{x}, t) \approx e^{-i\omega t + i\mathbf{k} \cdot \mathbf{x}}. \quad (1.27)$$

This perturbation analysis can be applied to the relevant set of equations to obtain a fundamental relation which defines the eigenmodes of the system, the so-called **dispersion relation** (DR) linking the frequency to the wave vector: $\omega = \omega(\mathbf{k})$. ω is a complex number: its real part corresponds to the frequency ω_R , while its imaginary part corresponds to the growth rate γ .

Moreover, the norm of the wave vector (or wave number) k is related to the wavelength λ by

$$k = \frac{2\pi}{\lambda}. \quad (1.28)$$

The wave front is propagating at the phase velocity \mathbf{v}_ϕ given by

$$\mathbf{v}_\phi = \frac{\omega}{k^2} \mathbf{k}, \quad (1.29)$$

while the wave packets (superposition of several harmonic waves) are propagating at the group velocity \mathbf{v}_g given by

$$\mathbf{v}_g = \frac{\partial \omega}{\partial \mathbf{k}}. \quad (1.30)$$

Finally, two types of instabilities can be distinguished [37]: **absolute instabilities**, for which an initial perturbation will generate a response growing in time at each spatial point; and **convective instabilities** for which the response to the perturbation will initially grow at a defined spatial point before being convected away. This notion of growth and convection, illustrated in figure 1.9, is very important for this work and is well-represented by the approximate conservation equation for the wave energy density W

$$\partial_t W + \underbrace{\nabla \cdot (v_g W)}_{\text{Convection}} = \underbrace{2\gamma W}_{\text{Growth}}. \quad (1.31)$$

Breathing mode (BM)

Hall thrusters are often subject to low-frequency oscillations of the discharge current, with a frequency of about 10-20 kHz [41, 42, 43] and an amplitude that can be as high as 100% of the discharge current mean value. These oscillations can be detrimental to the thruster operation, damage the power supply and hence reduce the thruster lifetime and performance. For these reasons, an electrical filter (often a RLC circuit) is used to damp these oscillations. The interaction between this RLC circuit and the BM oscillations have been studied numerically [44] and

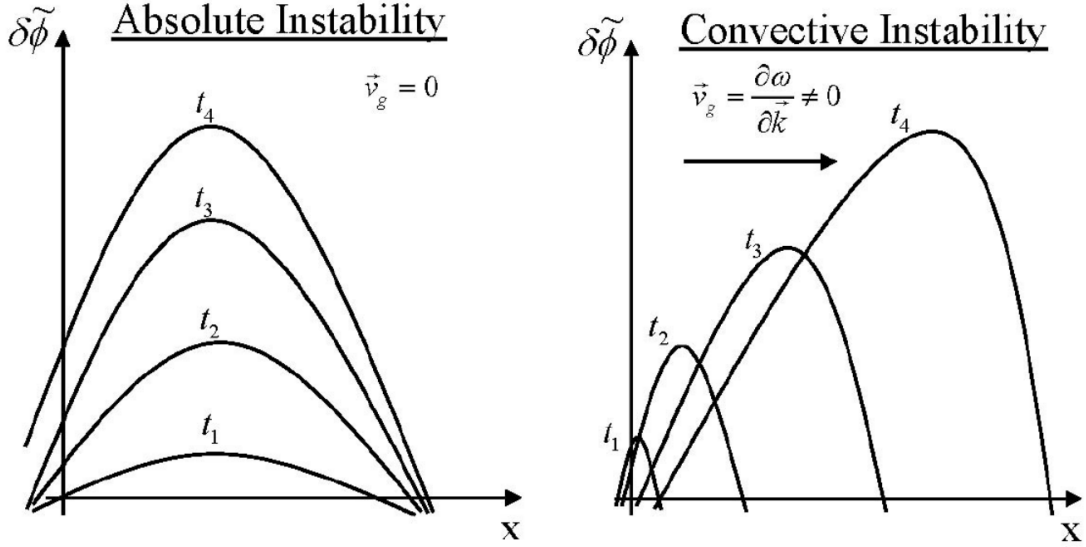


Figure 1.9 – From [40]: Illustrations of convective and absolute instabilities for a perturbed quantity $\delta\tilde{\phi}$ evolving at successive times t_i .

experimentally [45] but despite its strong influence on the discharge behaviour, this RLC circuit is scarcely accounted for in HT numerical simulations.

The first hypothesis that have been suggested by Fife [46] to explain this low-frequency oscillation is a predator-prey model (Lotka-Volterra model [47]) between the neutrals (prey) and the plasma (predator) [48], i.e. a competition between the neutrals that are ionized and the ions that cannot exist without the neutrals. More specifically, a BM oscillation can be decomposed in several steps:

1. First, the discharge channel fills up with neutrals from the anode. These neutrals are strongly ionized in the high magnetic field region which depletes their density profile.
2. Then, because there are not enough neutrals in the channel any more, the atom front moves towards the anode where the ionization is less efficient due to a higher electron mobility (lower magnetic field).
3. The discharge current hence decreases, the plasma is extracted by the axial electric field and the neutrals can replenish the channel. The ionization will take place again once the neutral density will be high enough.

The cycle repeats with a period depending on the time needed for the neutral atoms to fill the ionization region. This qualitative description was confirmed by a 1D model of Boeuf and Garrigues [49] who named this phenomenon, "breathing mode". Later, Barral and Ahedo [48] generalized the 0D predator-prey model in 1D.

While this simple explanation gives good order of magnitudes for the oscillation frequency $f = \frac{\sqrt{v_i v_n}}{2\pi L}$ (undamped harmonic oscillator, with v_i and v_n the ion and neutral velocity, respectively, and L the length of the acceleration region), two main assumptions are incorrect [50, 51]: the neutral mass flow rate is not

taken into account and in 0D, the discretization length for the spatial convection terms is not well-defined (is it the channel length or the ionization zone length?). Hence, this mode is still studied, for example by Hara *et al.* [52, 51] who highlighted the importance of electron energy equation to get a positive growth rate through a linear stability analysis; or by Romadanov *et al.* [53] who tried to control these oscillations by modulating externally the DC voltage applied on the HT. They also managed to reproduce their experimental results with a simplified 1D model of resistive-ionization mode in quasineutral plasma. This resistive behaviour was also found to be the origin of this instability by Chable and Rogier [54]: they related it to a Buneman instability, driven by a coupling between the electric field and the ion current.

All in all, the origin of this instability is still debated, with an onset criteria still not well-defined and hence, further investigations are needed.

Ion transit-time instability (ITTI)

These oscillations are characterized by a frequency in the range 100-500 kHz which corresponds to the transit time of ions in the acceleration region (around 1 cm): as they commonly travel with a velocity of around 1-5 km/s, their transit-time is on the order of 2-10 μ s. They were first measured and characterized experimentally by Esipchuk *et al.* [55]. They described it as a "quarter-wave standing mode" with an antinode near the anode and a node near the exit plane, along with plasma potential variations of the order of 10 to 30 % of U_d . More recently, Vaudolon *et al.* [56, 57] have also observed this instability through Laser Induced Fluorescence (LIF) measurements of the local Ion Velocity Distribution Function (IVDF). They noticed that the ion exhaust velocity was higher than the maximum theoretical velocity defined by the imposed potential difference. This so-called **wave-riding mechanism** can be explained as the following. In 1D, when a particle of mass m and charge q is created with zero velocity at an electric potential ϕ_0 , it will gain the following energy ϵ along its trajectory

$$\epsilon = \frac{mv^2}{2} = \int_0^T qE dx, \quad (1.32)$$

with $E = -\frac{\partial\phi}{\partial x}$ the axial electric field. Usually, we have $\int_0^T qE dx = -q(\phi - \phi_0)$ which gives the maximum velocity

$$v_{max} = \sqrt{\frac{2|q|(\phi - \phi_0)}{m}}. \quad (1.33)$$

However, because ϕ varies in time, we get

$$\frac{mv^2}{2} = -q(\phi - \phi_0) + \int_0^T \frac{\partial\phi}{\partial t} dt. \quad (1.34)$$

The electric field disturbance represented by the last term of equation 1.34 is responsible for the widening of the ion distribution: some ions "ride" the leading

edge of the electric field oscillations and others decelerate on the trailing edge. The phase velocity of the transit-time oscillations is close to the axial ion velocity and hence, some ions can gain or lose energy from the wave.

Numerically, Fife [46] was the first to observe this instability in a 2D axial-radial hybrid code, appearing only when the cross-field electron mobility near the anode was low, compared to the one at the exit plane. He described it as 3 successive steps:

1. The axial electric field E_x rises near the anode which implies a local reduction of the density.
2. The lower density further increases E_x by Ohm's law, which increases T_e through Ohmic heating.
3. The disturbance travels downstream led by the sharp electric field, up to the exit where it is mixed with other ions and exhausted.

Later, Hagelaar *et al.* [58] and Bareilles *et al.* [59] have also observed this ITT instabilities with a 2D axial-radial hybrid code. During a transit-time oscillation, they found that the position of the acceleration zone oscillates, as seen in figure 1.10:

1. The acceleration zone moves upstream: ions that are just accelerating see the electric field "slipping through their fingers" and do not experience the full voltage drop. A low-energy ions group appears.
2. Then, when it moves downstream, a "wave-riding" phenomenon makes the ions accelerate more than the total U_d .
3. It results in an ion beam with two populations: because the acceleration zone moves usually faster upstream, the low-energy ions are a smaller group of energy as low as 100 eV. First, we see that the slow group creates a maximum of ion density, which induces a maximum of potential. Second, when the fast group joins the slow group, the ion current can locally exceed the total current so that the electric field must change sign to maintain current continuity. The ion velocities are reduced by this electric field and the slow group slows down further to only $10 \text{ km} \cdot \text{s}^{-1}$ i.e 70 eV.

They state that the perturbation of the plasma density and ion flux cause in turn a perturbation of ϕ via the current conservation, providing the back coupling that maintains the transit-time oscillations. They also find that these transit-time instabilities can be reduced by increasing the anomalous electron conductivity.

More details on this instability will be given in chapter 6 in which its presence in our 2D axial-azimuthal simulations will be studied.

Electron Drift Instability (EDI)

The Electron Drift Instability (EDI), sometimes called Electron Cyclotron Drift Instability or $\mathbf{E} \times \mathbf{B}$ Electron Drift Instability, was first observed and extensively studied theoretically in other fields (such as shockwave propagation across

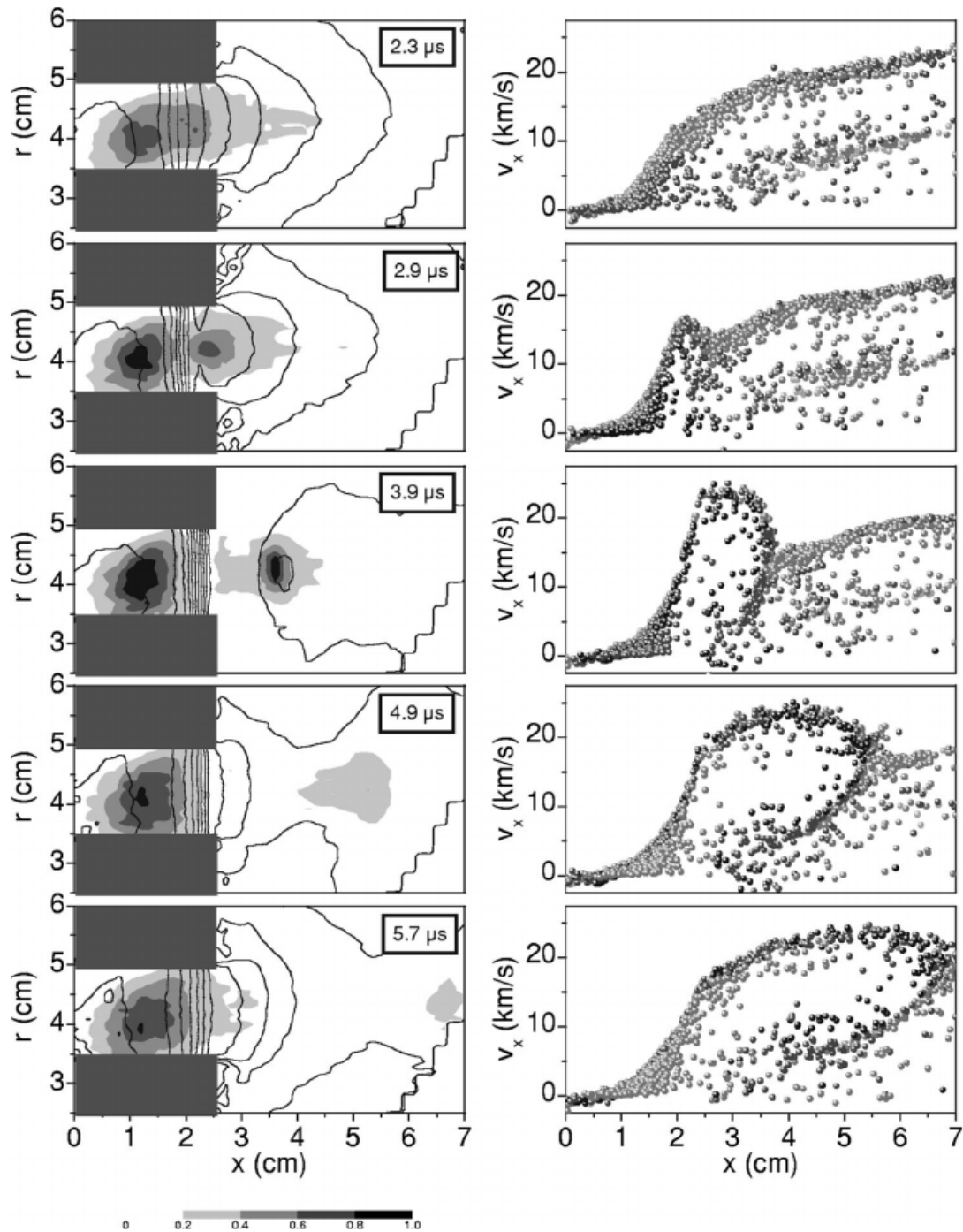


Figure 1.10 – From [59]: Effects of the transit-time oscillations on discharge properties through five moments of the oscillation period. On the left: electric potential lines spaced by 30 V for 300 V applied voltage and plasma density (gray scale, $3 \times 10^{18} \text{m}^{-3}$). On the right: phase-space diagram of ion axial velocities regardless of their radial positions/velocities.

a magnetic field) in the 1970s by Forslund *et al.* [60, 61], Gary and Sanderson [62], Lampe *et al.* [63, 64] and Biskamp and Chodura [65]. They found that this instability is kinetic in nature, with a dispersion relation that can be obtained by linearizing the electron Vlasov equation, coupled with Poisson's equation and ion cold fluid equations. It results from a coupling between electron Bernstein modes and ion acoustic modes.

In the HT context, the EDI was first found in the axial-azimuthal PIC simulations of Adam *et al.* [66], characterized by a short wavelength (in the mm range), a high frequency (in the MHz range) and a dominant propagation in the azimuthal direction. Later, the collective Thomson scattering measurements performed by Tsikata *et al.* [67, 68, 69] confirmed the presence of EDI in Hall thrusters by measuring the electron density fluctuations in the plume. Since then, EDI has been found in many 1D [70, 71, 72, 73] and 2D [74, 75, 76, 70, 77, 78, 79] PIC simulations and additional experimental diagnostics [80, 81].

Following the work of Ducrocq *et al.* [82], Cavalier *et al.* [83] have derived the EDI 3D dispersion relation and compared the numerical solutions to the measurements of [67] with a good agreement. Later, Lafleur *et al.* [70, 84, 85] have also extensively analysed these instabilities.

If we consider the 2D dispersion relation for this instability, neglecting the radial wave vector $k_z = 0$ (parallel to \mathbf{B}), we find that the azimuthal wave vector k_y is discrete, with large resonances near the cyclotron frequency (**cyclotron resonances**) [82]

$$k_{y,n} = n \frac{\omega_{ce}}{v_{e,y}}, \quad n = 1, 2.. \quad (1.35)$$

However, when the wave propagation along the magnetic field is included, one can show from the linear theory that the EDI can transition to an ion-acoustic instability (IAI) [62, 83, 85, 86]. Nonlinear effects can also potentially result in transition to the ion-acoustic instability [63, 84, 71]: the instability "smears out" the cyclotron resonances (**resonance broadening**). This transition is still debated (if the axial direction is not included, it seems that the cyclotron resonances are still present and a non-linear development of large scale modes is observed [87, 72, 88, 79, 73], related to a so-called **inverse energy cascade**) and the fact that the EDI wavelength $\lambda_{EDI} = 2\pi \frac{v_{e,y}}{\omega_{ce}}$ and the ion-acoustic wavelength $\lambda_{IAI} = 2\pi\sqrt{2}\lambda_d$ are both in the 1 mm range in HT, makes this question difficult to settle.

All in all, while the linear stage of the EDI is well understood, the transition to the nonlinear regime and the associated saturation mechanisms are still debated and insights from a 3D PIC code [89] would be definitely needed to be able to answer this question.

Other instabilities

Among the many other instabilities propagating in a HT, two more should be mentioned: the rotating spokes and the gradient-induced instabilities. They

are both azimuthally rotating modes, with a frequency in the 10-100 kHz range. However, they differ in several characteristics.

The rotating spokes have first been observed experimentally by Janes and Lowder [90] and further studied by McDonald and Gallimore [91] and Powis *et al.* [92]. The numerical studies are more recent, from the early work of Boeuf *et al.* [93, 75] to the analysis of Kawashima *et al.* [94] and Matyash *et al.* [95]. The current understanding of these instabilities is that they are due to an ionization inhomogeneity in the azimuthal direction. Hence, they are propagating mainly near the anode, with a phase velocity of around $0.2 \frac{E_x}{B_r}$. Griswold *et al.* [96] managed to damp these spokes by a feedback control in a cylindrical HT, and observed a reduction of 10% of the discharge current, which could mean that they contribute to axial electron transport. A similar conclusion was obtained earlier by Parker *et al.* [97].

The gradient-induced instabilities, first observed by Morozov *et al.* [98] are very similar to these spokes but exhibit a slightly higher frequency and are excited by gradients in density and magnetic field. Hence, they appear near the thruster exit plane, i.e. where the magnetic field is maximum. Contrary to rotating spokes, they seem to be damped for HT nominal operation and hence, they do not represent a major issue.

These two instabilities have been studied experimentally with high-speed camera imaging of a small HT but we chose not to detail the results in this manuscript. The reader can refer to the related publication [99] for more information.

1.2.3 Why do we keep studying Hall thrusters?

As described in the previous section, HT plasmas are very complex systems with many instabilities propagating. However, they have been successfully used since a few decades, and they are often considered as the best alternative for EP. The main interest of studying these thrusters (and hence, of performing this work) lies in the current problematic of New Space: the diversity of space missions requires broader and broader ranges of power and size.

Space agencies and companies did not wait for more comprehensive studies on HT to develop their thrusters but they relied on empirical techniques (try-and-error method) which are both money and time consuming. Simple scaling laws can however be derived, from the rich database of already-optimized thrusters. For example, Dannenmayer and Mazouffre [100] have found that the discharge current density J_D and the anode gas density are two parameters that are independent on the thruster power: the former should be around $1000 \text{ A} \cdot \text{m}^{-2}$ while the latter should be around $1\text{-}3 \times 10^{19} \text{ m}^{-3}$. They also found that to change the thruster power by a factor α , the best option is to increase the radial dimensions homothetically as $\alpha^{1/2}$, the mass flow rate as α and keep the same channel length and axial magnetic field profile. Other studies have been conducted for low-power [101] or high-power HT [102].

However, these works are very empirical and they are not able to optimize

important parameters such as the magnetic field or the wall materials. In this section, the two current most pressing issues for HT will be discussed: anomalous electron transport and wall erosion.

Anomalous electron transport

We have seen previously, in section 1.2.1, that the axial electron transport should normally be driven only by the classical collisions. However, if we write the electron momentum conservation equation (Eq. 1.22) in a more general way [70]

$$\underbrace{\frac{\partial}{\partial t}(mn_e\mathbf{v}_e) + \nabla \cdot (mn_e\mathbf{v}_e\mathbf{v}_e)}_{\text{Inertia term}} = \underbrace{qn_e(\mathbf{E} + \mathbf{v}_e \times \mathbf{B})}_{\text{Lorentz force}} - \underbrace{\nabla \cdot \mathbf{\Pi}_e}_{\text{Pressure gradient}} - \underbrace{m\nu_m n_e \mathbf{v}_e}_{\text{Collisions}}, \quad (1.36)$$

and if we use the same techniques as before and neglect the inertia and pressure terms, we can get the full expression for the classical mobility

$$\mu_{class} = \frac{v_{e,x}}{E_x} = \frac{\frac{|q|}{m\nu_m}}{1 + \frac{\omega_{ce}^2}{\nu_m}} \quad (1.37)$$

We can see that when there is no collision, i.e. when $\nu_m \rightarrow 0$, there is no axial electron transport any more ($\mu_{class} \rightarrow 0$). The neutral density in HT plasmas is relatively low and hence, the collision frequency is also low, which means that the axial electron transport should not be important, especially in the plume where the neutral density profile is strongly depleted. However, it has been observed experimentally by Meezan *et al.* [103] that the electron mobility is order of magnitudes higher than the one predicted by this classical collisional theory. This phenomenon, often called **anomalous electron transport**, is detrimental to the HT performances: indeed, the ideal case would be to have motionless electrons (in the axial direction) that will ionize as much neutral atoms as possible. On a more macroscopic view, if the electron conductivity is increased due to this anomalous transport, for an imposed discharge voltage, the discharge current would be higher. This would mean that for the same thrust (because the ion exhaust velocity is directly proportional to the discharge voltage, as seen in equation 1.33), the needed input power ($U_d I_d$) would be higher. Hence, we can see that ideally, we would like to decrease the anomalous transport to improve HT performances.

The central question is then: what make the electrons drift axially from one magnetic field line to another quicker than expected? In the early 2000's, the plasma/walls interactions were thought to be the major contributor to this anomalous transport [23], through Near-Wall Conductivity (NWC) enhanced by Secondary Electron Emission (SEE) [104, 105] or radial sheath instabilities [106, 107]. But while it is undeniable that the walls play a role on the electron transport, it is probably negligible compared to the one from instabilities propagating in the

plasma [108, 77, 109]. Indeed, Ducrocq [110] has observed clear correlation between the axial electron velocity and the EDI growth, which was also confirmed by other works [66, 76, 16, 111, 85]. Lafleur *et al.* [70, 84] highlighted the crucial role of EDI on anomalous transport. Indeed, they found that the correlation between electron density δn_e and azimuthal electric field δE_y azimuthal fluctuations induced by the EDI was enhancing the axial electron transport. This correlation term $\langle \delta n_e \delta E_y \rangle$ (positive when δn_e and δE_y are out-of-phase) is captured by the so-called electron-ion friction force

$$R_{ei} = q \langle \delta n_e \delta E_y \rangle, \quad (1.38)$$

which represents the effect of the EDI on the transport and should be accounted for as an additional term in the RHS of equation 1.36. Finally, other works have found that the anomalous transport could also come from gradient-driven fluid instabilities [112, 113, 114].

Wall erosion

While anomalous transport has a constant impact on the thruster performance, the degradation of the walls material is a slow process which decreases both the thruster performance and lifetime. This wall erosion often appears only after a couple hundreds of operating hours and is characterized by regular striations of the wall ceramic. The main origin of this erosion is still unknown and we only suppose that it is due to ion sputtering. Some groups have tried to simulate it [115] and others think that it might be related to EDI [111] but the overall process is still scarcely studied.

Many solutions have been investigated, and most of them consist in modifying the magnetic field profile: either by using a curved magnetic field [116] or making the magnetic field lines closer to the anode to achieve ideal equipotentialization of the lines of force near the walls [117, 31]. The latter technique is now widely used in the US, and the corresponding type of thruster are called Magnetically Shielded (MS) thrusters. Thanks to this change, the electron temperature is reduced near the walls and the acceleration zone is shifted towards the plume, which means that less ions can impact the walls. Moreover, other groups have decided to alter the thruster design, for example by removing the walls [118].

This plasma/wall interactions have been already studied in our group [119, 120] and no additional insight will be provided in this work. The reader can refer to the recent review of Brown and Walker [121] for additional information.

1.3 Hall thrusters - Modeling

As described in section 1.2.1, the Boltzmann equation describes the motion of all the particles in the plasma. Hence, to model HT discharges, the ideal method would be to be able to solve this equation. However, as the plasma density is very high and because the Boltzmann equation needs to be discretized

in the full phase-space, these so-called **Direct-Kinetic** (DK) models are very computationally costly and so, are scarcely used.

Some hypothesis need to be made to simplify the solving and increase the model efficiency. One option would be to group the charged particles in big ensembles (called macro-particles) and follow their individual motion in phase-space by accounting for external forces (here, only the Lorentz force) and collisions. This **Particle-In-Cell** (PIC) technique is the most commonly used as it gives many informations on the discharge behaviour. However, due to restrictive stability criteria, PIC simulations are also quite computationally expensive. Another option would be to solve the conservation equations, derived by taking the moments of the Boltzmann equation for each charged particles species, in order to obtain macroscopic quantities such as the density, velocity and pressure (given by equations 1.12, 1.13 and 1.14 respectively). Even though these **fluid models** can bring insights on the HT behaviour in a reasonable computational time, they often rely on many assumptions (quasi-neutrality, Maxwellian distribution functions, etc.) which validity remains questionable. Finally, the two previous techniques can be mixed in **hybrid models**, often accounting for electrons as a fluid and ions as particles (because the electron dynamics is the more restrictive one). The 3 main modeling techniques are illustrated in figure 1.11.

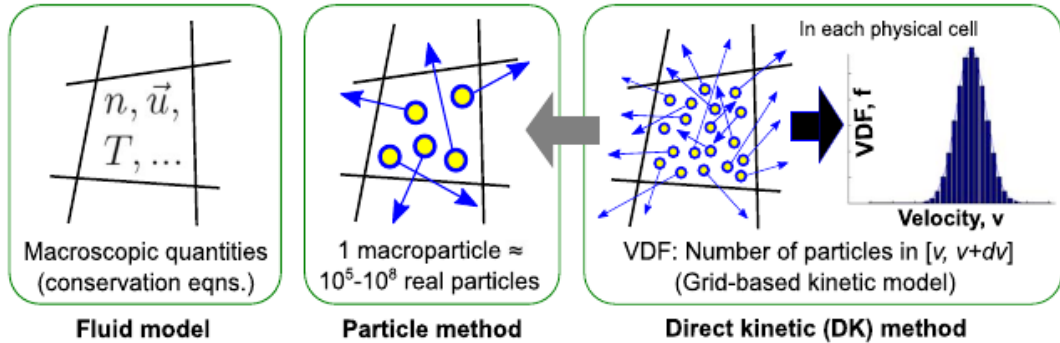


Figure 1.11 – From [122]: Plasma modeling techniques for HT discharge plasmas. The numerical techniques are approximations to the actual physics in which individual atoms and molecules move and collide with each other. Note that the blue arrows denote the particle velocities and the velocity distribution function (VDF) results from the ensemble of particles in the direct kinetic (DK) method.

As mentioned above, many key phenomena in HT (instabilities and turbulence) involve kinetic effects that cannot be captured by fluid simulations and moreover, the charged particle distribution functions are often not Maxwellians. For these reasons, a 2D PIC code will be used in this work to study the HT discharge. More details on PIC codes will hence be given in chapter 2.

In the following, key issues and various examples of fluid, PIC and hybrid models will be given, along with a brief description of their main contribution. This list is not intended to be exhaustive and the reader can refer to detailed reviews [22, 122, 123] for more informations.

1.3.1 Multi-fluid models

Most of the multi-fluid models of HT are based on the quasi-neutral (QN) assumption, i.e. they assume that the electron and ion densities are equal at every point of the domain [29, 124, 125]. The Poisson equation is not solved any more and the electric field is then computed from the continuity equation for the total current. However, even though this assumption is often valid in the bulk plasma, it is not true in the sheaths which are then supposed to be very thin compared to the bulk plasma. High-frequency oscillations can also hardly be captured as they are often related to small deviation from quasi-neutrality. Hence, to better study plasma/wall interaction and high-frequency instabilities (which are both considered as two important anomalous transport contributors), this QN assumption should not be used and it would be necessary to solve Poisson equation instead. To study the wall SEE, Ahedo [126] has solved Poisson equation similarly to Joncquieres *et al.* [127, 128] with their 10-moment formulation, but then with the numerical constraints to ensure accurate simulations, multi-fluid simulations become as computationally expensive as PIC.

Moreover, many codes [29, 125] neglect time-dependence and inertia effects, using the so-called Drift-diffusion approximation (or generalized Ohm's law). In this case, the electric field can be expressed as

$$\mathbf{E} = \eta \mathbf{j}_e + \eta \omega_{ce} \mathbf{j}_e \times \frac{\mathbf{B}}{B} - \frac{\nabla P_e}{en_e}, \quad (1.39)$$

with $\eta = \frac{m\nu_e}{e^2 n_e}$. This approximation removes the inherent non-linearity of the inertia terms and allow to easily relate the electric field to the electron flux and density. Recent works have studied new numerical schemes to efficiently account for two-fluid (electron and ion) equations, coupled to Poisson's equation, and including electron inertia [129, 130].

Finally, the current key challenge in fluid codes is to find how to account for anomalous electron transport which comes from kinetic effects. Often, additional terms are added to ν_m , the electron momentum-transfer collision frequency, such as $\nu_m = \nu_{class} + \nu_{ew} + \nu_{ano}$ with ν_{class} the contribution of classical collisions, ν_{ew} the one from the walls and ν_{ano} the one accounting for the anomalous transport. The latter is the hardest to predict: whereas typically a Bohm conductivity model (with $\nu_{ano} \propto \frac{\omega_{ce}}{16}$) was used [46, 131], it was found recently that the derivation of ν_{ano} is more complex [111] and is probably related to the EDI via the electron-ion friction force

$$R_{ei} = -mn_e v_{e,y} \nu_{ano}. \quad (1.40)$$

Despite several theoretical attempts based on EDI approximations [132, 133] or empirical attempts based on a machine-learning approach [134], this is still an open-question which needs to be answered.

The main challenge of fluid models lies in the so-called closure problem: when solving the conservation equation, an additional hypothesis needs to be made on the highest moment of the distribution function. Often, the ideal gas law is

considered to obtain the pressure but this relation is valid only for Maxwellian VDF. However, due to the weak-collisionality of HT plasmas, charged particles VDF (mostly electrons) are often non-Maxwellian [23], especially because of the strong magnetic field anisotropy and the interaction with the walls. Because this deviation from a Maxwellian can have important impact on key phenomena (instabilities, wall losses, anomalous transport, etc.), it needs to be taken into account by using kinetic approach such as Particle-in-Cell models [135].

1.3.2 Particle-In-Cell models

Plasma/wall interactions was the first mechanism thought to be involved in anomalous transport. As they are also probably related to wall erosion, these interactions were of major interest at the beginning of HT modeling. As explained previously, fluid codes are often quasi-neutral and hence, they cannot capture properly the sheath region near the walls. PIC simulations were hence used to model this non-neutral zone by solving Poisson equation and accounting for Secondary Electron Emission (SEE). The pioneer work of Taccogna *et al.* [136, 107] and Sydorenko *et al.* [104, 106, 137] with two independent 1D radial models accounting for SEE gave many insights, such as the importance of secondary electron beam electrons or a strong anisotropy between radial and axial directions. Later, Héron and Adam [74], Croes *et al.* [77, 16, 119], Janhunen *et al.* [87] and Tavant *et al.* [109, 138, 120] have added the azimuthal direction to account for the coupling between wall effects and EDI and see how it influences the anomalous transport. They have observed that while the SEE was increasing the near-wall mobility by a factor of 2, the cooling of electrons due to SEE was making the EDI saturate and hence, decreasing the bulk mobility. The overall effect of SEE on anomalous transport was found to be smaller than expected.

While some axial-radial models have been developed [139, 115] to self-consistently account for electron and ion source terms, it appeared quickly that the azimuthal direction was of paramount interest for PIC simulations. Indeed, Adam *et al.* [66] found with an axial-azimuthal model that high-frequency instabilities were propagating in this direction and contributing to the axial anomalous transport. These instabilities were studied more deeply with 1D azimuthal models [82, 75, 71] and the work of Lafleur *et al.* [70, 84] highlighted the crucial role of EDI on anomalous transport. Finally, numerous codes including both azimuthal and axial dimensions (as the latter should also be accounted for, due to wave convection) have been developed: by Coche *et al.* [76], Lafleur *et al.* [111, 86], Boeuf *et al.* [140], Taccogna *et al.* [78], Katz *et al.* [141] and Chernyshev *et al.* [142]. As they are closely related to this work, these axial-azimuthal models will be described in more details later, in section 5.1.

Even though 3D codes have also been developed [143, 144, 89], they all required artificial scalings (often using thruster downsizing) which probably impact the discharge behaviour. The increasing number of macroparticles to consider (around 10^3 - 10^4 per direction included) along with the PIC stability criteria,

make code parallelisation compulsory, which drastically increases the model complexity. Hence, code verification is needed and this issue will be dealt with in chapter 3.

1.3.3 Hybrid and Direct-Kinetic models

While fluid and PIC models are very efficient to give information on the macroscopic plasma behaviour or on kinetic effects, respectively, hybrid models are a good compromise that brought many physical insights in the last two decades. For example, the early models of Boeuf and Garrigues [49] (1D axial) or Fife [46] (2D axial-radial) were the first to observe the breathing mode and ion transit-time oscillations, and the latter is still even used in the community. Later, the ion-transit time instabilities were analysed in more details with the axial-radial hybrid model of Hagelaar, Bareilles *et al.* [58, 59], as described previously in section 1.2.2. Finally, the more recent axial-azimuthal model of Kawashima *et al.* [94] allowed them to give a new description of the on-set for rotating spokes.

However, hybrid models cannot capture high-frequency instabilities contrary to DK models, which are even better than PIC model because no numerical noise is present. DK models are also efficient to capture high density gradients and hence could provide a more accurate description of plasma/wall interactions. A review of these DK models has been done by Hara and Hanquist [145] and one can look at the recent 2D model of Raisanen *et al.* [146] who improved the 1D model of Hara *et al.* [147].

Finally, Lafleur *et al.* [86] has recently proposed an innovative hybrid scheme: a fluid solver could be used to obtain macroscopic quantities such as the electric field and electron density. Then the charged particles VDF would be calculated with a Monte-Carlo solver which will allow us to solve the dispersion relation and get the corresponding wave frequency and growth rate. The wave energy equation 1.31 would be solved to get the wave energy density. From this, the electron-ion friction force R_{ei} and hence the anomalous collision term ν_{ano} could be obtained and plugged into the fluid solver to self-consistently account for the electron transport. Then the loop would be repeated again. While this process accounts self-consistently for the instabilities and alleviate PIC stability criteria, some steps are currently out of reach: the wave energy equation is difficult to solve and the anomalous collision term, difficult to approximate. While the former is out of scope of this work [148], the latter will be discussed in chapter 4.

1.4 Scope and outline of the thesis

Even though some fluid codes managed to reproduce specific experimental results with empirical models for electron cross-field mobility, there is currently no self-consistent way to account for this anomalous transport. Hence, HT manufacturers rely on codes that are not fully predictive (such as the 2D fluid model *Hall2D* [125, 132] at the Jet Propulsion Laboratory (NASA) or a 1D axial fluid

model based on [29] at Safran Aircraft Engines) and usually perform several development tests before converging to an acceptable thruster design. Knowing that one development test corresponds to almost 10 000 hours of nominal operation and that additionally, the thruster performance is decreased when the anomalous transport increases, we can see that a better understanding of this phenomena is of great interest. As it is now mostly accepted that instabilities and turbulence are the main driver for this anomalous transport, the question is not *what* contributes to this transport, but *how* does it contribute. The main purpose of this work is hence to try to answer this fundamental question: how to model the anomalous transport and incorporate it in a fluid simulation? To this end, a PIC code is necessary to account for these kinetic effects and because 3D self-consistent PIC models are still out of reach, a 2D geometry including the azimuthal (in which the high-frequency instabilities are propagating) and axial (to account for wave convection and most of the gradients) directions will be considered. Finally, as we have seen in this chapter, HT discharges are very complex with a broad range of instabilities that can develop. Such a 2D PIC code could not only shed the light on the anomalous transport but also give insights on how to better control these instabilities that are known to affect the HT performances and lifetime.

The 2D PIC code *LPPic* built from scratch by Vivien Croes [119] and further used to study the HT radial-azimuthal directions [77, 16, 109, 138, 120] has been modified to consider now the axial-azimuthal directions. All these changes are described in chapter 2, along with extensive details on the code itself. As explained before, before using this complex code, it is necessary to verify it. This important step has been successfully done by performing a 2D axial-azimuthal benchmark against 6 other independently developed PIC codes: the whole process and final comparison are described in chapter 3. Once *LPPic* was verified, we used this simplified benchmark case to stress-test a quasi-linear kinetic theory (previously developed by Lafleur *et al.* [86]) for approximating the electron-ion friction force, thought to be the main contributor to the anomalous electron transport. This comparison, with an extensive parametric study, is detailed in chapter 4. However, to ease the benchmark work and reduce the computational time, an imposed ionization source term was considered for this simplified case, hence precluding any ionization oscillations to develop, such as the breathing mode. Hence, this constraint has been alleviated and self-consistent simulations with a neutral dynamics solver (hence calculating self-consistently the ionization source term) have been performed. However, from the breathing mode low frequency stems the need to simulate longer physical times and with it, the computational cost is drastically increased. To overcome this issue, the vacuum permittivity has been modified, hence relaxing the PIC stability criteria and significantly speeding-up the code. This scaling technique has an influence on EDI growth rate and hence, on the discharge behaviour. Chapter 5 focuses on this macroscopic behaviour. Finally, in chapter 6, insights on the complex interaction between the three main instabilities (BM, ITTI and EDI) are given.

Chapter 2

Code development: from radial-azimuthal to axial-azimuthal geometry

Initially, the code `LPPic` was developed to simulate the Hall thruster radial-azimuthal plane. Thanks to its versatility, we were able to keep most of the subroutines already developed and only bring some specific changes to replace the radial direction by the axial one. Hence, the code will briefly be presented in section 2.1 and the reader can refer to [119] and [120] for more details on the main subroutines. Two main changes concern the axial boundaries: neutral atoms are injected at the anode and electrons are emitted at the cathode. While only the local flux at the boundary needs to be known for the latter, the neutral dynamics should be solved in the whole simulation domain, at each time step. These two new models will be detailed in section 2.3 for the neutral dynamics, and in section 2.4 for the cathode. Other minor changes were also needed to simulate this axial direction: they have been gathered in the introductory section 2.2.

When these new modules were all implemented and verified, we have also tried to include additional physical phenomena such as plasma-wall interactions (see section 2.5.1) or doubly-charged xenon species (see section 2.5.2).

Contents

2.1	A quick overview of <code>LPPic</code>, a 2D PIC-MCC code	32
2.1.1	Code main structure	32
2.1.2	A powerful numerical tool	36
2.2	Preliminary modifications towards axial-azimuthal simulations	38
2.2.1	Magnetic field	38
2.2.2	Ionization process	39
2.2.3	Code optimization	40
2.3	Neutral dynamics	43
2.3.1	Context	43

2.3.2	Model description	44
2.3.3	Solver verification and validation	48
2.4	Cathode model	49
2.4.1	Current Equality condition	51
2.4.2	Quasi-neutrality condition	52
2.4.3	Setting positions and energies	52
2.4.4	Which model should we choose?	53
2.5	Further improvements of the model	53
2.5.1	Fake radial dimension	54
2.5.2	Doubly-charged xenon ions	54
2.6	Conclusion	55

2.1 A quick overview of *LPPic*, a 2D PIC-MCC code

2.1.1 Code main structure

As for all Particle-In-Cell (PIC) codes, it is important to distinguish in *LPPic* the grid (fields) and the particles. The former is defined on a Cartesian mesh of $N_x = x_{max}$ (axial direction) times $N_y = y_{max}$ (azimuthal direction) square cells of size dx , as displayed in figure 2.1. The fields (electric field, densities, etc.) are computed at the center of each cell. The charged particles (electrons and ions) are moving into the grid and are grouped into packets of identical size, called *macroparticles* and represented by the weighting factor q_f defined at the beginning of the simulation

$$q_f = \frac{n_p V_c}{N_{ppc}}, \quad (2.1)$$

with n_p the initial plasma density, V_c the cell volume and N_{ppc} the number of macroparticles in one cell, for one species. Hence, one macroparticle represents q_f real particles.

N_{ppc} is an important parameter for PIC simulations: if the number of macroparticles in one cell is too low, it can lead to numerical noise [149]. However, the computational load increases significantly with N_{ppc} , along with the memory requirement to store all the particles. A compromise needs to be found and often, the criteria $N_{ppc}=100$ is chosen in 2D. However, this value might be dependent on the studied case and hence, convergence studies are needed to avoid numerical noise and ensure reproducibility. This issue will be discussed more extensively in section 3.5.1.

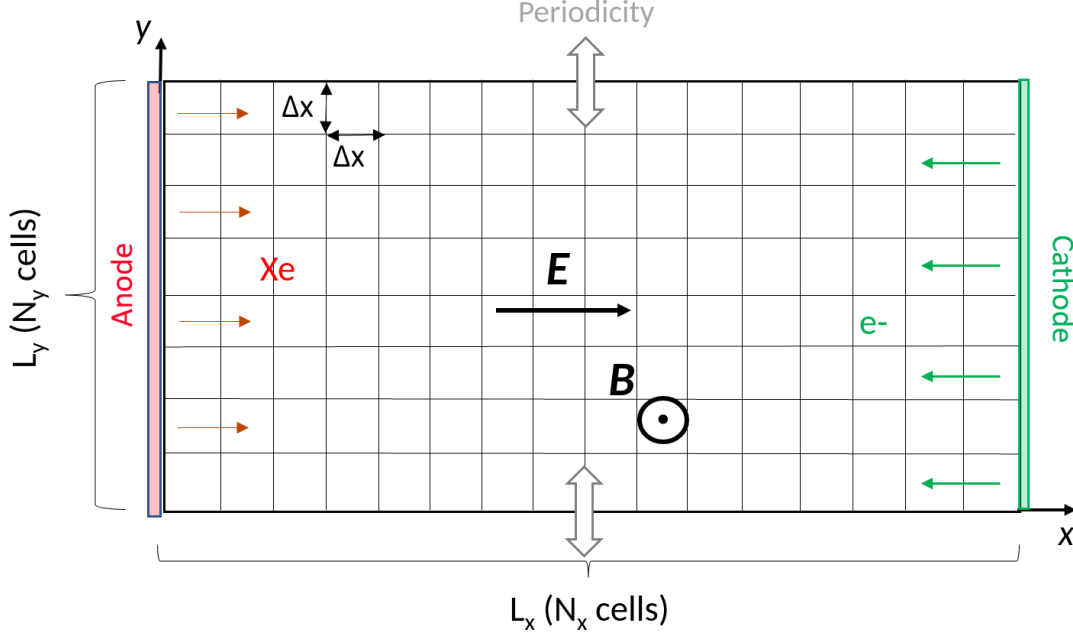


Figure 2.1 – Schematic of the typical Cartesian mesh used in this work .

Particle-In-Cell loop

In a PIC code, the same successive steps are performed every time step Δt , constituting the so-called PIC loop. As shown in figure 2.2, these steps are the following:

1. First, the **particle motion** is solved, using the second law of Newton. Even though the radial magnetic field can experience small variations of the order of 10% [142] due to the azimuthal current, it is assumed to be constant here. The Lorentz force is the only one acting on the particles

$$m d_t \mathbf{v} = q(\mathbf{E} + \mathbf{v} \times \mathbf{B}). \quad (2.2)$$

As explained before, ions are not magnetized and electrons are. While the motion of the former is solved using a simple leapfrog scheme [135], the latter are moved using the Boris scheme [150], hence including the rotation due to the magnetic field. The leapfrog scheme is performed in two steps with a shift of $\frac{\Delta t}{2}$ between the position and the velocity, that needs to be taken into account for the diagnostics.

2. The **boundaries** are then considered, as seen in figure 2.1: while the azimuthal direction is periodic, the particles crossing the axial boundaries are simply counted (to get the corresponding currents) and removed from the simulation. However, at the cathode (right axial boundary), electrons are emitted, as explained in section 2.4 and the ions reaching the anode (left axial boundary) can recombine into neutrals, as explained in section 2.3.
3. Some particles can undergo **collisions**, depending on the set of cross-sections considered. These collisions are treated using a Monte Carlo Col-

lision (MCC) module, with the null-collision method developed by Vahedi and Surendra [151] which allows to select only the right number of particles that will undergo collisions (and hence drastically reduce the computational time).

4. Once the eventual scatterings, particle creations or energy losses due to these collisions have been taken into account, all the particles are left with defined positions and velocity vectors. To be able to solve Poisson equation, the charge density ρ needs to be known at the grid points. Hence, a bilinear **interpolation of the densities** is performed, with the Cloud-In-Cell (CIC) scheme [135], from the particles to the grid points. This scheme represents a good compromise between numerical noise and computational speed.
5. With the knowledge of ρ , the **Poisson equation** can be solved

$$\Delta\phi = -\frac{\rho}{\epsilon_0}, \quad (2.3)$$

with Dirichlet boundary condition at the anode ($\phi > 0$ V) and at the cathode ($\phi = 0$ V). The algorithmic multi-grid method implemented in the open-source solver HYPRE [152] is used here. The electric field is then computed using finite differences from $E = -\nabla\Phi$.

6. When the electric field is known at each grid point, to be able to solve the particle motion again, each particle needs to know the fields at its position. Hence, a last step of **electric field extrapolation**, with again a CIC scheme, is performed.

Monte-Carlo Collision module

The collisions are solved with a probabilistic Monte-Carlo algorithm. Basically, for all the particles we consider the total cross-section $\sigma_T = \sum_{k=1}^N \sigma_k$ (sum of all the cross-sections σ_k) associated with the total collision frequency $\nu_t = \sigma_T v_r n_{target}$ with n_{target} the target particle density and v_r the relative velocity between the incident and target particles. The collision probability for the i^{th} particle of kinetic energy ϵ_k is then

$$P_i = 1 - \exp(-v_i \Delta t \sigma_T(\epsilon_k) n_{target}). \quad (2.4)$$

P_i is compared with a random number $R[0, 1]$ (i.e. from a uniform distribution between 0 and 1): if $R[0, 1] \leq P_i$, then the two particles collide and we draw another random number $R'[0, 1]$ to determine the collision type. However, with this method, the kinetic energy of all the particles in the domain needs to be known, which will drastically increase the computational time.

Hence in *LPPic*, the null-collision method described by Vahedi and Surendra [151] is used i.e. an additional "fake" collision is introduced in order to get a constant total collision frequency ν' , as shown in figure 2.3

$$\nu' = \max_x(n_{target}) \max_{\epsilon_k}(\sigma_T(\epsilon_k) v_r). \quad (2.5)$$

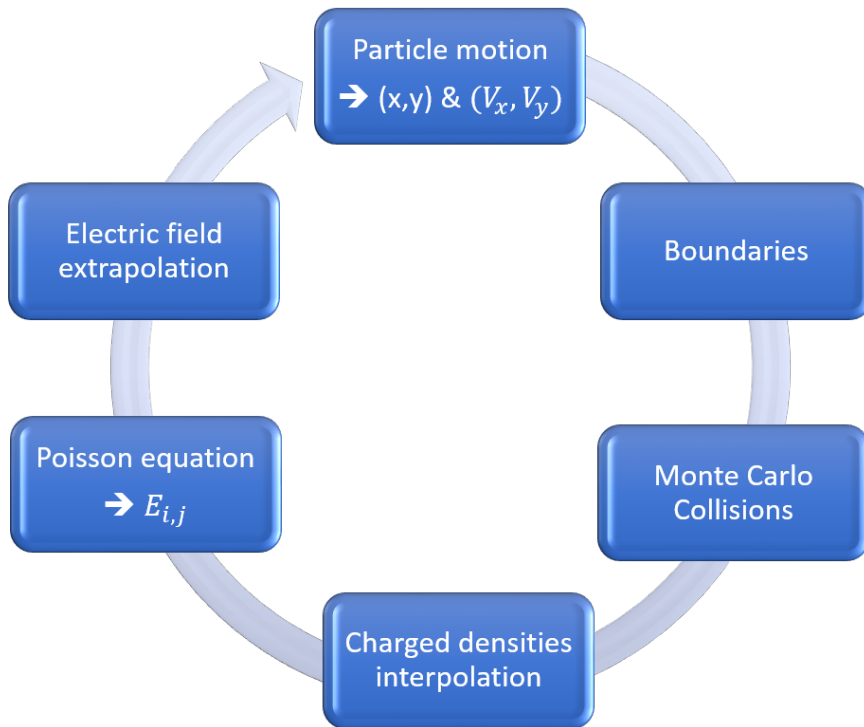


Figure 2.2 – Particle-In-Cell loop executed every time step.

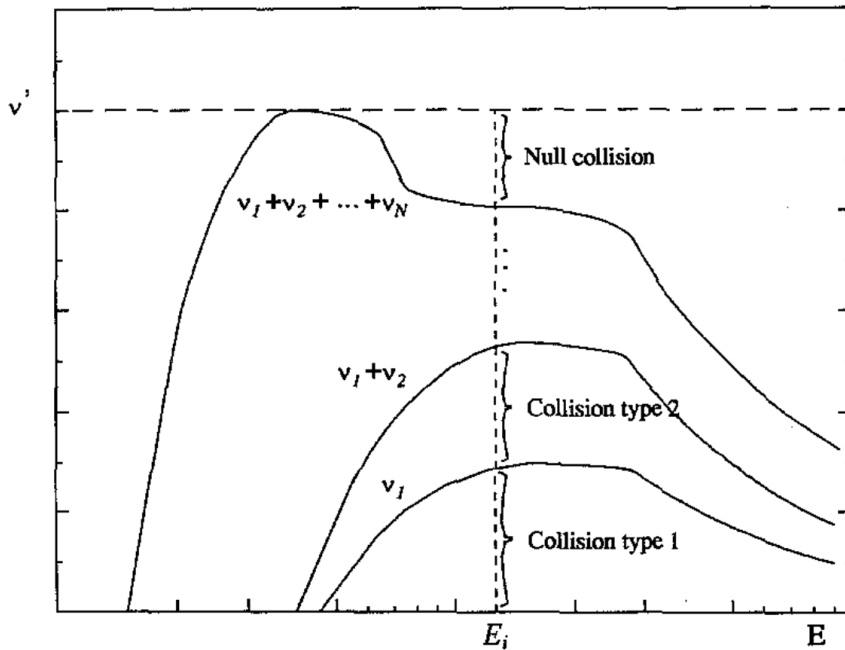
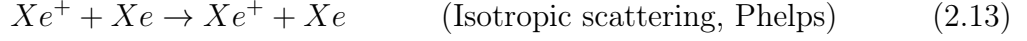
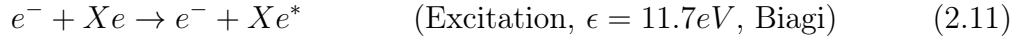
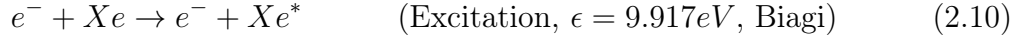
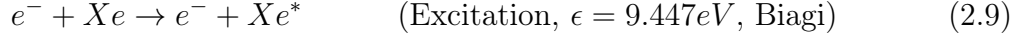
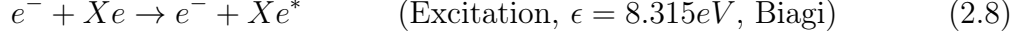


Figure 2.3 – From [151]: Null collision method.

The maximum number of particles that will undergo a collision is now given by

$$P_{null} = 1 - \exp(-\nu' \Delta t). \quad (2.6)$$

We can see that only a few particles are now treated, hence increasing the module efficiency. In *LPPic* with xenon, the following electron-neutral and ion-neutral collisions are considered, with the corresponding cross-sections extracted from the LXCat database [153, 154]



One can notice that we do not consider any short-range Coulomb collision here. Even though they are often neglected in HT simulations because their Mean Free Path (MFP) is longer than the channel length for the high T_e in the channel, it appears that for T_e of the order of few eVs, their cross-sections become comparable to the ones of electron-neutral collisions. It has been shown that these collisions tend to smooth the EVDF towards a Maxwellian distribution and also reduce the electron temperature anisotropy [139]. While these effects can have an impact on plasma/wall interactions [155], we consider that the one on anomalous transport is negligible here, following the recent analysis of Lafleur *et al.* [85]. More insights will be provided in chapter 4.

2.1.2 A powerful numerical tool

In PIC simulations the Debye length λ_d and the electron plasma frequency ω_{pe} need to be resolved. Hence, it gives the two following stability conditions on the time step Δt and the cell size Δx [135]

$$\begin{cases} \Delta t \leq \frac{0.2}{\omega_{pe}} \\ \Delta x \leq \lambda_d \end{cases} \quad (2.15)$$

Looking at equations 1.9 and 1.10, we can see that these two criteria are proportional to the electron density n_e : if n_e is high, Δt and Δx are small. Typically, for axial-azimuthal simulations, we use $\Delta x \approx 2 - 5 \times 10^{-5}$ m and $\Delta t \approx 2 - 5 \times 10^{-12}$ s. Hence, if we would like to simulate a standard domain of (4×1) cm² for 200 μ s (to capture several breathing mode periods), we would need 10^6 cells and 10^8 time steps, which cannot be achieved with a single computer.

For this reason, *LPPic* has been parallelized, using the Message Passing Interface (MPI) library. The computational domain is splitted (regularly in both directions) between the different Central Processing Units (CPUs) used and hence, each CPU treats a specific zone of the domain. For more details on this domain decomposition, the reader can refer to [119]. Currently, the code exhibits a good scalability up to 1500 CPUs and then the performances decrease, due to the HYPRE Poisson solver which cannot handle too-small domains. However, an extensive work to improve the code performance and scalability, in partnership with the High Level Support Team of CINES (National Computing Center for Higher Education), has been started recently and is ongoing. Additional insights on the code performance can be found in [120]. More details on the computational time will be given later, but depending on the initial conditions, simulations typically take between 5-15 days on 360 CPUs for the simplified cases (chapters 3 and 4) and up to 2 months on 1260 CPUs for the self-consistent cases (chapters 5 and 6). Due to the limited computational time available for one simulation on the different clusters used, a restart procedure was adopted: when the cluster wall-time is almost reached, the current simulation state (i.e. the particle array) is saved, in order to be able to relaunch the simulation again.

Unless otherwise stated, all the diagnostics performed with *LPPic* have been obtained by averaging over $N_{average}$ time steps, with $N_{average}=5000$. As for the electric field, a bilinear CIC interpolation is used to get the field values at the grid points and the resulting data are gathered in a HDF5 file. Moreover, the main advantage of PIC codes is to have access to kinetic informations, such as the charged particle distribution functions. The crude way to obtain these distributions is to directly use the particle arrays (gathering particle positions and velocities). However, as the total number of macroparticles can be as high as 10^9 , the size of the corresponding HDF5 files would make them inconvenient to use. Hence, a diagnostic has been implemented directly inside the code, calculating the distribution functions in each direction, every 100 time steps (and averaged over $N_{average}$). It is mainly the latter diagnostic that is used in the following work.

LPPic has been developed *ex-nihilo* for radial-azimuthal HT simulations, by Croes [119] who verified independently each module and also performed the 1D Helium CCP benchmark of Turner *et al.* [156]. It has later been improved by Tavant [120] in the same configuration, and Lucken [157] on a gridded thruster. Many parameters can hence easily be changed, such as the geometry (periodicity and boundaries), the magnetic field profile, the gas, etc. This versatility and good scalability makes *LPPic* a very powerful tool to efficiently study various electrical thrusters.

Prior to detail the different code developments, it is important to mention that in this work, two distinct simulation cases have been performed: a simplified benchmark case for the chapters 3 and 4 and a self-consistent case for the chapters 5 and 6. To guide the reader, the main input parameters for these two cases have been gathered in Table 2.1.

Table 2.1 – Nominal input parameters for the simplified benchmark case (chapters 3 and 4) and the self-consistent simulations (chapters 5 and 6).

Parameter	Symbol	Benchmark case	Self-consistent case	Unit
Computational parameters				
Time step	Δt	5×10^{-12}	2×10^{-12}	s
Cell size	$\Delta x = \Delta y$	5×10^{-5}	2×10^{-5}	m
Final time	T_{final}	20×10^{-6}	150×10^{-6}	s
Cells in axial direction	N_x	500	2000	
Cells in azimuthal direction	N_y	256	512	
Channel length	$x_{B,max}$	0.75	2.5	cm
Axial length	L_x	2.5	4	cm
Azimuthal length	L_y	1.28	1.02	cm
Initial state				
Macroparticles per cell	$N_{ppc,ini}$	75/ 150 /300	400	
Plasma density	$n_{p,ini}$	5×10^{16}	1×10^{18}	m^{-3}
Electron temperature	$T_{e,ini}$	10	1	eV
Ion temperature	$T_{i,ini}$	0.5	0.05	eV
Physical parameters				
Discharge voltage	U_0	200	300	V
Magnetic field maximum	B_{max}	100	170	G
Simulation models				
Ionization source term	S_{iz}	Fixed (Eq. 2.16)	Self-consistent	
Cathode model		Current-Equality	Quasi-Neutrality	

2.2 Preliminary modifications towards axial-azimuthal simulations

As explained before, the first step of this work consisted in adapting *LPPic* in order to replace the radial direction by the axial one. While a 2D Cartesian mesh with periodicity in the azimuthal direction is still used, we now use Dirichlet conditions for Poisson equation at the two axial boundaries: the plasma potential is fixed at the anode (often hundred of volts) and at the cathode (0 V). In this section, we briefly list the preliminary modifications that stems from the inclusion of this axial direction.

2.2.1 Magnetic field

While it was constant prior to this work, the radial magnetic field is now varying axially, often with a Gaussian shape as seen in figure 1.8(a). The axial position of the maximum radial magnetic field corresponds here to the exit plane of the thruster: even though no plasma/wall interaction will be considered in this work, this exit plane will often be mentioned for convenience. The local value of the magnetic field is then taken into account when solving the equation of motion (Eq. 2.2), more specifically in the Boris rotation [150].

In a real HT, the Hall current can generate a self-magnetic field. However, this self-field has been experimentally measured and found negligible compared to the imposed magnetic field [158, 159] (less than a few percent), which might not be the case any more for high-power HT. As we consider here only low-to-mid power HT, the magnetic field profile will always be constant in time.

2.2.2 Ionization process

The ionization rate depends mainly on the neutral density and electron temperature. As the neutral density is now varying axially, this rate needs to be calculated dynamically. For the self-consistent simulations in chapters 5 and 6, the ionization process is directly included in the MCC module, as explained in the previous section.

However, for the simplified cases described in chapters 3 and 4, no collisions are considered and hence, ionization events are taken into account as a source term for the plasma to sustain the discharge. To do so, electron-ion pairs are injected at each time step according to the profile of a given ionization rate $S(x)$, dependent on x only (uniform in azimuthal direction). $S(x)$ has a cosine shape, as shown in figure 3.2

$$\begin{cases} S(x) = S_0 \cos\left(\pi \frac{x - x_m}{x_2 - x_1}\right) & \text{for } x_1 \leq x \leq x_2 \\ S(x) = 0 & \text{for } x < x_1 \text{ or } x > x_2 \end{cases} \quad (2.16)$$

with $x_1 = 0.25$ cm, $x_2 = 1$ cm and $x_m = \frac{x_1 + x_2}{2} = 0.625$ cm.

The maximum ion current density J_M can be extracted from the steady-state continuity equation, accounting for the ionization profile in equation 2.16 by:

$$J_M = e \int_0^{L_x} S(x) dx = \frac{2}{\pi} (x_2 - x_1) e S_0. \quad (2.17)$$

Hence, we impose the value of J_M by fixing the maximum value of the ionization profile S_0 .

The number of electron-ion pairs to inject at each time step Δt is given by $L_y \Delta t \int_0^{L_x} S(x) dx$ and the positions (x_i, y_i) are chosen randomly such as

$$\begin{cases} x_i = x_m + \sin^{-1}(2r_1 - 1) \frac{(x_2 - x_1)}{\pi} \\ y_i = r_2 L_y \end{cases} \quad (2.18)$$

with r_1 and r_2 two random numbers uniformly distributed over the interval $[0,1]$. For one pair, the electron and the ion are injected at the exact same position. Their velocities are chosen from a Maxwellian distribution with the same temperature as initialisation ($T_e=10$ eV and $T_i=0.5$ eV).

2.2.3 Code optimization

In previous radial-azimuthal simulations, the plasma density was rather constant because we were at a fixed axial position. In this work, the plasma density is very inhomogeneous throughout the discharge channel (with variations of one or two orders of magnitude) and it also varies significantly in time because of the breathing mode oscillations. Hence, the number of macroparticles can be very different from one cell to another and consequently, the CPU load (i.e. the number of macroparticles in each CPU) can also be very inhomogeneous. Moreover, as the axial dynamics is considered, low-frequency oscillations appear and hence we need to increase the simulated physical time to capture them. Long simulation time and high number of macroparticles make these axial-azimuthal simulations very expensive. Hence, to be able to perform enough simulations during the allocated 3 years, a focus on code performance was needed.

To reduce the computational time, we used mainly four techniques described below: a dynamic load balancing, a particle sort, an ion subcycling and a scaling of permittivity. Whereas the two first techniques are only meant to optimize the CPUs efficiency, the two other ones are affecting the physics and hence, their influence on the discharge behaviour has been studied.

Load balancing

As described before, LPPic is parallelized using CPU domain decomposition i.e. each CPU is considering one part of the simulation domain. However, as the plasma density experiences big variations axially and in time, if we keep the same CPU decomposition, the CPU near the ionization zone (where the plasma density is higher) will have to handle many more macroparticles (up to 10-20 times) than the one near the sheath. Hence, this CPU will slow down the others and the overall computational time will be increased.

To palliate this issue, a dynamic load balancing is used, which means that we adapt the CPU domain decomposition (in the axial direction) in order to have approximately the same number of macroparticles per CPU (i.e. the total number of macroparticles in the simulation domain, divided by the number of CPU used). In other words, the CPUs where the plasma density is low will have more axial cells than the ones where the plasma density is high. The number of CPUs in azimuthal direction is kept constant because the plasma density is not varying much in this direction. This load balancing is done periodically, often every 150000 time steps.

Particle sort

As described previously, the mesh and the particles need to exchange information twice during a PIC loop, via an interpolation (from the particles to the grid points) and an extrapolation (from the grid points to the particles). For these operations, we chose to use the 1st order bilinear CIC scheme which represents a good compromise between the 0th order Nearest-Grid-Point scheme (faster) and the 2nd order quadratic spline scheme (less noise) [160]. However, because this operation needs to be performed for every macroparticle in the system, every time step, it ends up being one of the most costly subroutine in term of computational time.

To optimize this operation, one can look at how the information is stored inside one CPU. Basically, to speed-up memory accesses, a hierarchical organisation is adopted with the main CPU memory at the bottom, the CPU processor at the top and in between, numerous caches labelled L1 (highest), L2, L3, etc. When some information is needed by the processor, it first seeks in the various caches, before going down to the main memory until the information is found. If it is found in a cache, the operation is fast and we call it a "cache-hit". On the contrary, if the processor needs to reach the main memory, the operation is slow and we call it a "cache-miss". Without going into more computer-science details, the idea here is hence to reduce the number of cache-misses, by making the needed data available in the first cache levels.

Usually, the particle array is not sorted and the particles are located at a random position with respect to the mesh, and hence, when the interpolation/extrapolation process is called, the processor sometimes needs to go through the whole particle array several times to find all the particles close to one grid point. To avoid these cache-misses, we can sort the particle array by mesh location and then, all the particles in one cell will be accessed easily in the L2 cache. To do so, we used an hybrid counting sort adapted from [161], every 70 time steps (a compromise between the time taken by this sort and the particle displacement in the grid). Other types of sort exist and might be more efficient, such as a cycle sort [162], but it has not been tested yet. This hybrid counting sort was not needed for the simplified case of chapters 3 and 4 and was only used for the self-consistent simulations of 5 and 6. The speed-up was not significant (around 5-10 %) but it should also be coupled with more efficient handling of grid diagnostics, which is left for future work.

Electron subcycling

For the gases considered here, electrons have a negligible mass compared to ions. Hence, the ions are moving much slower than the electrons and it is not needed to solve their motion at each time step. To reduce computational time, we can choose to solve the ion motion every α_{sub} electron time steps, i.e. the ion time step will be: $\Delta t_i = \alpha_{sub} \Delta t_e$. In [163], Adam *et al.* have studied the numerical instabilities that could appear if this process (called electron subcycling) is used.

They have observed that α_{sub} must be an even number and that a numerical instability can arise if $\omega_{pe}\Delta t_i \approx \pi$ which gives, using the stability criterion on Δt_e (equation 2.15)

$$\alpha_{sub} = \frac{\Delta t_i}{\Delta t_e} \leq \frac{\pi}{0.2} \approx 15.7. \quad (2.19)$$

In this work (otherwise stated), an electron subcycling with $\alpha_{sub} = 11$ has always been used, speeding-up the simulations by around 30%. We have verified on the simplified case described in chapter 3 that it has negligible effect on the results observed. The last electric field value has been used to push the ions after α_{sub} electron time steps. Additional tests need to be performed to see if using instead the averaged (over these α_{sub} electron time steps) electric field affect the discharge behaviour.

Scaling of permittivity

Looking at the PIC stability criteria (Eq. 2.15), and recalling that $\lambda_d = \sqrt{\frac{\epsilon_0 k_B T_e}{n_e e^2}}$ and $\omega_{pe} = \sqrt{\frac{n_e e^2}{m \epsilon_0}}$, it appears that if we change the vacuum permittivity ϵ_0 , we will be able to relax these stability constraints and use bigger time step and cell size. Hence, the computational time will be reduced, while keeping the stability. For a scaling factor α_ϵ such as $(\epsilon_0)' = \alpha_\epsilon \epsilon_0$, we can use : $(\Delta x)' = \sqrt{\alpha_\epsilon} \Delta x$ and $(\Delta t)' = \sqrt{\alpha_\epsilon} \Delta t$.

However, this scaling has an influence on the simulation results. The more obvious one is the fact that the plasma characteristics are changed (Debye length and plasma frequency) and, as most of the instabilities observed depend on these parameters (especially the EDI [84]), using a scaling of the permittivity will affect the instabilities observed. Moreover, according to Poisson equation (Eq. 2.3), if we increase the vacuum permittivity, we will need higher charge difference to get the same electric field. Hence, scaling up this parameter induces a violation of the quasi-neutrality that could also affect the discharge behaviour.

All in all, this technique has only been used for the self-consistent simulations of chapters 5 and 6 because we are not able to simulate a "real" case without relaxing the PIC stability constraints. Hence, the influence of this scaling technique will be discussed in more details in these chapters.

Other possible techniques to speed-up the simulations

One can also use other scaling techniques such as artificially decreasing the heavy particle masses (ions and neutrals) or down-sizing the system geometry. The mass-ratio scaling makes the heavy particles move faster, decreasing significantly their transit-time in the discharge and hence decreasing the number of time steps needed to capture the low-frequency dynamics [164, 139, 165]. However, it requires to change the collisional cross-sections which induces an artificial increase of the axial transport and changes the discharge characteristics. With the down-sizing of the system geometry, we can simulate a smaller number of cells

thanks to this geometrical scaling factor and hence speed-up significantly the computation [166, 89]. However, the surface-to-volume ratio is modified which makes it difficult to account properly for the wall effects and most importantly, the convection rate of the instability in the axial direction would be greatly enhanced, reducing the instability amplitude. Hence, these two techniques have not been implemented in *LPPic*.

Moreover, because the crucial parameter is the number of macroparticles in each cell N_{ppc} which should be high enough to avoid numerical noise, the ideal situation would be to be able to keep this number approximately constant in each cell, through the whole simulation. To do so, one can use a so-called *merging-splitting algorithm* [167, 168] which changes dynamically the particle weight q_f to keep N_{ppc} approximately constant: decreasing q_f when there are not enough particles (splitting), increasing it when there are too many particles (merging). However, if not implemented correctly, this kind of algorithm is known to affect significantly the distribution functions and hence, lead to wrong results. Due to the complexity of the implementation, this has been left for future work and might be needed to perform long self-consistent simulations.

2.3 Neutral dynamics

2.3.1 Context

The density of the neutral gas exhibits large variation in the axial direction of the thruster: it is maximum at the injection point (anode) and it is strongly depleted before the exit plane of the thruster due to ionization, reaching values in the plume around one order of magnitude lower than at the anode. This profile is also varying in time, mainly due to the low-frequency axial oscillations known as the breathing mode instabilities. Hence, for the self-consistent simulations presented in chapters 5 and 6, we need to resolve accurately the neutral dynamics in order to capture the correct discharge behaviour.

A first simple way consists in solving only the continuity equation to obtain the neutral density ρ , as follows

$$\partial_t \rho + u \partial_x \rho = -S_{iz}, \quad (2.20)$$

with boundary condition $\rho(x = 0) = n_{injected,anode} = constant$ and a constant neutral velocity $u = 200 \text{ m} \cdot \text{s}^{-1}$. The ionization source term S_{iz} is obtained at each time step depending on the local electron density and temperature. The neutral dynamics is only solved in the axial direction because its variations are mostly in this direction. The main drawback of not considering the azimuthal direction is related to rotating spokes that may originate from an azimuthal variation of neutral density [94] and hence, cannot be captured in our simulations.

This method of considering only the continuity equation was used previously by Lafleur *et al.* [111, 86] and we implemented it in the first version of *LPPic*. However, on long simulation times, we observed a very high sensitivity of the

simulation results to the neutral density profile and moreover, the neutral velocity has been measured experimentally to increase axially by a factor of 2 to 3 [169]. Hence, we decided to implement a more accurate neutral dynamics solver by taking into account the complete 1D Euler system

$$\begin{cases} \partial_t \rho + \partial_z(\rho u) = S_1 \\ \partial_t(\rho u) + \partial_z(\rho u^2) = -\partial_z P + S_2 \\ \partial_t E + \partial_z(Eu) = -\partial_z(Pu) + S_3 \end{cases} \quad (2.21)$$

with S_1 and S_2 collisional source terms, S_3 energy source term, P the neutral pressure, and E the neutral energy per volume unit such as

$$E = \frac{P}{\gamma - 1} + \frac{1}{2}\rho u^2, \quad (2.22)$$

with γ the heat capacity ratio, equal to 5/3 in monoatomic gases.

2.3.2 Model description

The 1D Euler system described by equations 2.21 can be written in balance form

$$\partial_t \mathbf{w} + \partial_x f(\mathbf{w}) = \mathbf{S}(\mathbf{w}), \quad (2.23)$$

with \mathbf{w} the state vector

$$\mathbf{w} = \begin{pmatrix} \rho \\ \rho u \\ \rho E \end{pmatrix}, \quad (2.24)$$

$f(\mathbf{w})$ the flux

$$\mathbf{f}(\mathbf{w}) = \begin{pmatrix} \rho u \\ \rho u^2 + P \\ u(E\rho + P) \end{pmatrix}, \quad (2.25)$$

and \mathbf{S} the source term which can be expressed as

$$\mathbf{S} = \begin{pmatrix} \rho S_{iz} \\ \rho u S_{iz} \\ \frac{E - E'}{\tau} \end{pmatrix}. \quad (2.26)$$

Only the effect of ionization has been taken into account in the source terms S_1 and S_2 and the source term S_3 for the energy equation includes a parameter τ that is set in order to impose an isothermal neutral dynamics i.e. the neutral temperature is kept constant and equal to $T_n = 640$ K. Practically, the value of τ is set as low as possible, while still complying to the CFL criteria (typically, we have $\tau \approx 10^{-11}$ s), to make the energy E converge to the imposed energy E' corresponding to the temperature T_n

$$E' = \frac{\rho R T_n}{\gamma - 1} + \frac{1}{2}\rho u^2. \quad (2.27)$$

One can notice that imposing this neutral temperature makes the system isothermal, hence the energy equation becomes meaningless. However, it has been included for two reasons: first, it makes the numerical resolution more robust and more importantly, we can later easily account for any sources or losses of neutral.

If we add to equation 2.23 the initial condition

$$\rho(x, t = 0) = \rho_{ini}(x), \quad (2.28)$$

and the boundary conditions

$$\rho(x = 0, t) = \rho_L(t) , \rho(x = L_x, t) = \rho_R(t), \quad (2.29)$$

we obtain a general Initial Boundary Value Problem (IBVP). If we discretize the domain in x_{max} cells in the axial direction, we can solve this IBVP using the following explicit Euler finite volume scheme. The value of the state vector \mathbf{w} in each cell i can be found at time step $(n + 1)$ by

$$\mathbf{w}_i^{n+1} = \mathbf{w}_i^n - \frac{\Delta t}{\Delta x} (F_{i+\frac{1}{2}} - F_{i-\frac{1}{2}}) - \mathbf{S}\Delta t, \quad (2.30)$$

with $F_{i-\frac{1}{2}}$ and $F_{i+\frac{1}{2}}$ the left and right numerical fluxes respectively. Here, we have used a first order Euler temporal scheme. A second order Runge-Kutta scheme has also been implemented but, as seen later in figure 2.5, the results were very similar and hence, this first-order scheme has been kept to reduce computational time.

HLLC Riemann solver

The finite volume scheme needs a mathematical expression for the numerical fluxes. Harten, Lax, and van Leer, proposed a numerical scheme for the homogeneous version of the system 2.23 (i.e. without the source terms): the HLL Riemann solver [170]. It considers two waves separated by three constant states which give the values of the inter-cell fluxes $F_{i+\frac{1}{2}}$. Based on this work, Toro *et al.* [171] improved this scheme to account for contact discontinuities by using a three-waves model, namely the HLLC Riemann solver (C stands for Contact). As illustrated in figure 2.4, there is now an intermediate velocity S^* additionally to the left and right velocities S_L and S_R . They delimit 4 states: the left and right state vectors w_L and w_R , and the left and right intermediate state vectors w_L^* and w_R^* . Only a brief description of this scheme will be given here, the reader may refer to [172] for extensive details.

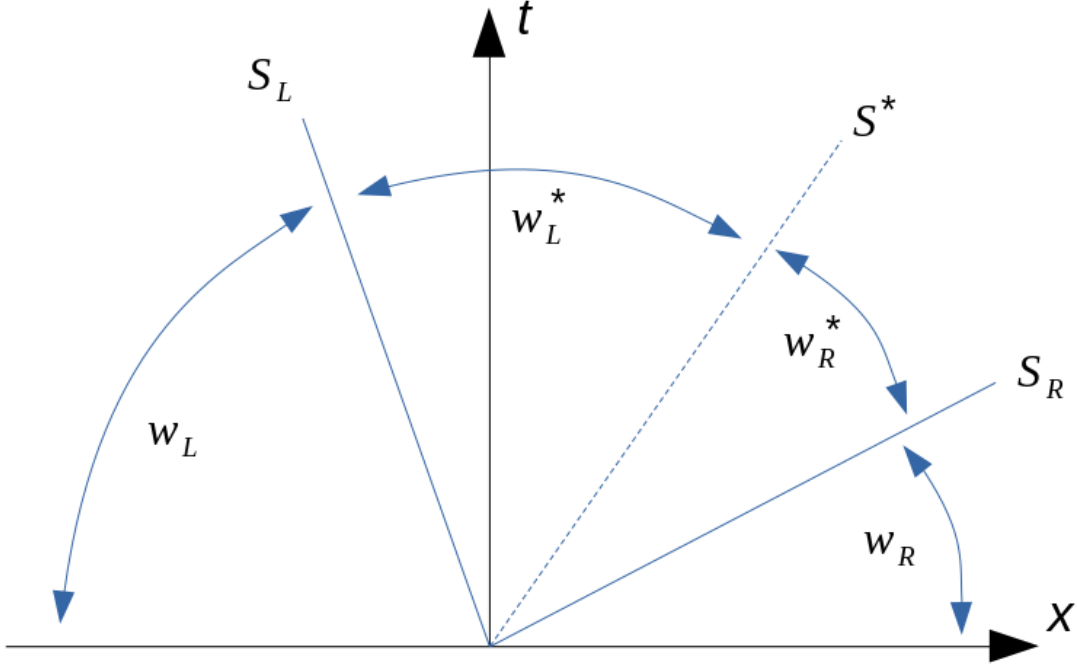


Figure 2.4 – HLLC approximate Riemann solver. Solution in the intermediate region consists of two constant states separated from each other by a middle wave of speed S^* .

The procedure to find the intercell fluxes $F_{i+\frac{1}{2}}$ at the interface of the left cell (L) and the right cell (R), is the following:

1. Compute the intermediate pressure P^* given by

$$P^* = P_L + \rho_L(u_L - S_L)(u_L - S_M) = P_R + \rho_R(u_R - S_R)(u_R - S_M). \quad (2.31)$$

2. Compute the different velocities. The left and right velocities are

$$\begin{cases} S_L = u_L - c_L q_L \\ S_R = u_R + c_R q_R \end{cases} \quad (2.32)$$

with (for $K = L, R$)

$$q_K = \begin{cases} 1 & \text{if } P^* \leq P_K \\ \sqrt{1 + \frac{\gamma+1}{2\gamma} \left(\frac{P^*}{P_K} - 1 \right)} & \text{if } P^* > P_K \end{cases} \quad (2.33)$$

and c_K the sound speed.

The intermediate velocity is

$$S^* = \frac{P_R - P_L + \rho_L u_L (S_L - u_L) - \rho_R u_R (S_R - u_R)}{\rho_L (S_L - u_L) - \rho_R (S_R - u_R)}. \quad (2.34)$$

3. Use these velocities to find the corresponding values for $F_{i+\frac{1}{2}}$

$$F_{i+\frac{1}{2}} = \begin{cases} F_L & \text{if } S_L > 0 \\ F_L^* & \text{if } S_L \leq 0 \leq S^* \\ F_R^* & \text{if } S^* \leq 0 \leq S_R \\ F_R & \text{if } S_R < 0 \end{cases} \quad (2.35)$$

F_L and F_R are respectively the left and right Euler fluxes that can be found using equation 2.25 and F_L^* and F_R^* are respectively the left and right intermediate fluxes that can be found by (for K=L,R)

$$F_K^* = F_K + S_K(w_K^* - w_K). \quad (2.36)$$

Boundary conditions

At the right boundary (outlet), the neutral flow is supersonic. Hence, as the information is only leaving the system, a simple linear extrapolation can be used as boundary condition

$$\mathbf{w}_{x_{max}+1} = \mathbf{w}_{x_{max}} \quad (2.37)$$

However, we have a subsonic flow at the left boundary (inlet) and then the information can come from both directions. A simple extrapolation can not be used to get the values of \mathbf{w}_1 from \mathbf{w}_2 . Based on previous work [173, 174], we chose to fix two parameters: the mass flow rate Q and the neutral temperature T_n . By discretizing the thermostatic law for a polytropic perfect gas

$$Pu = \frac{(\gamma - 1)c_v QT}{S} \quad (2.38)$$

and the characteristic equation

$$\frac{\partial P}{\partial t} - \rho c \frac{\partial u}{\partial t} = -(u - c) \left(\frac{\partial P}{\partial x} - \rho c \frac{\partial u}{\partial x} \right) \quad (2.39)$$

we can get the increment of velocity Δu from the values in cells 1 and 2

$$\Delta u = \frac{u_1^2(u_1 - c_{s1})(P_2 - P_1 - \rho_1 c_{s1}(u_2 - u_1))}{\left(\frac{Q}{S}T_n R - \rho_1 c_{s1}\right)\left(\frac{\Delta x}{\Delta t} - (u_1 - c_{s1})\right)} \quad (2.40)$$

with $c_{s1} = (\gamma P_1 / \rho_1)^{1/2}$ the sound speed in the first cell and S the anode surface.

Then, it gives us the new values of the state vector \mathbf{w}_1^{n+1} in cell 1

$$\begin{cases} u_1^{n+1} = u_1^n + \Delta u \\ \rho_1^{n+1} = \frac{Q}{u_1^{n+1} S} \\ P_1^{n+1} = \rho_1^{n+1} R T_n \end{cases} \quad (2.41)$$

Ion recombination at the anode

Originally, the ions impacting the anode were simply lost from the system. However, we have observed that at some instant of a breathing mode oscillation, the ionization source term was important near the anode and hence the neutral density was highly depleted there. As we impose a constant mass flow rate, the neutral velocity was increasing and hence, we were slowly losing neutrals throughout the simulation. Hence, it appeared that it was necessary to include the fact that in a real Hall thruster, the ions impacting the anode should recombine into neutral atoms. This new source of neutrals was at first added as a source term S_{recomb} but it was found to generate discontinuities. It appeared that computing the ion flux impacting the anode at each time step and adding it to the inflow boundary condition was more physical. Hence, the mass flow rate Q at the anode is now given by

$$Q = Q_{ini} + Q_{recomb}, \quad (2.42)$$

with Q_{ini} a fixed flow rate (often $5 \text{ mg} \cdot \text{s}^{-1}$) and Q_{recomb} the ion flux at the anode. These newly created neutrals represent around 10% of the imposed mass flow rate, as seen later for the self-consistent simulations, in figure 5.3.

Moreover, additional effect may impact the neutral gas dynamic. The most important might be the recombination of some ions at the radial channel walls that can create more neutrals along the discharge channel. Also, the collisions of the neutrals with the ions can increase the neutral velocity. While the former process might be difficult to implement self-consistently in an axial-azimuthal code, the latter can be taken into account by adding the following term to the momentum equation source term

$$S_2 = \rho(u - v_i)\nu_{in}, \quad (2.43)$$

with v_i the velocity of ions that collide with the neutrals and ν_{in} the ion-neutral collision frequency. This term has been implemented but its use has been left for future work.

2.3.3 Solver verification and validation

Sod test case and analytical solution

One common way of testing the implementation of our solver is to use the so-called Sod test case [175]. This test has been described in appendix A and more details can be found in the Master's thesis of Tordeux [176].

Tordeux has also derived a simple analytical solution for a 1D steady case close to a real HT. He considered the continuity and momentum equations and obtained an excellent agreement [176] between the Riemann solver solution and the analytical profile, which increased further the confidence in our solver.

Solution for an imposed ionization source term

Before implementing the solver in LPPic, it has been tested with an imposed ionization source term with a Gaussian shape displayed in figure 2.5, close to the one of a real HT. The initial density profile used in previous axial-azimuthal simulations [76, 111] is used, along with a constant velocity of $200 \text{ m} \cdot \text{s}^{-1}$ (which gives a mass flow rate of $5 \text{ mg} \cdot \text{s}^{-1}$) and temperature of 640 K. We can see in figure 2.5 that the velocity is increasing by a factor of almost 2 in the plume, which corresponds to experimental observations [169] and justify the need to use a more complex solver for the neutral dynamic. One can notice that, as imposed by the very small relaxation coefficient τ , the neutral temperature is kept constant at 640K.

Moreover, the choice of an Euler scheme for the temporal discretization of equation 2.30 might be questionable. We have also tested a 2nd order scheme (Runge-Kutta 2) and as seen in figure 2.5, it gives the same results for this particular test case. As the neutral dynamics has very long characteristic times compared to the plasma dynamics (the PIC time step value is usually around 10^{-12} s while the breathing mode period is around 10^{-4} s), it can be considered as quasi-stationary which means that high-order schemes are probably not needed. For efficiency consideration, the 1st order Euler scheme has hence been kept.

2.4 Cathode model

While the neutral injection at the anode is fixed by the mass flow rate imposed, the electron emission at the cathode is more complex. The cathode emits electrons for two reasons: ionize the neutral atoms in the discharge channel and neutralize the ions that are expelled out of the thruster (the plume should be neutral to avoid any charge deposition on the satellite). There have been many works on how to model the cathode itself [177, 178, 179] but the inclusion of a cathode in a thruster model has been scarcely studied [139, 180, 181], even though it has been observed experimentally that the cathode position has an influence on the discharge behaviour [182, 33].

The influence of the cathode model in an axial-azimuthal (PIC, hybrid or fluid) simulation has never been studied before but Szabo described in his PhD thesis [139] two methods to model the electron emission (in a PIC radial-axial code), based on a Current Equality (CE) condition (between the anode and the cathode) or a Quasi-Neutrality (QN) condition (as the plume should be quasi-neutral). In a 2D axial-azimuthal code, the cathode position (often at the top of the cylindrical thruster channel) cannot be accounted for and we make the simplification of having a "cathodic plane" by emitting electrons from an imposed axial position, often at the right domain boundary. Basically, to model the cathode, we can identify two different steps:

1. Choose the number of electrons injected per time step, with one of the two aforementioned models.

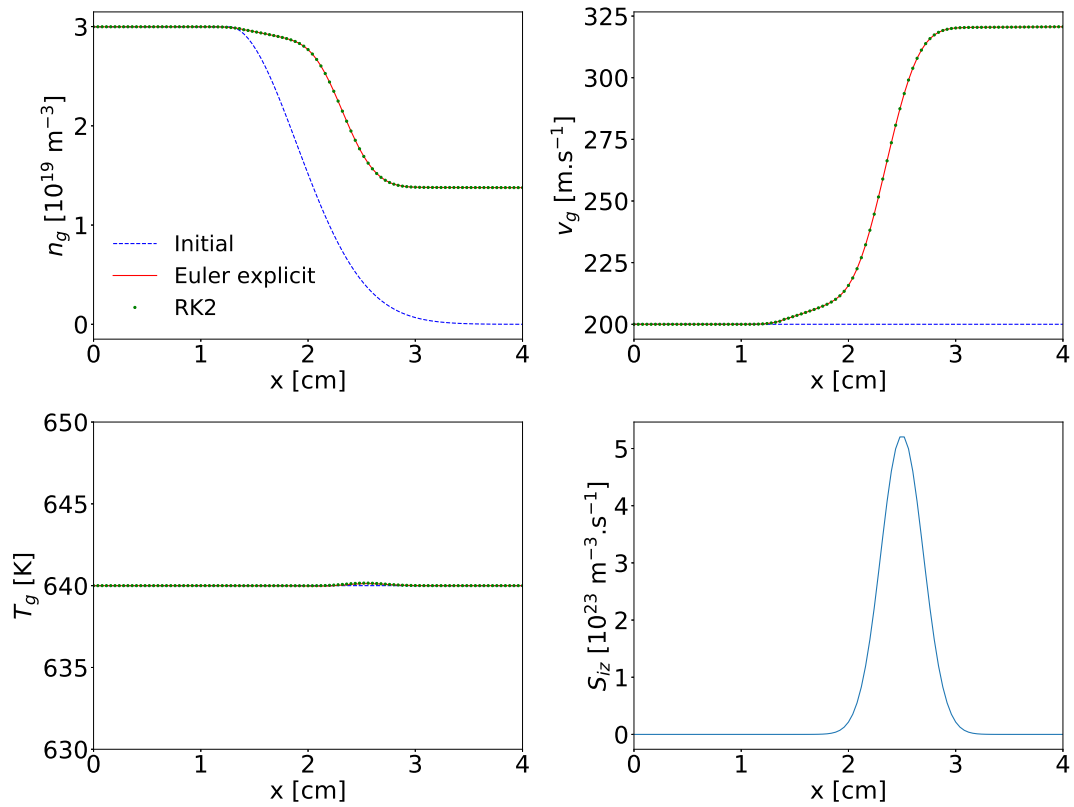


Figure 2.5 – Axial profiles of neutral density (top left), velocity (top right) and temperature (bottom left) for a given ionization profile (bottom right) when using a 1st order Euler scheme (red line) or a 2nd order Runge-Kutta scheme (orange line). 100 cells are considered, with a CFL of 0.5 and a coefficient of relaxation $\tau=10^{-8}$.

2. Choose their position and energy.

Although the first step can be considered as the most important, the emitted electron temperature can also affect the discharge behaviour, as seen later in section 3.6. In the following, we will describe these two methods and give some insights on which one is the best suited for axial-azimuthal PIC simulations.

2.4.1 Current Equality condition

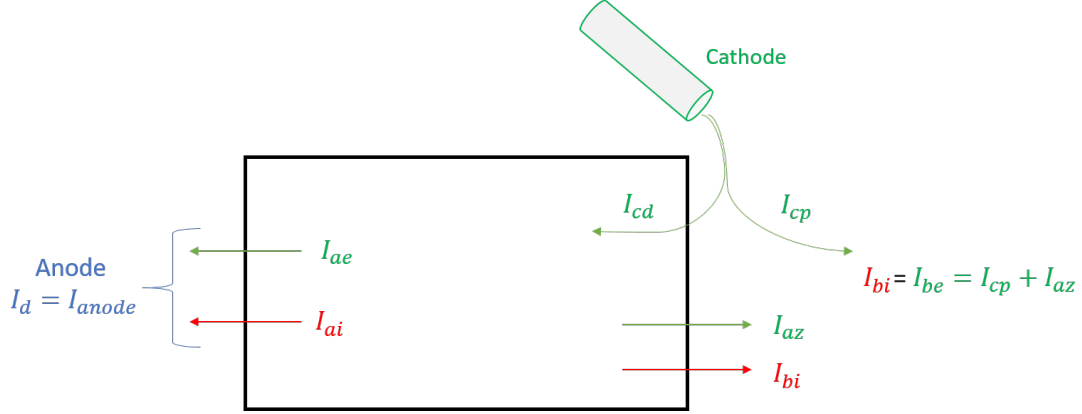


Figure 2.6 – Currents in a HT. I_d : discharge current. I_{ae} and I_{ai} : electron and ion anode currents, respectively. I_{cd} and I_{cp} : cathode electron currents in the plume and in the discharge, respectively. I_{az} and I_{bi} : electron and ion currents leaving the domain through the right axial boundary, respectively.

In figure 2.6, the different currents in a HT are displayed. At stationary state, the discharge current $I_d = I_{ae} - I_{ai}$ must be equal to the cathode current $I_c = I_{cp} + I_{cd}$ i.e.

$$I_d = I_c, \quad (2.44)$$

with I_{ai} and I_{ae} the anode ion and electron currents respectively, I_{cp} and I_{cd} the cathode electron currents in the plume and in the discharge, respectively.

The plume should be neutral so

$$I_{bi} = I_{be} = I_{cp} + I_{az}, \quad (2.45)$$

with I_{az} and I_{bi} the electron and ion currents leaving the domain through the right axial boundary, respectively. Combining these equations, we find the cathode discharge current

$$I_{cd} = I_d - I_{bi} + I_{az}. \quad (2.46)$$

Hence, we know the number of electrons to be injected per time step

$$\frac{dN_{e,inj}}{dt} = I_{cd} \implies N_{e,inj} = I_{cd} \Delta t. \quad (2.47)$$

In LPPic, these different currents are calculated by counting the number of particles that leave the simulation domain at the anode and cathode (i.e. left and right boundary domain, respectively), every time step.

2.4.2 Quasi-neutrality condition

The problem with the previous method is that it is only valid for a stationary state. If at initial state, the charge distribution has an unusual shape, the transient regime will disturb even more this charge distribution and we will have a non quasi-neutral plasma in the plume [139].

To overcome this issue, we can directly impose a quasi-neutral condition at the cathode and use this condition to compute the number of electrons to be injected. To do so, at each time step, we compute the charge difference at each grid point i of the cathode (i.e. the last axial cell) and then we sum this difference along the whole cathode (y_{max} azimuthal points)

$$Q_{fs} = \sum_{i=1}^{y_{max}} (N_i(i) - N_e(i)), \quad (2.48)$$

with N_i and N_e the number of ions and electrons at the cathode, respectively. If $Q_{fs} > 0$, we inject $N_{e,inj} = Q_{fs}$ electrons. If not, we do nothing but because the electrons are lighter, the condition $Q_{fs} > 0$ is almost always satisfied.

One can wonder if imposing the neutrality in several axial cells (instead of only the last one) would be more robust. A compromise needs to be found then, not to affect the behaviour of the bulk. This has not been investigated here and is left for future work.

2.4.3 Setting positions and energies

After determining the number of electrons to inject at each time step, we need to know where we should inject them. To determine their azimuthal position, a local quasi-neutrality is imposed in [139] by following the next steps, until all electrons have been injected.

1. We consider the charge difference as a distribution $Q_i = N_i(i) - N_e(i)$,
2. We use a first random number $R[0,1]$ to get a position $pos_y = R L_y$,
3. We use a second random number $R'[0,1]$ that gives $p = R' Q_{max}$, with Q_{max} the maximal value of charge difference,
4. We compare p and $Q(pos_y)$: if $p < Q(pos_y)$ we inject an electron at the azimuthal position pos_y .

Even though this procedure enhances the plume local quasi-neutrality, we decided to simplify it and inject uniformly the electrons in the azimuthal direction, to ease the comparison with previous simulation works [76, 111, 140].

The electron energies are chosen with a temperature $T_{e,inj}$, from a full Maxwellian distribution in the azimuthal and radial directions and a Maxwellian flux distribution in the axial direction according to [183, 135], as described in the appendix of [184], i.e. their axial velocity is $v_x = -v_{th} \sqrt{-\ln(R[0,1])}$ with R a random number between 0 and 1 and $v_{th} = \sqrt{\frac{2qT_{e,inj}}{m}}$ their thermal velocity.. A small

axial shift is also used to avoid any charge accumulation along the emission plane i.e. $pos_x = L_x - R'[0, 1] \Delta t V_x$.

Another injection method, used in [140] and later in [185] will be detailed in chapter 3. In a few words, the emission plane is shifted axially (1 mm from the right boundary) and then a simplified current equality condition is used, given directly by: $I_{cd} = I_{ae} - I_{ai}$. The potential is also shifted in order to get an azimuthally averaged zero potential at the emission plane. Hence, we can neglect the cathodic sheath between the emission plane and the right boundary of the domain.

2.4.4 Which model should we choose?

Recently, an implicit 2D axial-azimuthal PIC code has been developed by Chernyshev *et al* [142] with a different cathode model. In this model, the emitted electron current is kept constant and a small amount of ions are also injected at the cathode, given by

$$N_{ion,inj} = \sqrt{\frac{m_e}{m_i}} \times N_{elec,inj} \approx \frac{N_{elec,inj}}{500}. \quad (2.49)$$

The authors claim that this ion current is needed because some ions are periodically extracted from the hollow cathode. This method was implemented but it has not been studied extensively.

All in all, it is difficult to make a definitive decision on the best way to model the cathode in 2D axial-azimuthal PIC simulations. For this reason, we will try to give more insights on this issue in the rest of the work, by studying the impact of the chosen cathode model on the observed discharge behaviour. The reader can directly refer to section 3.6 for the simplified benchmark case, or section 5.2.3 for the self-consistent simulations.

2.5 Further improvements of the model

The axial-azimuthal model will always be an approximation of a real Hall thruster. However, to get closer to reality, we identified two other phenomena that could be included in the model. The most important one might be the addition of thruster walls, using what we call a "fake radial dimension". Moreover, it has been observed that around 10% of the thruster ions are doubly-charged [186, 187] and that these doubly-charged ions could generate additional instabilities [188]. Hence, this new species could also be added to our model.

We detail here the implementation of these two phenomena. However, their influence on the discharge physics will not be discussed in this manuscript, to ease the analysis of the results obtained.

2.5.1 Fake radial dimension

As explained above, the code *LPPic* was originally used to simulate the radial-azimuthal plane of a HT. Because no dissipation mechanism was included in the system, a "fake" axial dimension was implemented in order to limit the growth of electron energy. Indeed, even though the Poisson equation is not solved in the third direction, the particle position is still tracked. Hence, any charged particle that was crossing an artificial limit in the third direction was reinjected with a lower energy. The detail process can be found in the original work of Croes [119] and has been further improved by Tavant [120]. Here, the "fake" radial dimension is used to take into account particle and energy losses at the wall. Two methods have been implemented:

- The local electron temperature is used as a criteria for getting rid of hot electrons i.e. when $E_e > 5 T_e$, the electron is removed.
- A finite radial length L_r is considered. At every time step, we remove from the system all the ions that cross this artificial boundary. As the electrons are moving faster than the ions, more electrons will cross the boundary during one time step. Hence, we decide to remove the same number of electrons, considering the ones with the highest energy. The other low-energy electrons are specularly reflected.

While the first method has been scarcely tested, the second one was mainly used by Tavant [120]. The noteworthy effect was to decrease the electron temperature and density. A different process is used in [66, 76] in which a sheath potential is fixed at 20 V and every electron with higher radial energy will undergo a collision, with a frequency given by $\nu_{ew} = \frac{v_r}{L_r}$, with v_r the electron radial velocity and L_r the imposed radial length. If the collision occurs, the electron is isotropically reflected and does not suffer from any energy losses.

One can notice that Secondary Electron Emission (SEE) has not been taken into account yet and its implementation is left for future work.

2.5.2 Doubly-charged xenon ions

Recently, Lucken has adapted *LPPic* to consider more than two charged particle types (electron and ion) [157]. To take advantage of this new feature, we added doubly-charged xenon ions. The first difficulty was to select the appropriate cross-sections set. Following the choice of Taccogna and Minelli [89], the doubly-charged Xe^{2+} are produced from direct double ionization of Xe atoms (cross-sections from [189])



and single ionization of Xe^+ atoms (cross-sections from [190])



While the first reaction could be directly included in the MCC module, the second one concerns two charged species and hence a different procedure needs to be used. Based on the work of Nanbu [191], this collision is treated using a Direct Simulation Monte Carlo (DSMC) procedure. At each time step, the maximum number of collisions N_{max} that can occur in a cell between electrons (noted A) and Xe^+ ions (noted B) is calculated using:

$$N_{max} = N_A N_B \frac{W}{V_C} g_{max} \sigma_T(g_{max}) \delta t, \quad (2.52)$$

with N_A and N_B the number of electrons and Xe^+ ions respectively, V_C the cell volume, W the weight, σ_T the total cross-section and g_{max} the upper limit of the relative speed between the two species. At initial time, $g_{max} = 2.5 \sqrt{\frac{2RT_{ref}}{\mu_{AB}}}$ with T_{ref} equal to the initial electron temperature and $\mu_{AB} = \frac{m_A m_B}{m_A + m_B}$ the reduced mass. Then, we repeat N_{max} times the following two steps:

1. Choose randomly a pair (i,j) of electron and Xe^+ ion and compute the collision probability $q_{ij} = \frac{g_{ij} \sigma_T(g_{ij})}{g_{max} \sigma_T(g_{max})}$ with $g_{ij} = |\mathbf{v}_i - \mathbf{v}_j|$ the relative speed.
2. Then, call a random number $R[0,1]$. If $q_{ij} < R$, the pair does not collide. If $q_{ij} > R$, the pair collides and the post-collision velocities are given by:

$$\begin{cases} \mathbf{v}'_i = \frac{1}{m_A + m_B} (m_A \mathbf{v}_i + m_B \mathbf{v}_j + m_B g_{ij} \mathbf{R}) \\ \mathbf{v}'_j = \frac{1}{m_A + m_B} (m_A \mathbf{v}_i + m_B \mathbf{v}_j - m_A g_{ij} \mathbf{R}) \end{cases} \quad (2.53)$$

with \mathbf{R} a unit vector with a random direction.

The value of g_{max} is then updated for the following time steps with the maximum value obtained for g_{ij} .

As mentioned above, this implementation has not yet been tested and hence, no doubly-charged ions will be accounted for in this work.

2.6 Conclusion

In this chapter, the 2D PIC code *LPPic* was presented, with its main sub-routines and performances. Initially used to simulate the radial-azimuthal HT configuration, it has been adapted for this work to the axial-azimuthal configuration. The small changes needed to switch from the radial to the axial direction have been detailed here, along with two new features: the neutral dynamics and the cathode model.

Even though the dynamics of the neutral gas has long been solved with the simplest model (continuity equation), it appeared that it has a great impact on the discharge behaviour, especially due to the breathing mode oscillations. It

was the reason why this more complex model was developed, to include the non-negligible variations of neutral velocity.

As the electrons emitted by the cathode are also a main driver of the discharge behaviour, a careful attention has been drawn to the cathode model. Following the findings of previous works, a quasi-neutral condition is used, with a uniform azimuthal injection at the right axial domain boundary.

Whereas additional developments have been made to include the wall effects or doubly charged ions, it is now important to verify that the base version of *LPPic* gives correct results when simulating axial-azimuthal HT configurations.

Chapter 3

Code verification: 2D axial-azimuthal benchmark

In order to verify LPPic, specific unit tests have been performed, along with the 1D helium Benchmark of Turner et al. [156], as described in [119]. However, a benchmark case closer to the configuration of interest (i.e. with a 2D geometry and an imposed magnetic field perpendicular to the electric field) was needed. To this end, a collaboration was started with 6 other research groups who were also developing similar 2D codes. The lead was given by our group and we managed to define the case, make all the 7 codes converge towards the same solution, and wrap-up the results, in less than 8 months. This successful benchmark activity paved the way to extensive collaboration in the $\mathbf{E} \times \mathbf{B}$ community, with further benchmarks in different configurations, in the framework of the LANDMARK project [192]. This chapter and the following have been made more general by considering $\mathbf{E} \times \mathbf{B}$ discharges, to which Hall thruster belong to.

Most of the content of this chapter has been adapted from [185]. Here, after a brief contextualisation in section 3.1, the simulation model and algorithms used are described in section 3.2. Then, the specificities of each independent PIC code are given in section 3.3 along with the computational times and resources. Section 3.4 is dedicated to the comparison of the results. Azimuthally and time averaged (at steady state) axial profiles of main discharge parameters (axial electric field, ion density and electron temperature) are first compared before looking at the characteristics of the azimuthal instabilities. The sensitivity of the benchmark and the numerical convergence according to the number of macroparticles per cell is then discussed in section 3.5, prior to conclude on the agreement obtained between all the codes. Finally, this benchmark could be used to challenge numerical models in collaboration with several groups who managed to perform it. An example on the cathode model study is given in section 3.6.

Contents

3.1	Why do we need this benchmark?	58
3.2	Description of the model	59

3.2.1	Simulation domain	60
3.2.2	Imposed axial profiles	61
3.2.3	Boundary conditions	61
3.3	Code specificities	63
3.4	Results	64
3.4.1	Main plasma parameters	67
3.4.2	Azimuthal instabilities	68
3.5	Discussion	72
3.5.1	Numerical convergence	72
3.5.2	Case sensitivity	75
3.6	A tool to challenge numerical models - Example of the cathode injection	77
3.6.1	Studied cathode models	79
3.6.2	Main plasma parameters	80
3.6.3	Azimuthal instabilities	82
3.7	Conclusion	83

3.1 Why do we need this benchmark?

The $\mathbf{E} \times \mathbf{B}$ cross-field configuration is not only specific to HT but can also be applied to other LTP applications such as magnetron discharges for plasma processing [193, 194]. As explained in chapter 1, the presence of the magnetic field can trigger many fluctuations, thus increasing significantly the physics complexity. Moreover, due to the relatively high plasma density, small cells and time steps are required to simulate device scale phenomena and, in addition to the multi-dimensional nature (axial convection, azimuthal $\mathbf{E} \times \mathbf{B}$ drift, radial wall effects) of the plasma flow, it makes PIC simulations of $\mathbf{E} \times \mathbf{B}$ discharges computationally expensive.

In the last decade, the growing performances of computer facilities have stimulated the development of simulation codes, that have become indispensable tools in plasma studies. However, as the numerical models have become more and more complex, the validity of the results must be investigated. They could be affected by various numerical errors and uncertainties (such as numerical noise), algorithms and models used, or even by the configuration of input parameters. Therefore, there is an increasing need for **Verification and Validation** (V&V) of simulation codes. While validation implies comparison with real experiments, verification could be done in many ways such as unit and mezzanine tests for specific parts of a code [195], or benchmarking, i.e. code-to-code verification. The early work of Surendra *et al.* [196], in which the results of twelve different codes (kinetic, hybrid and fluid) on a 1D low-pressure (30, 100 and 300 mTorr) radio-frequency discharge in helium were compared, is considered as a pioneer for the benchmarking of simulation codes in the low-temperature plasma community. Later, a similar 1D case in helium was benchmarked by Turner *et al.* [156] with

five independently developed PIC codes, and they demonstrated that the results obtained for 4 pressures (30, 100, 300 and 1000 mTorr) were statistically indistinguishable. It paved the way to an increased benchmarking activity for different types of plasma discharges. In particular, in [197], two 1D PIC codes have been compared on a parallel plate glow discharge in helium at 3.5 Torr. In [198], six 2D fluid codes have been compared on the simulation of axisymmetric positive streamers in dry air at atmospheric pressure on three test cases of increasing complexity, and the authors stated that "the results agree reasonably well".

Even though a 1D helium benchmark is an efficient tool to verify the main algorithms of a PIC code (such as the Poisson solver and equations of motion) along with the MCC module, this case is only one dimensional with no magnetic field and hence, it would be beneficial for the low-temperature plasma community to benchmark simulation codes using a more complex model, such as $\mathbf{E} \times \mathbf{B}$ discharges. Moreover, it has been observed recently by Janhunen *et al.* [71, 87] that numerical noise may influence the results of PIC simulations by imitating the effect of collisions and hence, it is important to better understand the influence of the numerical parameters. The chosen simulation model should exhibit the relevant physics of an $\mathbf{E} \times \mathbf{B}$ discharge (high peak value of axial electric field, azimuthal instabilities, etc.) and in the meantime, it should be simple enough to be simulated in a reasonable computational time.

To this end, a 2D simulation model close to the one proposed by Boeuf and Garrigues [140] is adopted, with a longer azimuthal length and a higher number of macroparticles per cell to assess numerical convergence. The advantage of this test case is that a steady state is reached quickly, which facilitates comparison of the results. Moreover, the computational cost of PIC simulations has increased the need for quicker algorithms and made code parallelization compulsory. Hence, the seven independent codes considered here exhibit different features to decrease computational times and it makes this benchmarking activity even more relevant. An agreement on insightful parameters of the discharge will strengthen the confidence in *LPPic* and legitimize it for further analysis of HT discharges.

3.2 Description of the model

To study the azimuthal $\mathbf{E} \times \mathbf{B}$ electron drift instability and the associated axial electron transport, a 2D axial-azimuthal Particle-In-Cell benchmark case is considered with conditions close to those of a typical $\mathbf{E} \times \mathbf{B}$ discharge. Some simplifying assumptions have been made to make the case reproducible in a reasonable computational time. Indeed, the intermolecular collisions and neutral transport are neglected while a given ionization source term is imposed [140] and hence, we are able to obtain a steady state result in a short time (i.e. 10 μs).

3.2.1 Simulation domain

As illustrated in figure 3.1, the computational domain corresponds to a 2D structured Cartesian mesh, which models the axial (x) and azimuthal (y) directions of an $\mathbf{E} \times \mathbf{B}$ discharge. Hence, the curvature of the (x,y) plane is neglected. The left-hand side boundary of the domain represents the anode plane, with a fixed potential of 200 V, while the right-hand side corresponds to the cathode plane, where electrons are emitted. The distance between the anode and the cathode corresponds to the axial length of $L_x=2.5$ cm, with the position of radial magnetic field maximum at $x=0.75$ cm. To reduce computational times, a small region ($L_y=1.28$ cm) in the azimuthal direction is taken into account and periodic boundary conditions are imposed.

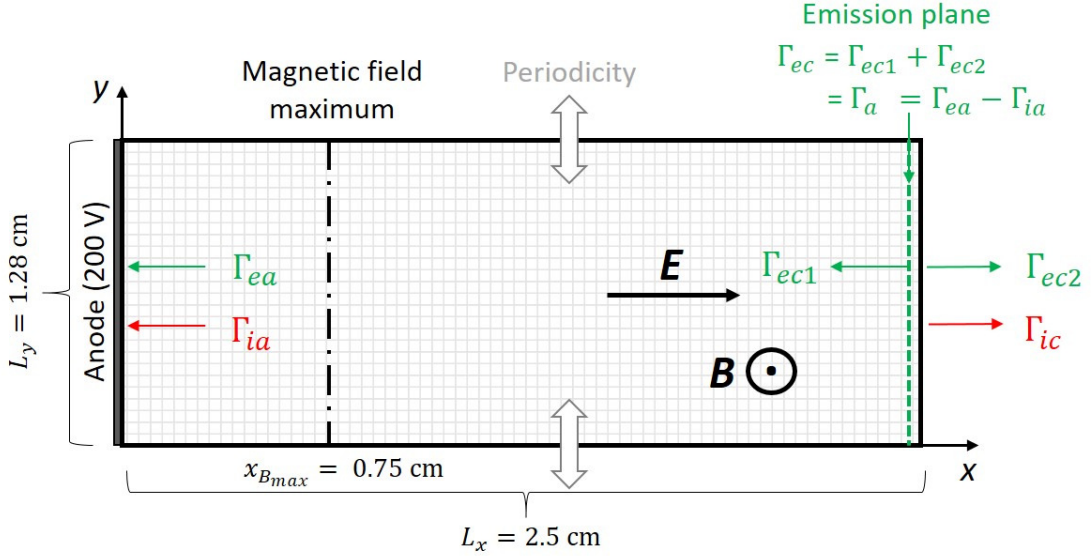


Figure 3.1 – Simulation domain. x is the axial direction, y the (periodic) azimuthal direction. Black pointed dashed line ($x_{B_{max}} = 0.75$ cm): position of maximum radial magnetic field. Green dashed line ($x_e = 2.4$ cm): plane from which electrons are emitted uniformly along the azimuthal direction. The azimuthally averaged fluxes are represented. Γ_{ea} and Γ_{ia} : respectively electron and ion fluxes through the left boundary. Γ_{ec1} : electron flux from the emission plane going into the discharge. Γ_{ec2} and Γ_{ic} : respectively electron and ion fluxes through the right boundary.

As most of the codes used are explicit, the cell size Δx and time step Δt need to satisfy the PIC stability conditions given by equations 2.15. In our case, the current density is fixed at $400 \text{ A} \cdot \text{m}^{-2}$, which gives a maximum plasma density of around $5 \times 10^{17} \text{ m}^{-3}$ and electron temperatures of about 50 eV. Hence, the minimum values for Δt and Δx will respectively be $6 \times 10^{-12} \text{ s}$ and $70 \mu\text{m}$. For the benchmark case, a time step of $\Delta t = 5 \times 10^{-12} \text{ s}$ and a grid spacing of $\Delta x = 50 \mu\text{m}$ with a grid of 500×256 cells are used. 4×10^6 time steps are simulated,

i.e. 20 μs of the discharge, and the diagnostics are averaged every 5000 time steps.

Electrons and ions are initially loaded with a density of $5 \times 10^{16} \text{ m}^{-3}$ uniformly throughout the simulation domain, with velocities chosen from a Maxwellian distribution with a temperature $T_e=10 \text{ eV}$ and $T_i=0.5 \text{ eV}$, respectively. To reduce numerical heating due to statistical noise, the number of macroparticles per cell at initialisation for the nominal case is fixed at $N_{ppc,ini} = 150$ (case 1), i.e. 150 electrons and 150 ions per cell. Then, approximately $N_{ppc,fin} \approx 550$ macroparticles per cell are obtained at stationary state. As mentioned before, this parameter could have an influence on the numerical results and hence, an extensive study of code convergence has also been conducted by simulating two other cases with $N_{ppc,ini} = 75$ (case 2) and $N_{ppc,ini} = 300$ (case 3).

All the simulation parameters are summarized in the third column of Table 2.1.

3.2.2 Imposed axial profiles

Radial magnetic field

The axial profile of the radial magnetic field is imposed with a Gaussian shape, as shown in figure 3.2

$$B(x) = a_k \exp\left(-\frac{(x - x_{B_{max}})^2}{2\sigma_k^2}\right) + b_k, \quad (3.1)$$

with $k = 1$ for $x < x_{B_{max}}$ and $k = 2$ for $x > x_{B_{max}}$. The values of the a_k and b_k coefficients can be easily calculated from the given parameters: $B_0 = B(x=0)=6 \text{ mT}$, $B_{L_x} = B(x=L_x)=1 \text{ mT}$, $B_{max}=10 \text{ mT}$, $x_{B_{max}} = 0.3L_x=0.75 \text{ cm}$ and $\sigma_1 = \sigma_2 = 0.25L_x=0.625 \text{ cm}$.

Ionization profile

For this benchmark case, no collisions are considered and the ionization process has been described in section 2.2.2. We impose $J_M = 400 \text{ A} \cdot \text{m}^{-2}$ by fixing the maximum value of the ionization profile to $S_0 = 5.23 \times 10^{23} \text{ m}^{-3} \cdot \text{s}^{-1}$. The resulting ionization source term is displayed in figure 3.2.

3.2.3 Boundary conditions

Electrons and ions which cross the left or right boundary plane of the domain are removed from the simulation. However, to ensure current continuity and neutralization of the extracted ion beam, electrons are injected from the cathode plane. The cathode model is close to the Current-Equality condition described in section 2.4 but with small differences. The emission line is set on the downstream of the simulation domain, at 1 mm from the right domain boundary. The number of electrons injected at each time step is calculated using the current conservation

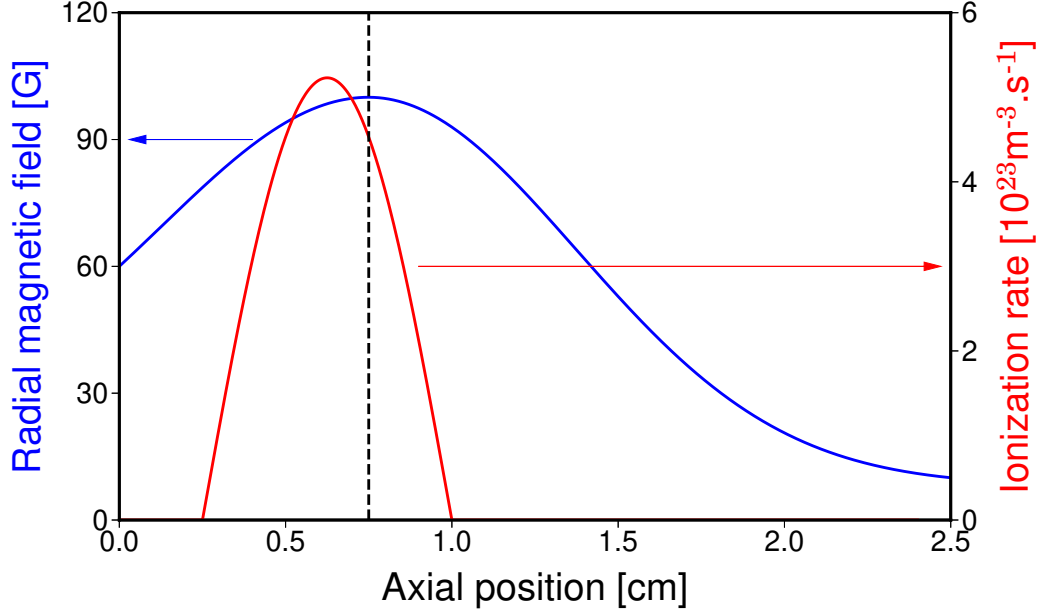


Figure 3.2 – Axial profiles of the imposed radial magnetic field and ionization rate. Dashed line corresponds to the position of maximum magnetic field.

through the discharge to obtain Γ_{ec} , the absolute value of azimuthally averaged emitted electron flux:

$$\Gamma_{ec} = \Gamma_a = \Gamma_{ea} - \Gamma_{ia}, \quad (3.2)$$

with Γ_{ea} and Γ_{ia} being respectively the absolute values of azimuthally averaged electron and ion fluxes to the anode side, displayed in figure 3.1. Hence, by counting the number of electrons and ions that cross the anode boundary at each time step (respectively ΔN_{ea} and ΔN_{ia}), the corresponding number of electrons emitted from the emission plane can be calculated as:

$$\Delta N_{e,emi} = \Delta N_{ea} - \Delta N_{ia}. \quad (3.3)$$

These electrons are injected uniformly in the azimuthal direction, with a Maxwellian velocity distribution with a temperature $T_{e,emi}=10$ eV.

However, this method for calculating the number of emitted electrons does not prevent an artificial cathode sheath to form. To suppress artificially this sheath, the emission plane is shifted by 1 mm from the right boundary plane (i.e. to the position $x_e=2.4$ cm) and its potential is adjusted at each time step by imposing a zero azimuthally averaged potential at this location. Hence, the azimuthally averaged potential drop between the anode and the emission plane is maintained constant and equal to the applied voltage (200 V). To do so, we solve the Poisson equation for U :

$$\Delta U = -\frac{e}{\epsilon_0}(n_i - n_e), \quad (3.4)$$

with boundary conditions $U(0, y) = U_0$ and $U(L_x, y) = 0$. Then, we obtain the electric potential ϕ by subtracting the azimuthally averaged potential at the emission plane \overline{U}_e from the solution $U(x, y)$ of Poisson equation:

$$\phi(x, y) = U(x, y) - \frac{x}{x_e} \overline{U}_e, \quad (3.5)$$

with:

$$\overline{U}_e = \frac{1}{L_y} \int_0^{L_y} U(x_e, y) dy. \quad (3.6)$$

The right boundary plane will have a varying negative potential but this drop in potential between the emission plane and the right boundary plane does not have any useful physical meaning and does not affect the main discharge physics.

3.3 Code specificities

Seven groups participated in this study, each group using its own independently developed simulation code. While the codes are all Particle-In-Cell (PIC) codes, they mainly differ in the way the equation of motion and the Poisson equation are solved. All the codes are using a bilinear interpolation scheme (CIC) and ions are considered unmagnetized, due to their large Larmor radius compared to the domain dimensions. The exact physical charge-to-mass ratio for ions (here Xenon ions are considered) is used by all the codes. Moreover, the choice of the Random Number Generator (RNG) appeared to have a non-negligible influence on the discharge results. Hence, the RNG used has been given and its influence will be further discussed in section 3.5.

As the benchmark cases are quite computationally expensive, the code performances are obtained through parallelization. This could be done via MPI (Message Passing Interface), combined or not with OpenMP (Open Multi-Processing), or using Graphics Processing Units (GPUs) instead of CPUs. Each processor can consider one portion of the computational grid (domain decomposition, like in *LPPic*) or one portion of the particles in the domain (particle decomposition) in order to speed-up the computation. Another way of decreasing significantly the computational time is to use the electron subcycling technique described in section 2.2.3.

A summary of the codes specificities is provided in table 3.1, along with the simulation times for the 3 benchmark cases. Extensive details on the different codes can be found in the original paper [185]. In the rest of the chapter, *LPPic* will be referred as code **LPP**.

One can notice that the computational times and resources needed to simulate these cases are quite high, with around 10 days in average for the nominal case (which corresponds to around 60000 CPU hours). Compared with the computational time of the 1D helium benchmark of Turner *et al* [156] that was around a couple of hours, parallelization of computational codes is needed to increase drastically the code performances. Moreover, it can be seen that the 7 codes

simulate the cases with a broad range of computational times (between 2.5 and 21 days for the nominal case) and it shows that this benchmark is also a powerful tool to characterize the performance of a simulation code. As the codes display many different characteristics, it is difficult to know why some are quicker than the others but we can at least see that for this particular case, the particle decomposition seems more efficient than the domain one which is explained by the fact that the number of macroparticles in the system is quite high compared to the system size. Moreover, we can see that using only single floating-point precision for the Poisson solver seems not to affect the discharge behaviour and is expected to speed-up significantly the computation.

Table 3.1 – Main codes specificities.

	LPP	LAPLACE	CERFACS	RUB	USask	TAMU	PPPL
Algorithms							
Pusher solver	Explicit	Explicit	Explicit	Implicit	Explicit	Explicit	Explicit
Poisson solver	Hypre	Pardiso	Maphys	FFT Thomas	FFT	Hypre	Hypre
Floating-point precision	Double	Single(pushers) Double (Poisson)	Double	Single(pushers) Double (Poisson)	Double	Double	Double
Random Number Generator	Fortran 2003	RANDU	Fortran 95	Xorshift128	Mersenne Twister 19937	C Standard GUL	Fast Mersenne Twister
Code acceleration							
Architecture	CPU	CPU	CPU	GPU	CPU	CPU	CPU
Parallelization	MPI	MPI/OpenMP	MPI	CUDA	MPI	MPI	MPI/OpenMP
Decomposition	Domain	Particle	Domain	Both	Domain	Particle	Particle
Language	Fortran	Fortran	Fortran	C+CuDa C	Fortran	C++	C
Simulation times (days (CPU number))							
Case 1 ($N_{ppc,ini} = 150$)	8 (360)	5 (108)	7 (360)	14 (1 GPU)	21 (32)	15 (300)	2.5 (224)
Case 2 ($N_{ppc,ini} = 75$)	5 (360)	3 (108)	4 (360)	9 (1 GPU)	11 (32)	11 (200)	2.5 (112)
Case 3 ($N_{ppc,ini} = 300$)	14 (360)	6 (180)	13 (360)	14 (2 GPU)	20 (64)	22 (400)	2.5 (448)

3.4 Results

Prior to performing any detailed benchmarking, it was important to make sure that all codes converge to a steady state. To do so, the time evolution of the electron axial current is compared. The electron current density injected at the

emission plane J_{ec} is split in two parts : $J_{ec} = J_{ec1} + J_{ec2}$, where J_{ec1} corresponds to the electron current density entering the channel and J_{ec2} is used to neutralize the extracted ion beam $J_{ec2} = J_{ic}$, fixed by the imposed ion current density. Hence, J_{ec1} could be used to characterize the anomalous cross-field transport in the discharge. For the comparison of results, J_{ec1} is normalized by the imposed total ion current $J_M = J_{ia} + J_{ic}$, which is set to $400 \text{ A} \cdot \text{m}^{-2}$ at steady state.

The time evolution of $\frac{J_{ec1}}{J_M}$ is shown in figure 3.3(a) for all simulation codes. It can be seen that all simulation codes reach a steady state after around $10 \mu\text{s}$. However, it can be noticed that a small oscillation appears at steady state, with a frequency of the order of hundreds of kHz, as shown in figures 3.3(b) and 3.3(c) for code **LPP**. As this phenomena is retrieved for all the codes, we decided to average our results in time to smooth out these oscillations, which could be physical or numerical, focusing on benchmarking of time-averaged phenomena. The period has been chosen as a compromise between the need to capture enough oscillation periods at steady state and keeping a reasonable computational time, i.e. $4 \mu\text{s}$ between 16 and $20 \mu\text{s}$.

Moreover, as mentioned before, some high-frequency instabilities propagate in the azimuthal $\mathbf{E} \times \mathbf{B}$ direction, as seen in figure 3.4 for the azimuthal electric field and the ion density, obtained with code **LPP** at $t = 20 \mu\text{s}$. To make the benchmarking of large-scale phenomena, it was decided to average in this direction. It can also be noticed that two distinct zones for the oscillations of the azimuthal electric field exist: a short wavelength zone between the anode and the location where the radial magnetic field is at maximum, called zone (I), and a long wavelength zone downstream, called zone (II). Such transition of the plasma waves is discussed more in detail in section 3.4.2.

Below in section 3.4.1, the azimuthally and time averaged axial profiles of the main discharge parameters (axial electric field, ion density and electron temperature) are first analysed. Due to the interest towards understanding the effects of azimuthal plasma waves on the electron anomalous transport, the azimuthal instabilities are compared in section 3.4.2, investigating their dominant mode characteristics (wavelength and frequency). These comparisons are done for the 3 cases considered in this benchmark, that differ only by their number of macroparticles per cell, given in Table 3.2.

Table 3.2 – Three benchmark cases. N_{ppc} is the number of macroparticles per cell. The nominal case is Case 1.

Case	$N_{ppc,ini}$ at initialisation	$N_{ppc,fin}$ at steady state
1	150	550
2	75	275
3	300	1100

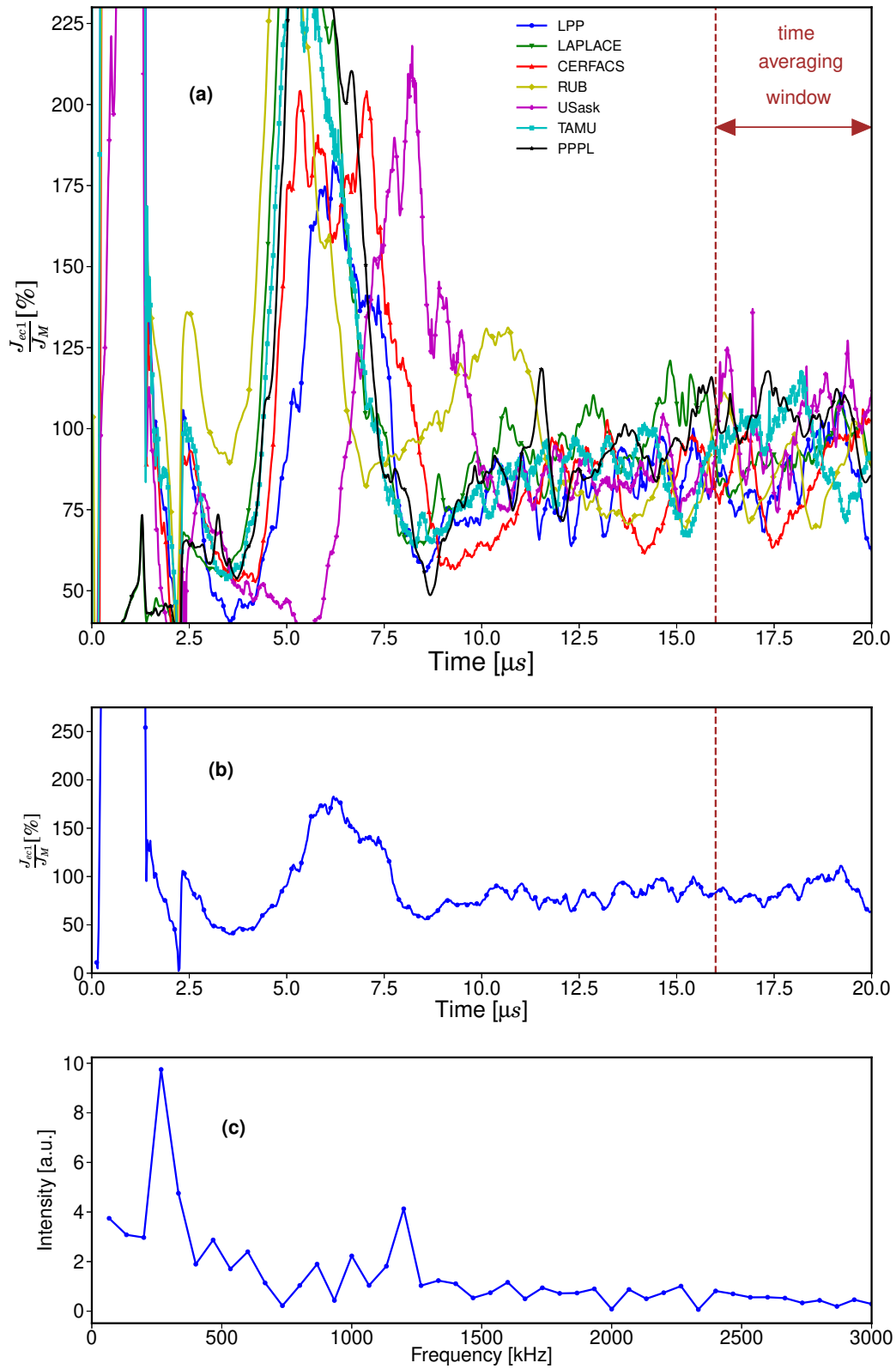


Figure 3.3 – (a) : Time evolution of $\frac{J_{ecl}}{J_M}$ for Case 1 for all the codes. Brown dashed line: beginning of time averaging interval (until 20 μs). (b) : Time evolution of $\frac{J_{ecl}}{J_M}$ for Case 1 with code **LPP**. (c) : Corresponding Fast-Fourier-Transform taken from data between 12 and 20 μs .

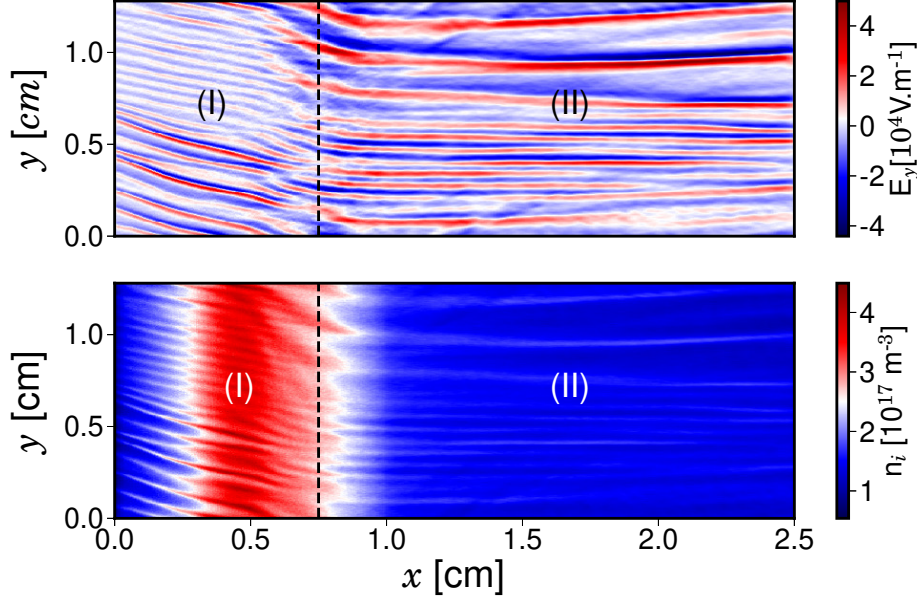


Figure 3.4 – 2D axial-azimuthal snapshots of the azimuthal electric field (top) and ion density (bottom) obtained with code **LPP** at $t = 20 \mu\text{s}$. Dashed line corresponds to the position of maximum magnetic field that separates zone (I) and zone (II).

3.4.1 Main plasma parameters

For benchmarking purposes, three parameters are chosen to be shown in this work: the axial electric field, the ion density and the electron temperature. Since the low-frequency oscillations on the order of hundreds of kHz are not the focus of the benchmarking, the results are averaged in the azimuthal direction and in time (between 16 and 20 μs) to obtain a steady state result.

The axial profiles for the nominal case are shown in figure 3.5. We can see that the 7 codes display a good agreement for all the parameters. The differences are mainly on the peak value and the profile in zone (II) but the overall mean relative error is less than 5%. This difference is measured by using the mean value between all the curves and calculating the mean relative error for every curve, that has a maximum below 5 %. It is also important to notice that all results from different codes capture the characteristics of an $\mathbf{E} \times \mathbf{B}$ discharge: a high axial electric field peaks near the maximum of radial magnetic field while the ion density is high on the anode side, just before the magnetic field peak. In particular, the results display an important feature of HT, namely the overlapping between the ion density peak (ionization zone) and the axial electric field peak (acceleration zone). One can notice the sharp increase of the axial electric field near the right boundary that is due to the artificial sheath created outside of the region of interest (between the emission plane ($x_e = 2.4 \text{ cm}$) and the right boundary). It has been shown in [140] that this region does not affect the main

discharge results: because the plasma potential at the emission plane is rescaled to zero at each time step, the anode-cathode potential difference is imposed in the region of interest.

The same comparison is done for the two other cases and the results are displayed in figures 3.6 and 3.7 respectively. They both exhibit a similar behaviour than the nominal case shown in figure 3.5, with an overall mean relative error between the codes less than 5%. The main reason for the slight discrepancies comes from the low-frequency oscillation behaviour, as can be seen from figure 3.3.

3.4.2 Azimuthal instabilities

In addition to the time-averaged plasma properties, the instabilities propagating in the azimuthal direction, shown in figure 3.4, also serve as a useful phenomenon for benchmarking of different simulation codes. As explained in section 1.2.2, the EDI can transition to an ion-acoustic instability when the wave propagation along the magnetic field is included or because of nonlinear effects. The quasilinear theory of the anomalous transport based on the modified ion-acoustic instability in the conditions of Hall thruster has been proposed [85, 86]. The dispersion relation for the ion-acoustic instability in plasmas with moving ions has the form:

$$\omega_R \approx \mathbf{k} \cdot \mathbf{v}_i \pm \frac{kc_s}{\sqrt{1 + k^2 \lambda_d^2}}. \quad (3.7)$$

A 2D Fast-Fourier-Transform (FFT) is applied here to the azimuthal electric field at fixed axial positions (between 16 and 20 μs) to get the corresponding spectrum. The results for two different axial positions are displayed in figure 3.8 for code **LPP**. It is shown that in zone (I) (at $x = 0.3$ cm) a continuous dispersion relation is well fitted to the analytical expression of equation 3.7. This continuous behaviour was already observed in experiments [67] and in other 2D PIC codes that are self-consistent with the plasma generation [111]. However, closer to the cathode in zone (II) (at $x = 1.5$ cm), the dispersion relation exhibits a different behaviour, which seems more discrete.

As this chapter is focused on the benchmarking of different simulation codes, detailed study of the dispersion relations of the plasma waves is out of scope and more insights will be given in chapter 4. Instead, to be able to compare the results of the different codes, it was decided to extract the dominant mode at each axial position. Hence, the wave characteristics (wavelength and frequency) are compared as function of the axial position.

This axial dependence of the dominant mode characteristics for all the codes is shown in figure 3.9 for the nominal case. It can be seen that, in all simulation results, the wavelength and the frequency change abruptly at the position of maximum radial magnetic field. In zone (I) near the anode, the oscillations have a small wavelength ($\lambda \approx 0.5$ mm) and a high frequency ($f \approx 5$ MHz) while near the cathode in zone (II), the frequency drops to $f \approx 3$ MHz with

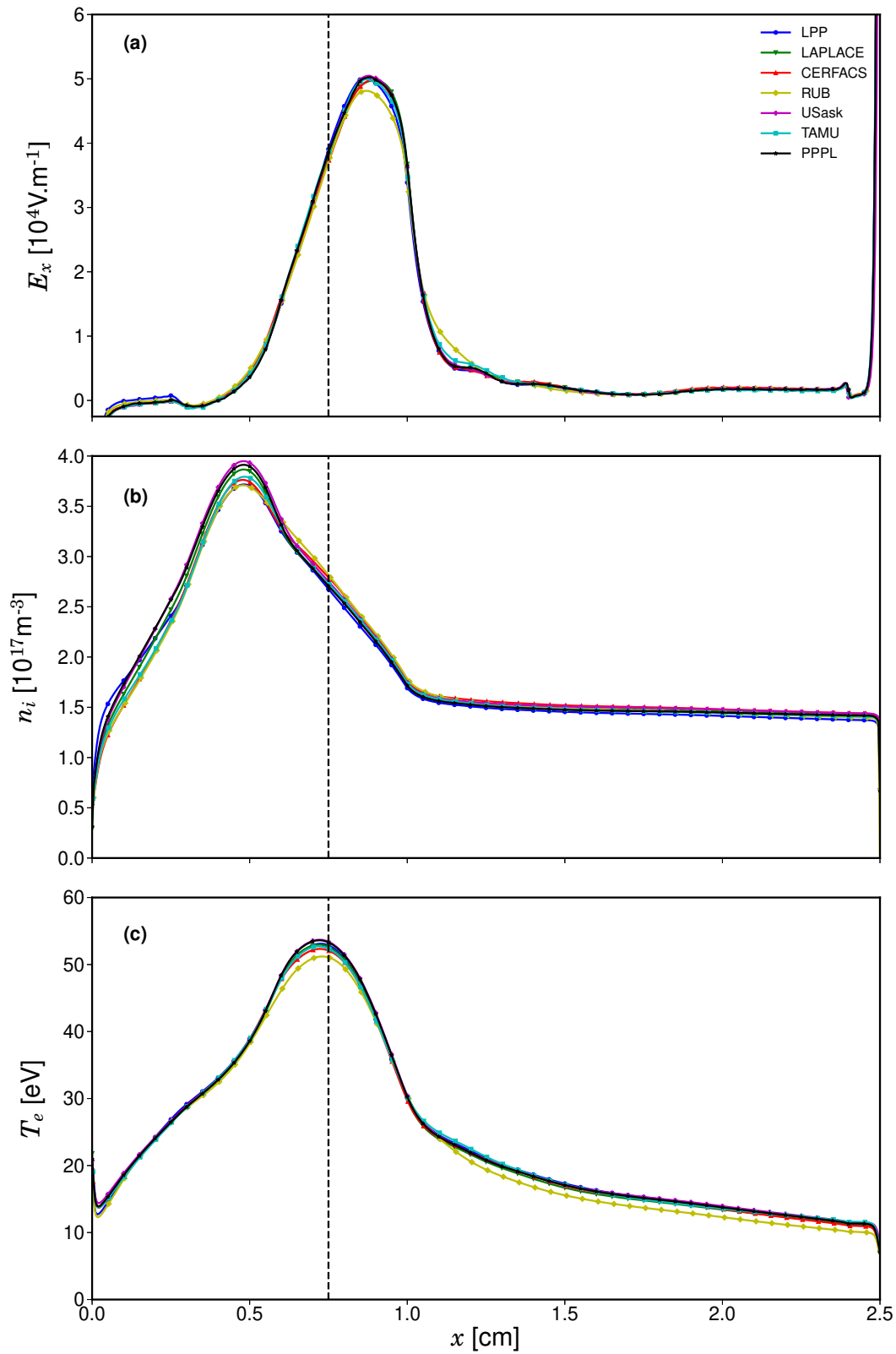


Figure 3.5 – **Case 1** : Azimuthally and time (between 16 and 20 μs) averaged axial profiles of axial electric field (a), ion density (b) and electron temperature (c). Dashed line corresponds to the position of maximum magnetic field.

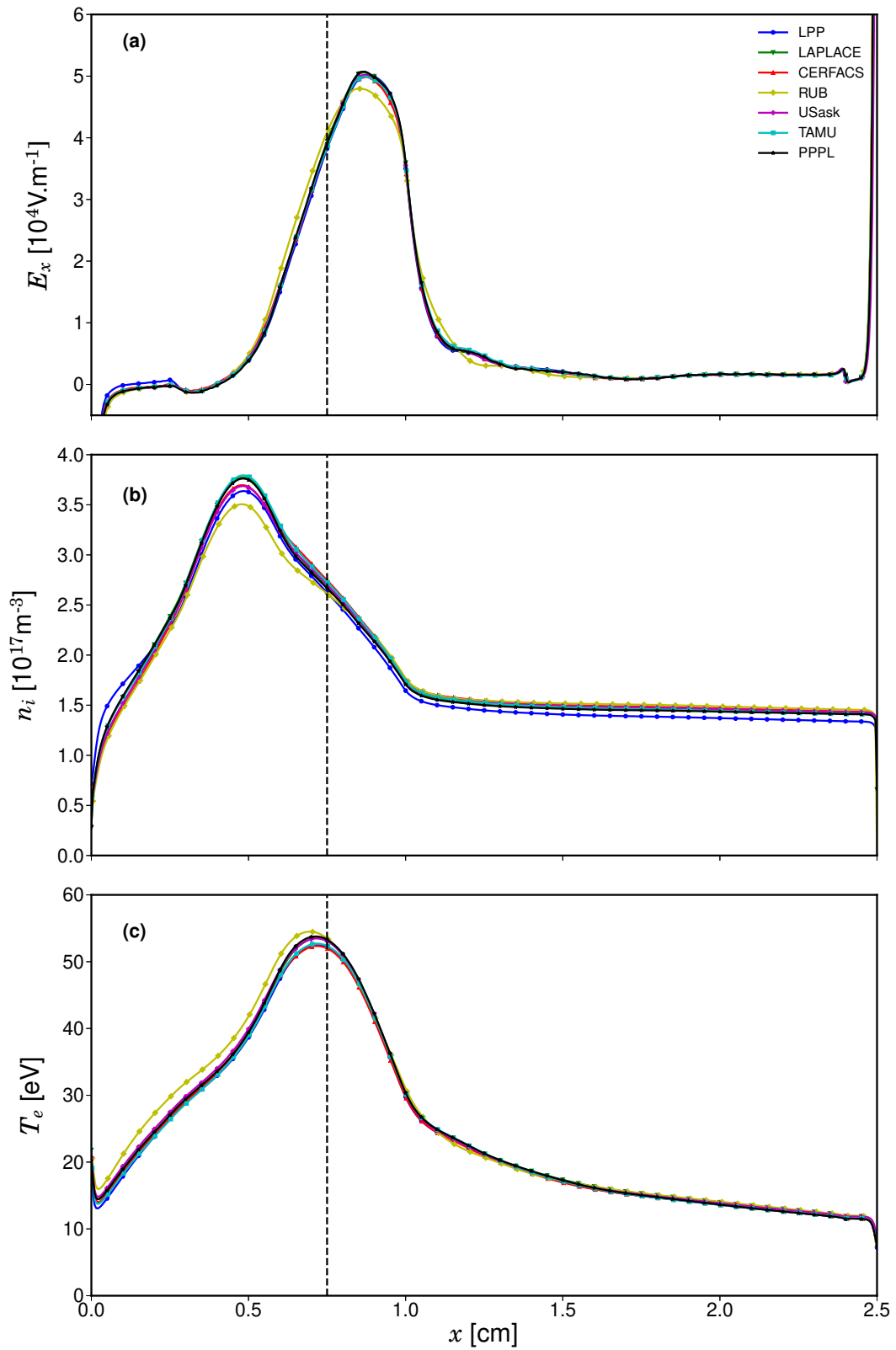


Figure 3.6 – **Case 2** : Azimuthally and time (between 16 and 20 μs) averaged axial profiles of axial electric field (a), ion density (b) and electron temperature (c). Dashed line corresponds to the position of maximum magnetic field.

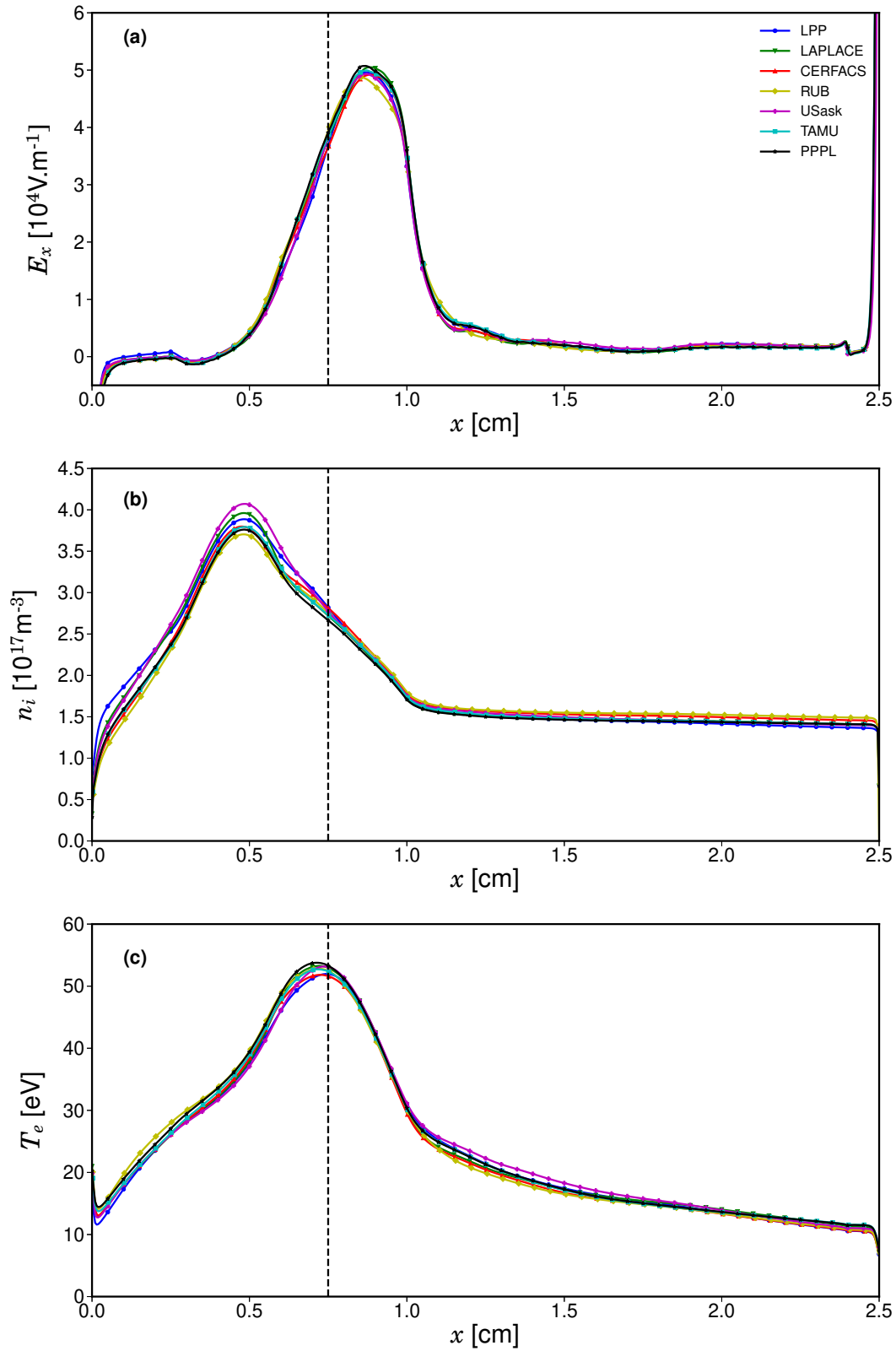


Figure 3.7 – **Case 3** : Azimuthally and time (between 16 and 20 μs) averaged axial profiles of axial electric field (a), ion density (b) and electron temperature (c). Dashed line corresponds to the position of maximum magnetic field.

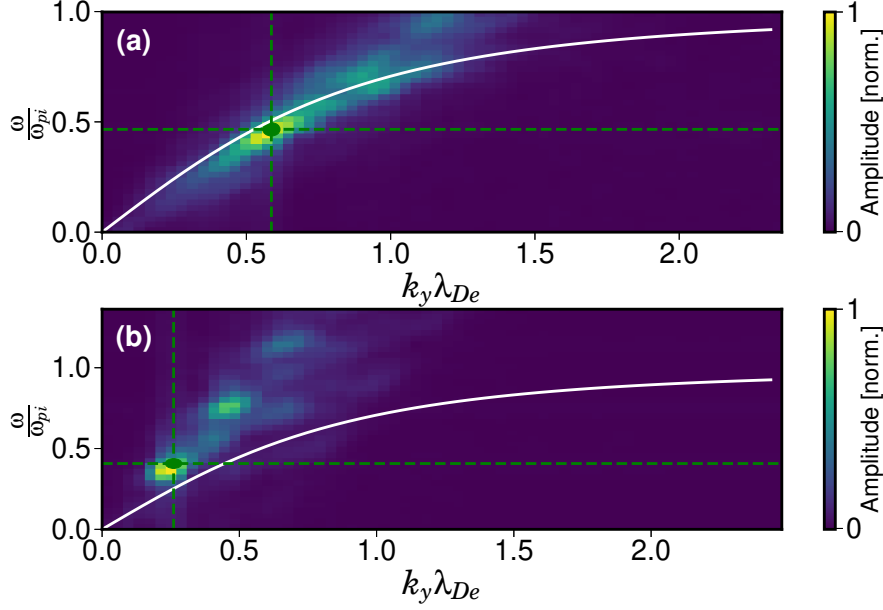


Figure 3.8 – 2D FFT of the azimuthal electric field at $x=0.3$ cm (a) and $x=1.5$ cm (b), obtained with code **LPP**. Solid white line: ion acoustic dispersion relation. Green dashed lines: wavelength and frequency of the dominant mode.

a wavelength almost 4 times bigger ($\lambda \approx 2$ mm). The Debye length and ion plasma frequency are displayed on the bottom row for comparison. The same behaviour is retrieved for the two other cases, as seen in figures 3.10 and 3.11. Considering the complexity of the phenomena involved, the agreement between the codes is satisfactory. The maximum wavelength for the dominant mode is around 2 mm which is well-resolved by the length in the azimuthal direction of 1.28 cm. However, further development of long-wavelength structures may be limited either by this limited azimuthal length or by the axial convection of the modes (due to the ion flow) from the most unstable region. As this work is focused on a benchmark comparison with a simplified domain, this question will require further studies with a larger domain and additional insights will be given later in section 6.3.2.

3.5 Discussion

3.5.1 Numerical convergence

In a PIC simulation, we consider finite-sized particles and hence, numerical collisions play a role. They can lead to fluctuations induced by thermal noise and this noise could have an impact on the study of the azimuthal instabilities and the related anomalous electron transport.

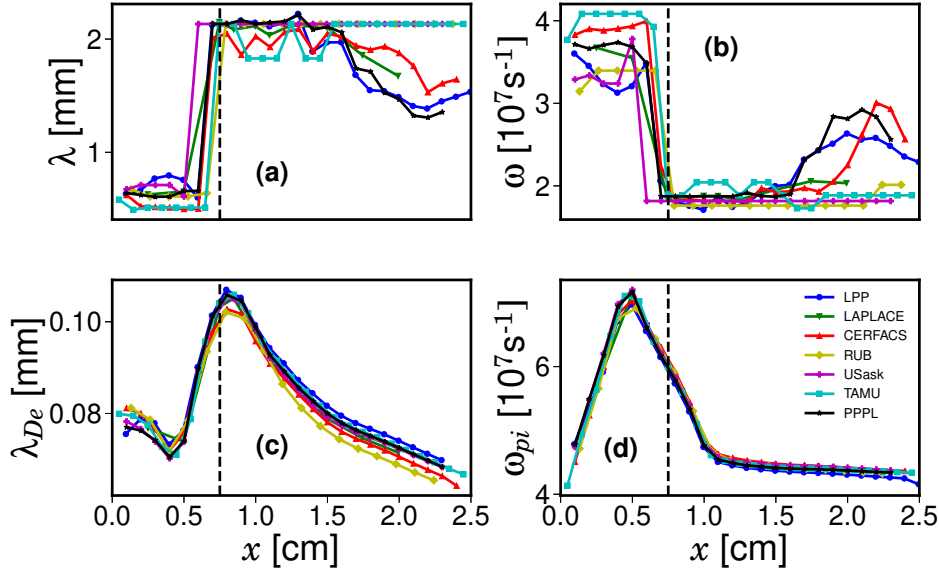


Figure 3.9 – **Case 1**: Axial evolution of dominant mode characteristics for azimuthal electric field (azimuthal instabilities). (a) Wavelength. (b) Frequency. (c) Debye length. (d) Ion plasma frequency. Dashed line corresponds to the position of maximum magnetic field.

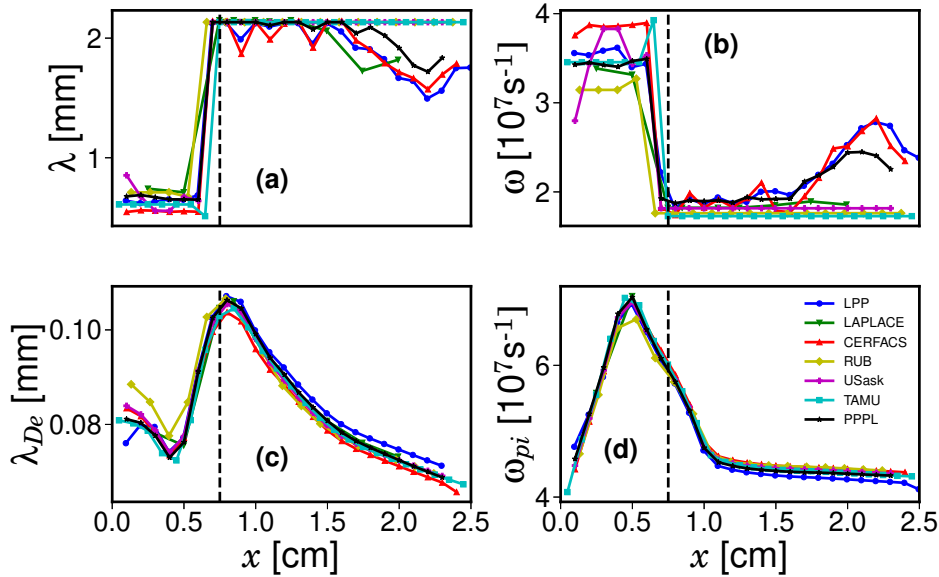


Figure 3.10 – **Case 2**: Axial evolution of dominant mode characteristics for azimuthal electric field (azimuthal instabilities). (a) Wavelength. (b) Frequency. (c) Debye length. (d) Ion plasma frequency. Dashed line corresponds to the position of maximum magnetic field.

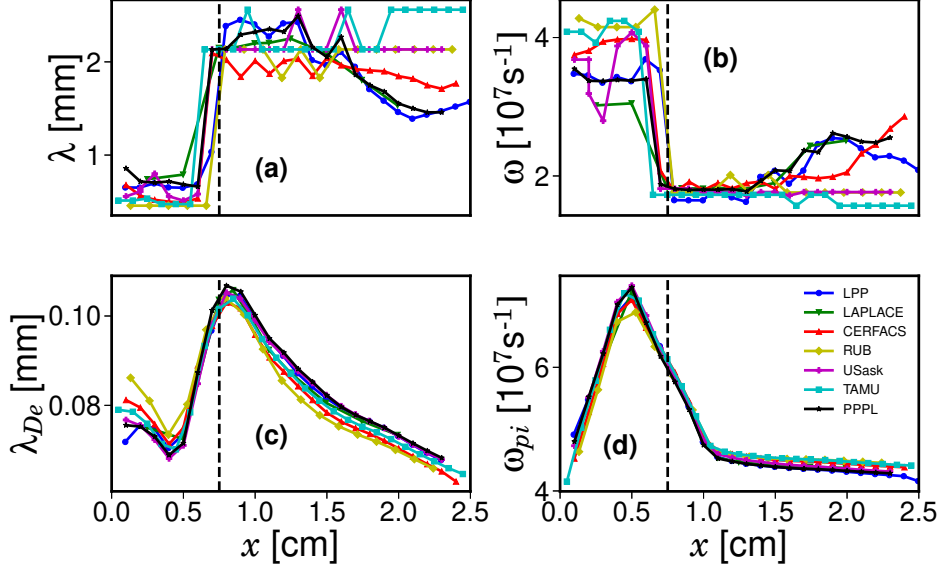


Figure 3.11 – **Case 3**: Axial evolution of dominant mode characteristics for azimuthal electric field (azimuthal instabilities). (a) Wavelength. (b) Frequency. (c) Debye length. (d) Ion plasma frequency. Dashed line corresponds to the position of maximum magnetic field.

Okuda and Birdsall [199] defined a frequency for these numerical collisions in 2D simulations:

$$\nu_{num} \approx \frac{\pi\omega_{pe}}{16N_D}, \quad (3.8)$$

with N_D the number of macroparticles in a Debye sphere. For our nominal case (Case 1, $N_{ppc,ini}=150$), we will have around $N_{ppc,fin} \approx 550$ macroparticles per cell at steady state, in average. Looking at figure 3.9, we can see that the minimum Debye length is around $70 \mu\text{m}$ and hence, we have around 2π cells in a Debye sphere (worst case). It corresponds to a numerical collision frequency of $\nu_{num} \approx 5.6 \times 10^{-5}\omega_{pe}$. Turner [149] has shown that the numerical collisions can be neglected if $\frac{\nu_{num}}{\omega_{pe}} \leq 10^{-4}$ and hence our case complies with this criterion.

It is also important to assess the numerical convergence of this benchmark case more rigorously, by varying the number of macroparticles per cell. The mean value at steady state of the ratio $\frac{J_{ec1}}{J_M}$ of electron current entering the channel to the total ion current was used as a convergence criterion. Indeed, as mentioned earlier, this ratio is related to the electron axial transport in the discharge. This transport can be enhanced by numerical collisions and hence, decreasing N_{ppc} will increase the transport and $\frac{J_{ec1}}{J_M}$ will be higher. We can retrieve this behaviour by looking at how the averaged profiles of ion density and axial electric field evolve when the number of macroparticles per cell is decreased. We observe in figure 3.12 for code **LPP** that if N_{ppc} is decreased, the axial electric field is increased and the ion density is decreased which is characteristic of a higher axial transport.

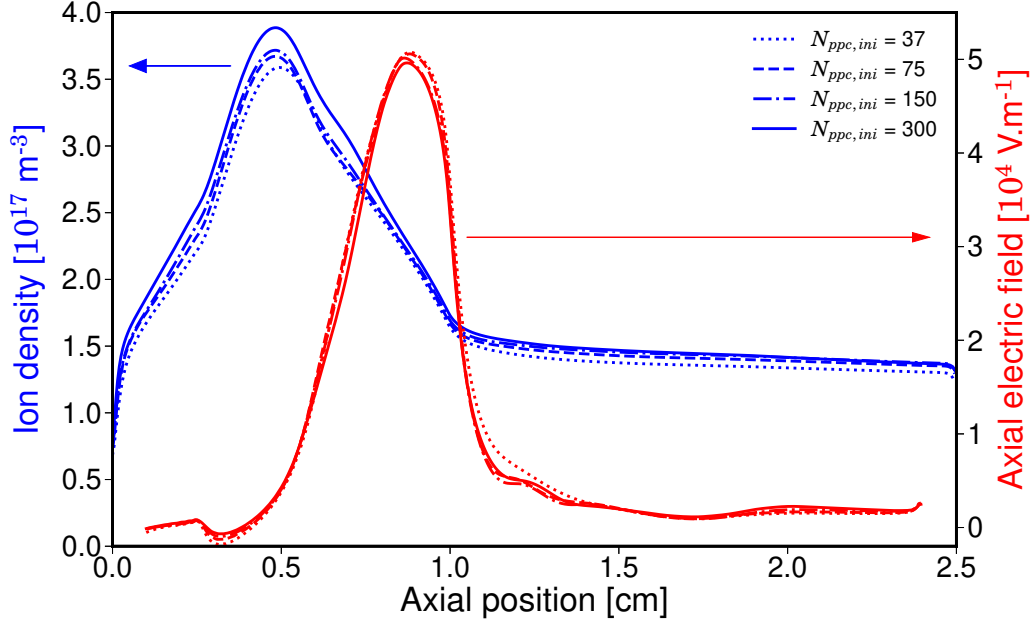


Figure 3.12 – Azimuthally and time (between 16 and 20 μs) averaged axial profiles of axial electric field and ion density for different number of macroparticles per cell at initialisation $N_{ppc,ini}$. Results obtained with code **LPP**.

Figure 3.13 shows the mean value of $\frac{J_{ec1}}{J_M}$ at steady state for all seven codes, as function of the number of macroparticles per cell at steady state. We can see that we obtain a good convergence: when N_{ppc} is increased, $\frac{J_{ec1}}{J_M}$ is decreased and reaches a plateau. This plateau corresponds to the three benchmark cases that we have chosen (Case 1 with $N_{ppc,final}=550$, Case 2 with $N_{ppc,final}=275$ and Case 3 with $N_{ppc,final}=1100$). It is interesting to notice that the curve has a knee at around 250 macroparticles per cell which gives a numerical collision frequency close to the criterion of [149]. Furthermore, this benchmark case shows that the number of macroparticles per cell commonly used in 2D PIC simulations (i.e. $N_{ppc,final}=100$) is not enough to reach convergence. This need to increase the number of macroparticles per cell to prevent numerical collisions was also reported in [66] and more recently in [111], in which 800 macroparticles per cell were used on average at the end of the simulation.

One can also notice that the differences between the codes are this time bigger than 5%. The origin of this discrepancy still remains unclear and its analysis is let as future work.

3.5.2 Case sensitivity

The agreement obtained between the seven codes in section 3.4 is good, but it is worth noting that the results obtained are not "statistically indistinguishable"

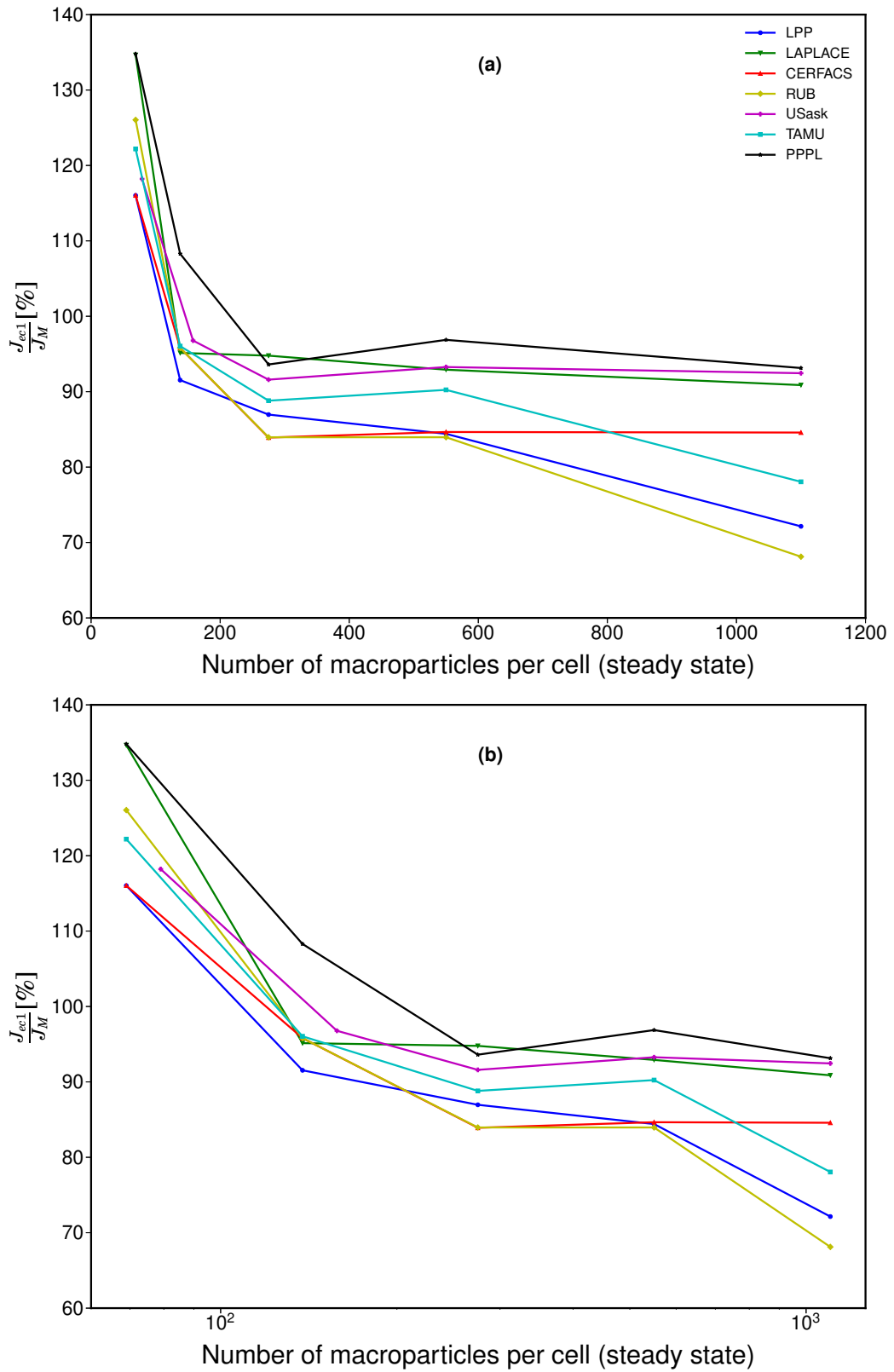


Figure 3.13 – Mean value (between 12 and 20 μs) of $\frac{J_{ec1}}{J_M}$ depending on $N_{ppc,final}$ in normal scale (a) and semi-log scale (b). The three benchmark cases correspond to $N_{ppc,final} = 550$ (Case 1), $N_{ppc,final} = 275$ (Case 2) and $N_{ppc,final} = 1100$ (Case 3).

(corresponding to less than 1% difference) as in the 1D helium benchmark [156]. As the present benchmarking test case is more challenging and more complex (two dimensions, magnetic field, emitting cathode, etc.) with the presence of turbulent phenomena, it is expected to obtain bigger differences.

To better characterize the sensitivity of this benchmark case, one code (code **LPP**) is used and the same simulation (same input parameters, corresponding to Case 2) is repeated 3 times. Figure 3.14(a) shows the different time evolutions of the $\frac{J_{ec1}}{J_M}$ ratio for these 3 simulations. It can be seen that while the beginning of the transient state (first 4 μs) is quite similar, some differences appear quickly and the oscillations at steady state become quite different. In fact, when time averaging is done between 11 and 15 μs , different axial profiles are retrieved for the ion density and axial electric field (the electron temperature is not shown here but displays a similar behaviour), as seen in figure 3.14(b). These differences are of the order of 5% and could be considered as the closest agreement we would get between the seven codes.

There is a reason why identical results are not obtained with the same code. In fact, as described in section 3.2, a RNG is frequently used for routines that are crucial for the discharge behaviour (ionization and electron emission). Hence, as this RNG is seeded randomly depending on the processors used, differences are expected on the random numbers that will propagate due to the inherent chaotic behaviour of the discharge.

To verify this assumption, the seed number of this RNG has been fixed with the **LPP** code (and the same procedure as before was repeated). We can see in figure 3.15 that, now, a perfect overlap is obtained for the time evolution of the current (and hence for the averaged parameters). It should be noted that this perfect overlap was not obtained for the first attempt: indeed, because the CPUs (hardware) used are not the same between two simulations, two runs that should be identical were taking different computational time and hence, the restart procedure described in 2.1.2 was done at different time steps, and this little shift was strong enough to make the results diverge by around 2%. This study has shown clearly that the intrinsic turbulent nature of the discharge makes this case very sensitive and it made us more confident on the quality of the agreement obtained for this benchmark.

3.6 A tool to challenge numerical models - Example of the cathode injection

Now that we know that the 7 codes give similar results, this simplified test case can be used to challenge the numerical models used. In this last section, we discuss the influence of the cathode injection model in the LPP code on the main plasma parameters and then, on the azimuthal instabilities.

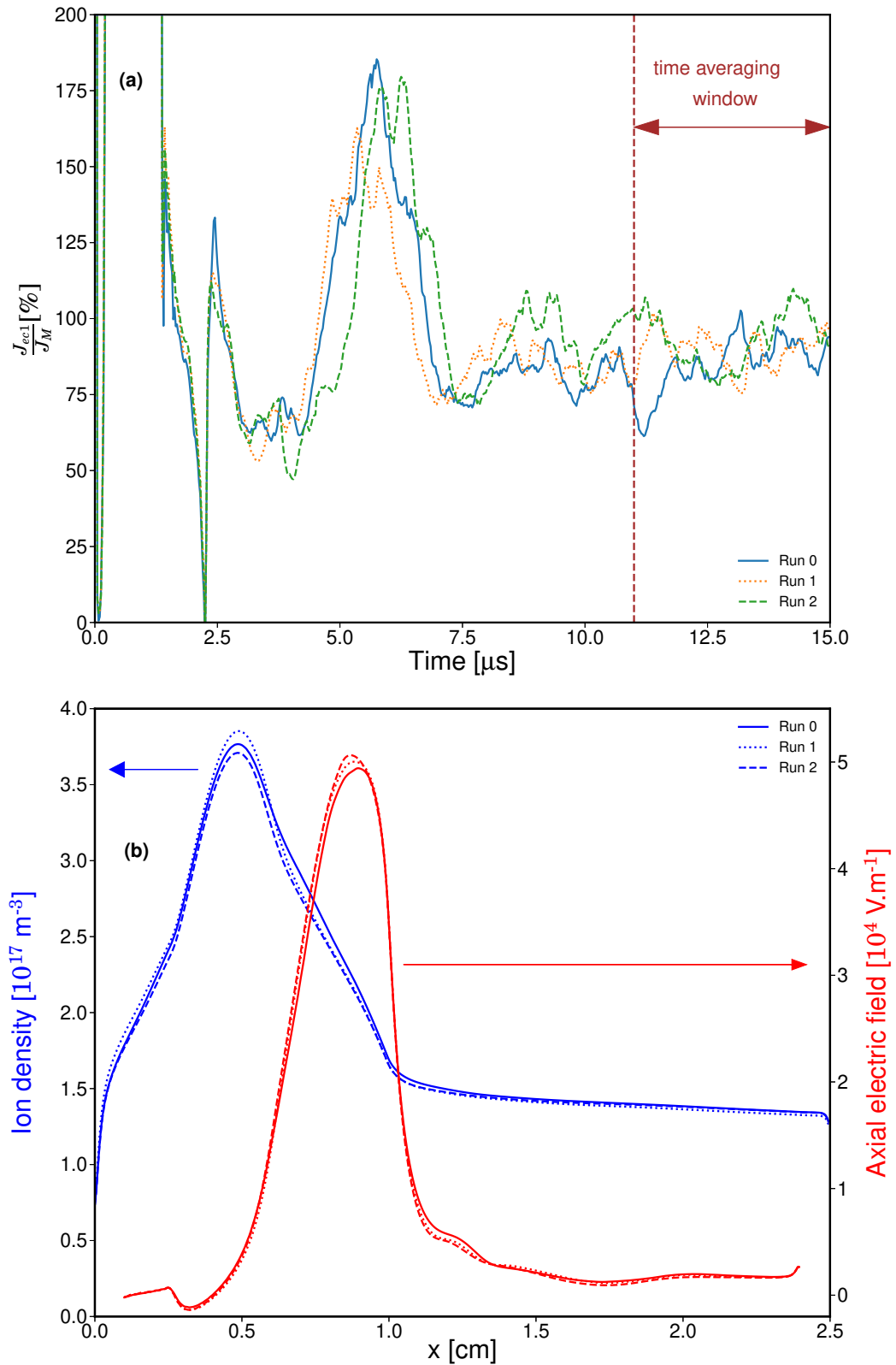


Figure 3.14 – Comparison of 3 simulations with the same code (**LPP**) for the same input parameters (Case 2). (a): Time evolution $\frac{J_{ec1}}{J_M}$. (b): Azimuthally and time (between 11 and 15 μs as shown on (a)) averaged axial profiles of ion density (blue) and axial electric field (red).

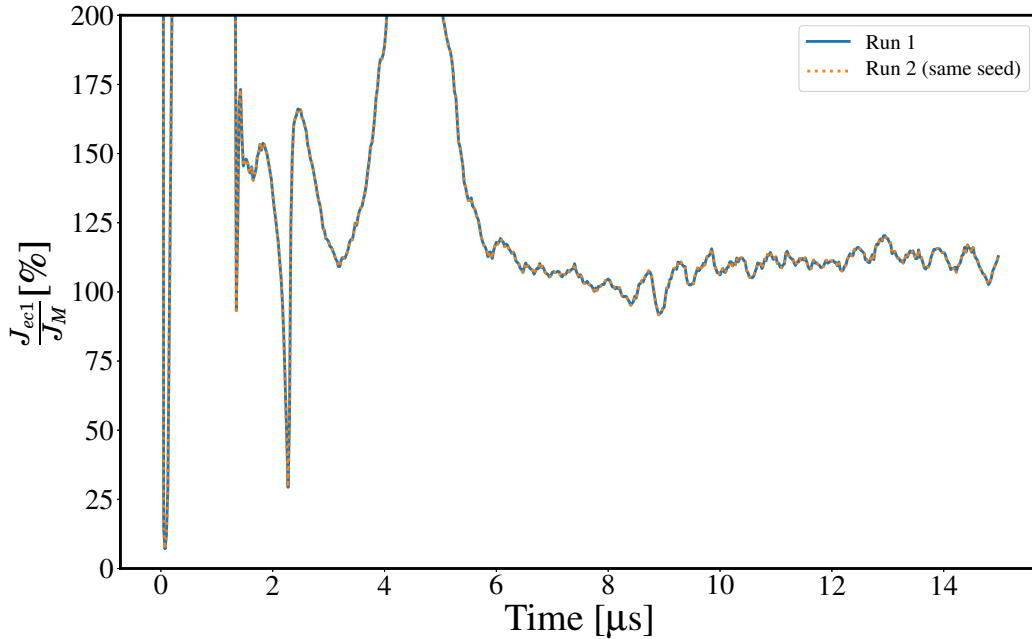


Figure 3.15 – Time evolution of $\frac{J_{ec1}}{J_M}$ for 2 simulations with the same code (**LPP**) for the same input parameters (Case 2), and the same seed for their RNG.

3.6.1 Studied cathode models

The best way to model the hollow cathode of a HT in a 2D PIC axial-azimuthal code has still not been found. Indeed, the absence of radial direction makes it difficult to properly account for the electron injection. As described previously in section 2.4, two models are usually used: one based on a Current-Equality (CE) in the whole system, or another one based on the fact that the plume is Quasi-Neutral (QN). The model used in this benchmark is similar to the former, but with a small axial shift of 1 mm. We decided here to compare this model to the QN one and see how it affects the discharge behaviour. Moreover, the temperature of the electrons injected was chosen arbitrarily ($T_{e,inj} = 10$ eV) for this benchmark. This value should depend on the cathode used, but also vary in time. Because we cannot include these effects in our simulation, it is important to be sure that the discharge behaviour is not too much affected by this arbitrary parameter. Hence, we have simulated two more cases, with a lower injection temperature of 0.1 eV. The four studied cases has been gathered in table 3.3.

The input parameters correspond to case 2 of table 3.2 which has been run until 30 μs , and only the cathode model have been changed.

Case	Cathode model	$T_{e,inj}$ [eV]
1	Benchmark (BM)	0.1
2	Benchmark (BM)	10
3	Quasi-Neutral (QN)	0.1
4	Quasi-Neutral (QN)	10

Table 3.3 – Cathode models simulated. The case in bold (case 2) represents the nominal case.

3.6.2 Main plasma parameters

The time evolution of $\frac{J_{ec,1}}{J_M}$ and the total number of macroparticles N_{mp} have been displayed in the top row of figure 3.16. Before comparing the different cases, we can notice first that they all reach a steady-state, and we have verified that the total ion current was corresponding to the imposed $J_M = 400 \text{ A} \cdot \text{m}^{-2}$. Then, we can see that decreasing $T_{e,inj}$ for the benchmark model greatly enhances the electron axial transport and hence, there are less particles in the discharge. The quasi-neutral model seems less sensitive to the injection temperature: the axial electron transport is increased by around 30% and it is mainly the beam electron current that is affected (not shown here): indeed the electron Larmor radius is proportional to T_e and hence, when $T_{e,inj}$ is increased, more electrons tend to leave the computational domain directly after being injected (we recall that for this QN model, we inject at the right domain boundary without any axial shift). Finally, it is interesting to notice that for $T_{e,inj} = 0.1 \text{ eV}$, the two cathode models are closer than with $T_{e,inj} = 10 \text{ eV}$.

The axial evolution of several plasma parameters have been computed by averaging azimuthally and in time over the last $10 \mu\text{s}$, and they have been displayed in the two other rows of figure 3.16. Again, we retrieve the previous observation that the QN model seems to be less sensitive to the temperature of injected electrons, compared to the benchmark model. While the nominal benchmark case (BM - $T_{e,inj} = 10 \text{ eV}$) displays a lower axial current (and hence higher density and lower axial electric field), we can notice that the anodic sheath is way smaller than for the other cases and hence the axial electric field seems less sensitive to the abrupt change of ionization source term at $x = 0.25 \text{ cm}$. Moreover, the electron temperature in both directions is similar for all the cases except the nominal benchmark case which exhibits a lower temperature in the discharge. Hence, counter-intuitively, the electron temperature in the discharge is higher for lower $T_{e,inj}$. This could be related to the higher axial electric field and axial electron current which can increase the Joule heating. The ion temperatures seem to follow the same trend.

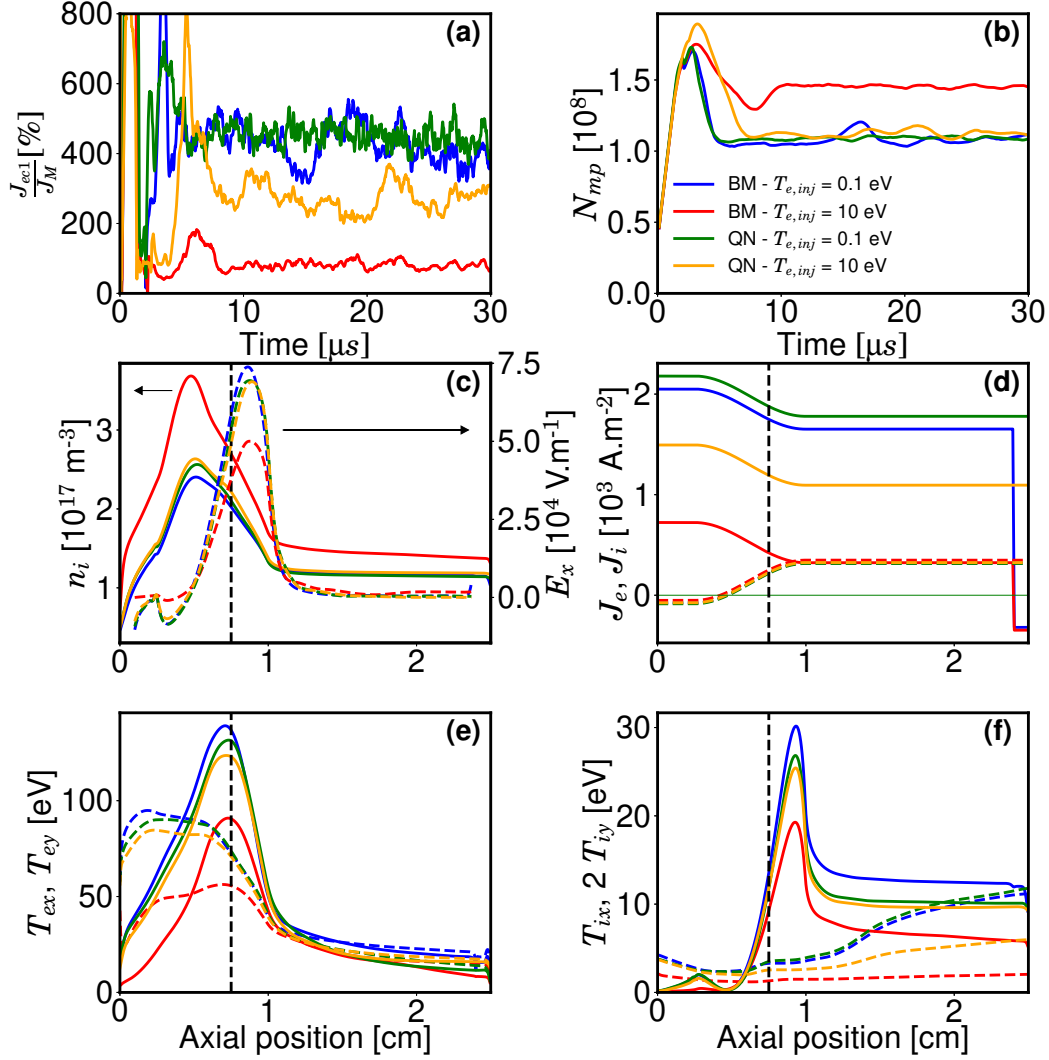


Figure 3.16 – For different cathode models: (a) Time evolution of $\frac{J_{ec,1}}{J_M}$. (b) Time evolution of the total number of macroparticles. Axial profiles (averaged in time and azimuthally) of (c) ion density (solid lines) and axial electric field (dashed lines), (d) axial electron (solid lines) and ion (dashed lines) currents, (e) axial (solid lines) and azimuthal (dashed lines) electron temperatures, (f) axial (solid lines) and azimuthal (dashed lines) ion temperatures. The black horizontal line corresponds to the position of maximum magnetic field.

3.6.3 Azimuthal instabilities

We can look now on the azimuthal instabilities with the 2D snapshots of azimuthal electric field (at $t = 30 \mu\text{s}$) displayed in figure 3.17, along with the corresponding 2D FFT at $x = 0.4 \text{ cm}$ and $x = 1.5 \text{ cm}$ (between 19 and 29 μs). First, we can see that inside the thruster ($x = 0.4 \text{ cm}$), the behaviour is similar for all the cases, with a continuous spectrum that can be well-fitted by an ion-acoustic approximation. However, outside the thruster ($x = 1.5 \text{ cm}$), the discrete behaviour of the nominal benchmark case is smoothed when $T_{e,inj}$ is decreased and tends to disappear if we use the quasi-neutral model.

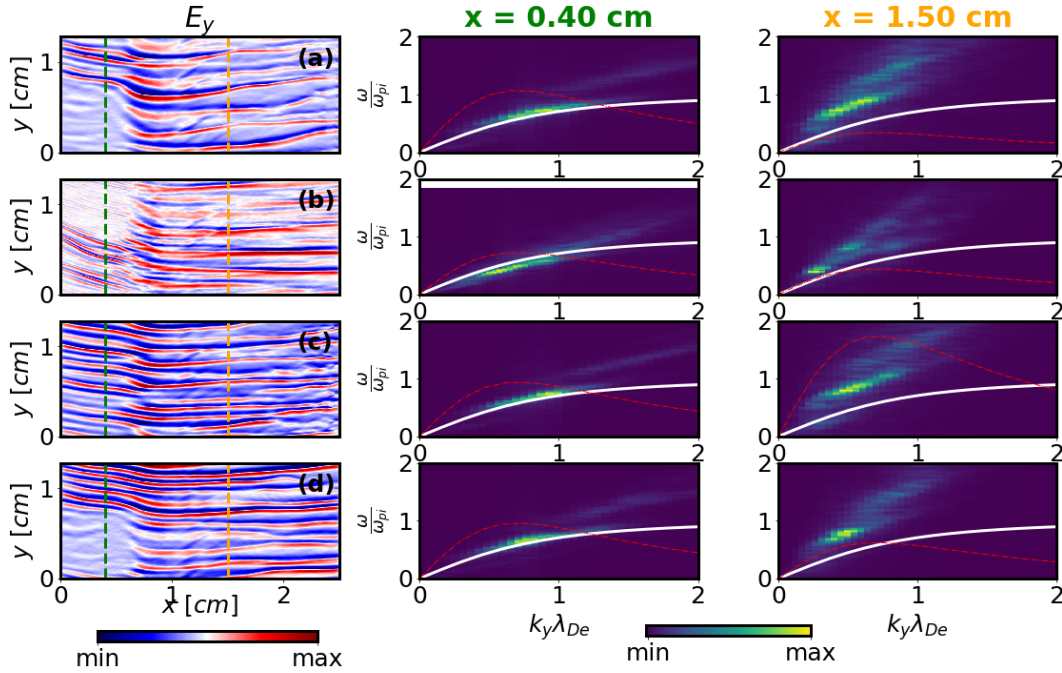


Figure 3.17 – (Left column) 2D maps of azimuthal electric field at $t = 26 \mu\text{s}$. The green and red vertical dashed lines indicates the position of the FFT. The black vertical dashed line corresponds to the position of maximum magnetic field. (Middle column) Corresponding 2D FFT at $x=0.4 \text{ cm}$. (Right column) Corresponding 2D FFT at $x=1.5 \text{ cm}$. White thick line: ion-acoustic dispersion relation. Red dashed line: ion-acoustic growth rate rescaled by a constant factor to fit the image. The spectrum has been zoomed to focus on the zone of interest. Each row corresponds to a different cathode model: (a) BM - $T_{e,inj} = 0.1 \text{ eV}$. (b) BM - $T_{e,inj} = 10 \text{ eV}$. (c) QN - $T_{e,inj} = 0.1 \text{ eV}$. (d) QN - $T_{e,inj} = 10 \text{ eV}$.

All in all, the parametric study performed in this section has shown that the cathode model was impacting significantly the discharge behaviour. Compared to the quasi-neutral model, the benchmark model (based on current-equality) was found to be more sensitive to the temperature of injected electrons, which might stem from the fact that the electrons are injected directly into the plume and

not at the domain boundary. Hence, the QN model might be more appropriate for 2D axial-azimuthal simulations, a conclusion that was already made by Szabo for 2D axial-radial PIC simulations [139]. However, it does not invalidate the conclusions in this chapter and the following: it just means that the discharge behaviour is probably different in real HT, but this case can still be used to verify codes and stress-test theoretical developments in a configuration close to reality. More insights on the cathode model will be given later for self-consistent simulations in section 5.2.3.

3.7 Conclusion

A 2D axial-azimuthal benchmark model for low-temperature partially magnetized plasmas has been presented in this chapter. Seven independently developed Particle-In-Cell (PIC) codes have been used to simulate this case and their results are compared. Despite the relative complexity of this benchmark, a good agreement was obtained on the averaged axial profiles of the main discharge parameters (axial electric field, ion density and electron temperature). All codes show the presence of a very strong kinetic instability propagating in the $\mathbf{E} \times \mathbf{B}$ azimuthal direction that plays a significant role on the cross-field electron transport. The characteristics of the dominant mode of these instabilities have been compared and exhibit a good agreement between all the codes. The remaining differences of around 5% are explained by the inherent unstable nature of the discharge in this case, correlated with the fact that different Random Number Generators (RNG) were used between the codes. The issue of numerical noise due to a too-low number of macroparticles was also assessed. It appears that around 250 macroparticles per cell were needed to get convergence in this 2D benchmark, which is however much less than the 10000 macroparticles per cell used in the 1D case studied in [71].

The seven participants converged on the main purpose of this 2D benchmark that was to increase confidence in our codes by verifying that the results produced were consistent with other implementations. Moreover, as mentioned earlier, these codes are often used to simulate cases that are very computationally expensive. With this in mind, this work also gave insights on the computational efficiency of different solvers, with computational times that could vary from 2.5 to 21 days for the nominal case. It is important to highlight that for simulations of $\mathbf{E} \times \mathbf{B}$ discharges, the required computing resources are quite large (around 60000 CPU hours in average for the nominal case of this benchmark) and it makes the need for benchmarking even more important.

Even though the case chosen here enabled to test different aspects of a 2D axial-azimuthal electrostatic PIC code, some simplifying assumptions have still been made, particularly concerning the absence of collisions. The earlier work of Turner *et al.* [156] could be used to verify the Monte Carlo Collision (MCC) module of PIC codes, or another benchmark case could be defined with a self-consistent treatment of ionization with the addition of neutrals and collisions.

Hence, the work presented in this chapter should be considered as a step towards the benchmarking of PIC codes of low-temperature partially magnetized plasmas.

Now that *LPPic* has been verified against similar codes in the $\mathbf{E} \times \mathbf{B}$ community, we used it to get more insights on the cathode model influence on the discharge behaviour and it appears that the Quasi-Neutral model was less sensitive to the emitted electron temperature. Indeed, we can take advantage of this simplified test case to challenge the physics and the numerical models used. Despite the strong simplifications (imposed ionization source term and no collision), many characteristics of a HT discharge are retrieved and above all, the relatively short computational time required makes this case suitable for extensive parametric studies. Moreover, every code which managed to comply to these benchmark results could be part of a collective effort by simulating specific cases: hence, if several research groups simulate different cases, it could provide a huge data base to analyse. This collective parametric study was started as part of the LANDMARK project [192].

Finally, we can also use this simplified case to get more physical insights on the discharge behaviour and stress-test theoretical developments. This will be the topic of the next chapter.

Chapter 4

Instability-enhanced electron transport: comparisons of PIC simulation results with theoretical models

Before going towards self-consistent simulations, we took advantage of the relatively short computational time required for the simplified benchmark case described in the previous chapter. Even though we are aware that some simplifications could impact the physics (fixed ionisation profile, no collisions, etc.), it was a good opportunity to stress-test theoretical models meant to approximate the electron-ion friction force (Eq. 1.38), expected to contribute significantly to the electron anomalous transport. In this chapter, the results of extensive parametric studies are presented, varying the magnetic field maximum value, the current density, or adding specific ion-neutral collisions. A recent model developed by Lafleur et al. [86] to approximate this friction force is tested with these various discharge behaviours, along with other models which can be found in the literature. Overall this theory is found to be in very good agreement with the simulation results for all cases studied; verifying the underlying physical mechanisms leading to enhanced electron transport. We demonstrate however that the friction force depends sensitively on the shape of the electron velocity distribution function, thus posing significant challenges to fully self-consistent, first principles, modelling of anomalous transport in fluid simulations.

Most of the content of this chapter has been adapted from [200]. After a brief reminder of the context in section 4.1, the importance of the instability-enhanced electron-ion friction force on the axial electron transport is highlighted in the beginning of section 4.2, before giving an overview of previous models for approximating it and finally re-deriving the recently developed kinetic model (adding further simplification steps) explicitly. These models are all compared with the nominal case presented in the previous chapter. Then, in section 4.3, the recent kinetic model is stress-tested against the results of several PIC simulations for which various

parameters have been varied. Finally, the role of specific ion-neutral collisional processes is analyzed in Section 4.4.

Contents

4.1	Context	86
4.2	Theoretical models for enhanced electron transport	87
4.2.1	Electron-ion friction force	87
4.2.2	Theoretical models	89
4.2.3	Comparison with the nominal simulation case	95
4.3	2D PIC simulations	97
4.3.1	Model & Parametric studies	97
4.3.2	Comparison with parametric PIC results of the friction force derivation accounting for non-Maxwellian electrons	105
4.3.3	Ion-electron friction force	108
4.4	Influence of ion-neutral collisions	108
4.5	Discussion and Conclusion	112

4.1 Context

We have seen in chapter 1 that the most recent and probable explanation for the electron anomalous transport in $\mathbf{E} \times \mathbf{B}$ discharges (and hence, in Hall Thrusters) is the electron-wave scattering from short-wavelength instabilities propagating predominantly in the azimuthal direction. However, few experimental diagnostics [42, 201, 202, 67, 81, 203] can currently be used to study these so-called Electron Drift Instabilities (EDI). Furthermore, the comparison of theoretical models of the drag force produced by EDIs with fluid simulations using ad-hoc mobilities or collisionalities (derived empirically from experiments) is a challenge, as different parameter scalings can give similar results in fluid codes (i.e. the differences are often within the experimental uncertainty of current diagnostics) [204]. Hence, self-consistent Particle-In-Cell (PIC) simulations appear to be the best tools available to find and test new first principles theoretical models.

For several reasons, the simulation model described in the previous chapter, presents itself as a useful candidate tool to help test and challenge any new theoretical transport models. Firstly, the simulation domain and operating conditions are clearly specified, and 7 independent research groups have obtained similar results. Secondly, the model is representative of an $\mathbf{E} \times \mathbf{B}$ discharge, and since an ionization source term is imposed, the simulation rapidly reaches a steady state which drastically reduces the computational time. Finally, the influence of specific parameters (such as the magnetic field, the discharge current density or the presence of neutral collisions) on the azimuthal instabilities can easily be tested and understood.

Recently, a model based on aspects of quasi-linear kinetic theory was developed [86] to predict the level of enhanced transport. However, this theory has

only been compared with PIC simulations in limited testing at only a single set of operating conditions. Hence, in this chapter, we challenge this model more extensively against a broad range of PIC simulation results based on the aforementioned simplified simulation benchmark model.

4.2 Theoretical models for enhanced electron transport

4.2.1 Electron-ion friction force

Prior to derive theoretical models to approximate the electron-ion friction force, the importance of this force term needs to be justified. We will hence focus here on all the force terms contributing to the electron transport to better understand the cause of the anomalous electron transport in the axial direction. To do so, the electron momentum conservation equations can be derived from the electron kinetic equation. As described in detail in Lafleur *et al* [111], this derivation gives the following equations (averaged over the azimuthal direction, and over short times) in the axial and azimuthal directions, respectively

$$qn_e v_{e,y} B = \partial_t(mn_e v_{e,x}) + \partial_x(mn_e v_{e,x}^2) + \partial_x(\Pi_{e,xx}) - qn_e E_x - R_{en,x} - R_{ei,x}, \quad (4.1)$$

$$-qn_e v_{e,x} B = \partial_t(mn_e v_{e,y}) + \partial_x(mn_e v_{e,x} v_{e,y}) + \partial_x(\Pi_{e,xy}) - qn_e E_y - R_{en,y} - R_{ei,y}, \quad (4.2)$$

with the electron distribution function moments, the electron-neutral collisional momentum loss and the electron-ion friction force respectively defined as

$$\left\{ \begin{array}{l} n_e = \int_{-\infty}^{\infty} f_e(\mathbf{w}) d^3 w, \\ n_e \mathbf{v}_e = \int_{-\infty}^{\infty} \mathbf{w} f_e(\mathbf{w}) d^3 w, \\ \Pi_e = m \int_{-\infty}^{\infty} (\mathbf{w} - \mathbf{v}_e)(\mathbf{w} - \mathbf{v}_e) f_e(\mathbf{w}) d^3 w, \end{array} \right. \quad (4.3)$$

$$\mathbf{R}_{en} = -mn_g \int_{-\infty}^{\infty} \sigma_m(w) w \mathbf{w} f_e(\mathbf{w}) d^3 w, \quad (4.4)$$

$$\mathbf{R}_{ei} = q \langle \delta n_e \delta \mathbf{E} \rangle = q \langle [\langle n_e \rangle_t - n_e(t)] [\langle \mathbf{E} \rangle_t - \mathbf{E}(t)] \rangle_t, \quad (4.5)$$

with σ_m the momentum transfer electron-neutral cross-section and the angled brackets $\langle \dots \rangle_t$, a time average.

We can define

- $F_{B,x} = qn_e v_{e,y} B$ and $F_{B,y} = -qn_e v_{e,x} B$ respectively the axial and azimuthal magnetic force terms,
- $F_{t,x} = \partial_t(mn_e v_{e,x})$ and $F_{t,y} = \partial_t(mn_e v_{e,y})$ respectively the axial and azimuthal temporal inertia terms,

- $F_{in,x} = \partial_x(mn_e v_{e,x}^2)$ and $F_{in,y} = \partial_x(mn_e v_{e,x} v_{e,y})$ respectively the axial and azimuthal spatial inertia terms,
- $F_{p,x} = \partial_x(\Pi_{e,xx})$ and $F_{p,y} = \partial_x(\Pi_{e,xy})$ respectively the axial and azimuthal pressure tensor terms,
- $F_{E,x} = -qn_e E_x$ and $F_{E,y} = -qn_e E_y$ respectively the axial and azimuthal electric force terms,
- $F_{en,x} = -R_{en,x}$ and $F_{en,y} = -R_{en,y}$ respectively the axial and azimuthal electron-neutral momentum collisional drag force terms,
- $F_{ei,x} = -R_{ei,x}$ and $F_{ei,y} = -R_{ei,y}$ respectively the axial and azimuthal instability-enhanced electron-ion friction force terms.

Note that these instability-enhanced force terms are referred to as an "electron-ion friction force", because the force is produced due to the relative drift between electron and ion species, and acts to decrease the electron drift speed, while increasing the ion drift speed. This is completely analogous to the drag force experienced by two gases drifting through each other. An important implication of the word "friction", is that the electron-ion force term should be equal and opposite to the ion-electron force term. This is explicitly demonstrated in Section 4.3.3 below. A similar analysis relating wave properties to an effective drag force density term in the fluid conservation equations has also been performed by Davidson and Krall [205] in the context of ion acoustic waves in high-temperature discharges with cross-field currents.

Axial profiles of the different terms in equations 4.1 and 4.2 are shown in figure 4.1 for the benchmark case of chapter 3 (with $N_{ppc,ini} = 75$, called here "nominal case"). In the axial direction (figure 4.1(b)), we retrieve the behaviour observed in [140]: only the pressure gradient term (diamagnetic term) $F_{P,x}$ and the axial electric field term $F_{E,x}$ contribute to the electron drift, the former being dominant near the anode while the latter being dominant near the exit plane. As expected, the amplitude of the force terms is orders of magnitude higher than in the azimuthal direction: electrons have an axial velocity that is negligible compared to the azimuthal drift velocity. The above results are also in agreement with those obtained in [111].

While the PIC simulations correctly resolve long-range electron-ion collisional effects with a wavelength of the order of the Debye length or greater, short-range Coulomb collisions are not explicitly modelled. It is nonetheless interesting to evaluate the expected friction force density from such Coulomb collisions, and compare it with the instability-enhanced friction force density obtained in the simulations. As discussed in further detail in [85], the classical electron-ion friction force in a stable plasma can be found from the momentum moment of the Lenard-Balescu equation [206, 207], which for singly charged ions and a quasi-neutral plasma yields

$$F_{ei}^{LB} \approx \frac{2.7n_e^2|q|^3 \ln\Lambda}{(4\pi\epsilon_0)^2 T_e}, \quad (4.6)$$

where $\ln\Lambda$ is the Coulomb logarithm. This force density is shown in figure 4.1(a),

and as expected, is found to be negligible compared to the instability-enhanced friction force. It is interesting to note that the difference in magnitude (of the order of a factor of 500) is similar to that estimated theoretically in previous work [85].

The azimuthal direction, shown in figure 4.1(a), is of more interest as the left-hand side of equation 4.2 corresponds to the electron axial velocity and hence the right-hand side displays all of the terms that contribute to the axial transport. We observe that the instability-enhanced friction force $F_{ei,y}$ is the main contributor to the axial electron transport, and that this leads to cross-field electron transport even in the absence of electron-wall or electron-neutral collisions. In previous work [111] which used a self-consistent PIC simulation, the terms of the electron momentum balance equation were similarly evaluated, and the spatial inertia $F_{in,y}$ and pressure $F_{p,y}$ terms in the azimuthal direction were found to be very small. Observation of figure 4.1 shows that these terms become relatively large at the location where the imposed ionization profile first starts (when moving towards the anode region). Since electrons are continually, and artificially, added into the simulation in the ionization region, and since in general these electrons have a different temperature and velocity distribution function compared to the other self-consistently evolved simulation electrons, the azimuthal inertia and pressure terms (which are off-diagonal tensor terms), may undergo a sudden change. Such a change is not observed if all electrons and collisional processes were evolved smoothly and self-consistently, as seen later in section 5.3.1.

4.2.2 Theoretical models

As we have seen before in section 1.3.1, the prediction of the anomalous collision frequency (and hence, of the force term leading to enhanced transport) is crucial for fluid and hybrid models. In the previous decade, many attempts have been made to find an accurate and flexible model [58, 84, 132, 134]. Four models have been selected here to be compared with the PIC results for the nominal simulation case. The kinetic theory model developed in [86] is further detailed and will be tested more extensively in section 4.3.2. Even though these models are usually formulated in term of collision frequencies, we will use here anomalous force terms (via equation 1.40) to relate with the electron-ion friction force that has been shown in the previous section to be the dominant contributor to the anomalous transport.

Empirical model

One of the first models that was developed is based on Bohm diffusion, which gives the formula [208]

$$\nu_{bohm} = \frac{K}{16} \omega_{ce}, \quad (4.7)$$

with K an empirical parameter. Hagelaar *et al.* [58] have used this Bohm approximation in the plume region of a two-dimensional hybrid model and managed

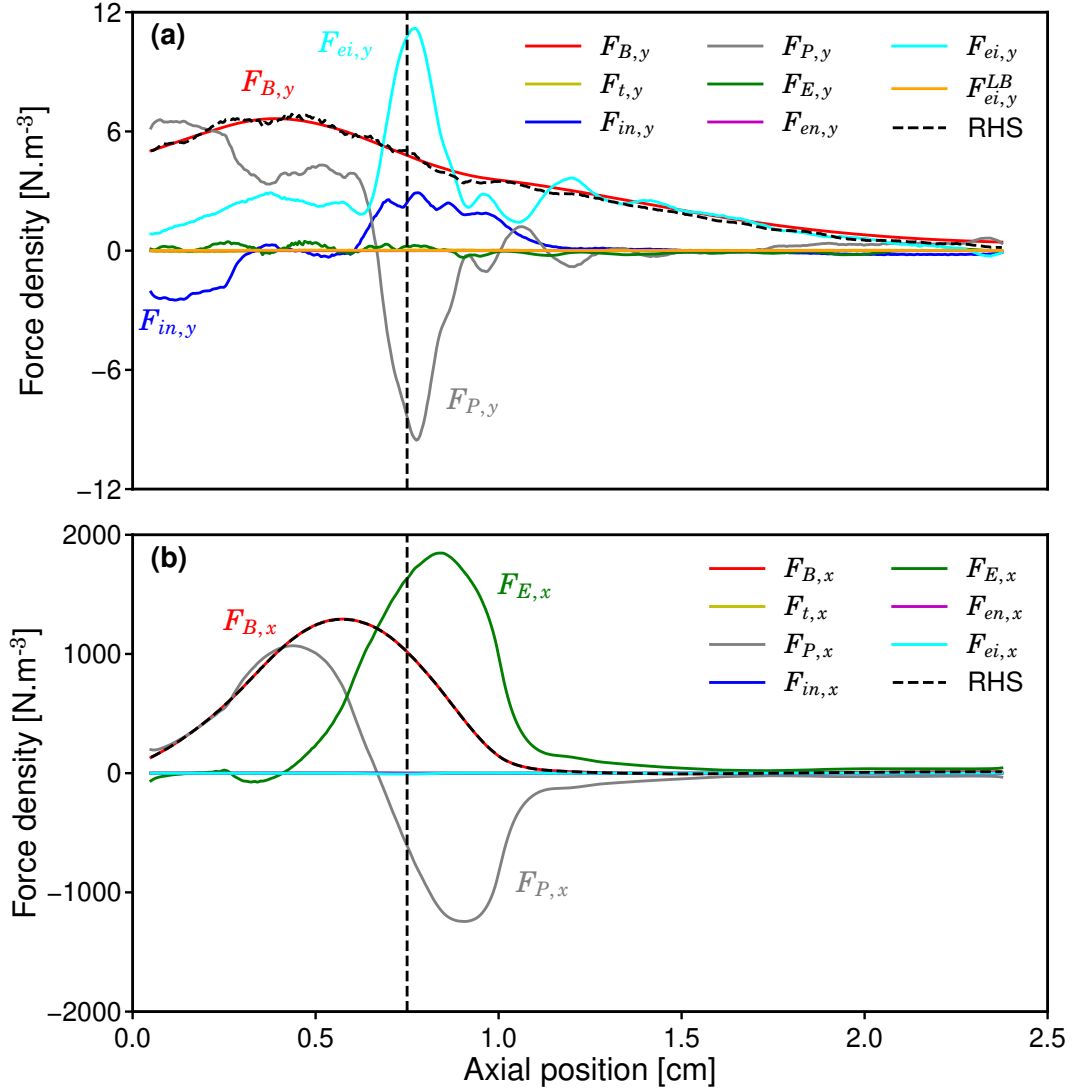


Figure 4.1 – Electron momentum force density terms for the nominal case ($B = 100$ G and $J = 400$ A · m⁻²) in the azimuthal direction (a) and the axial direction (b). The curves labelled "RHS" represent the sum of all of the individual terms on the right-hand side of equations 4.1 and 4.2. The vertical black dashed lines correspond to the position of the maximum magnetic field.

to qualitatively reproduce the experimental ionization oscillations and their parameter scalings, along with a good estimation of the thrust [59]. In the thruster chamber, they considered the effect of the walls by using a different empirical formula

$$\nu_{wall} = \alpha \nu_{ref}, \quad (4.8)$$

with $\nu_{ref} = 10^7 \text{s}^{-1}$ a reference frequency for wall collisions and α an additional empirical parameter. We can then get the corresponding anomalous force term

$$\begin{cases} R_{ei,empirical} = -mn_e v_{e,y} \alpha \nu_{ref} & (\text{inside}), \\ R_{ei,empirical} = -n_e v_{e,y} \frac{K}{16} qB & (\text{outside}). \end{cases} \quad (4.9)$$

Other empirical models can be found in the literature, such as those based on machine-learning developed recently by Jorns [134], but we have selected only a single representative model here for clarity.

Quasi-linear kinetic theory with ion-trapping saturation

In Lafleur *et al.* [84], a kinetic theory was developed which explained the anomalous transport in terms of an instability-enhanced friction force, with the azimuthal instabilities saturating due to ion-wave trapping. Taking into account a more accurate ion-trapping magnitude which comes from [111], the force can be written as

$$R_{ei,saturated} = \frac{q}{16\sqrt{6}c_s} |\nabla(v_{i,x} n_e T_e)|, \quad (4.10)$$

where c_s is the ion sound speed, $v_{i,x}$ the axial ion drift velocity and T_e the electron temperature expressed in eV. This formula was shown to match the empirical electron mobility profile needed in fluid simulations to get agreement with experiments [84, 25], and was further used by Croes *et al.* [77] in which good agreement was found for 2D radial-azimuthal PIC simulations (in which the observed instabilities saturated at a similar level to that predicted by ion-wave trapping).

Quasi-linear kinetic theory

In [86] a quasi-linear kinetic model for the instability-enhanced force was derived. A similar approach has been used by Davidson and Krall [205] in the context of ion acoustic waves in discharges with cross-field currents. This derivation is given here in more detail, and extended by further simplification steps allowing a more transparent and compact formula. Considering the equations of quasi-linear kinetic theory, we recall that the anomalous friction force density, \mathbf{R}_{ei} , can be written as [84, 86]

$$\mathbf{R}_{ei} = q \langle \delta n_e \delta \mathbf{E} \rangle, \quad (4.11)$$

where δn_e is the perturbed electron density, and $\delta \mathbf{E}$ is the perturbed electric field.

By taking the Fourier transform of the perturbed Vlasov equation, and considering only a single dominant wave mode, Eq. 4.11 can be written as [86]

$$\mathbf{R}_{ei} = -\frac{e^2 \mathbf{k} |\delta \mathbf{E}|^2}{2mk^2} \text{Im} \left\{ \int_{-\infty}^{\infty} d^3v \frac{\mathbf{k} \cdot \nabla_{\mathbf{v}} f_{e0}}{\omega - \mathbf{k} \cdot \mathbf{v}} \right\}. \quad (4.12)$$

Here \mathbf{k} and ω are the instability wavevector and complex frequency, \mathbf{v} is the electron velocity phase space coordinate, f_{e0} is the equilibrium (i.e. time-averaged over the short time scales of the instability) Electron Velocity Distribution Function (EVDF), and $\nabla_{\mathbf{v}}$ is the gradient operator with respect to the velocity.

Equation 4.11 has been derived using two important assumptions that are worth highlighting further:

- Firstly, since the PIC simulations are electrostatic, only electrostatic instabilities have been considered in the theory so as to allow a more relevant comparison. This does not however necessarily mean that electromagnetic modes are not important; only that we are not yet able to test or investigate this further. Some experimental measurements [209] have observed magnetic field fluctuations in HTs, suggesting that electromagnetic modes may be present.
- Secondly, we have made use of a linear dielectric response function for the plasma which considers unmagnetized electrons. Rigorous justification for the validity of quasi-linear theory can often be challenging to establish, but a typical approximate criterion is that the level of potential energy fluctuations be much less than the thermal energy of the plasma, i.e. $\frac{\delta \phi}{T_e} \ll 1$. From Section 4.2.3, this criterion is well satisfied everywhere in the plasma. However, since the instabilities appear to saturate, and ion wave trapping is observed, nonlinear effects may well be important in some regions of the discharge. In this case, the use of a linear dielectric response function would seem unjustified, and since a reasonably strong magnetic field is present, so would the assumption of unmagnetised electrons. Lampe *et al.* [64] have analysed the nonlinear evolution of beam-cyclotron instabilities (similar to the electron cyclotron drift instability considered here), and by considering magnetised electrons and an approximate nonlinear plasma dielectric response function, showed that a transition to an unmagnetised, linear ion acoustic instability occurs. The large amplitude, largely coherent nonlinear wave acts to “smear” out the electron cyclotron resonances, and the plasma is left with its ion acoustic character. This fortuitous result allows us to consider the electrons as unmagnetised, and to use the much simpler linear plasma dielectric response function, from which we obtain equation 4.11. In this case, the only role of the magnetic field is in providing the large azimuthal electron drift velocity which drives the instability.

If we consider now an instability that is predominately in the azimuthal (y) direction, the friction force in the azimuthal direction (that will be noted R_{ei} in the following for the sake of clarity) can then be simplified to give

$$R_{ei} = \frac{e^2 n_e |\delta \mathbf{E}|^2}{2m k_y} \text{Im} \left\{ \int_{-\infty}^{\infty} dv_y \frac{\frac{dF_{e0}}{dv_y}}{v_y - \zeta} \right\}, \quad (4.13)$$

where $\zeta = \frac{\omega}{k_y}$ is the instability phase velocity, and where

$$F_{e0}(v_y) = \frac{1}{n_e} \int_{-\infty}^{\infty} dv_x dv_z f_{e0}(\mathbf{v}), \quad (4.14)$$

with n_e the time-averaged electron density. Thus $\int_{-\infty}^{\infty} dv_y F_{e0}(v_y) = 1$. We can define the energy density of the wave electric field, ϵ_{wave} , as

$$\epsilon_{wave} = \frac{1}{2} \epsilon_0 \langle |\delta \mathbf{E}| \rangle_{rms}^2 = \frac{1}{4} \epsilon_0 |\delta \mathbf{E}|^2, \quad (4.15)$$

where the subscript refers to the Root Mean Square (RMS) value, defined as

$$\langle \delta E \rangle_{rms} = \sqrt{\frac{1}{L_y} \int_0^{L_y} (\delta E_x^2 + \delta E_y^2) dy}. \quad (4.16)$$

Using Eq. 4.15 in Eq. 4.13, and simplifying, we obtain

$$R_{ei} = \frac{2\omega_{pe}^2 \epsilon_{wave}}{k_y} \text{Im} \left\{ \int_{-\infty}^{\infty} dv_y \frac{\frac{dF_{e0}}{dv_y}}{v_y - \zeta} \right\}. \quad (4.17)$$

We recall that the simplified ion-acoustic dispersion relation can be expressed as [84, 85]

$$\omega_R \approx \mathbf{k} \cdot \mathbf{v}_{di} \pm \frac{k c_s}{\sqrt{1 + k^2 \lambda_{De}^2}}, \quad (4.18)$$

$$\gamma \approx \pm \sqrt{\frac{\pi m}{8M}} \frac{\mathbf{k} \cdot \mathbf{v}_{de}}{(1 + k^2 \lambda_{De}^2)^{3/2}}, \quad (4.19)$$

with \mathbf{v}_{de} and \mathbf{v}_{di} the azimuthal electron and ion drift velocities respectively and M the ion mass. From these relations, the maximum growth rate occurs for $k_y \lambda_{De} = \frac{1}{\sqrt{2}}$. Thus Eq. 4.17 becomes

$$R_{ei} = 2\sqrt{2} \omega_{pe}^2 \lambda_{De} \epsilon_{wave} \text{Im} \left\{ \int_{-\infty}^{\infty} dv_y \frac{\frac{dF_{e0}}{dv_y}}{v_y - \zeta} \right\}. \quad (4.20)$$

If we focus now on the integral term, the Plemelj relation gives

$$\int dx \frac{g(x)}{x - \zeta} = \text{P} \int dx \frac{g(x)}{x - \zeta} + i\pi g(\zeta), \quad (4.21)$$

with P denoting the Cauchy principal value. Thus, we can write the integral term

in Eq. 4.20 as

$$\int_{-\infty}^{\infty} dv_y \frac{\frac{dF_{e0}}{dv_y}}{v_y - \zeta} = \text{P} \int_{-\infty}^{\infty} dv_y \frac{\frac{dF_{e0}}{dv_y}}{v_y - \zeta} + i\pi \left. \frac{dF_{e0}}{dv_y} \right|_{v_y=\zeta}. \quad (4.22)$$

Thus Eq. 4.20 simplifies to

$$R_{ei} = 2\sqrt{2}\pi\omega_{pe}^2 \lambda_{De} \epsilon_{wave} \left. \frac{dF_{e0}}{dv_y} \right|_{v_y=\zeta}. \quad (4.23)$$

Therefore, if the normalised time-averaged electron distribution function is known, the derivative at the instability phase velocity can be used to determine the anomalous friction force. We can go slightly further by noting that the instability phase velocity is typically of the order of the ion sound speed, $\zeta \sim c_s = \sqrt{\frac{eT_e}{M}}$. Since the ion sound speed is much smaller than the electron thermal velocity, Eq. 4.23 simplifies to

$$R_{ei,quasi-linear} = 2\sqrt{2}\pi\omega_{pe}^2 \lambda_{De} \epsilon_{wave} \left. \frac{dF_{e0}}{dv_y} \right|_{v_y=0}. \quad (4.24)$$

This dependence of particle transport on the derivative of the velocity distribution function is a common feature of quasi-linear theory, which shows the presence of velocity space diffusion [37, 210, 211], and has been applied, for example, to streaming instabilities in both high-temperature and low-temperature plasmas [212, 205, 213, 214].

Quasi-linear kinetic theory with a Maxwellian Electron Velocity Distribution Function

If the EVDF is a Maxwellian, we have that

$$F_{e0} = \frac{1}{\sqrt{\pi}v_{Te}} \exp\left[-\frac{(v - v_{de})^2}{v_{Te}^2}\right], \quad (4.25)$$

where $v_{Te} = \sqrt{\frac{2eT_e}{m}}$ is the electron thermal velocity. Thus for a Maxwellian, the anomalous friction force from Eq. 4.23 becomes

$$R_{ei,maxwellian} = -4\sqrt{2}\pi\omega_{pe}^2 \lambda_{De} \epsilon_{wave} \frac{(\zeta - v_{de})}{v_{Te}^3} \exp\left[-\frac{(\zeta - v_{de})^2}{v_{Te}^2}\right]. \quad (4.26)$$

Since $\zeta \sim c_s \ll v_{de}$, Eq. 4.26 simplifies to give

$$R_{ei,maxwellian} = 4\sqrt{2}\pi\omega_{pe}^2 \lambda_{De} \epsilon_{wave} \frac{v_{de}}{v_{Te}^3} e^{-v_{de}^2/v_{Te}^2}. \quad (4.27)$$

4.2.3 Comparison with the nominal simulation case

In figure 4.2, the axial profile of the measured electron-ion friction force for the nominal case is displayed, along with the models described above: the empirical model $R_{ei,empirical}$ (Eq. 4.9), the ion-trapping saturation model $R_{ei,saturated}$ (Eq. 4.10) and the Maxwellian approximation $R_{ei,maxwellian}$ (Eq. 4.27). The more general non-Maxwellian model, $R_{ei,quasi-linear}$ (Eq. 4.24), will be discussed in more detail later. The values of the two empirical parameters α and K for $R_{ei,empirical}$ have been set to 0.4 and 0.17 respectively, in order to obtain the best fit. While $R_{ei,saturated}$ behaves quite differently than the PIC results near the thruster exit, $R_{ei,maxwellian}$ exhibits a similar shape but overestimates the force density by a factor of about 3. $R_{ei,maxwellian}$ also changes direction between about $x = 1.25$ cm and $x = 1.75$ cm. The empirical formula seems to match quite well for $x < 1$ cm, but the coefficients α and K have been adjusted here to best-fit the PIC data, and hence this model is not predictive. Furthermore, this model assumes that the anomalous transport inside the thruster is largely due to electron-wall collisions, which are completely absent in the PIC simulation. One can also notice that $R_{ei,empirical}$ quickly goes to zero in the plume, whereas the PIC values still remain significant. Overall, none of these three formulae accurately matches the measured friction force throughout the simulation domain. Although we only show the comparison in figure 4.2 for the nominal simulation case, similar results are obtained for the other simulation cases.

The discrepancies observed in figure 4.2 are expected to occur because of either simplifying assumptions used, or because of the incomplete or ad hoc nature of the models themselves. To gain further insight into why these models do not fit well with the simulation results, we focus now on checking two of the main assumptions used. $R_{ei,maxwellian}$ assumes that the electron distribution is described by a drifting Maxwellian, while $R_{ei,saturated}$ assumes that the EDI saturates everywhere in the discharge due to ion-wave trapping.

EVDF

EVDFs obtained directly from the PIC simulations for the nominal case are shown in figure 4.3. We can see that in the axial and azimuthal directions, the distributions are strongly non-Maxwellian, especially in the near-anode region. Since the friction force depends on the exact details of the electron distribution function [111], this explains why equation 4.27 is not a good approximation.

Wave energy density ratio

Along with the energy density of the wave electric field ϵ_{wave} defined in Eq. 4.15, we can define the electron thermal energy density ϵ_{th} as

$$\epsilon_{th} = \frac{3}{2}en_eT_e. \quad (4.28)$$

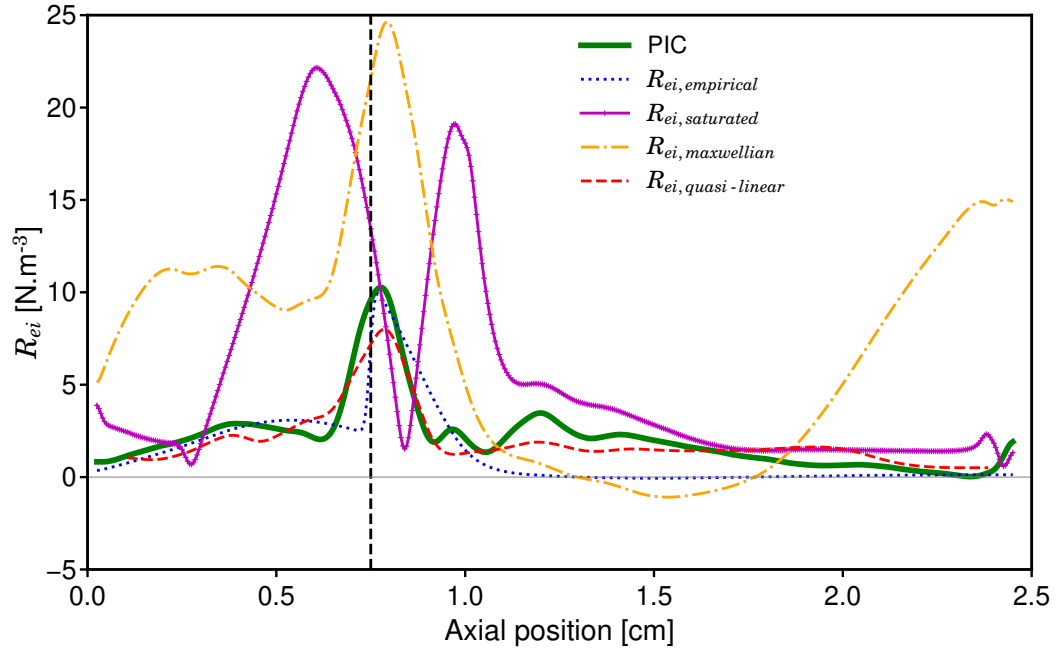


Figure 4.2 – Comparison of the anomalous force approximations with the PIC simulation results for the nominal case. Blue dotted line: $R_{ei,empirical}$ from equation 4.9. Purple line: $R_{ei,saturated}$ from equation 4.10. Orange dotted line: $R_{ei,maxwellian}$ from equation 4.26. Red dotted line: $R_{ei,quasi-linear}$ from equation 4.24. The vertical black dashed line corresponds to the position of the maximum magnetic field.

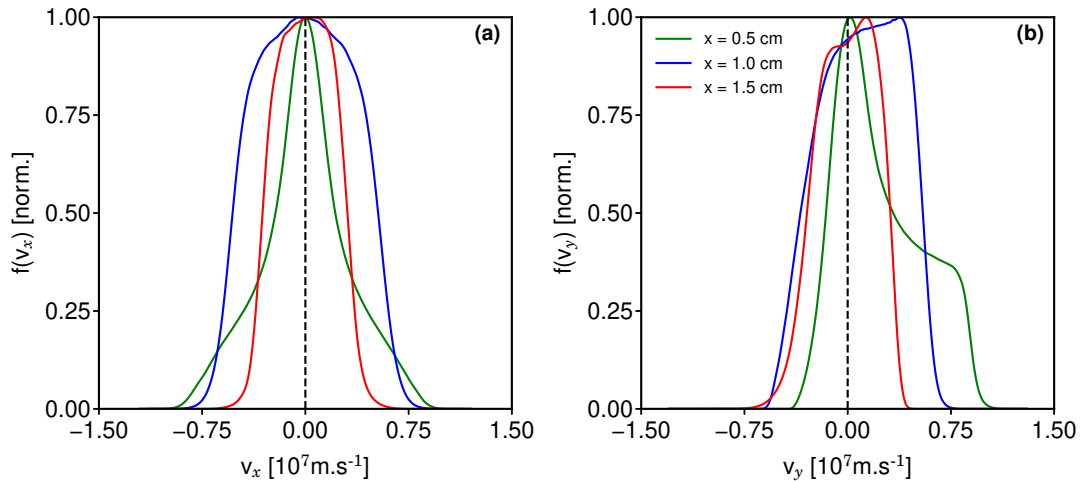


Figure 4.3 – Electron Velocity Distribution Functions in the axial (a) and azimuthal (b) directions for the nominal simulation case at different axial positions. The vertical black dashed line splits the negative and positive velocities.

For an instability that saturates due to ion-wave trapping, the rms electric field amplitude is [111]: $\langle |\delta \mathbf{E}| \rangle_{rms} = \frac{T_e}{12\lambda_d}$. This gives an upper limit to the wave energy density ratio

$$\frac{\epsilon_{wave}}{\epsilon_{th}} = \frac{1}{432}. \quad (4.29)$$

The axial profiles of wave energy density ratio, along with the above ion-wave trapping saturation limit, are shown in figure 4.4. We will come back later to the other simulation cases but for the nominal case ($B = 100$ G and $J = 400$ A · m⁻²), we can see that the wave energy density ratio is below the saturation limit, which is reached only near the cathode. This result agrees with that obtained previously [111], and explain why equation 4.10 overestimates the friction force.

Although large amplitude azimuthal instabilities have been observed in a number of other PIC simulations [74, 75, 70, 77], the fluctuation levels of these instabilities, $\frac{\langle \delta n_e \rangle}{n_e}$, are in the range of 15-20%, which is in apparent poor agreement with those measured experimentally downstream of HTs [67] where values of about 1% are found. In comparison to these previous PIC simulations (which do not include the axial thruster direction, and hence do not correctly account for wave convection), other 2D PIC axial-azimuthal PIC simulations [111], as well as the present simulations, observe a fluctuation level that varies spatially in the discharge. Within the thruster itself, the fluctuation level is about 10%, but this decreases to only a few percent just downstream of the thruster exit, which is very close to previous experimental measurements [67] made in this region. Further downstream of the exit, the fluctuation level again rises, reaching maximum values of the order of 10%. Thus, the fluctuation level shows a strong spatial dependence, and any comparison with experiment needs to account for this. More recent experimental measurements using an improved setup [215], have observed values as high as 8.7% in a smaller thruster.

Finally, we can consider now the more general non-Maxwellian force model, $R_{ei,quasi-linear}$. Although equation 4.24 allows the friction force to be calculated for a non-Maxwellian distribution, the model is incomplete because there is no easy self-consistent way in which to actually determine this distribution function (and similarly for the wave energy density). Nonetheless, the basic physics of this model can be tested by using the local EVDFs and wave energy densities obtained directly from the PIC simulations. $R_{ei,quasi-linear}$ is shown in figure 4.2 and we retrieve very well the behaviour of the measured friction force for the nominal simulation case, in both the near-anode region, and the plume.

4.3 2D PIC simulations

4.3.1 Model & Parametric studies

Now that we have seen that for the nominal benchmark case of chapter 3 the electron-ion friction force represented the dominant contribution to the electron

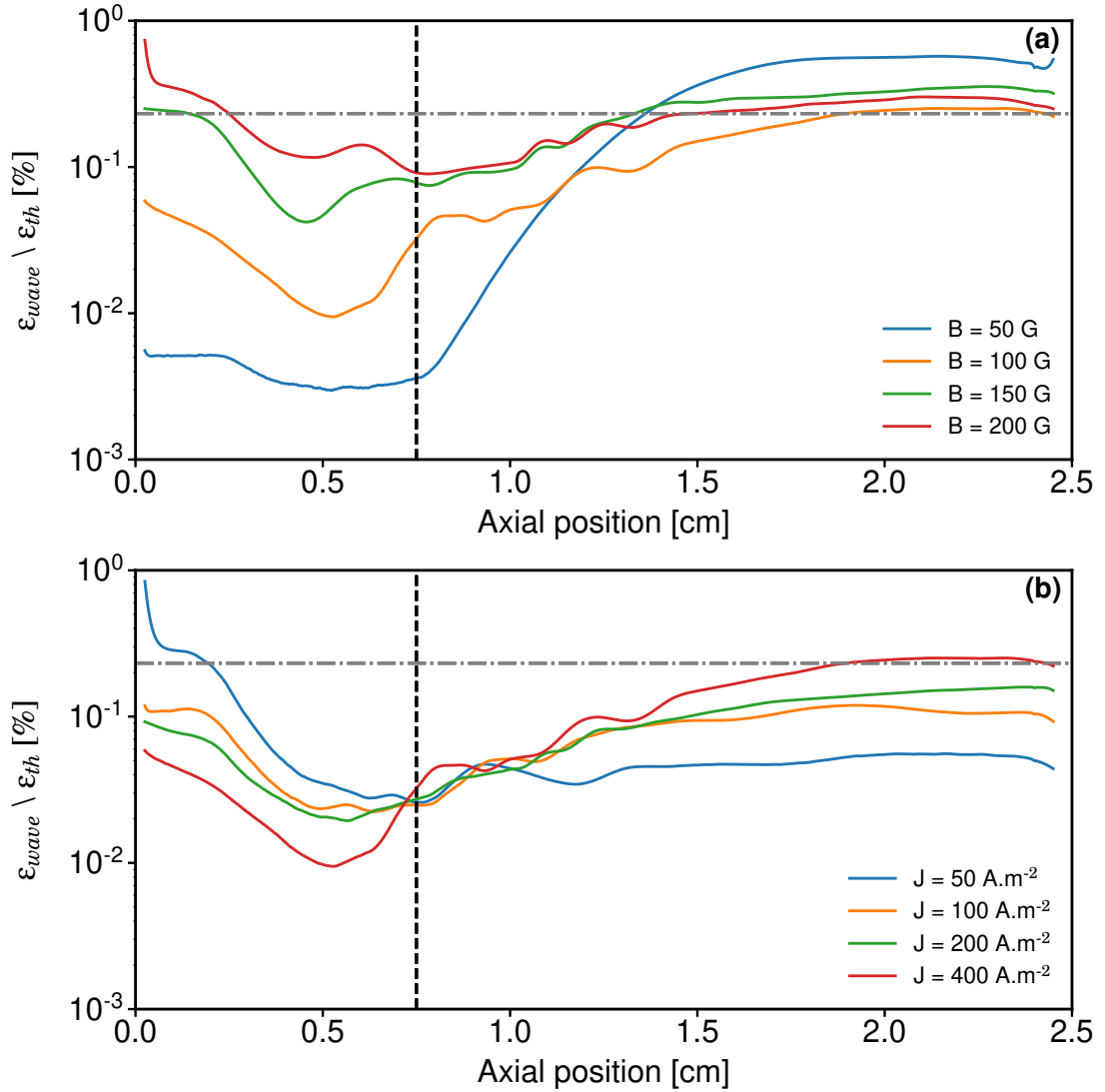


Figure 4.4 – Ratio of the time-averaged wave energy density to the electron thermal energy density as a function of axial position for different magnetic fields strengths with $J = 400 \text{ A} \cdot \text{m}^{-2}$ (a), and discharge current densities with $B = 100 \text{ G}$ (b). The horizontal grey dot-dashed line corresponds to the ion-wave trapping saturation limit. The vertical black dashed lines correspond to the position of the maximum magnetic field.

anomalous transport and that the quasi-linear kinetic theoretical model described in section 4.2.2 was approximating very well this friction force, it was important to see if these results were retrieved for other discharge behaviours. To this end, we have varied several parameters that were expected to change this discharge behaviour, and more specifically, the azimuthal instabilities observed in the domain. Firstly, the maximum value of the radial magnetic field, which had a nominal value of 100 G, has been changed to 50, 150 and 200 G, while keeping the same axial profile. Then, for the nominal value of 100 G, the current density of $400 \text{ A} \cdot \text{m}^{-2}$ has been decreased to 200, 100 and $50 \text{ A} \cdot \text{m}^{-2}$, which is equivalent to decreasing the plasma density by a corresponding factor. These 7 simulation cases will be used in this section. Finally, the effect of ion-neutral collisions (specifically charge-exchange or isotropic reactions) are studied in section 4.4. All of the above simulation cases are summarized in Table 4.1. We recall that the numerical model is the same as the one described in section 3.2. The initial number of macroparticles per cell has been set to 75, to obtain 250 macroparticles per cell on average at steady state, which corresponds to case 2 of the previous chapter and is enough to ensure numerical convergence (see section 3.5.1). For the case with lower current density, the number of macroparticle per cell is lower but because the Debye length is longer, the number of macroparticle per Debye sphere is kept constant (equation 3.8).

Table 4.1 – Simulation cases. Case 0 represents the nominal case.

Case	Magnetic field maximum [G]	Current density [$\text{A} \cdot \text{m}^{-2}$]	Collisions
0	100	400	No
1	50	400	No
2	150	400	No
3	200	400	No
4	100	50	No
5	100	100	No
6	100	200	No
7	100	400	Only charge-exchange
8	100	400	Only isotropic scattering
9	100	400	All collisions

Influence of the maximal value of the magnetic field

Figure 4.5 shows contour plots of the azimuthal electric field and ion density at the magnetic field values indicated after the simulations have reached equilibrium (at $t = 15 \mu\text{s}$). As seen, the oscillations exhibit different behaviour depending on

the magnetic field strength. The sharp difference between the near-anode region and the plume region (also observed for the nominal case ($B = 100$ G) in the previous chapter) is smoothed when the magnetic field is increased: the long-wavelength plume zone seems to extend to the near-anode region. By contrast, when B is decreased to 50 G, the short-wavelength region seems to extend to the plume. The axially averaged profiles of some discharge parameters are shown in figure 4.6. One can notice that while the behaviour of the discharge for the 3 cases $B=100, 150$ or 200 G is quite close, the case $B = 50$ G exhibits a stronger density peak and an axial shift of the axial electric field towards the cathode, which is probably related to the fact that its wave energy density ratio goes above the ion-wave trapping saturation value in the plume region, as seen in figure 4.4(a).

The sharp change in oscillation wavelength between the near-anode and plume regions is not yet fully understood, particularly since it is only present at low magnetic field strengths. One hypothesis may be that azimuthal waves are predominantly excited in the near anode region (where the plasma density maximum occurs), and as these waves propagate downstream, the dominant wavelength changes so that the local dispersion relation is continually satisfied. A similar effect has previously been analysed in the context of collisionless resistive shock waves [216]. Since the plasma density in the downstream region is lowest at the lowest magnetic field, this may explain why the effect is more prominent at 50 G.

Influence of the current density

In figures 4.7 and 4.8, the results obtained for different current densities are presented. As in the previous work of Boeuf and Garrigues [140], in which a similar case was simulated, we observe similar behaviour in figure 4.7: when the current density (and hence the plasma density) is decreased, the wavelength of the azimuthal instabilities increases. This behaviour is expected if the ion-acoustic approximation of the azimuthal instabilities is considered: indeed, for an ion-acoustic instability, the wave number giving the maximum growth rate is [84]: $k_{max} = (\lambda_d \sqrt{2})^{-1}$. When the current density is increased, the plasma density increases, which in turn decreases the Debye length, and hence the instability wavelength decreases. Finally, we can see in figure 4.4 that while the wave energy seems to increase with higher current density in the plume, the trend is reversed inside the thruster.

All in all, we can see that, for all of the above test cases, the azimuthal instabilities exhibit different characteristics, and hence, they represent a good database to verify in different configurations the results obtained in the previous section.

It should be noted that in a real HT discharge, the ionization source term is expected to change when the magnetic field profile or the current density are modified. Hence, it is important to keep in mind the limitation of an imposed ionization source term, which would naturally preclude the existence of certain types of low to mid frequency waves in the discharge, such as the breathing mode

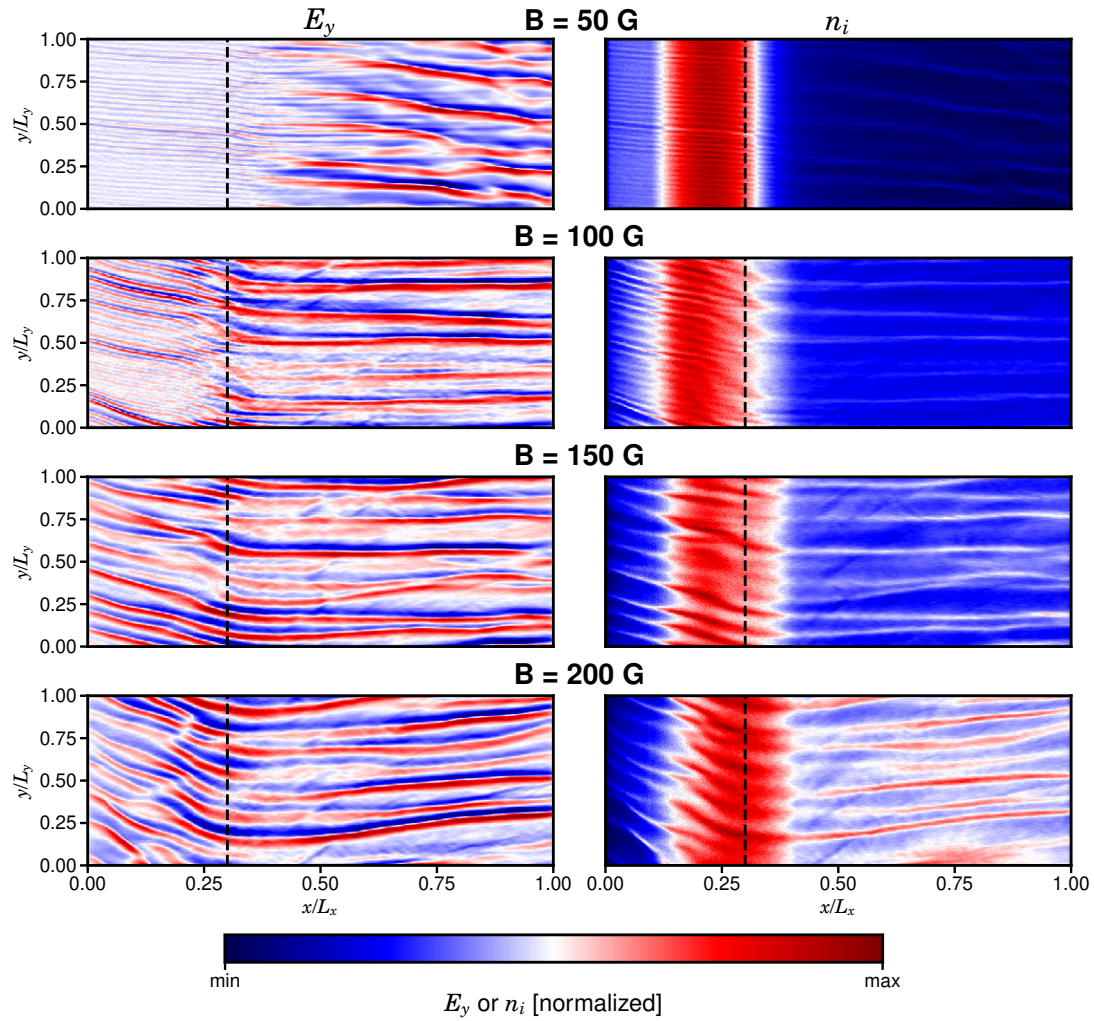


Figure 4.5 – 2D maps of the azimuthal electric field (left column) and ion density (right column) at $t = 15 \mu\text{s}$ for **different magnetic field strengths**. The vertical black dashed lines correspond to the position of the maximum magnetic field.

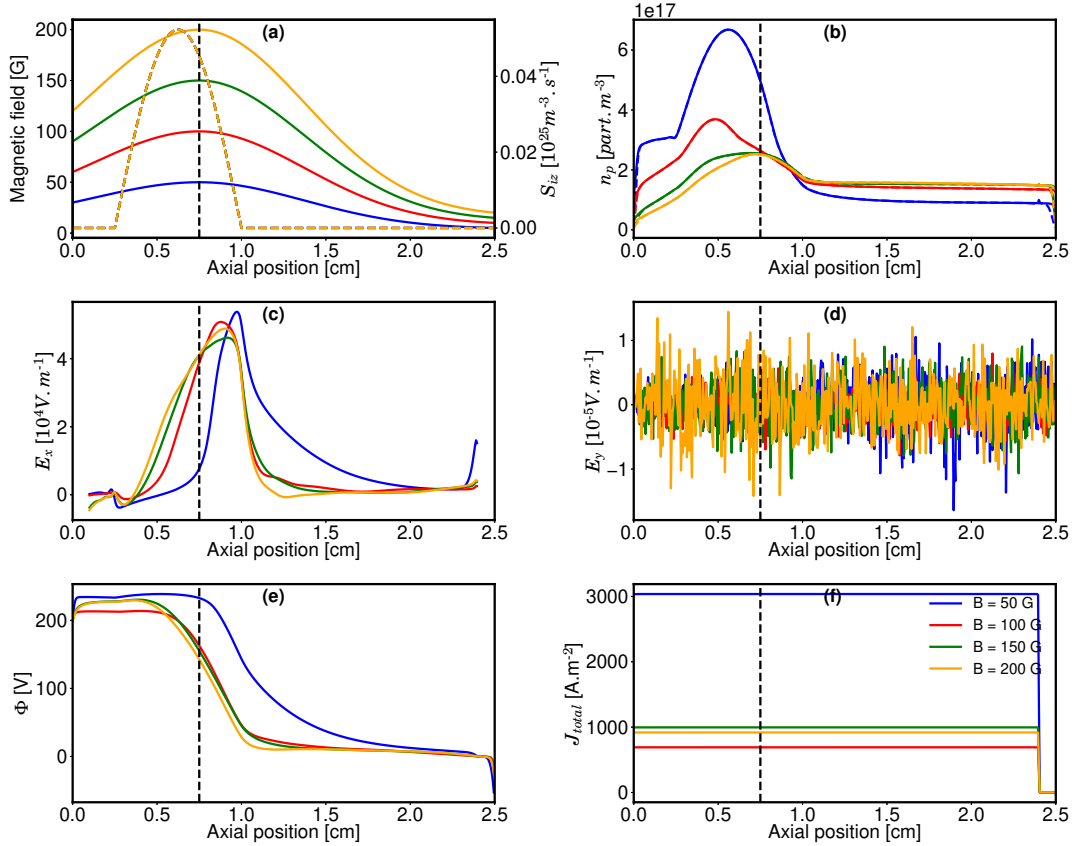


Figure 4.6 – Axial profiles (azimuthally and time averaged over the last 10 μs) of: (a) Magnetic field and ionization source term, (b) Ion (thick line) and electron (dashed line) densities, (c) Axial electric field, (d) Azimuthal electric field, (e) Plasma potential, (f) Total axial current; **for different magnetic field strengths**. The vertical black dashed lines correspond to the position of the maximum magnetic field.

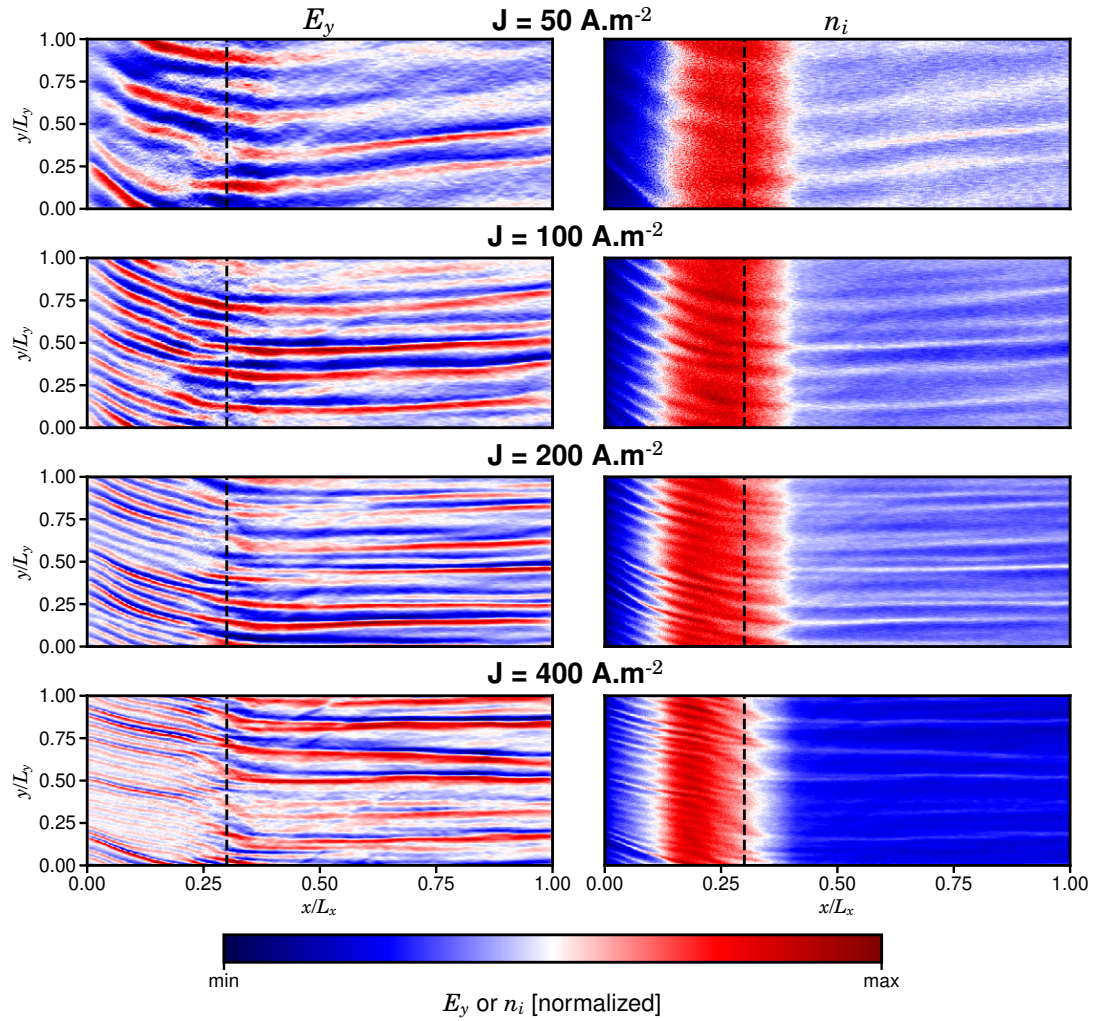


Figure 4.7 – 2D maps of the azimuthal electric field (left column) and ion density (right column) at $t = 15 \mu\text{s}$ for different discharge current densities. The vertical black dashed lines correspond to the position of the maximum magnetic field.

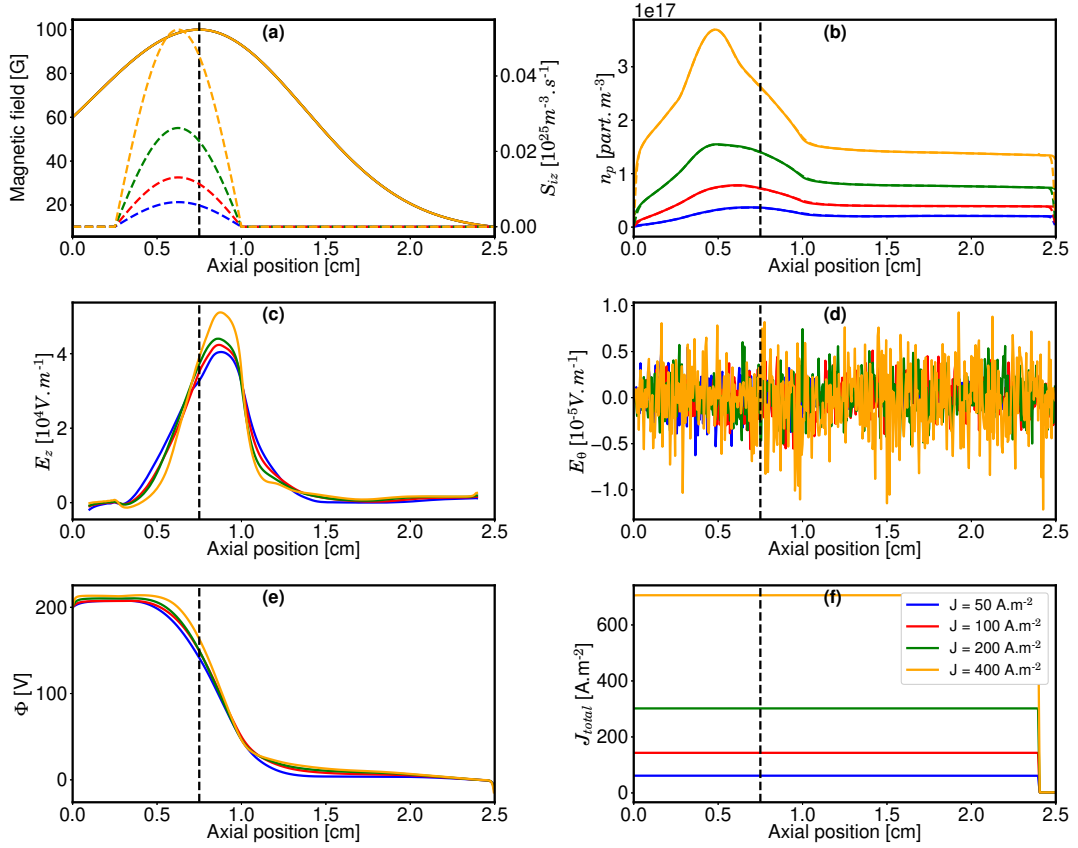


Figure 4.8 – Axial profiles (azimuthally and time averaged over the last $10 \mu\text{s}$) of: (a) Magnetic field and ionization source term, (b) Ion (thick line) and electron (dashed line) densities, (c) Axial electric field, (d) Azimuthal electric field, (e) Plasma potential, (f) Total axial current; **for different discharge current densities**. The vertical black dashed lines correspond to the position of the maximum magnetic field.

(BM), and possibly also any ion transit-time instabilities (ITTI). Such waves are known to have a large effect on the plasma discharge, which would then affect the growth of any high-frequency azimuthal instabilities. We stress though that the main purpose of the different simulation cases used in this chapter are focused specifically on a fundamental understanding of the azimuthal waves, and to challenge theoretical models for the resulting anomalous transport over a broad range of discharge behaviours. The BM and ITTI oscillations will then further be studied with the self-consistent simulations of chapters 5 and 6.

4.3.2 Comparison with parametric PIC results of the friction force derivation accounting for non-Maxwellian electrons

First, the azimuthal electron momentum force terms for simulation cases with different magnetic field strengths and current densities are shown in figure 4.9 (the force terms $F_{t,y}$, $F_{E,y}$ and $F_{en,y}$ are negligible and hence, they are not displayed for the sake of clarity). One can note that the force terms exhibit a broad range of magnitudes, and for all configurations, the electron-ion friction force is the main contributor to the axial electron transport. The dependence on the current density observed in Section 4.3.1 is retrieved here: when the current density (and hence the plasma density) is decreased, the electron-ion friction force decreases, together with the overall axial electron transport. This is expected because the oscillation amplitude of the azimuthal instabilities is also decreased when the current density decreases, and the friction force is proportional to this amplitude (as seen in the next section with equation 4.24). One can see that there is a direct correlation for this decrease: when the current density is divided by 2, the electron-ion friction force is also divided by 2. The trend for the magnetic field variations is less clear. It seems that the electron-ion friction force increases when the magnetic field increases, with a distinct peak occurring in the plume when $B = 50$ G.

For different configurations, the instability-enhanced electron-ion friction force has been observed to be the main cause of the axial electron transport. Hence, it highlights the importance of finding an approximate model for this force term that can be added to fluid codes to more self-consistently model anomalous electron transport.

To this end, we have extensively tested the quasi-linear kinetic force model, $R_{ei,quasi-linear}$ for these various simulation cases. We can see in figure 4.10 that this approximation is in very good agreement with the measured friction force for all these cases. This demonstrates that knowledge of the electron distribution function (or more specifically, of its derivative at the instability phase velocity) is crucial to properly quantifying the enhanced cross-field electron transport. One can also notice in figure 4.10 that the friction force exhibits a broad range of magnitudes (between 0.5 and $20 \text{ N} \cdot \text{m}^{-3}$) and diverse spatial profiles depending on the magnetic field and current density, and that the model given by equation

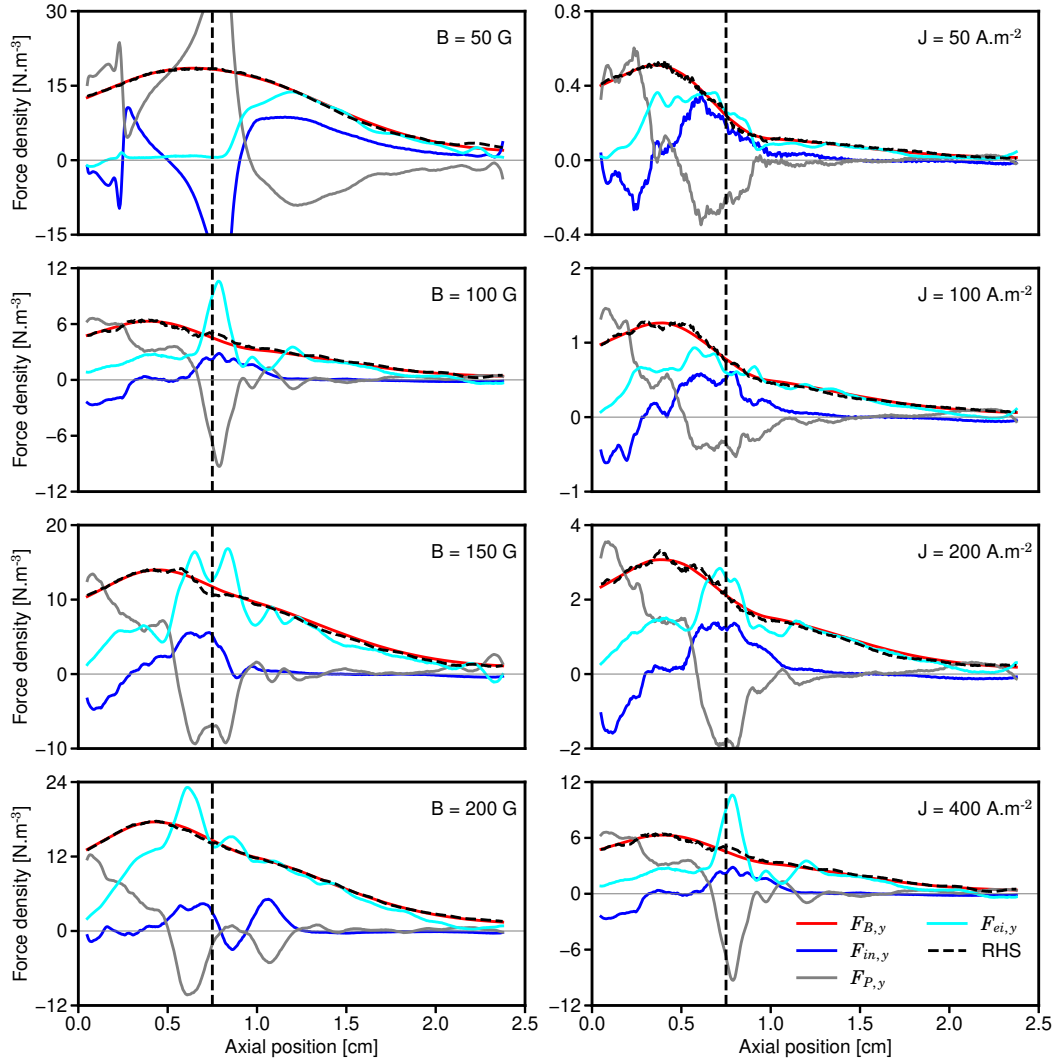


Figure 4.9 – Azimuthal electron momentum terms for different magnetic fields with $J = 400 \text{ A} \cdot \text{m}^{-2}$ (left column) and current densities with $B = 100 \text{ G}$ (right column). The nominal case, shown in figure 4.1(a), corresponds to $B = 100 \text{ G}$ and $J = 400 \text{ A} \cdot \text{m}^{-2}$. The vertical black dashed lines correspond to the position of the maximum magnetic field. The force terms $F_{t,y}$, $F_{E,y}$ and $F_{en,y}$ are not shown for the sake of clarity but are still included in the curve labelled "RHS" that represent the sum of all of the individual terms on the right-hand side of equations 4.2.

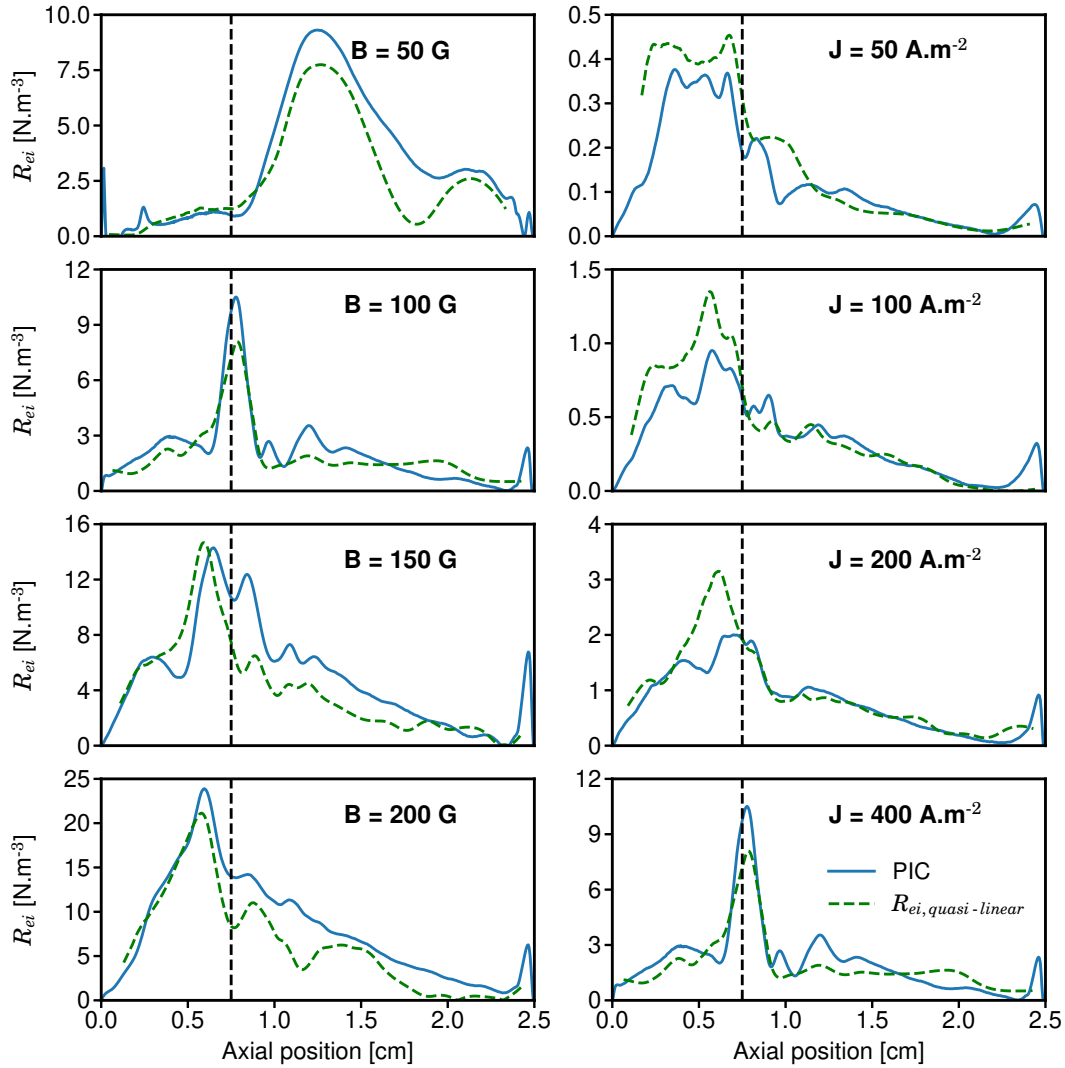


Figure 4.10 – Friction force as a function of axial position for different magnetic field strengths (left column) and discharge current densities (right column). The blue thick line corresponds to the PIC results, while the green dashed line corresponds to the Non-Maxwellian approximation. The vertical black dashed lines correspond to the position of the maximum magnetic field.

4.24 is able to capture all of this behaviour remarkably well given the complexity of the problem.

4.3.3 Ion-electron friction force

In some of the theoretical models discussed above, the anomalous force term is viewed as an instability-enhanced electron-ion friction force. This force term, $F_{ei} = -R_{ei}$, corresponds to a drag force between the electrons and ions that is formed due to the difference between the electron and ion drift velocities (and which is mediated by the instability electric field). If this term is truly a friction force however, then momentum conservation requires that the corresponding force term on the ions should be equal in magnitude, but opposite in direction. That is, $R_{ie} = -R_{ei}$. Figure 4.11 shows a comparison of the force terms $R_{ei} = -q\langle\delta n_e\delta E_y\rangle$ and $R_{ie} = q\langle\delta n_i\delta E_y\rangle$ computed directly in the PIC simulations. As seen, these force terms are in excellent agreement throughout the discharge, and for all of the simulation cases tested. Thus, the force term R_{ei} can indeed be viewed as an electron-ion friction force.

4.4 Influence of ion-neutral collisions

For all the results shown in the previous sections, electron-neutral and ion-neutral collisions were not taken into account. In this section, we consider an imposed axial profile of the neutral density shown in figure 4.12. This profile has been obtained by solving the 1D Euler equations (Eq. 2.21) for the neutral xenon gas, until a steady state is reached, with S_{iz} the imposed ionization source term of figure 3.2. As in the previous chapter, a discharge current density of $400 \text{ A} \cdot \text{m}^{-2}$ is considered, which is lower than in "real" thrusters [18] with discharge current densities of around $1000 \text{ A} \cdot \text{m}^{-2}$. Hence, to be consistent for the computation of the neutral density profile, the Xenon mass flow rate was set to $1.5 \text{ mg} \cdot \text{s}^{-1}$ with an inner and outer channel radius of 2 and 4 cm, respectively. We consider here the collisions listed in section 2.1.1. The ionization is still treated in a non-self-consistent way by using the imposed ionization source term shown in figure 3.2. No energy loss is taken into account and hence, the impact of the ionization process on the electrons is not analysed here. As described in Table 4.1, three cases are simulated with inclusion of: only ion-neutral isotropic collisions (equation 2.13, i.e. the ion velocity norm is conserved but its direction is modified), only ion-neutral charge-exchange collisions (equation 2.14, i.e. the ion velocity is reduced to the one of the neutral atom), or all of the ion-neutral and electron-neutral collisions detailed above.

The electron-ion friction force has been calculated for these 3 cases and its axial profile at steady-state is shown in figure 4.13, along with the nominal simulation case without any collisions. The friction force approximation of equation 4.24 is overlaid, where it can be seen that it still approximates very well the observed friction force. One can notice that this friction force (and hence the

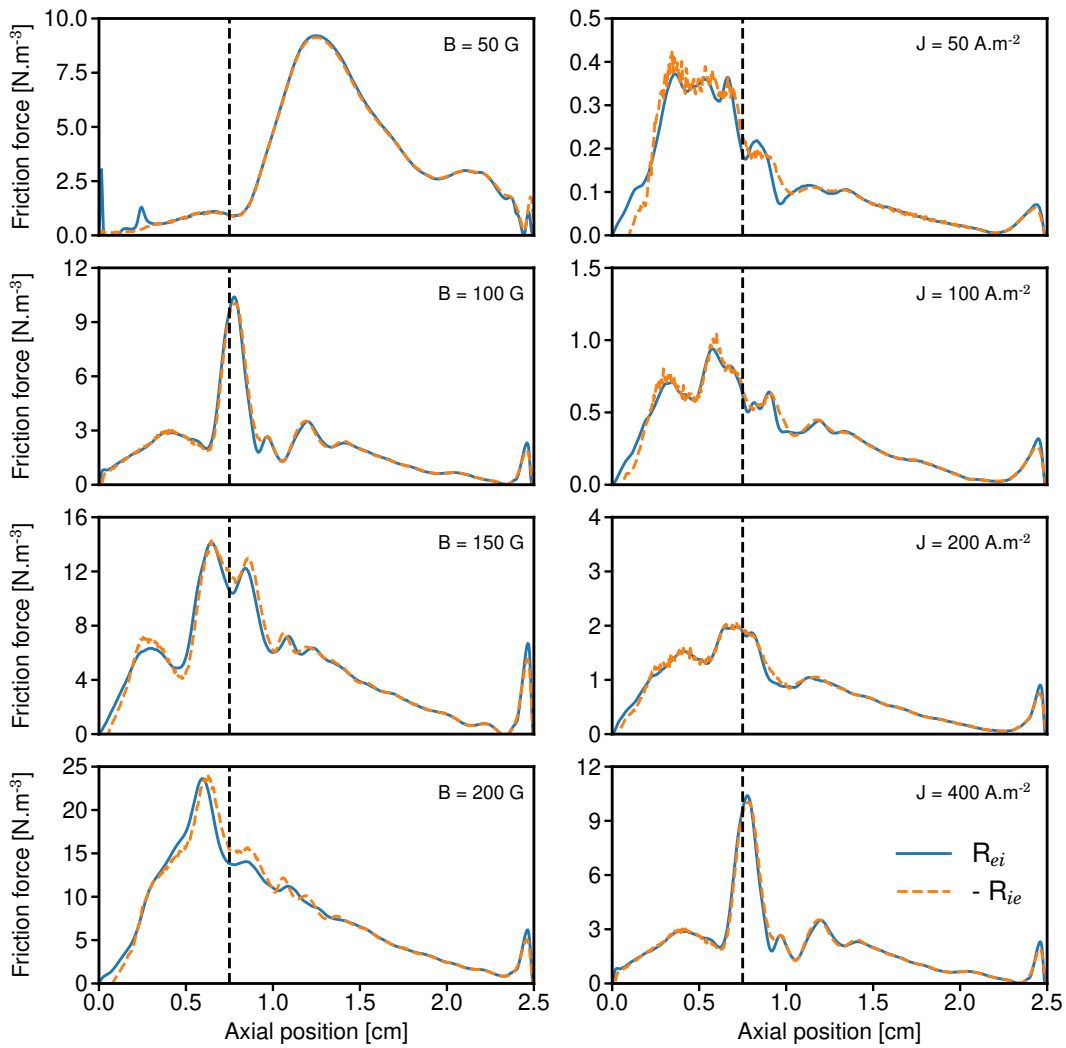


Figure 4.11 – Comparison between the azimuthal electron-ion and ion-electron force density terms for all of the simulation cases tested. The vertical black dashed lines correspond to the position of the maximum magnetic field.

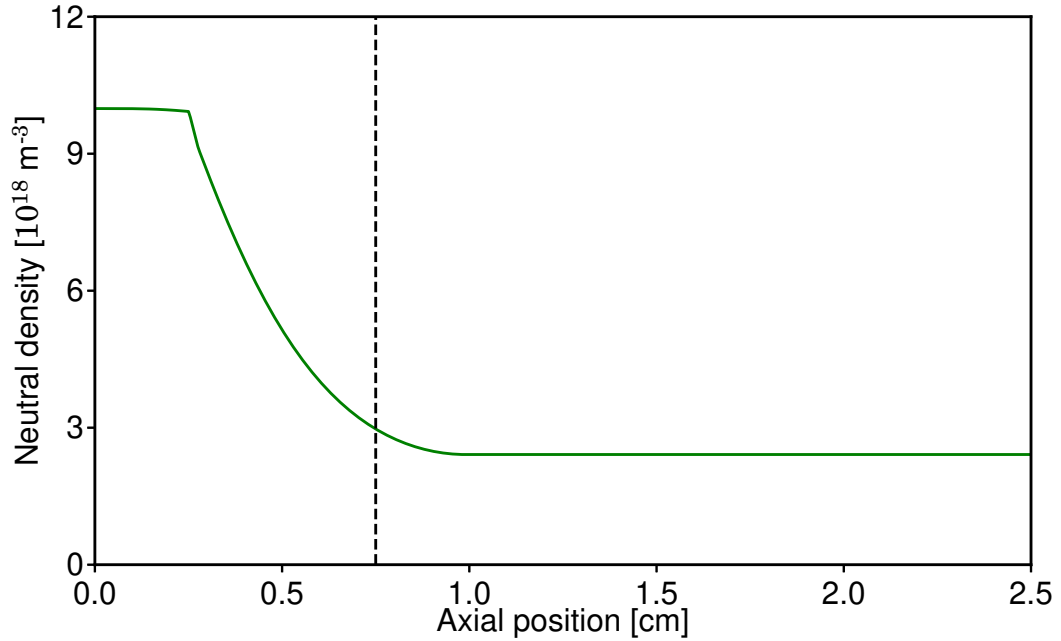


Figure 4.12 – Axial profile of the imposed neutral density for the cases in section 4.4.

axial electron transport) is greatly enhanced (by almost a factor 2) when all collisions (electron-neutral and ion-neutral) are taken into account. The ion-neutral isotropic scattering collisions do not have any significant effect on the friction force which stems from the fact that the corresponding collision frequency is low and no energy is exchanged. On the contrary, the ion-neutral charge-exchange collisions enhance the friction force, and hence play an important role for the axial transport. In figure 4.13(d), the electron-neutral momentum collisional drag force term has been displayed and we can notice that, as already observed in previous simulations [111, 217], the contribution of classical electron-neutral collisions to the axial electron transport is negligible compared to the electron-ion friction force.

The electron-ion friction force enhancement by the ion-neutral charge-exchange collisions could be explained by considering the growth rate of the azimuthal instabilities, γ . A possible cause of damping for γ might be the linear Landau damping, as postulated in [218]. Charge-exchange collisions create low-energy ions from the main high-energy ion beam, and thus the ion velocity distribution is modified, which in turn is expected to change the instability growth rate. Indeed the wave energy density is found to increase when charge-exchange collisions are taken into account. The observation of low-energy ions contributing to the axial electron transport has already been observed by Katz *et al.* [141] in a simplified 2D axial-azimuthal PIC configuration.

The enhancement of the electron-ion friction force by electron-neutral colli-

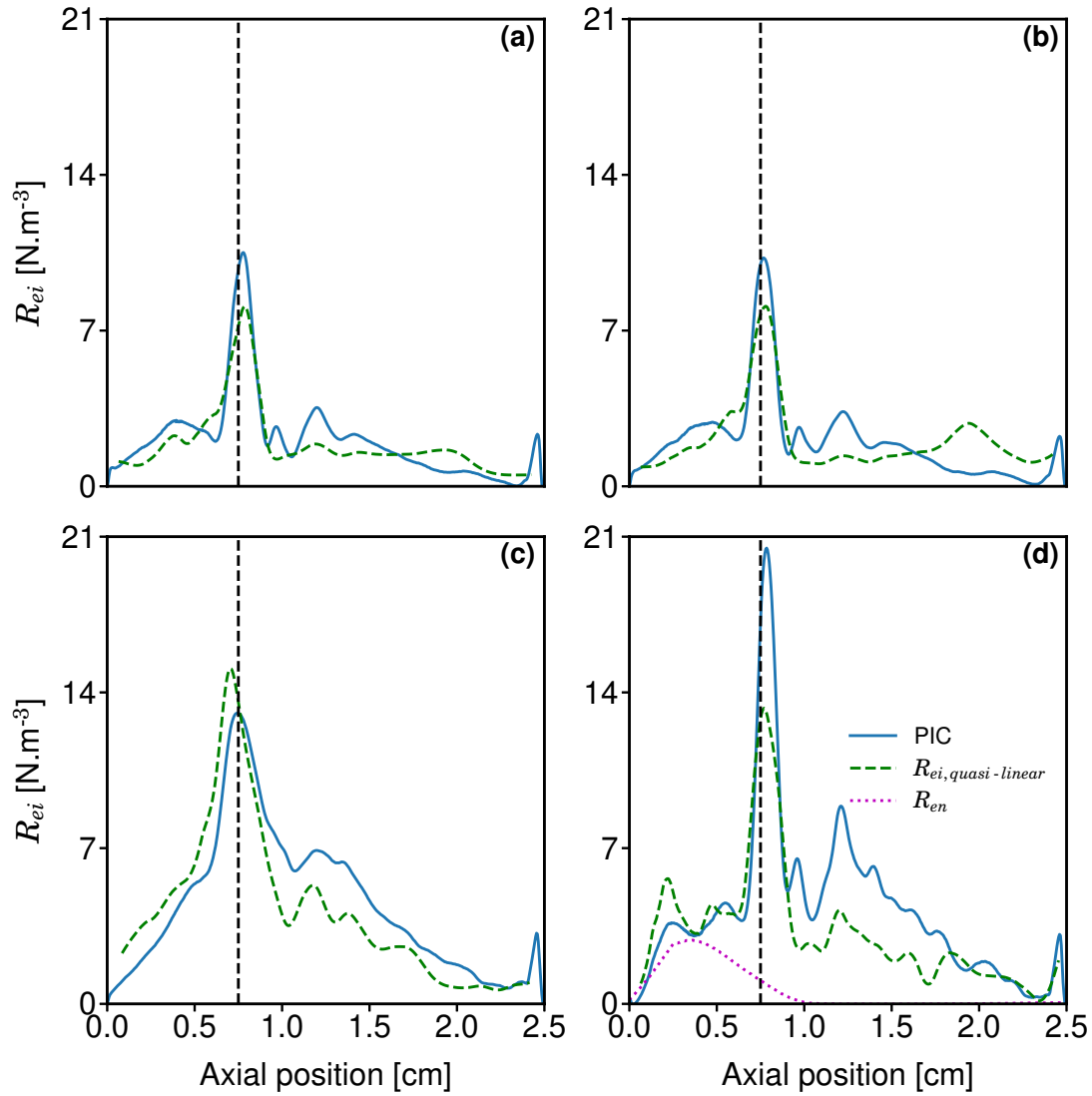


Figure 4.13 – Friction force approximation if: no collisions (i.e. nominal case) (a), only ion/neutral isotropic collisions (b) only ion/neutral charge-exchange collisions (c) all collisions electron/neutral and ion/neutral (d). Vertical black dashed lines correspond to the position of the maximum magnetic field. R_{en} correspond to the electron-neutral momentum collisional drag force term.

sions remains unclear, but may be related to a change in the electron distribution function (which then affects both the instability growth rate, and friction force). A deeper analysis is left for future work.

4.5 Discussion and Conclusion

In this chapter, the 2D axial-azimuthal Particle-In-Cell simulation model of chapter 3 has been used as a baseline for extensive parametric studies. The radial magnetic field strength, discharge current density and neutral collisional processes have been varied, which gives a discharge that displays different instability behaviour and properties. These simulation results were used to challenge a recently developed theoretical model that quantifies the anomalous force leading to enhanced cross-field electron transport. Good agreement was obtained for all of the simulation cases tested. Hence, the kinetic theory appears to describe very well the anomalous transport, and the concept of this anomalous force as an electron-ion friction force was emphasized by showing that $R_{ei} = -R_{ie}$, i.e. this friction force does indeed correspond to a drag force between electrons and ions.

The theoretical model shows that the instability-enhanced friction force is very sensitive to the electron distribution function, which is in general strongly non-Maxwellian, and diverse in shape throughout the discharge. This explains the large challenge in modelling anomalous electron transport, and highlights the real difficulty in finding a first principles model that can be incorporated into a fluid simulation. Although the model was shown to be in good agreement with the simulation results and gives additional insight into the anomalous transport, it cannot yet be incorporated into a fluid simulation, as there is no self-consistent way to determine the electron velocity distribution function, or the instability wave energy density. While quasi-linear kinetic theory provides a relevant kinetic equation that can in principle be used to determine the distribution function, this equation is very complicated and challenging to solve. Furthermore, if this equation could be solved, there would then be no need to actually use a fluid model since all relevant plasma properties could be obtained from moments of the distribution function itself. Aside from more detailed experimental measurements to confirm the importance of the instability-enhanced force, further theoretical work is needed to address these issues.

The validity of the quasi-linear approximation in the context of electron drift instabilities in HTs still requires further investigation. Even though in this work, the level of potential energy fluctuations does not exceed the ambient thermal energy of the plasma (which is often an approximate criterion for the validity of quasi-linear theory), nonlinear effects, such as ion-wave trapping, seem to be important. In the theoretical and numerical work by Lampe *et al.* [64], the non-linear regime considering electron magnetization was found to reduce to the linear regime with unmagnetized electrons. The large amplitude coherent waves cause electron scattering that smears out the electron cyclotron resonances, and leaves the plasma with an ion acoustic character. Since experimental measurements in

HTs have observed linear dispersion relations consistent with such ion acoustic instabilities [80, 67], it appears that this result is valid. Although the quasi-linear model may not be complete, at present it appears to give very reasonable accuracy, and agrees with multiple, independent PIC simulations [111, 77, 140].

The fact that the nominal simulation case has been simulated by 6 other research groups around the world, all obtaining similar results as seen in chapter 3, increases the confidence in the results obtained in this chapter. They are also in agreement with previous axial-azimuthal PIC simulations using the same configuration and imposed ionization profile [140], and similar to fully self-consistent simulations with no artificial ionization profile [111] (where good agreement with quasi-linear theory was also observed). Moreover, the instability fluctuation levels in the simulations now appear to be comparable with experimental measurements [67, 215]. Further work is however needed to perform a more rigorous comparison, and to correctly account in the experiments for the observed spatial variation of these fluctuation levels in the simulations.

It has been observed that the nature of the predicted instabilities, and the resulting distribution of energy across different length scales, could be modified for longer azimuthal simulation lengths leading to an inverse energy cascade [71, 72, 81]. Although such a cascade has not been observed in recent axial-azimuthal simulations [219] similar to those used here, the role of the azimuthal length, and its impact, if any, on the electron drift instability needs to be clarified, and more insights will be given later in section 6.3.2. The fact that the model is 2D and not 3D also precludes certain phenomena, such as electron loss on the radial thruster walls, and intense secondary electron emission. However, aside from any possible issues associated with energy cascades, we think that the form of the quasi-linear model should still be valid in 3D since even though the electron distribution function may change, the model is anyway written in terms of the distribution function (which is to say that the enhanced electron transport will be naturally and automatically modified). Even though previous work with a self-consistent ionization source term [86, 217] has shown that the quasi-linear theory remains valid, at least during the rising part of the discharge current during a breathing mode cycle, the imposed ionization source term used here nonetheless prevents the onset of these breathing mode oscillations; which could affect the growth of azimuthal instabilities during some moments of the discharge. This represents the next logical step in verifying the quasi-linear model, and we will try to bring new insights in the next two chapters.

Chapter 5

Towards self-consistent simulations of Hall thrusters: on the use of vacuum permittivity scaling to simulate the low frequency breathing mode

Even though the simplified benchmark case has the advantage of being fast enough to perform parametric studies and stress-test theoretical developments, it lacks important parts of the HT physics. The strongest simplification lies in the ionization source term being imposed, which preclude the onset of the breathing mode oscillations. Whereas specific collisions can be artificially added, as done in the previous chapter, the neutral density needs to be described self-consistently to capture their actual impact on the discharge behaviour. Hence, for the two last chapters of this manuscript, the collisions (including the ionization) are now self-consistently accounted for, by solving the neutral dynamics.

However, due to the low-frequency character of this instability, the physical time that we need to simulate to capture several Breathing Mode (BM) oscillations is significantly higher than the one of the simplified benchmark case. In addition to the strong variations of the plasma density induced by these oscillations, it makes these simulations very computationally expensive. Hence, the vacuum permittivity has been artificially increased to relax the PIC constraints and speed-up the computation.

The presence of BM oscillations increases significantly the complexity of these self-consistent simulations. Hence, after briefly giving the state-of-art of 2D axial-azimuthal PIC simulations in section 5.1 and describing the numerical model in section 5.2, we will only focus in this chapter on the axial electron transport during a BM oscillation in section 5.3, verifying in the same time if the friction force approximation of chapter 4 is still valid, and quantifying the influence of the artificial scaling technique used. Finally, we will see that the EDI is not the

only instability propagating in the azimuthal direction.

Contents

5.1	Motivation	116
5.2	Numerical model	117
5.2.1	Case description	117
5.2.2	Importance of neutral dynamics and anode ion recombination	121
5.2.3	Cathode model	121
5.3	Axial electron transport during a breathing mode oscillation	123
5.3.1	Case closer to reality ($\alpha_\epsilon = 4$)	123
5.3.2	Influence of vacuum permittivity scaling factor	126
5.3.3	VDF and plasma fluctuations	131
5.3.4	Azimuthal instabilities	138
5.4	Conclusion	141

5.1 Motivation

Adam *et al.* were the first ones to develop a 2D axial-azimuthal PIC code in the framework of HT [66]. As their code was treating self-consistently the neutral dynamics (with variable neutral density and velocity, but a different solver than in *LPPic*), they managed to observe the breathing mode, along with the EDI. However, to speed-up their code, they used an implicit scheme for the electron motion and later, Coche [220] observed that this scheme was inducing an artificial electron cooling when a magnetic field was present. Hence, it is uncertain if the code of Adam was capturing the discharge dynamics in a fully consistent way.

Coche *et al.* decided to use the same code but changing the scheme from implicit to explicit for the electrons [76]. They also observed the breathing mode oscillations and noticed that different waves developed for the increasing and decreasing part of the discharge current. However, because of the PIC stability constraints, they needed to use the vacuum permittivity scaling technique described in section 2.2.3, with a factor of 80. This high scaling factor could have an important damping effect on the EDI growth (due to the growth rate dependence on the vacuum permittivity, as seen in equation 4.19). Moreover, the time step and cell size chosen were not fine enough to resolve λ_d and ω_{pe} , respectively, during a whole BM oscillation and no information was given on the number of particles per cell used. This can be source of error and numerical instabilities [135] which could invalidate any physical analysis performed.

Later, Laffleur *et al.* [111, 86] developed a highly resolved 2D PIC code, without any artificial scaling technique. They managed to characterize the EDI and estimate the associated electron-ion friction force R_{ei} which was seen (similarly

to in Chapter 4) to contribute significantly to the electron anomalous transport. However, due to memory issues, they were only able to study the rising part of a BM oscillation and they considered only the continuity equation for the neutrals. Katz *et al.* [141] decided to focus only on the HT acceleration region for very short physical times (around 10 μs) and they managed to observe that the low-energy ions were playing a role in the axial electron transport. Boeuf and Garrigues [140] (and later, Charoy *et al.* [185]) chose another simplification method and imposed the ionization source term to study the EDI for a steady-state case, as described in chapter 3. Taccogna *et al.* [78] chose to impose the neutral density profile to reach a steady-state, also precluding the BM growth. Hence, for these 5 studies, no interaction between EDI and BM was considered.

Finally, Chernyshev *et al.* [142] have recently used a new implicit scheme [221] that is designed to conserve the energy and they managed to observe the BM oscillations, along with EDI and Gradient-Drift Instabilities (GDI). However, this implicit 2D PIC code has not been verified by any benchmark yet and as the method is novel, further benchmarking with standard methods is needed. Moreover, the charged particle density was artificially reduced by a factor of 50. This scaling method is not well-documented but one can infer from equations 1.9 and 1.10 as decreasing the charge density should have the same impact on λ_d and ω_{pe} than increasing the vacuum permittivity and hence it should impact the EDI in the same way.

All in all, the simulations presented in this chapter (and in chapter 6) are designed to overcome the previously mentioned limitations by tackling the following aspects:

- being performed with a code that has been verified with a 2D benchmark, with a simulation case close to a real HT configuration.
- resolving properly λ_d and ω_{pe} throughout the whole BM oscillations. Also, the number of macroparticles per cell is specified and is higher than 200 in average.
- capturing several BM oscillations.
- using a low vacuum permittivity scaling factor and analyzing the impact of this scaling factor on the discharge behaviour.

5.2 Numerical model

5.2.1 Case description

The simulation domain is close to the one used for the two previous chapters, with a 2D Cartesian mesh shown in figure 5.1. However, the full 2.5 cm of the channel length are now included, and 1.5 cm of the plume are also simulated, which gives a total axial domain length of $L_x = 4$ cm. The imposed potential at the anode ($x = 0$ cm) is 300 V while the one at the cathode ($x = L_x = 4$ cm) is 0 V. Again, to speed-up the simulations, only a small part of the HT

azimuthal direction is simulated ($L_y = 1$ cm) and periodic boundary conditions are imposed in this direction. The influence of this L_y on the discharge behaviour will later be discussed in the next chapter (section 6.2). The axial profile of the imposed radial magnetic field is displayed in figure 5.2 and the position of its maximum corresponds to the exit plane of the thruster. This time however, electron-neutral and ion-neutral collisions are taken into account (as described in section 2.1.1) and the ionization is calculated self-consistently, thanks to the neutral dynamics solver (described in section 2.3). The initial neutral density axial profile is displayed in figure 5.2 and the initial neutral velocity is considered uniform and equal to $200 \text{ m} \cdot \text{s}^{-1}$. The neutral temperature is kept constant at 640 K throughout the simulation by adding a thermal relaxation source term to the energy equation. The neutral mass flow rate at the anode is fixed at $\dot{m} = 5 \text{ mg} \cdot \text{s}^{-1}$ and the ions leaving the domain at the anode are recombined in neutral atoms. These parameters, along with the radial magnetic field profile, are similar to those used by Lafleur *et al* [111] in which only the neutral continuity equation was solved and a constant axial velocity of the neutral gas was then assumed.

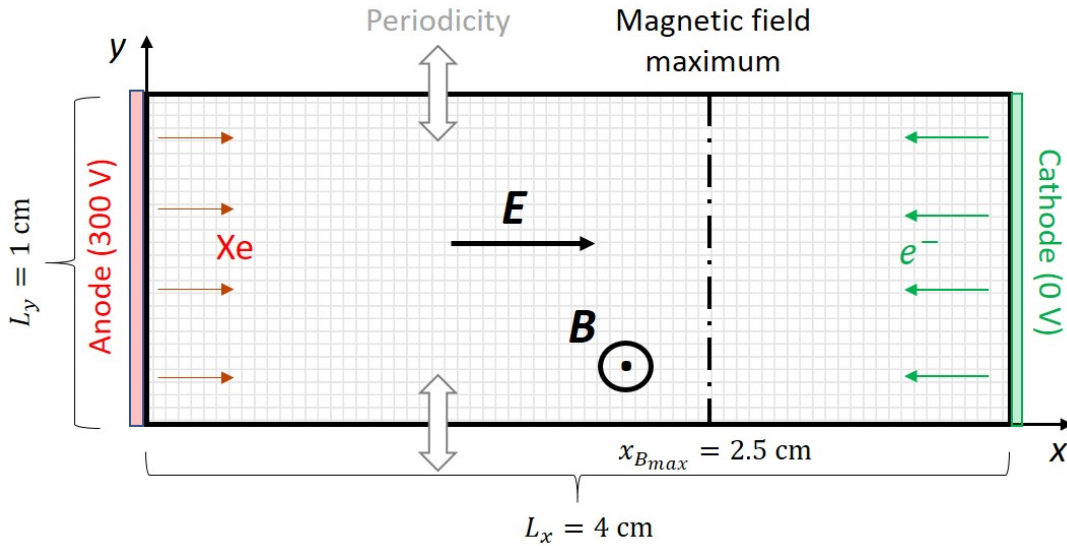


Figure 5.1 – Simulation domain. x is the axial direction, y the (periodic) azimuthal direction. Black pointed dashed line ($x_{B_{max}}=2.5$ cm): position of maximum radial magnetic field. Xenon atoms are injected at the anode and electrons are emitted from the cathode.

Because of the BM oscillations, the plasma density can vary by almost a factor of 5 (from $n_e \approx 5 \times 10^{17} \text{ m}^{-3}$ to $n_e \approx 2.5 \times 10^{18} \text{ m}^{-3}$). When the plasma density is maximum, the electron temperature is around 20 eV. Hence, to comply with the PIC stability criteria of equations 2.15, the time step Δt and the cell size Δx has been fixed to 2×10^{-12} s and 2×10^{-5} m, respectively. It gives a computational mesh of $N_x=2000$ cells in the axial direction and $N_y=512$ cells in the azimuthal direction. At initialisation, the particles are loaded uniformly with a density of

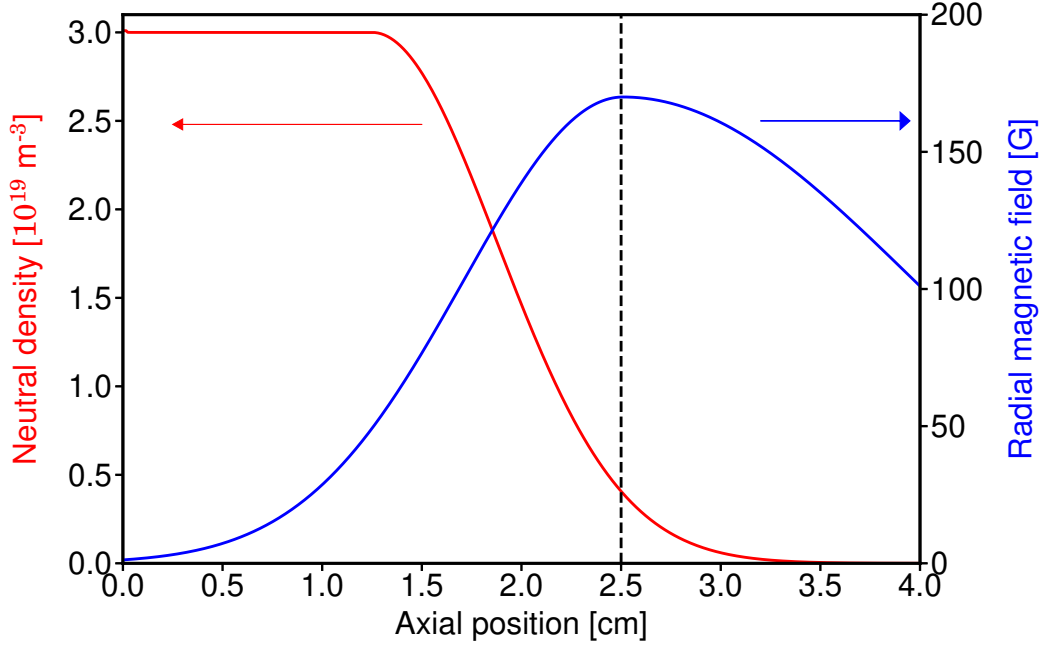


Figure 5.2 – Axial profiles of the imposed radial magnetic field and initial neutral density. Dashed line corresponds to the position of maximum radial magnetic field.

$n_{p,ini} = 10^{18} \text{ m}^{-3}$ and the initial number of macroparticles per cell has been fixed at 400 to reduce numerical noise. As the BM frequency is around 20 kHz, the simulation cases have been run to at least $150 \mu\text{s}$ to capture several periods of the BM oscillations. Finally, the diagnostics have been averaged and outputted every $N_{average} = 5000$ time steps, except for the case $\alpha_\epsilon = 4$ for which $N_{average} = 10000$. The main simulation parameters are summarized in the fourth column of Table 2.1.

The electron emission at the cathode needed to sustain the discharge is treated differently than in the last two chapters, in which a current equality into the whole system was considered. Indeed, as mentioned already in previous work [139, 111], this cathode model appears to create a cathode sheath and violate the current conservation during any transient state. Hence, electrons were injected according to a quasi-neutrality assumption, as described in section 2.4. The influence of this cathode model is briefly discussed in section 5.2.3.

In this chapter, we first present 4 cases with different values of the vacuum permittivity scaling factor: $\alpha_\epsilon = 4, 16, 64$ and 256 . Hence, the time step and cell size has been increased by a corresponding factor of $\sqrt{\alpha_\epsilon}$ (while keeping the same axial and azimuthal length) which reduces significantly the computational time. Despite this scaling technique, the simulation cases remain very computationally expensive, as seen on table 5.1. The cases of section 6.2 are also displayed, for which the azimuthal length L_y has been varied with a scaling factor of $\alpha_\epsilon = 64$.

To ease the comparison, the computational times correspond to the first 150 μs of simulation, but often, longer times have been simulated to be able to capture steady BM oscillations. Moreover, one can wonder why a factor 4 for α_ϵ was used between each case. It is due to the fact that the HYPRE library used to solve the Poisson equation requires a number of cells N_y equal to a power of 2 in the periodic azimuthal length. Hence, to keep L_y constant, N_y can only be increased or decreased by a factor of 2, which gives a factor of 4 for α_ϵ (as Δx will vary proportionally to $\sqrt{\alpha_\epsilon}$).

Case	α_ϵ	L_y (cm)	N_{CPU}	Time (days)	CPU hours (k)	$N_{part,max}$	Simulated time ([μs])
1	4	1	1260	60	1800	2×10^8	150
2	16	1	840	7	140	6×10^7	250
3	64	1	360	5	45	1×10^7	400
4	256	1	96	1	2.3	3×10^6	400
5	64	2	700	5	90	2×10^7	350
6	64	4	1120	9	240	1×10^8	425
7	64	8	1680	12	480	3×10^8	300

Table 5.1 – Typical computational requirements to simulate 150 μs of physical time. The total simulated time is indicated in the last column.

We can see that currently, even though we would like to show results for the real case $\alpha_\epsilon = 1$, it would require both a very long time (probably around 1 year on 1500 CPUs) and a lot of CPU memory (to store around 10^9 macroparticles), which is not possible with the current code version. To speed-up the computation and at the same time reduce the number of macroparticles, one can use a merging-splitting algorithm to make the number of particles per cell constant independently on the time and position. However, we have seen before in section 2.2.3 that such an algorithm, as well as impacting the distribution function (which could affect the electron transport, as seen in chapter 4), is quite cumbersome to implement. Hence, we do not make use of any merging-splitting algorithm, and we needed to use here at least $\alpha_\epsilon = 4$.

Finally, it is important to remind that in a real HT, a RLC circuit is used between the power supply and the thruster to filter the low-frequency BM oscillations [222, 44, 45], as they are known to damage the power supply and decrease the thruster efficiency and lifetime [23]. Due to the complexity of the implementation, which has never been done before in a HT 2D PIC code, this circuit has not yet been properly included (some preliminary tests have been performed) and hence, the observed BM oscillations will have a higher amplitude than in a real case. Moreover, no fake-radial dimension, as described in section 2.5.1, is included here, and they were also expected to damp these oscillations by removing high-energy charged particles. These two limitations of our model should be kept in mind throughout this chapter and the following.

5.2.2 Importance of neutral dynamics and anode ion recombination

Initially, only the continuity equation for the neutral species was solved, similarly to what has been done in Lafleur *et al.* [111, 86]. However, experimental diagnostics have shown that the neutral velocity is not constant axially, but increases by a factor of 2 to 3 [169]. If a constant neutral velocity of $500 \text{ m} \cdot \text{s}^{-1}$ was used, BM oscillations were developing but for $200 \text{ m} \cdot \text{s}^{-1}$, the discharge was extinguishing after an initial transient. Whereas Lafleur *et al.* [111, 86] were only focusing on this initial transient, we wanted here to capture several BM oscillations and hence, the model for the neutral dynamics has been improved by considering the full Euler system, as described in section 2.3. Quick comparisons have been performed between this new solver and the old one and it appeared that this variable neutral velocity was playing an important role in the discharge behaviour, especially in the onset of BM oscillations.

Moreover, a first set of simulations has been performed without accounting for the anode ion recombination, and some preliminary results were presented in [217]. However, it appeared that the ionization zone was periodically moving towards the anode (due to the BM oscillations), hence significantly decreasing the neutral density there. Because the mass flow rate and temperature are imposed at the anode boundary condition for the neutral dynamics (as described in section 2.3), the neutral velocity was increasing and the neutral density was permanently decreasing, in absence of any additional source term. For this reason, we decided to account for the recombination in neutral atoms of the ions which leave the simulation domain at the anode and it appeared that they were contributing to around 10% of the total neutral mass flow rate (depending on α_ϵ), as seen in figure 5.3. This ion back-flow is due to the anodic potential drop which is higher when α_ϵ is lower.

All the simulations have hence been run again and the results in this chapter and the following have been obtained with this ion anode recombination, unless otherwise stated. However, because the initial state has been chosen arbitrarily, the transient can be abrupt (i.e. the discharge current can peak to very high values, leading to very high plasma densities) and the required memory to store all the particles can be very high (up to 10^9 macroparticles in total). It happens for the case $\alpha_\epsilon = 4$ (only if the anode ion recombination is included) and for this reason, we decided to use a smoother initial state by using the profiles for the plasma and neutral densities obtained at steady-state for the case $\alpha_\epsilon = 16$.

5.2.3 Cathode model

The different cathode models, initially described in section 2.4, were later tested with the simplified benchmark case and the results were presented in section 3.6. We have seen that the discharge behaviour was significantly affected by the chosen cathode model and it was important to check if this trend was similar for self-consistent simulations. Because the simulation times are quite heavy,

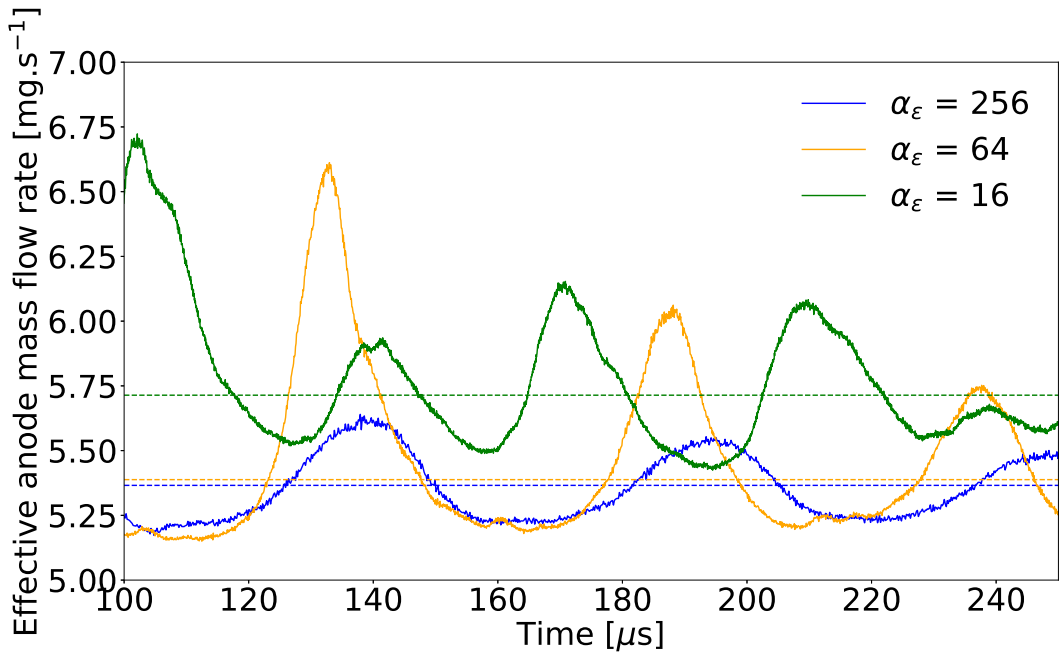


Figure 5.3 – Time evolution (from $100 \mu\text{s}$) of the effective anode mass flow rate Q for different values of the vacuum permittivity scaling factor α_ϵ . The dashed lines corresponds to the averages. Q_{ini} has been set to $\dot{m}=5 \text{ mg}\cdot\text{s}^{-1}$.

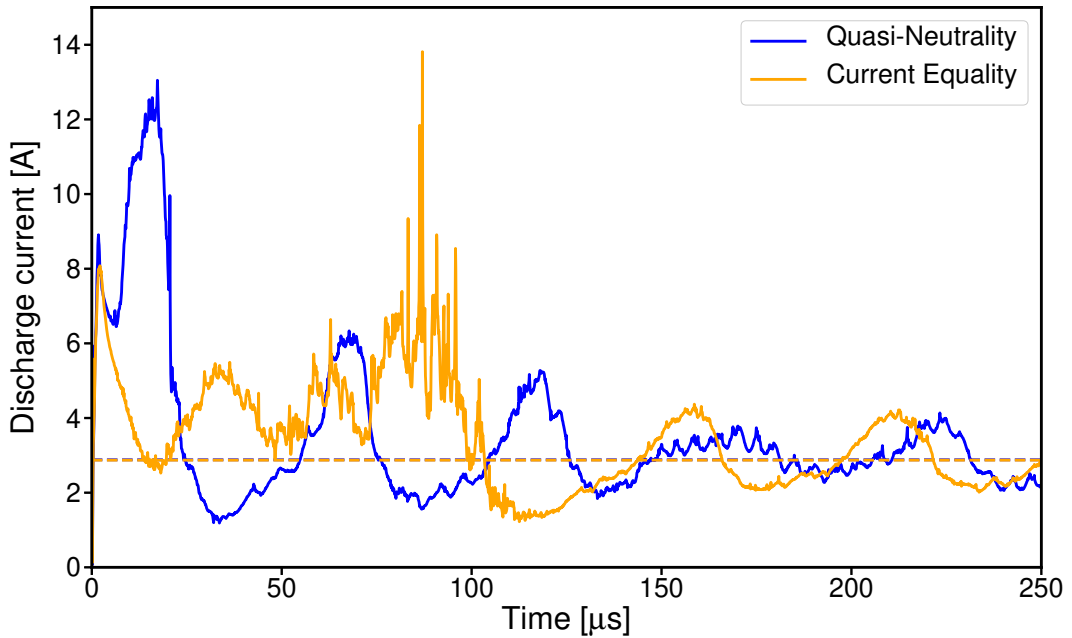


Figure 5.4 – Time evolution of discharge current for two different cathode models, with $\alpha_\epsilon=64$ (and no anode ion recombination). The dashed horizontal lines (overlapped here) correspond to the mean value at steady state.

only one comparison has been performed here: instead of using the quasi-neutral (QN) model (as in the rest of the chapter), a current equality (CE) condition was used to infer the number of electrons to inject at each time step. Because this condition is now applied at the right-hand-side domain boundary (similarly to Coche *et al.* [76] but differently than the simplified case of chapters 3 and 4), the complete condition given by equation 2.46 is used. The case has been performed with a scaling factor $\alpha_\epsilon = 64$ and an azimuthal length $L_y = 1$ cm, with no ion recombination at the anode.

We can see in figure 5.4 that while the transient state for the CE cathode model is very different, the plasma seems to reach a steady-state that looks quite similar to the one with the QN cathode model. The main effect of the CE model is to induce a big cathodic sheath that does not seem to affect the global discharge behaviour of the plasma. It could have been expected because when the QN model is used, the current equality of equation 2.46 has been observed to be satisfied at each time (not shown here). More work is however still needed to study if the injected electron temperature affect the HT discharge behaviour and perform similar tests for different values of α_ϵ .

5.3 Axial electron transport during a breathing mode oscillation

First, we will study in this section how the axial electron transport evolves throughout a BM oscillation. The behaviour for the case closer to reality $\alpha_\epsilon = 4$ is described before analysing the influence of this vacuum permittivity scaling factor on the transport.

5.3.1 Case closer to reality ($\alpha_\epsilon = 4$)

Because this case is the most costly in terms of computational time, it has only been run until 150 μs . The time evolution of the discharge current is displayed in figure 5.5. We can notice that we obtained a smooth transient thanks to the initialization from the steady state of the case with $\alpha_\epsilon = 16$. Even though the BM oscillations have an irregular shape (because of the turbulent and chaotic nature of the numerous local oscillatory phenomena), we tried to use a representative peak of discharge current to analyse the discharge behaviour during a BM oscillation. The same analysis was performed on the first BM oscillation to ensure the reproducibility of the results and we also retrieved similar trends for the axial electron transport to when the anode ion recombination was not taken into account [217].

Electron momentum terms

As done previously in section 4.2.1 for the simplified case, the different terms of the azimuthal electron momentum equation have been computed at four different

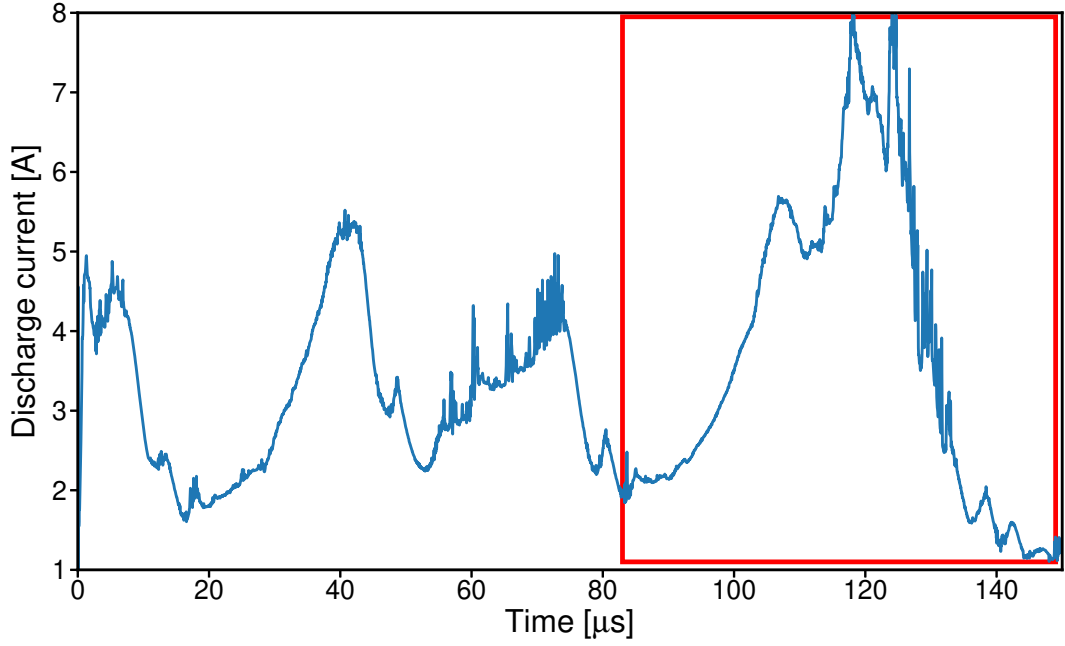


Figure 5.5 – $\alpha_\epsilon = 4$: Time evolution of discharge current. Red rectangle corresponds to the BM oscillation analysed in this section.

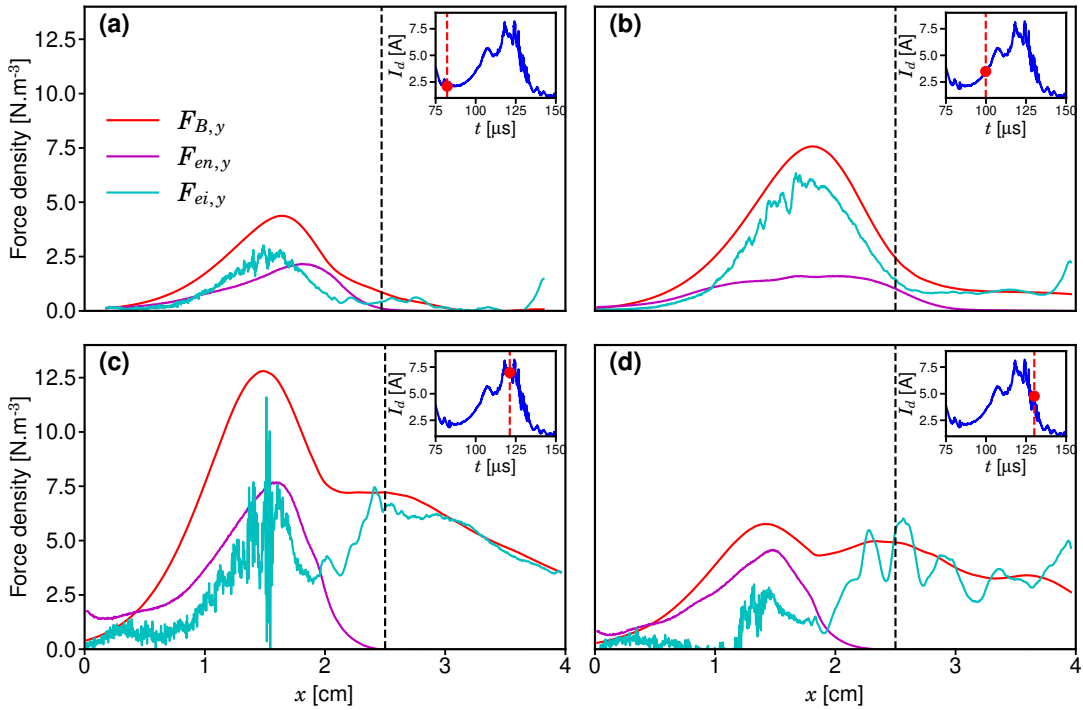


Figure 5.6 – $\alpha_\epsilon = 4$: Azimuthal terms of electron momentum conservation equation 4.2 for four moments of a breathing mode oscillation: minimum (a), increase (b), maximum (c) and decrease (d). The red line corresponds to the magnetic force term $F_{B,y} = -qn_e Bv_{e,x}$ related to the axial electron transport. The cyan $F_{ei,y}$ line corresponds to the instability-enhanced drag force on the electrons. The magenta line corresponds to the electron-neutral collision term $F_{en,y}$. Inset: Time evolution of discharge current, red dot indicating the corresponding time.

moments of a BM oscillation. Only the dominant terms are displayed in figure 5.6: the $F_{ei,y}$ term (cyan line) corresponding to the electron-ion friction force, the $F_{en,y}$ term (magenta line) corresponding to the classical electron-neutral collisions and $F_{B,y}$ the magnetic force term. We recall that $F_{B,y} = -qn_e B v_{e,x}$ and hence, this force term is related to the electron axial transport. The reader can refer to equation 4.2 for more details on these force terms. We highlight that, contrary to the simplified benchmark case for which the spatial inertia $F_{in,y}$ and pressure $F_{p,y}$ terms in the azimuthal direction were found relatively large (figure 4.1), these two terms are here compensating each other (and hence they are not shown in the figures).

One can notice that when the discharge current is minimum, in figure 5.6(a), the electron-ion friction force $F_{ei,y}$ and the electron-neutral collisions $F_{en,y}$ contribute equally to the electron axial transport, inside the thruster. However, when the discharge current increases, in figure 5.6(b), the axial electron transport is increasing significantly in the thruster (with a maximum around $x = 1.8$ cm) because the electron-ion friction force is growing and dominates now the classical collision force. This friction-force enhancement is explained by the increased plasma density: the modified ion-acoustic growth rate is related to λ_d^{-3} (equation 4.19), hence it increases when the plasma density is increased. In both cases, the friction force is always dominant in the plume where the electron-neutral collisions are scarce, because the neutral density is strongly depleted. While the plume transport is negligible when the discharge current is minimum, it becomes more important when I_d increases, due to the friction-force contribution (the EDI is convected towards the cathode). One can notice the abrupt increase of $F_{ei,y}$ near the cathode which is only a boundary-induced effect.

When I_d is maximum, in figure 5.6(c), the axial electron transport is maximum and one can notice the significant increase of classical collisions due to the increase of the electron temperature. The friction force is almost the same inside the thruster than during the increasing part of discharge current but it has now reached the same value in the plume. When I_d decreases, in figure 5.6(d), the friction-force decreases first inside the thruster and the plume value is still quite high. One can notice that these two last figures are more noisy than the previous one, as the system is more unstable. The fact that the friction force increases more in the plume has already been observed by Lafleur *et al.* [111, 86] at the discharge current maximum.

Hence, we have shown that, similarly to what was obtained for the simplified benchmark case, the instability-enhanced electron-ion friction force is the main contributor to the electron axial transport. When the discharge current increases, the azimuthal instabilities amplitude grows and it enhances this friction force. Its relative importance to the electron axial transport is then increased compared to the one of classical electron-neutral collisions.

Friction force approximation

Now that we have shown its importance on the electron anomalous transport, it would be very useful to be able to quantify the electron-ion friction force, as done previously in chapter 4 for the simplified benchmark case. The friction force approximation is hence tested at different moments of the BM oscillation (even though the diagnostics are different, we intend to use the same moments as the ones of figure 5.6). We compare the friction force derived from the PIC with the quasi-linear kinetic approximation $R_{ei,quasi-linear}$ (Eq. 4.24), the Maxwellian approximation $R_{ei,maxwellian}$ (Eq. 4.27) and a new derivation $R_{ei,quasi-linear,fft}$ for which we have alleviated one hypothesis which led us to $R_{ei,quasi-linear}$: the azimuthal wave vector is not taken equal to the dominant mode of the modified ion-acoustic DR (Eq. 4.18) any more. Instead, we use a FFT to determine the wavenumber of the dominant azimuthal mode.

First, it appears in figures 5.7(a) and 5.7(b) that for the increasing part of I_d , the theoretical derivation $R_{ei,quasi-linear}$ approximates rather well the PIC friction force, compared to the Maxwellian approximation $R_{ei,maxwellian}$, which again overestimates it. However, the fitting is not perfect (particularly for $x \geq 2$ cm) and hence, we have used the approximation $R_{ei,quasi-linear,fft}$, with no hypothesis on the wavenumber of the dominant azimuthal mode, now directly computed from a FFT. One can notice that a perfect agreement with the PIC values is then observed. Hence, it means that the instability is not perfectly described by the modified ion-acoustic DR for $x \geq 2$ cm, as we will see in section 5.3.4.

If we now look at the decreasing phase of I_d in figures 5.7(c) and 5.7(d), we can see that even though $R_{ei,quasi-linear}$ approximates the PIC data better than the Maxwellian approximation, it under-estimates the friction-force in the plume. We can see that by computing manually the dominant wavenumber ($R_{ei,quasi-linear,fft}$), we obtain a rather good agreement with PIC simulations in the thruster for $x \leq 2$ cm, but it still underestimates the friction force for $x \geq 2$ cm. Hence, it means that in this zone, one of the hypothesis used to derive equation 4.24 might not be valid for this discharge current decreasing part, which was not analysed by Lafleur *et al.* [86]. It seems that the convection of the EDI towards the cathode is not enough to explain the important increase of the friction force in the plume region (more precisely, in the region where $x \geq 2$ cm). In the following, more insights will be given to explain this unexpected behaviour.

5.3.2 Influence of vacuum permittivity scaling factor

Now that we have studied the axial electron transport for the case closer to reality, it is important to wonder to which extent the vacuum permittivity scaling technique is affecting the results obtained. In this perspective, we will compare in this section the results for 4 simulations with $\alpha_\epsilon = 4, 16, 64$ or 256.

First, if we look at the time evolution of the discharge current, in figure 5.8, we can see that its mean value is increasing when the scaling factor is decreased.

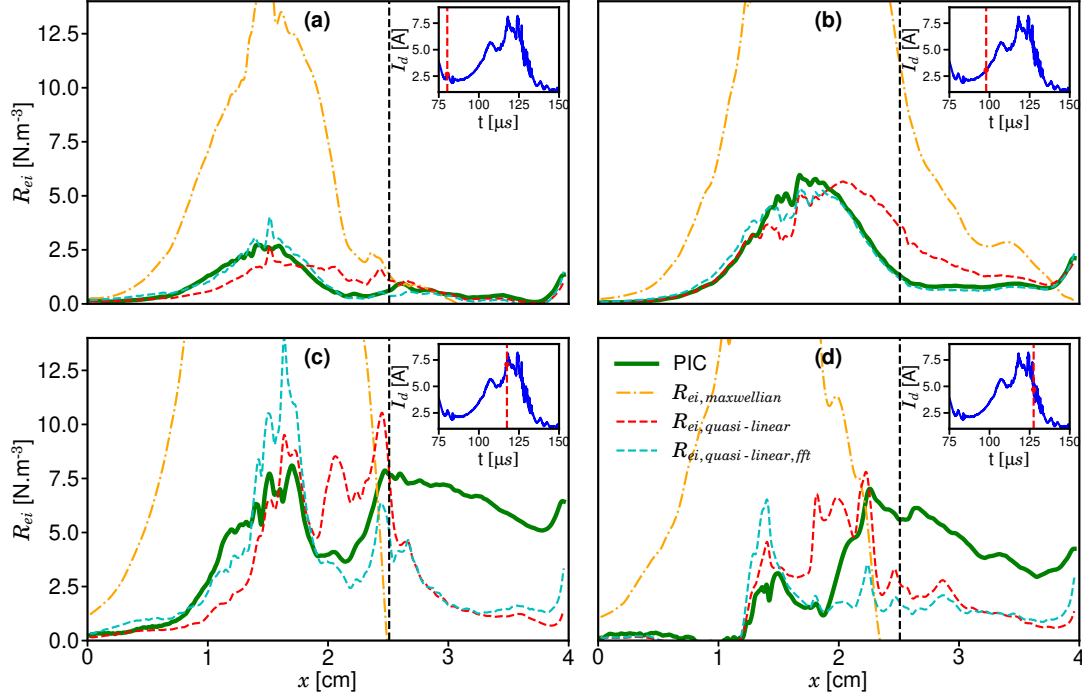


Figure 5.7 – $\alpha_\epsilon = 4$: Friction force approximation at different breathing mode moments: (a) minimum, (b) increase, (c) maximum and (d) decrease. PIC values (green) are compared with the Maxwellian approximation (yellow) and the non-maxwellian approximation with the dominant mode from the ion-acoustic approximation (red) or directly from the FFT (cyan). Inset: Time evolution of discharge current, red dot indicating the corresponding time.

Moreover, the amplitude of discharge current oscillations does not seem to be related to α_ϵ : the discharge current is definitely more noisy for low α_ϵ but the BM amplitude seems to be more impacted by the initial conditions than by the scaling factor. For example, it seems that the BM is strangely damped for the case $\alpha_\epsilon = 16$. We recall that the case $\alpha_\epsilon = 4$ has been initialized more smoothly (with the steady state of the case $\alpha_\epsilon = 16$) which explains the absence of a first abrupt transient peak.

When put in perspective with the results obtained without anode ion recombination of Charoy *et al.* [217], it seems quite difficult to draw definitive conclusions from the mean value and amplitude of the discharge current. More local analysis will hence be performed in the following by focusing on how the discharge behaves throughout one BM oscillation. It is important to keep in mind that the BM oscillations are not perfectly regular, hence we have verified that the results displayed here for one particular oscillation were retrieved for the other ones. The results reproducibility has also been verified for the analysis performed in section 6.2.

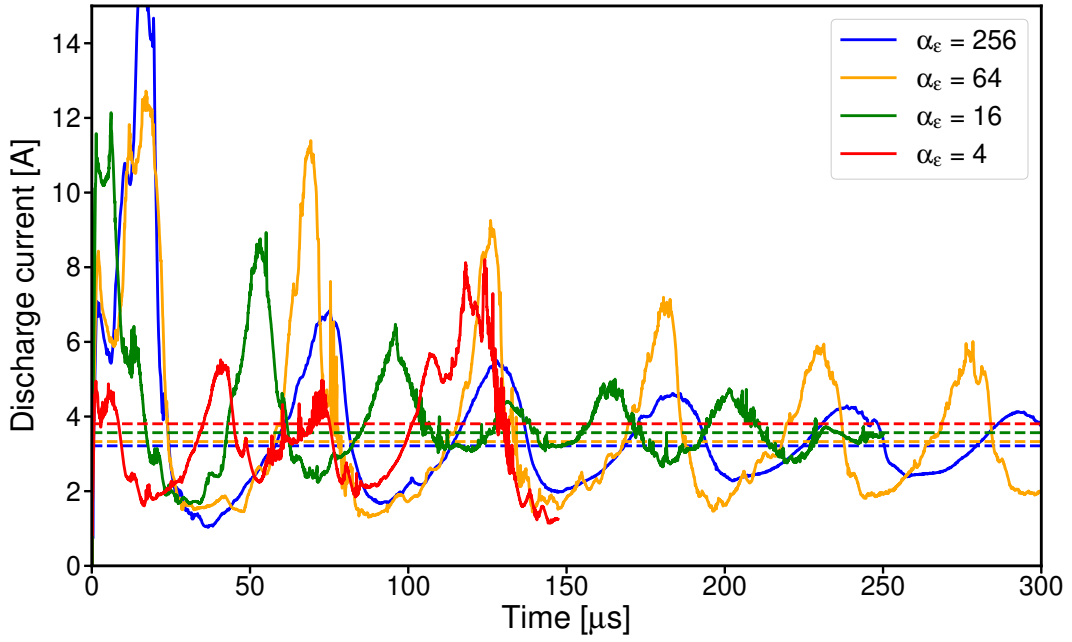


Figure 5.8 – Time evolution of discharge current for 4 values of α_ϵ . The dashed horizontal lines correspond to the mean value at steady state.

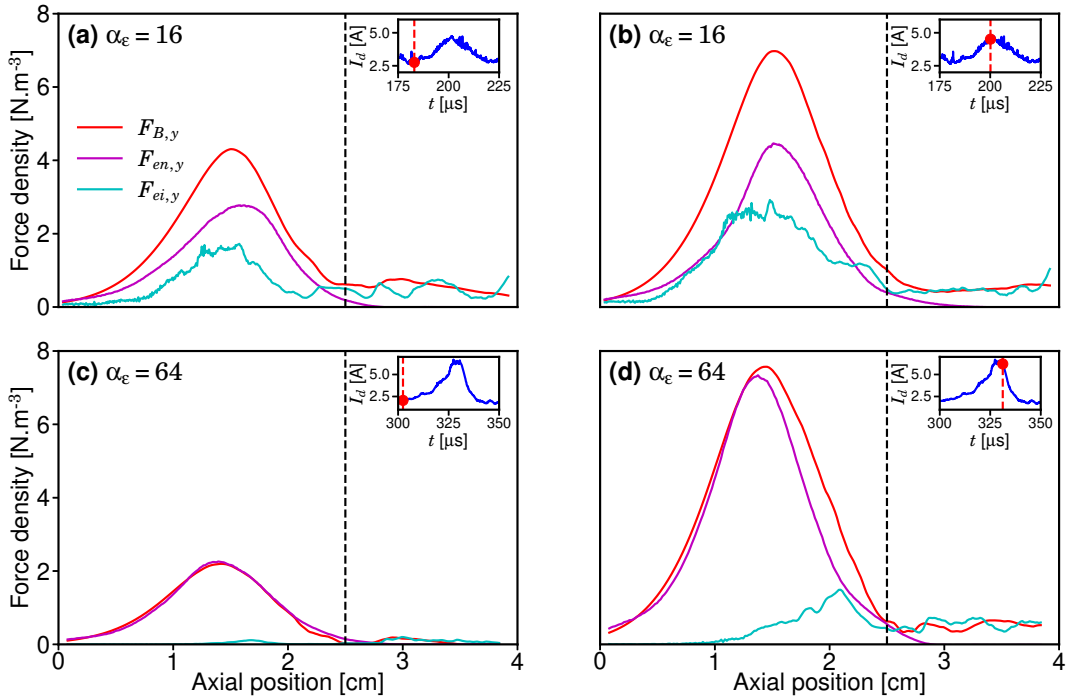


Figure 5.9 – Azimuthal terms of electron momentum conservation equation when the discharge current is minimum (right column) or maximum (left column), for $\alpha_\epsilon=16$ (top row) or $\alpha_\epsilon = 64$ (bottom row). Only the dominant terms contributing to $F_{B,y}$ related to the electron axial transport are displayed: instability-enhanced drag force on the electrons $F_{ei,y}$ (cyan) and electron-neutral collisions force $F_{en,y}$ (magenta). Inset: Time evolution of discharge current, red dot indicating the corresponding time. Vertical black dashed line corresponds to the position of maximum radial magnetic field.

Electron-ion friction force

We know that this scaling technique is impacting the growth rate of the azimuthal waves propagating in the system. Indeed, the modified ion-acoustic growth rate given by equation 4.19 is related to $\epsilon_0^{-3/2}$. Hence, the higher α_ϵ , the more the wave will be damped. In figure 5.9, the axial electron transport main contributions are shown for two values of α_ϵ , when the discharge current is minimum or maximum (which roughly corresponds to the respective minimum or maximum of n_e and T_e).

We can see that, again, the friction force is higher when the discharge current is higher. Moreover, as expected, when α_ϵ is increased, the friction force is damped and the dominant contribution becomes the classical collisions, even when the discharge current is maximum.

If we now average over several BM oscillations, in figure 5.10, we retrieve the expected observation that the use of the vacuum permittivity scaling factor damps the electron-ion friction force and hence, it damps the axial electron transport. One can then conjecture that for a "real" 2D simulation (without scaling), as the EDI will be even stronger, the friction-force (and hence the anomalous electron transport) will be more important. Finally, we can link this observation to the fact that the discharge current mean value (figure 5.8) was higher for lower α_ϵ : when the axial electron transport is more important, the discharge current is increased.

Axial profiles of plasma parameters

In figure 5.11, some plasma parameters have been averaged over several BM oscillations and their axial profiles are displayed for different values of α_ϵ . First, we notice that the plasma density along with the electron temperatures are higher when α_ϵ is decreased. The increase of electron temperature is related to the axial electron current which is increased when α_ϵ is low (more anomalous transport, as we have seen before): the Joule heating $\mathbf{J} \cdot \mathbf{E}$ is then enhanced and T_e increases. This might also explain why n_e is higher, due to an enhanced ionization. The azimuthal ion temperature is also increased when α_ϵ is lower, which might be due to the fact that the electron-ion friction force is larger and therefore, ions take more energy from electrons.

Independently to any α_ϵ comparison, it is also interesting to notice that the electron temperatures are highly anisotropic, with an axial temperature higher than the azimuthal one. Moreover, the azimuthal ion temperature $T_{i,y}$ is also enhanced compared to the initial value of 0.05 eV: the instability is causing a heating, predicted by the kinetic theory [85] and already observed in [111]. Finally, the overlap and axial position of the density and axial electric field profiles are similar to what is expected in HT discharges.

Let us look now at the electron momentum terms, also averaged over several BM oscillations. Unfortunately, this diagnostic is time-consuming and hence it

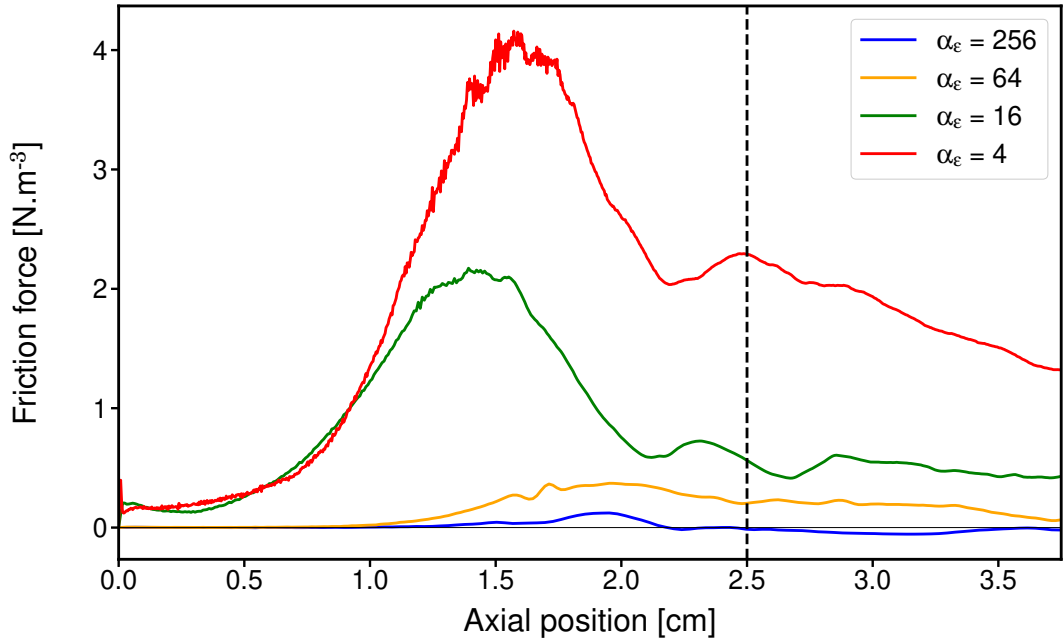


Figure 5.10 – Axial profiles of electron-ion friction force averaged over several breathing mode cycles, for different values of α_ϵ . Vertical black dashed line corresponds to the position of maximum radial magnetic field.

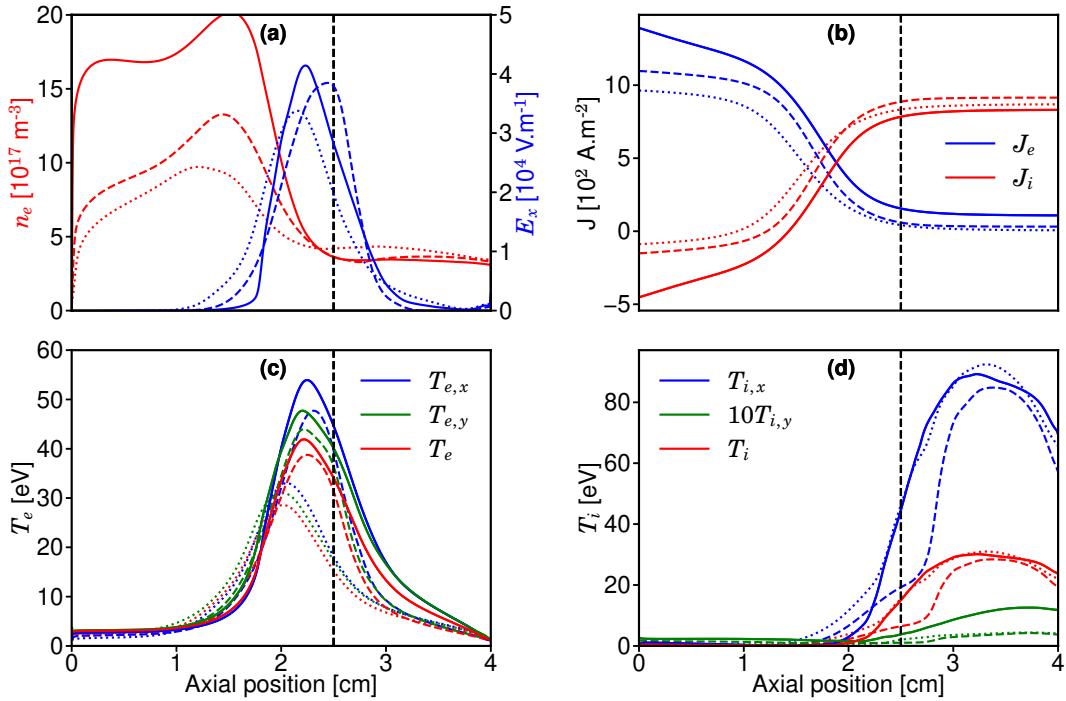


Figure 5.11 – Axial profiles of some plasma parameters (averaged over several BM oscillations and azimuthally) for $\alpha_\epsilon = 4$ (solid line), $\alpha_\epsilon = 16$ (dashed line) and $\alpha_\epsilon = 64$ (dotted line). (a): Axial electric field (blue) and electron density (red). (b): electron (blue) and ion (red) axial current densities. (c): axial (blue), azimuthal (green) and total (red) electron temperatures. (d): axial (blue), azimuthal (green) and total (red) ion temperatures.

has not been used every $N_{average}$. However, if we average over enough samples, it still gives a good overview of what terms are contributing to the axial transport over several BM oscillations. As usual, only the dominant terms have been displayed in figure 5.12. First, one can notice that, as observed before and expected, the more α_ϵ is decreased, the more the friction force contribution is important. However, inside the thruster, the classical collisions also contribute significantly to the transport. Hence, even though the electron-ion friction force $F_{ei,y}$ increases by almost a factor 50 when α_ϵ is decreased from 256 to 4, the overall axial electron transport $F_{B,y}$ increases only by around 50%. This is not the case in the plume in which the friction force is the only contributor to the axial electron transport which is hence significantly increased for low α_ϵ . One can notice the sign inversion for the magnetic force term $F_{B,y}$ in the case $\alpha_\epsilon = 256$ which is due to a poorly resolved time average (we can see in figure 5.11(b) that $v_{e,x}$ is always negative).

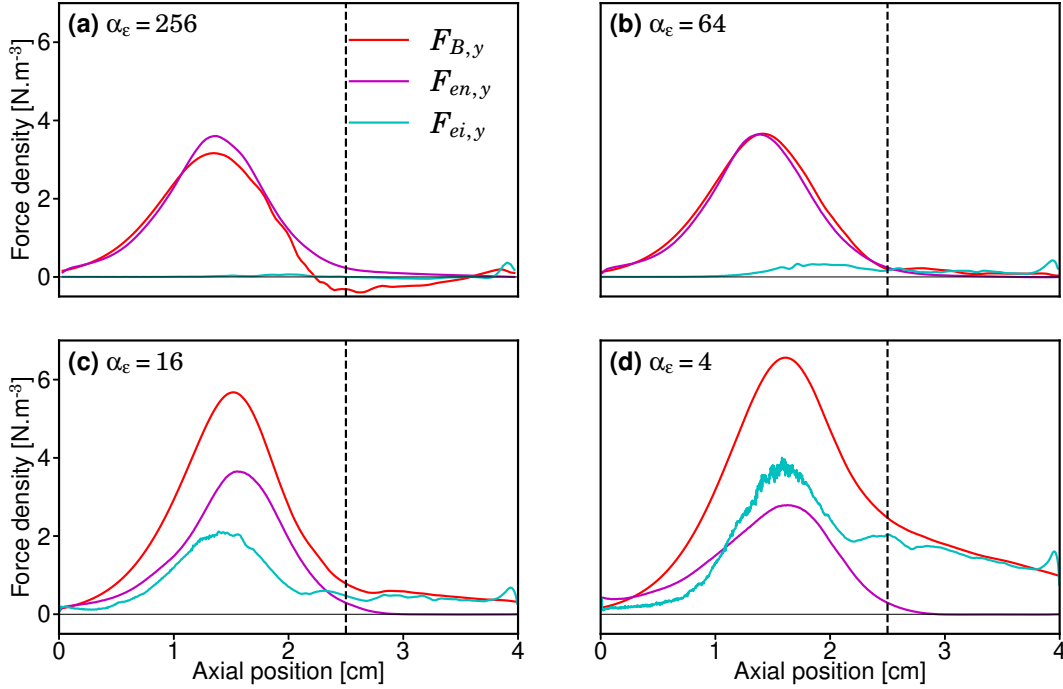


Figure 5.12 – Azimuthal electron momentum terms averaged over several BM oscillations, for different values of α_ϵ . The red line corresponds to $F_{B,y} = -qn_e Bv_{e,x}$, related to the axial electron transport. The cyan $F_{ei,y}$ line corresponds to the instability-enhanced drag force on the electrons. The magenta line corresponds to the electron-neutral collision term $F_{en,y}$.

5.3.3 VDF and plasma fluctuations

Because the axial electron transport, via the electron-ion friction force, is related to the distribution functions and the azimuthal electric field fluctuations, we

will study in this section how they behave during a BM oscillation and depending on α_ϵ .

EVDF

The EVDFs for different axial positions and scaling factors are displayed when I_d increases (figure 5.13) and when I_d decreases (figure 5.14). As observed previously [86], the azimuthal EVDFs are far from a Maxwellian with a positive mean velocity near the exit plane, where the azimuthal electron drift velocity is higher.

According to equation 4.24, the electron-ion friction force should be proportional to the derivative of the azimuthal EVDF at null-velocity. It is interesting to notice that when α_ϵ is decreased, the peak of the azimuthal EVDF seems to be shifted towards a null value, which decreases this derivative. Hence, this effect is supposed to reduce the friction force for low α_ϵ , which is the contrary of what was observed above (the friction force tends to increase with decreasing α_ϵ). It means that the increase of wave energy (when α_ϵ is decreased) is strong enough to compensate this effect and make the friction force increase.

Moreover, we observe a high-velocity tail for the azimuthal EVDF at $x = 1$ cm (more pronounced when I_d increases) that disappears when α_ϵ is lower. This is related to the axial profile of azimuthal velocity that is more peaked near the thruster exit plane for low α_ϵ , with hence a lower azimuthal velocity near the anode. We could have inferred this behaviour by looking at the axial electric field profile (figure 5.11) which goes abruptly to zero near the anode for low α_ϵ .

IVDF

The IVDFs for different axial positions and scaling factors are displayed when I_d increases (figure 5.15) and when I_d decreases (figure 5.16). Before comparing between the different cases, one can notice that we retrieve here the expected behaviour for the ions in a HT: they are created in the ionization zone (between $x = 1$ cm and $x = 2$ cm) and then, their axial velocity increases while they go through the acceleration zone. The main beam of ions reaches a velocity of around $20 \text{ km} \cdot \text{s}^{-1}$ in the plume, as expected with the imposed potential difference of 300 V. Moreover, we can also see that while the axial and azimuthal ion velocities are quite similar near the anode, the ion axial velocities increase up to one order of magnitude higher than their azimuthal velocities in the plume.

If we study now the behaviour depending on α_ϵ , we can first notice that when this factor is decreased, the axial velocity of the ions near the anode is more and more directed towards the anode. It can also be retrieved on the ion anodic current which is higher when α_ϵ is small, as seen in figure 5.11(b). It echoes with what we observed previously: there are more ions that hit the anode boundary when α_ϵ is low and hence, it is important to consider their recombination in neutral atoms. Moreover, we can see in figure 5.16 that when the discharge current is decreasing (and also in a smaller extent, when the discharge current is increasing), low-energy ions are created in the plume for all the cases except $\alpha_\epsilon =$

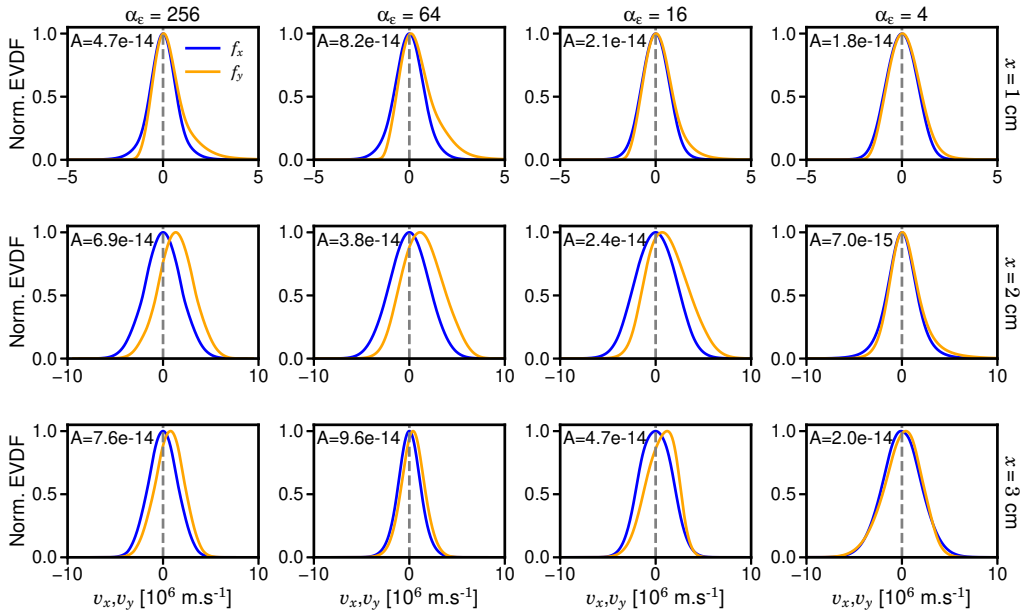


Figure 5.13 – Axial (blue) and azimuthal (orange) EVDF for 3 axial positions (rows) and for 4 values of α_ϵ (columns) when I_d increases. On the top left, the value of the azimuthal EVDF derivative at null-velocity (named A) is displayed. Careful, the x-axis range has been adapted for the best display.

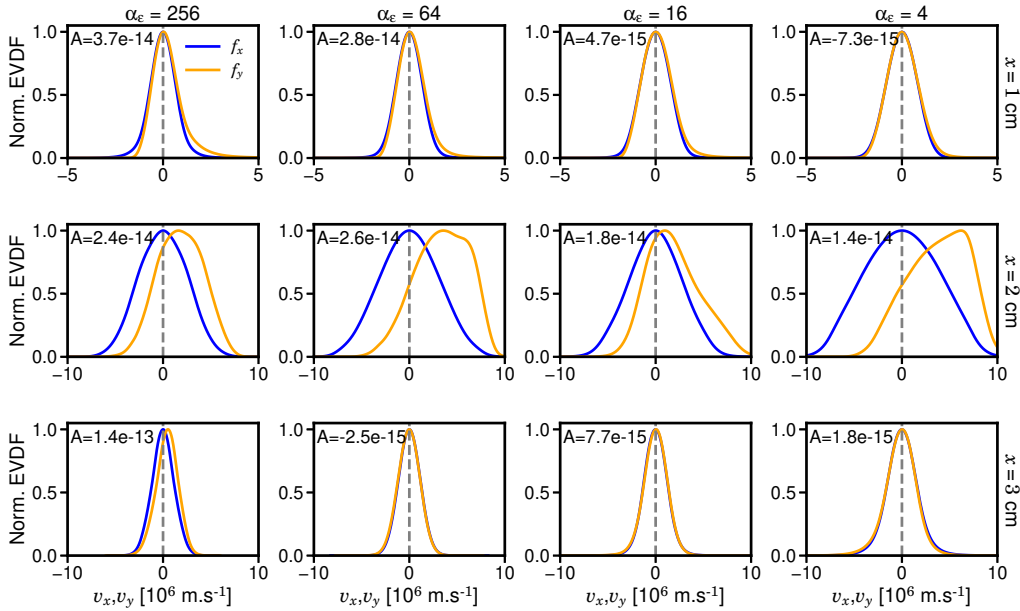


Figure 5.14 – Axial (blue) and azimuthal (orange) EVDF for 3 axial positions (rows) and for 4 values of α_ϵ (columns) when I_d decreases. On the top left, the value of the azimuthal EVDF derivative at null-velocity (named A) is displayed. Careful, the x-axis range has been adapted for the best display.

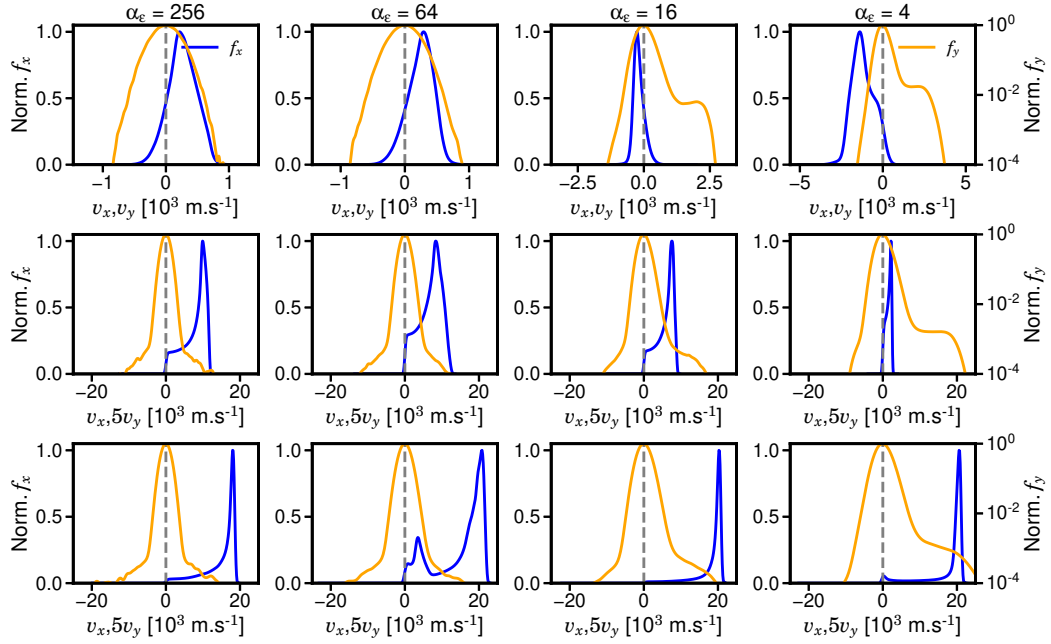


Figure 5.15 – Axial (blue) and azimuthal (orange) IVDF for 3 axial positions (rows) and for 4 values of α_ϵ (columns) when I_d increases. Top row: $x = 1$ cm, middle row: $x = 2$ cm and bottom row: $x = 3$ cm. Careful, the x-axis range has been adapted and the azimuthal IVDF y-axis has been put in log-scale for the best display.

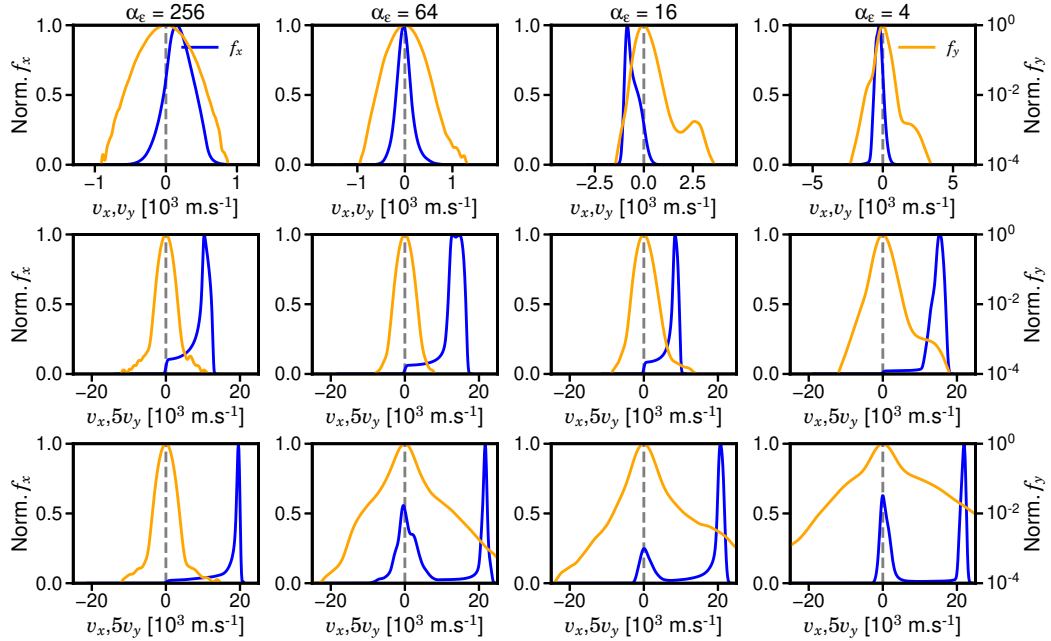


Figure 5.16 – Axial (blue) and azimuthal (orange) IVDF for 3 axial positions (rows) and for 4 values of α_ϵ (columns) when I_d decreases. Top row: $x = 1$ cm, middle row: $x = 2$ cm and bottom row: $x = 3$ cm. Careful, the x-axis range has been adapted and the azimuthal IVDF y-axis has been put in log-scale for the best display.

256. We will see later in section 6.1.4 that these ions are related to the so-called ion-transit time instabilities. It is not clear yet how they are impacting the axial electron transport.

Looking now at the azimuthal IVDF, we can observe that for both I_d phases, there are some trapped ions, similarly to what was observed previously in [111]. This trapping is not seen for high α_e because the instability does not have time to grow enough before being convected away (smaller growth rate). The trapping velocity is around $2.5 \text{ km} \cdot \text{s}^{-1}$ which corresponds approximately to the phase velocity of the EDI wave. The behaviour at $x = 3 \text{ cm}$ when I_d decreases is still not understood, with a significant increase of the number of ions with a higher azimuthal velocity.

Plasma fluctuations

In figure 5.17, the time evolutions of relevant plasma fluctuations (azimuthal electric field $\langle \delta E_y \rangle$, normalized electron density $\frac{\langle \delta n_e \rangle}{n_e}$ and normalized plasma potential $\frac{\langle \delta \phi \rangle}{T_e}$), along with the one of the axial electric field E_x , for the case $\alpha_e = 4$ are shown.

If we analyse first the azimuthal electric field fluctuations, we can see that at first glance, they are following the same trend as the discharge current: the wave is growing when the discharge current increases. However, we can distinguish here three different zones, delimited by the axial location at which the ion axial velocity is changing sign (green curve) and the axial location of the ion sonic point, i.e. where $v_{ix} = c_s$ (red curve). We can see that when I_d increases, the fluctuations of E_y are mostly located upstream of the ion sonic point. The wave seems to originate near the position of null ion axial velocity (which corresponds approximately to the zone where the plasma density is maximum, i.e. where the EDI growth rate is expected to be maximum) and propagates either towards the anode or towards the cathode, with a velocity close to the ion sound speed c_s : these EDI are ion-acoustic in nature, which will be confirmed in the next subsection. Moreover, we can notice that when the ions become supersonic, the wave seems to be strongly damped for the increasing I_d phase, but for the decreasing I_d phase, the fluctuations downstream of this sonic point are stronger, with no axial convection. It echoes with what we observed for the electron-ion friction force in figure 5.6: there is a change of behaviour for the wave at the sonic point: upstream the EDI has a modified ion-acoustic behaviour and then it is convected downstream with a damping when I_d increases, and an enhancement when I_d decreases. These observations are retrieved to a lesser extent on the normalized electron density and plasma potential fluctuations.

Furthermore, it is interesting to look at the evolution of the axial electric field: first, we retrieve an expected behaviour that the position of its maximum is moving axially throughout a BM oscillation, towards the cathode when I_d increases and towards the anode when I_d decreases. Also, we can notice that when the plume stationary wave for the azimuthal electric field is important (i.e.

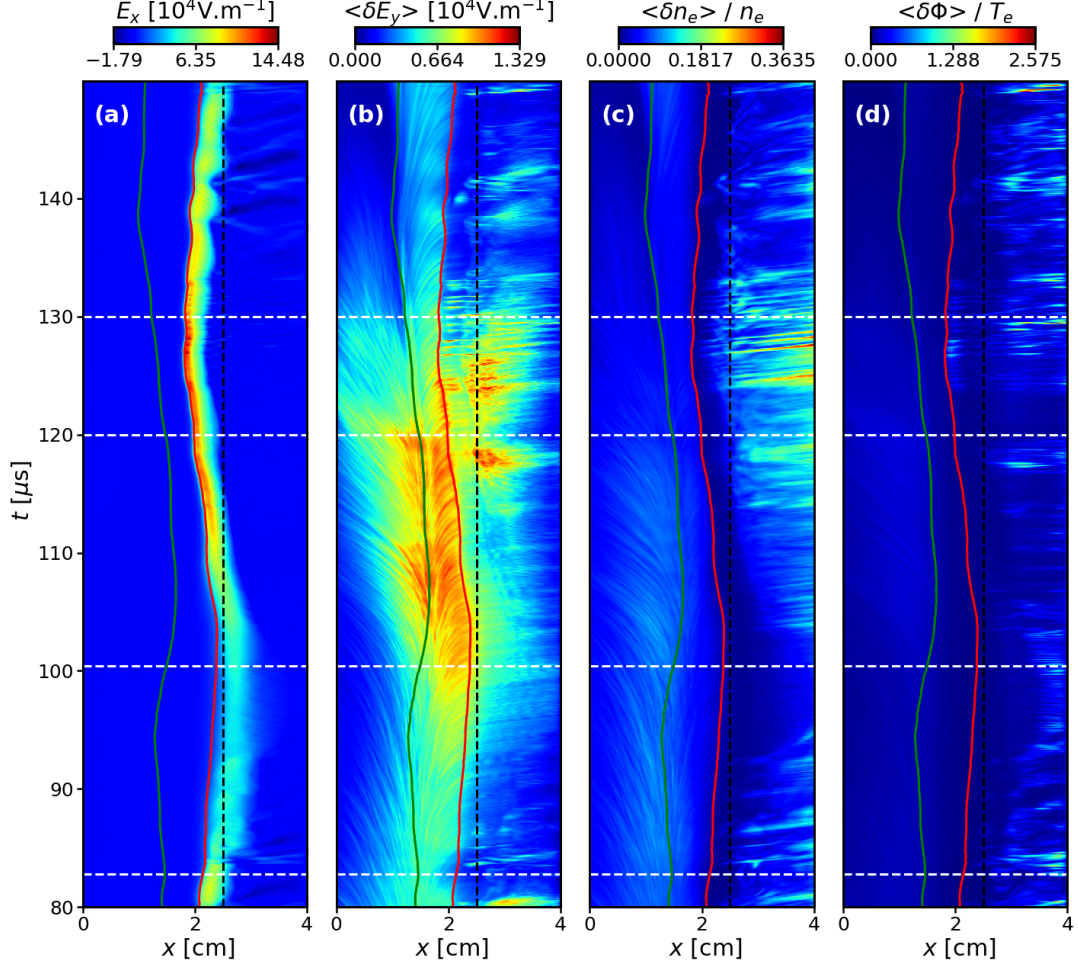


Figure 5.17 – $\alpha_\epsilon = 4$: Time and axial evolution during one BM oscillation of: (a) axial electric field, (b) azimuthal electric field, (c) normalized electron density and (d) normalized plasma potential fluctuations. Green vertical curve: axial position of null ion axial velocity. Red vertical curve: axial position of ion sonic point ($v_{ix} = c_s$). Horizontal white dashed lines: moments used to compute figure 5.18 (I_d maximum at $t=120\mu s$). Vertical black dashed lines: axial position of maximum magnetic field.

around $t = 125 \mu s$), the axial electric field is oscillating in a similar way, which could echo with what was previously observed by Coche *et al.* [76] and be linked to a new instability, the so-called ion transit-time instability (ITTI).

If we now focus on specific moments of a BM oscillation (same as the ones in figure 5.7), we obtain the curves in figure 5.18. We retrieve the growth of azimuthal electric field fluctuations upstream of the ion sonic point when I_d in-

creases, and downstream when I_d decreases. Moreover, we see that the normalized electron density and plasma potential fluctuations are very similar upstream of the sonic point (i.e. $\frac{\langle \delta n_e \rangle}{n_e} \approx \frac{\langle \delta \phi \rangle}{T_e}$), which was predicted by the quasi-linear kinetic theory [111]. However, the agreement is worse downstream due to the increase of the plasma potential fluctuations, while in the same time, the normalized fluctuations of plasma density seem to saturate in the plume to the value predicted by an ion-trapping saturation for an ion-acoustic instability ($\frac{\langle \delta n_e \rangle}{n_e} \approx \frac{1}{6\sqrt{2}}$), similarly to [111]. This increase of plasma potential fluctuations is more important when I_d decreases, and it could be related to the previous observations: the wave behaviour is different there.

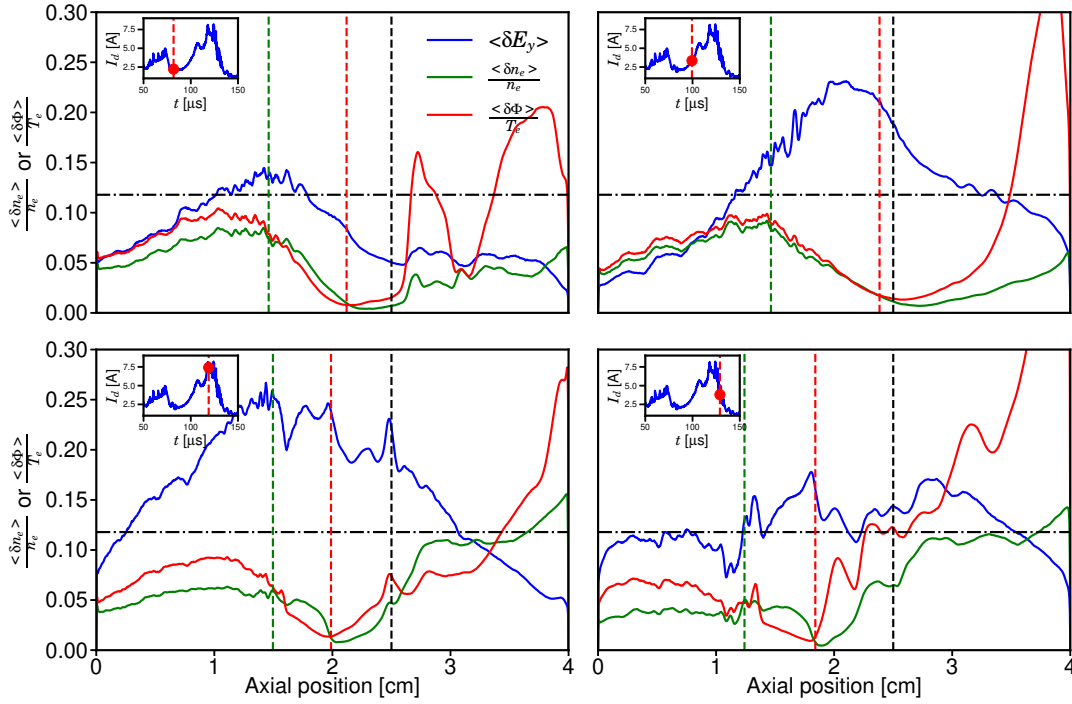


Figure 5.18 – $\alpha_\epsilon = 4$: Axial profiles of the azimuthal electric field (divided by 4×10^4), normalized electron density and normalized plasma potential fluctuations for different moments of a BM oscillation (same as the ones in figure 5.7). Vertical green dashed lines: axial position of null ion axial velocity. Vertical red dashed lines: axial position of ion sonic point ($v_{ix} = c_s$). Vertical black dashed lines: axial position of maximum magnetic field. Horizontal black dashed lines: expected amplitude for a fully-saturated ion-acoustic instability i.e. $\frac{1}{6\sqrt{2}}$. Inset: Time evolution of discharge current, red dot indicating the corresponding time.

Finally, it is interesting to notice that in average, we are retrieving the 10% value in the plume for the normalized plasma density fluctuations, obtained experimentally [215] and numerically [111].

All in all, after the analysis of these fluctuations, it seems that similarly to the simplified benchmark case, two zones can be distinguished depending on the

axial position, more particularly depending on the supersonic behaviour of the ions. Let us now study more precisely these azimuthal instabilities.

5.3.4 Azimuthal instabilities

2D snapshots of the azimuthal electric field for different α_ϵ have been displayed in figures 5.19 (when I_d increases) and 5.21 (when I_d decreases). The first striking observation is that, again, we can clearly distinguish two distinct zones for which the azimuthal instabilities exhibit different characteristics, with a transition corresponding almost exactly to the ion sonic point. Hence, we have computed the corresponding 2D FFT for an axial position upstream ($x = 1$ cm) and downstream ($x = 3$ cm) of this sonic point. They are shown in figures 5.20 (when I_d increases) and 5.22 (when I_d decreases). To compute these FFT, the azimuthal electric field values at $x = 1$ cm and $x = 3$ cm have been extracted for all azimuthal cells and for a number of time samples $N_{samples}$ corresponding to 5 μ s. Then, the built-in 2D FFT function of Python has been applied to this 2D array of size $N_y \times N_{samples}$. The modified ion-acoustic dispersion relation (DR) and the corresponding growth rate, given by equations 4.18 and 4.19 respectively, have also been displayed.

Upstream of the sonic point, we can notice that the modified ion acoustic DR is fitting quite well the spectrum, for both moments of the BM oscillation and for all α_ϵ (except for $\alpha_\epsilon = 4$ for which the spectrum is broader when I_d increases). We retrieve this trend looking at the E_y snapshots: inside the thruster, the oscillations have a well-defined wavelength that is decreasing when α_ϵ is decreased. The frequency is also decreased, which was also expected because of the dependence in $\sqrt{\epsilon_0}$ of λ_{de} and ω_p .

However, when the ions are supersonic, the instabilities are more difficult to analyse. When I_d increases, the instability has again a ion-acoustic behaviour for $\alpha_\epsilon = 4$ but then, when the scaling factor is increased, the spectrum broadens with a long-wavelength peak appearing. This behaviour can be retrieved on the azimuthal electric field snapshots: the instability wavelength is less defined, with long-wavelength structures that appear periodically. It is enhanced when I_d is decreasing, with still a long-wavelength peak and a spectrum that broadens even for $\alpha_\epsilon = 4$. Finally, despite the ion acoustic behaviour of the instability when I_d increases, the dominant wavelength is not located at the local maximum growth rate any more. It could be due to the convection of the wave which is created upstream and propagates towards the cathode.

The presence of this long-wavelength instability is quite unusual and it could explain why the friction-force approximation displayed in figure 5.7 matches better inside the thruster than in the plume.

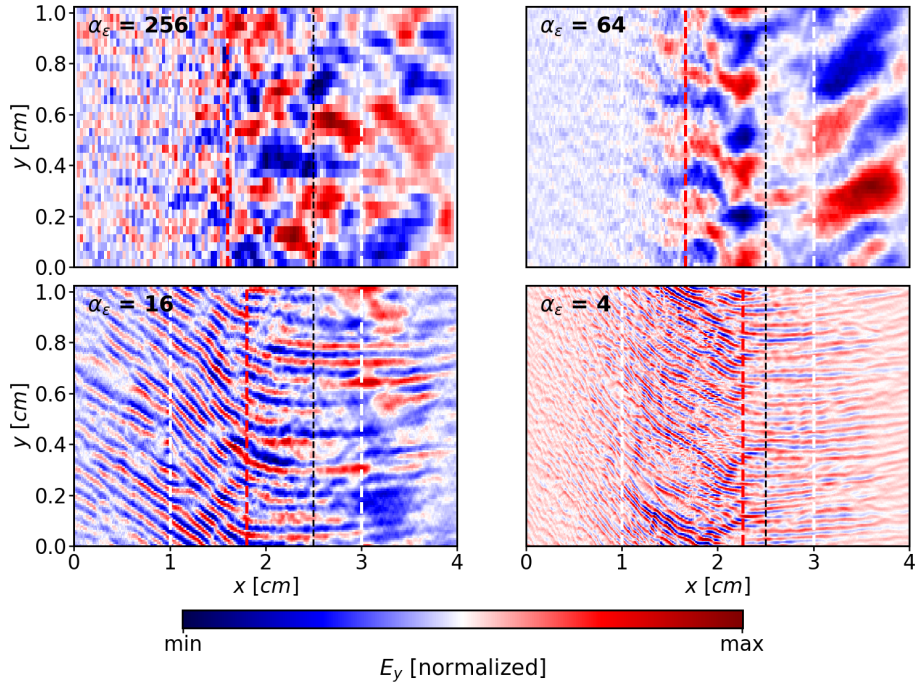


Figure 5.19 – 2D maps of azimuthal electric field for different α_ϵ , when I_d increases. Red dashed lines:axial position of ion sonic point ($v_{ix} = c_s$). White dashed lines: axial position of FFTs (figure 5.20). Black dashed line: position of maximum magnetic field.

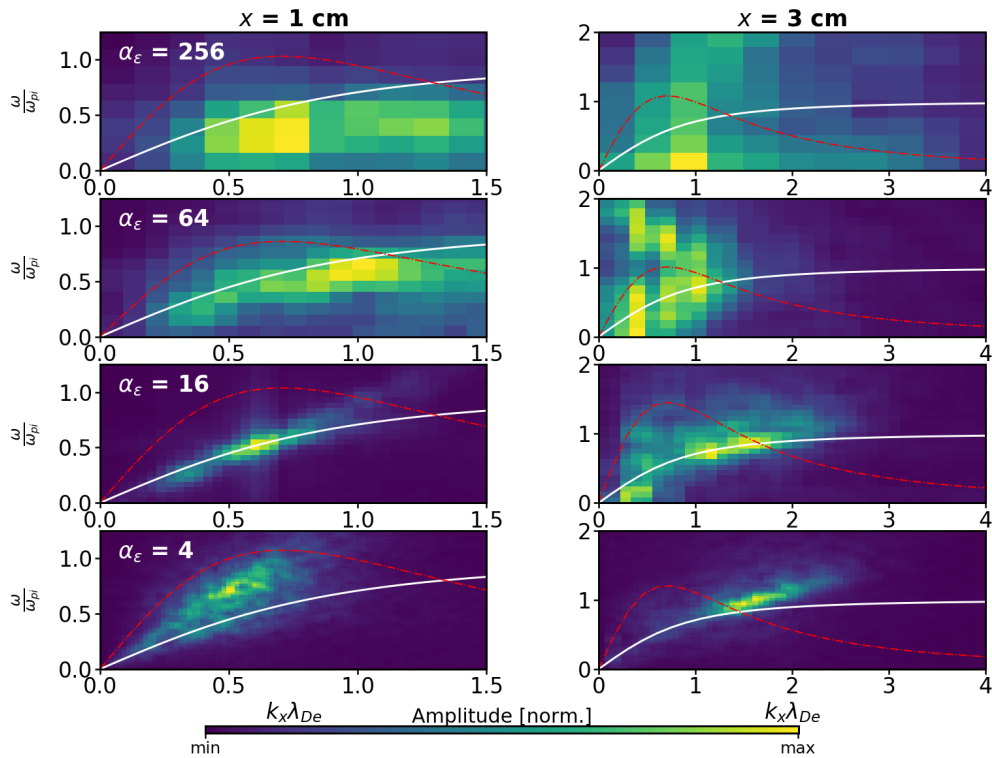


Figure 5.20 – Corresponding FFT for $x=1$ cm (left column) and $x=3$ cm (right column), when I_d increases. White thick line: ion-acoustic dispersion relation. Red dashed line: ion-acoustic growth rate rescaled by a constant factor to fit the image. The spectrum has been zoomed to focus on the zone of interest.

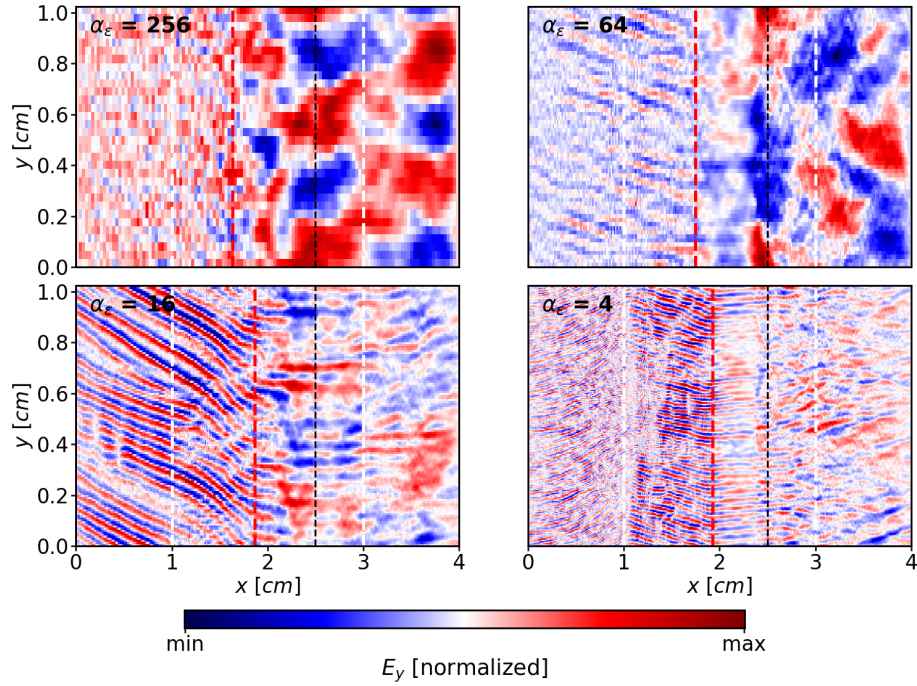


Figure 5.21 – 2D maps of azimuthal electric field for different α_ϵ , when I_d decreases. Red dashed lines: axial position of ion sonic point ($v_{ix} = c_s$). White dashed lines: axial position of FFTs (figure 5.22). Black dashed line: position of maximum magnetic field.

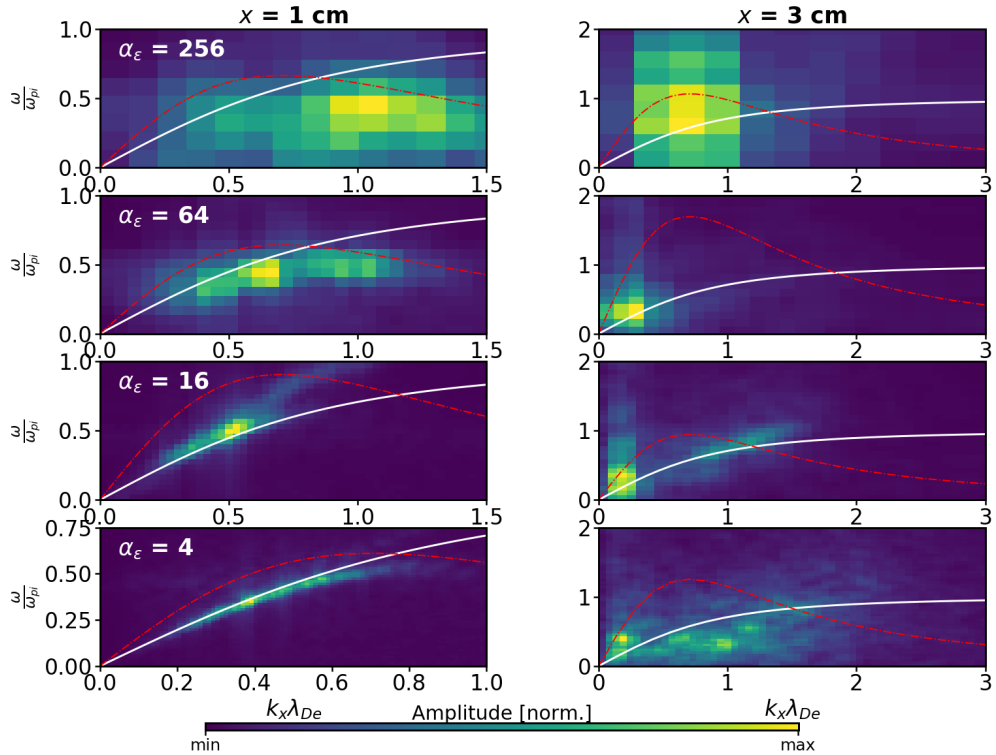


Figure 5.22 – Corresponding FFT for $x=1$ cm (left column) and $x=3$ cm (right column), when I_d decreases. White thick line: ion-acoustic dispersion relation. Red dashed line: ion-acoustic growth rate rescaled by a constant factor to fit the image. The spectrum has been zoomed to focus on the zone of interest.

5.4 Conclusion

In this chapter, 2D axial-azimuthal self-consistent PIC simulations have been performed, with a vacuum permittivity scaling technique. Breathing mode oscillations have been observed on a case with a scaling factor close to "reality" ($\alpha_\epsilon = 4$ instead of 1) and we have shown that the electron-ion friction force was increasing when the discharge current was increasing, which was expected because the electron density was also increasing. It appeared that this friction force was again the main contributor to the electron axial transport, throughout the whole BM oscillations. Hence, we tried to apply the quasi-linear kinetic theoretical model developed in the previous chapter and managed to successfully approximate the friction force, with some limitations in the plume in the BM phase of decreasing current. The influence of the artificial scaling technique on this transport has also been studied and, as expected, the friction force was seen to decrease for higher α_ϵ . Combining our results with the ones obtained in the BM phase of increasing current for a case without scaling [111], we can conjecture that throughout a BM oscillation, the axial electron transport inside the thruster is dominated by the electron-ion friction force, with a non-negligible contribution of the classical electron-neutral collisions, whereas in the plume, the electron-ion friction force is the only one enhancing the axial electron transport.

Moreover, we observed that the azimuthal instabilities were behaving differently depending on the axial position. More specifically, we found that the location of the ion sonic point was significantly affecting the plasma fluctuations: when the ions are subsonic, the azimuthal instabilities exhibit an ion-acoustic behaviour with a short wavelength and an axial convection towards the anode or the cathode, depending on the sign of the ion velocity, similarly to what was observed in previous works [77, 111, 140]. However, downstream of the ion sonic point, the instabilities exhibit a steady behaviour and, superimposed on the usual short-wavelength instabilities, some long-wavelength instabilities are growing, mostly in the BM phase of decreasing current. This unexpected behaviour probably explains why the quasi-linear approximation is under-estimating the friction-force in this zone: another phenomena is playing a role here and a preliminary analysis lead us to a correlation with the apparition of the axial ion transit-time instability, already observed by Coche *et al.* [76], which could affect the behaviour of the azimuthal instabilities.

More work is hence needed to understand this new instability and see how it interacts with the well-known EDI. This will be discussed in the next chapter.

Chapter 6

Instabilities in Hall thrusters

In the previous chapter, we decided to focus mainly on the evolution of the axial electron transport during a BM oscillation, along with the influence of the vacuum permittivity scaling technique used to speed-up the computation. It appeared that the position of the ion sonic point marked a transition on the characteristics of the azimuthal instabilities: upstream, the usual EDI was propagating, but when the ions were supersonic, a long-wavelength instability was sometimes growing in the plume, similarly to what was observed in previous 2D axial-azimuthal PIC simulations [76, 142]. In addition to the fact that this change of behaviour was related to the ion sonic point, we observed that the axial electric field was oscillating axially. Hence, it made us think that this phenomena could be related to the so-called Ion Transit Time Instability (ITTI).

Because this instability has been scarcely observed in PIC simulations [76], we will first study it by getting rid of the EDI. To do so, all the plasma parameters will be azimuthally averaged at every time step of the simulation, hence precluding any azimuthal instability to grow. This analysis will be presented in section 6.1 in which we will also try to get more insights on the origin of the ITTI. Then, we will come back in section 6.2 to the "realistic" simulations presented in the previous chapter, and we will increase the azimuthal domain length L_y to see how it affects the interaction between the ITTI and the EDI. Finally, we will give some additional insights on this interaction in section 6.3.

Contents

6.1 Ion transit-time instabilities	144
6.1.1 Current understanding	144
6.1.2 Analysis of ITT: "1D axial" simulations	145
6.1.3 Origin of the ITTI?	149
6.1.4 Evidence of ITTI in the self-consistent axial-azimuthal simulations	150
6.2 Influence of the azimuthal domain length L_y	155
6.2.1 Axial electron transport	155
6.2.2 Azimuthal instabilities	158

6.3	Interaction between ITTI & EDI	165
6.3.1	Preliminary analysis on the self-consistent simulations	165
6.3.2	Insights from the simplified benchmark case	168
6.4	Conclusion	171

6.1 Ion transit-time instabilities

6.1.1 Current understanding

Mid-range frequency (100-500 kHz) instabilities have been observed experimentally by Esipchuk *et al.* [55] and Vaudolon *et al.* [56, 57], and numerically by Fife [46], Hagelaar *et al.* [58] and Bareilles *et al.* [59] in a hybrid code, and Coche *et al.* [76] in a 2D axial-azimuthal PIC code. As detailed previously in section 1.2.2, they are related to the transit-time of ions in the acceleration region: a wave of axial electric field E_x is growing near the anode and propagating towards the cathode, creating a group of low-energy ions in the plume, along with some high-energy ions (with an axial velocity higher than the one induced by the applied potential difference) which gained energy through the wave-riding mechanism.

No consensus appeared to explain theoretically the origin of this instability. A linear analysis was first proposed by Esipchuk *et al.* [223] for quasi-longitudinal waves growing for a positive value of the magnetic field gradient. Then Barral *et al.* [224] have derived the dispersion relation by linearizing a simple system of 1D fluid equations for a discharge in which cold ions are accelerated between two electrodes in a quasi-neutral plasma. They found that the plasma perturbations consist of quasi-neutral ion acoustic waves superimposed on a background standing waves generated by I_d oscillations. At high ionization levels, the acoustic waves are amplified as they propagate, inducing strong perturbations of ion density and velocity. Later, Fernandez *et al.* [225] have further simplified the system by removing the effect of ionization and electron pressure, leading to a resistive mode. They obtained a growth rate that vary with the electron mobility as $\mu_e^{-1/2}$, which is consistent to previous numerical observations [46, 59]. They found that this resistive instability is of the convective type: perturbations originated in the region of low mobility are convected out of this region with roughly the ion velocity. While the disturbances are convected towards the cathode near the exit plane, upstream, in the region of reversed ion flow, the disturbances are convected towards the anode with a much lower velocity. They highlight many times that the coupling with azimuthal waves could have a big impact but has not been studied yet. It is interesting to note that a more elaborate version of their model (including a kinetic description of ions and neutrals and an electron energy equation) was used earlier by Chable and Rogier [54] to study low-frequency (1-100 kHz) oscillations. Whereas their main conclusion was on the breathing mode, induced

by resistive effects, they also observed high fluctuation power when the magnetic field is large, similarly to Fernandez *et al.* (low electron mobility). More recently, Koshkarov *et al.* [226] studied these axial resistive modes and found that the phase shift between the inertial response of the ions and the dissipative electron response can cause what they called the "resistive current flow instability".

In the rest of this section, we will see that we observe in our simulations an axial instability growing and propagating with similar characteristics as described above, and we will try to get additional insights on the onset of this instability.

6.1.2 Analysis of ITT: "1D axial" simulations

To focus only on the ITTI, we decided to get rid of any azimuthal oscillations, by simulating a simplified "1D axial" case. To do so, the plasma density was averaged in the azimuthal direction at each time step (and this averaged value was assigned at each axial position respectively), hence precluding the growth of any azimuthal perturbation. As in the previous chapter, we simulated cases with different vacuum permittivity scaling factor α_ϵ but due to its computational cost, the case $\alpha_\epsilon = 4$ was not simulated here. Hence, the results presented in this subsection will correspond to a case with $\alpha_\epsilon = 16$.

In figure 6.1, the time evolution of the discharge current is compared with the "nominal" case presented in the previous chapter, for which no azimuthal average was performed. After an initial transient state, we can see that the BM oscillations are strongly damped and the discharge current is now oscillating with a higher frequency of 120 kHz. Even though this frequency value is similar to the one of ITT instabilities, more evidences are needed before drawing any conclusion.

2D maps of E_x and n_i

If we ignore the transient, we can plot the time and axial evolution of the axial electric field E_x and ion density n_i , displayed in figure 6.2. We see that we retrieve similar oscillation patterns, with again a frequency of $f_{ITT} = 120$ kHz. It seems that the perturbation is created around $x = 1.5$ cm before being convected outside the thruster at a velocity of approximately $v_{ITT} = 1150$ m · s⁻¹. One can notice that when the axial electric field grows, the ion density is low, which is expected by Ohm's law (equation 1.39). On the contrary, because of the high electron density in the plume, the axial electric field perturbation seems to be damped near the position of maximum magnetic field, again as a consequence of the need to maintain current balance. Moreover, a perturbation is also propagating towards the anode, with almost a perfect symmetry at $x = 1.5$ cm: it is less visible on the axial electric field due to the colormap ranges but it has been observed to exhibit an amplitude of around 1 kV · m⁻¹ (and negative values).

Finally, the axial position of the ion sonic point ($v_{ix} = c_s \approx 3400$ m · s⁻¹) has been also displayed and we can notice that it corresponds perfectly to the origin of the axial electric field perturbation: this ion sonic transition probably plays a role in the on-set of the ITTI.

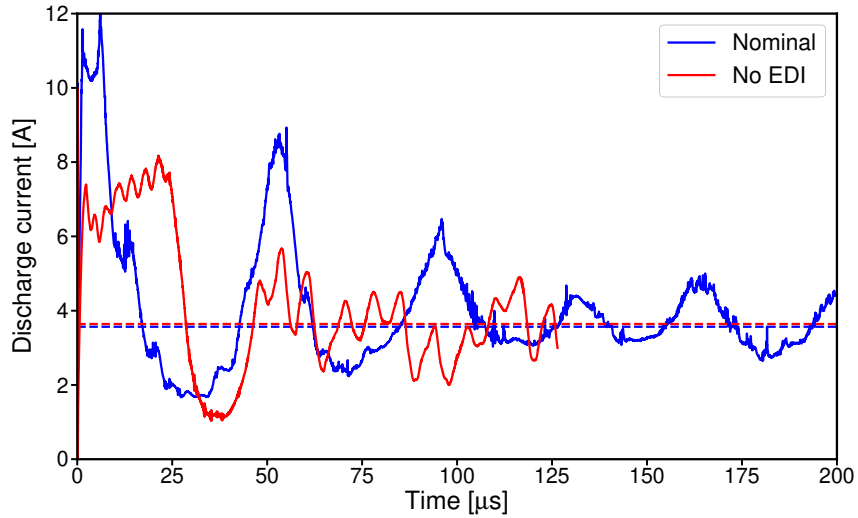


Figure 6.1 – $\alpha_\epsilon=16$: Time evolution of the discharge current for the nominal case and the case with EDI suppressed (by averaging azimuthally). Dashed horizontal lines: mean value at steady state.

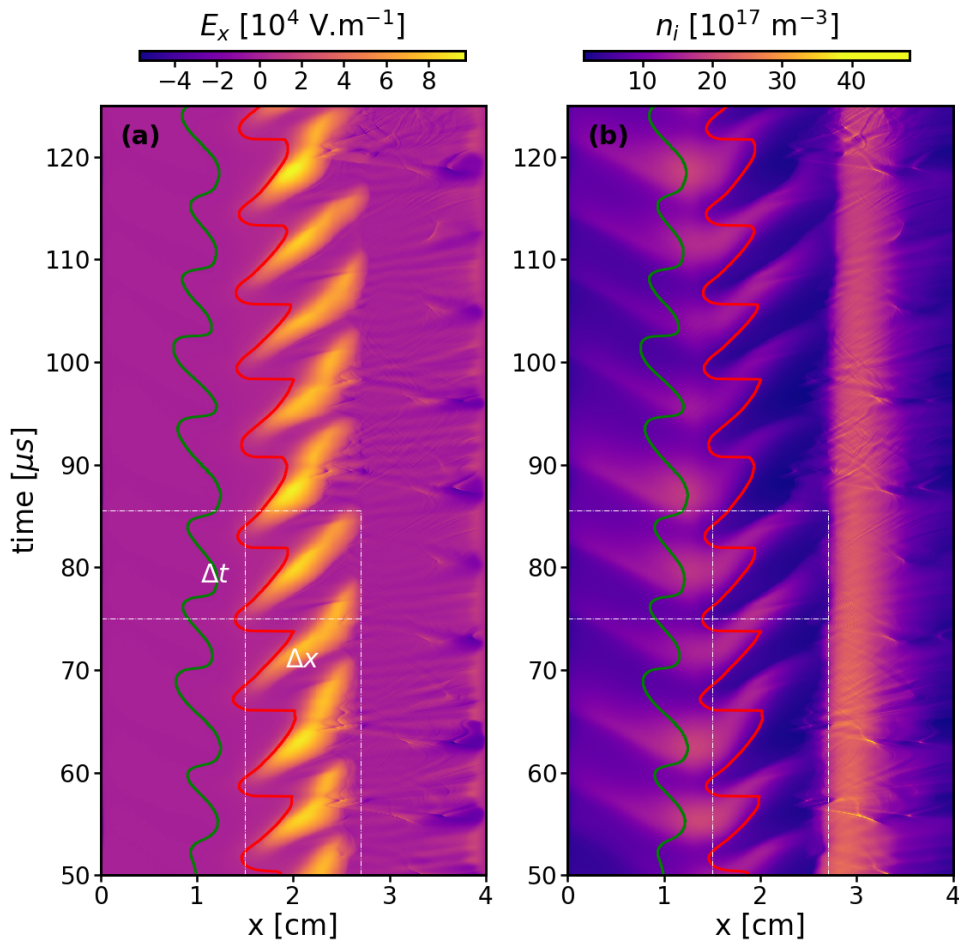


Figure 6.2 – $\alpha_\epsilon=16$ - **EDI suppressed**: Time and axial evolution of (a) axial electric field and (b) ion density. Green vertical curve: axial position of null ion axial velocity. Red vertical curve: axial position of ion sonic point ($v_{ix} = c_s$). The white dashed lines have been used to compute the wave velocity.

Axial ion phase-space

To get more insights on this wave, we can take advantage of the richness of PIC simulations and compute the axial ion phase-space at 4 moments of one transit-time oscillation. We can see in figure 6.3 that we retrieve some characteristics observed in figure 1.10 (obtained by the hybrid code of Hagelaar and Bareilles [59]):

1. First, at time 1, we can see in figure 6.3(a) that, in addition to the usual ion density peak near $x = 1.5$ cm, there is another density peak in the plume, due to the presence of a low-velocity ion population. These ions seem trapped because of the potential well inducing a negligible axial electric field there. The axial electric field has only one sharp peak near the exit plane and we see that another peak is starting to form near $x = 1.5$ cm, as seen already in figure 6.2. One can notice that in the plume, some ions have a velocity higher than the maximum ion velocity of equation 1.33 ($v_{i,max} = 20.9 \text{ km} \cdot \text{s}^{-1}$): there is evidence of ion wave-riding.
2. Then, at time 2, we can see in figure 6.3(b) that the axial electric field increases near $x = 1.5$ cm and a group of low-velocity ions, that were formed at this position, are propagating towards the cathode without being accelerated because they do not experience any axial electric field. They correspond to the ion density peak near the exit plane ($x = 2.1$ cm), between the two axial electric field peaks.
3. At time 3, in figure 6.3(c), the upstream axial electric field peak is almost maximum, while the downstream one has almost vanished. One could think that high-velocity ions of the plume are decelerating and join the group of low-velocity ions. However, we have to be careful when reading this phase-space: the negative axial electric field in the plume is not high enough to explain this deceleration and between each snapshot, ions with velocity of $21 \text{ km} \cdot \text{s}^{-1}$ will travel ≈ 0.42 cm so they will leave the domain. The ion group marked by a yellow circle hence corresponds to the ions with mid-velocity that have been convected towards the plume.
4. Finally, at time 4, we retrieve the initial situation in figure 6.3(d) of time 1, with again an ion wave-riding.

As seen previously in figure 6.2, we notice again some ions propagating towards the anode due to the small negative axial electric field there.

Time evolution of specific parameters

As the instability seems to form around $x = 1.5$ cm, the time evolution of some plasma parameters at this position is displayed in figure 6.4. We can notice that the ions become supersonic just after the growth of axial electric field. One can infer that already some ions were travelling at a velocity higher than c_s before and hence, it could explain the wave growth. Moreover, the ion density and axial electric field have a phase shift of π , while the axial ion velocity is in phase with

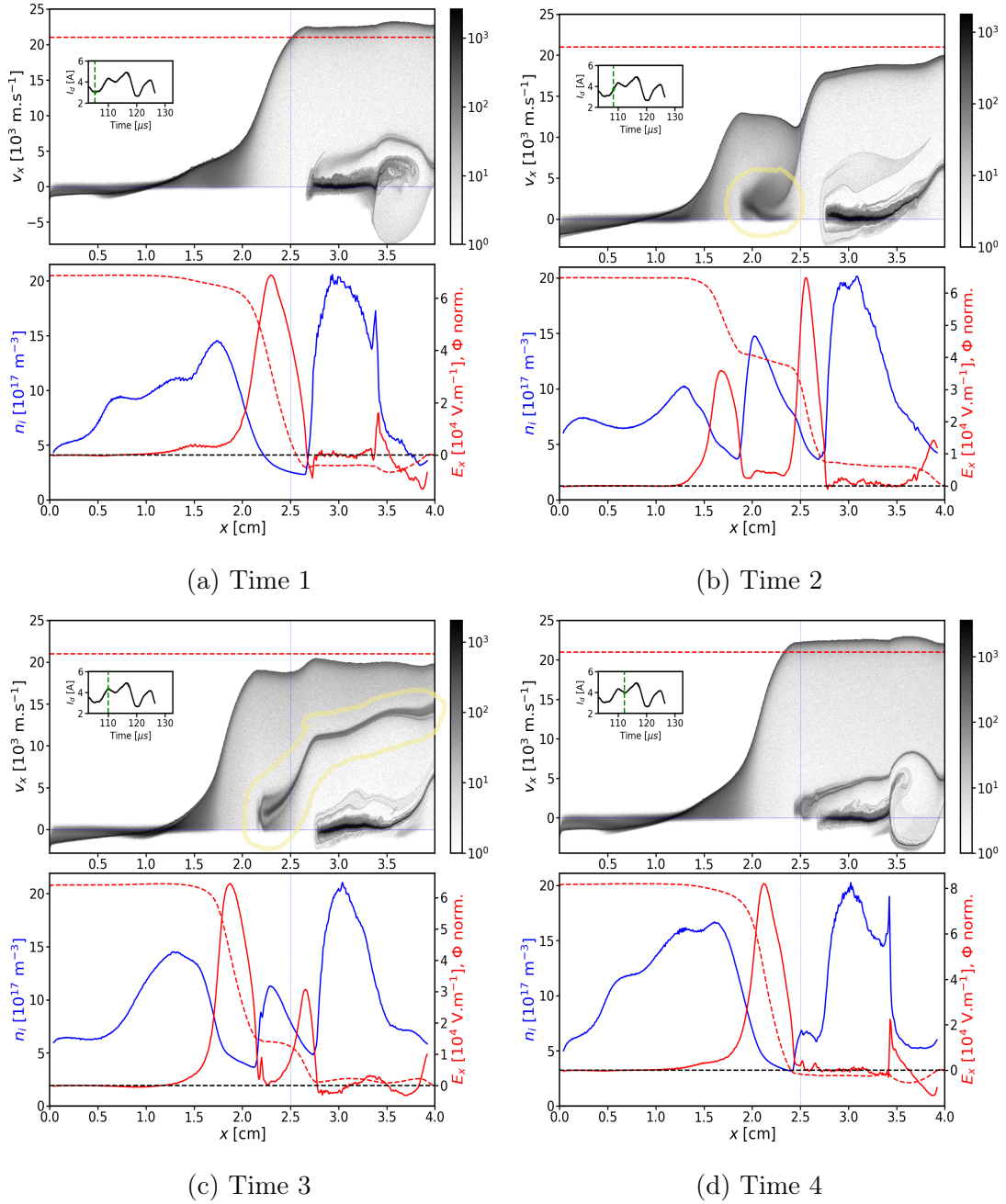


Figure 6.3 – $\alpha_\epsilon=16$ - EDI suppressed: 4 different moments of an ion transit-time oscillation. Top: Axial ion phase-space with $v_{i,max}$ given by the horizontal red dashed line and in inset, time evolution of discharge current with the green dot indicating the corresponding time. The yellow zones indicate the ions that will form the low-velocity group in the plume. Bottom: Corresponding profiles of ion density (blue line), axial electric field (solid red line) and electric potential (dashed red line, normalized).

the axial electric field. One can notice that when the axial electric field starts to grow, the ion axial velocity corresponds to the wave velocity.

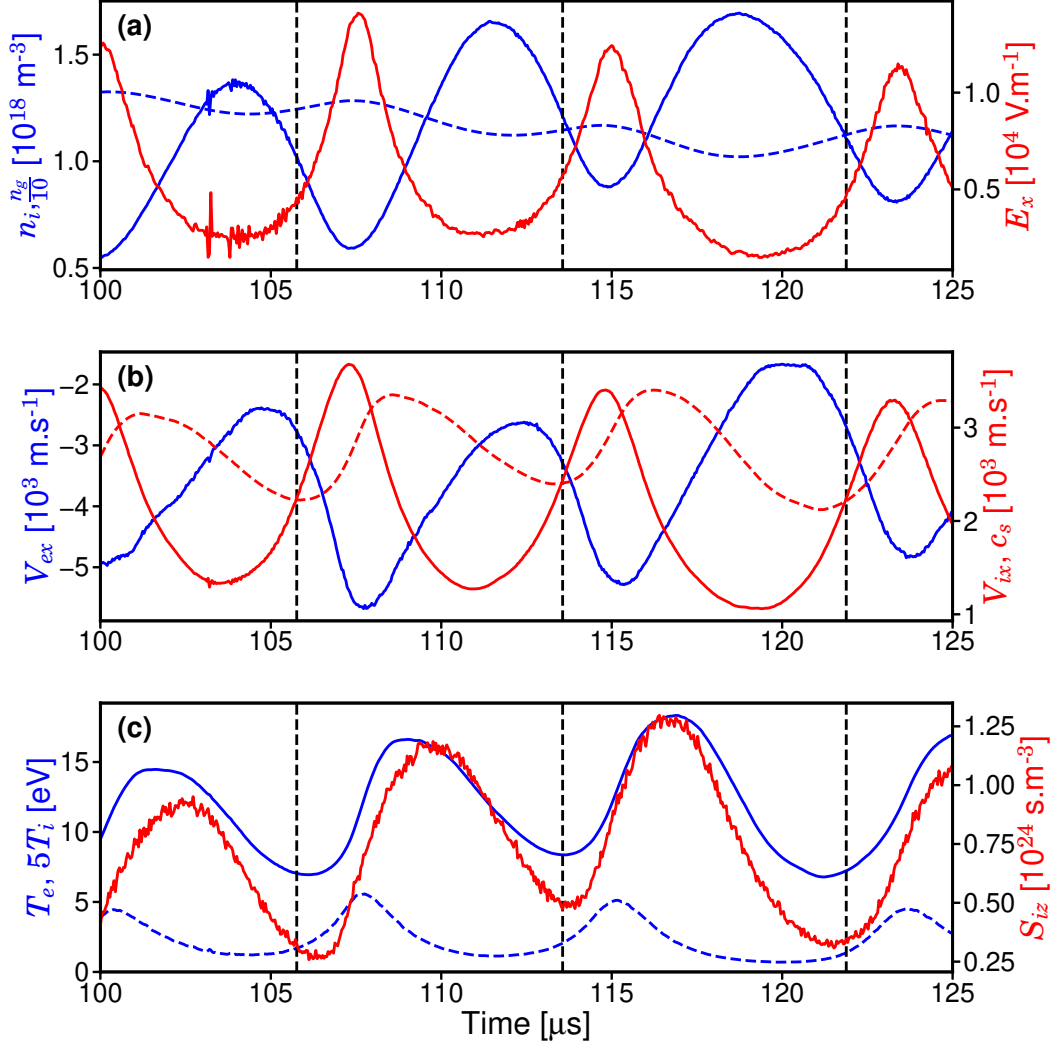


Figure 6.4 – $\alpha_\epsilon=16$ - EDI suppressed: Time evolution at $x = 1.5$ cm of: (a) ion density, neutral density (dashed blue) and axial electric field - (b) Axial ion and electron velocity and ion sound speed (dashed red) - (c) Electron and ion (dashed blue) temperatures and ionization source term. The vertical black dashed lines correspond to the time where the ions become supersonic ($v_{ix} > c_s$).

6.1.3 Origin of the ITTI?

Another way to get more insights on the origin of this instability is to perform a parametric study and see how it affects the wave growth. First, we have varied the scaling factor α_ϵ and we can see in figure 6.5 that the frequency is increased when $\alpha_\epsilon = 64$, instead of $\alpha_\epsilon = 16$. However, for $\alpha_\epsilon = 256$, the instability seems to

be damped and strangely, oscillations similar to the breathing mode are growing later.

Moreover, to know if the ITTI is related to the neutral dynamics, we used a simulation with $\alpha_\epsilon = 64$ and at some point, we "froze" the neutrals by keeping their axial profiles (density and velocity) constant. We can see in figure 6.6 that the oscillations are still present and hence, we can conclude that the ITTI is not related to the neutral dynamics.

Finally, we performed additional tests not displayed here. First, we have seen that the ion-neutral charge-exchange collisions and the cathode model do not seem to play any role. However, when we decreased the discharge voltage U_d from 300 V to 200 V, the wave amplitude was decreased and the frequency increased along with the wave velocity. This observation can echo with the fact that the instability is related to the ion sonic point: a change of U_d affects the electron temperature (and hence the ion sound speed) along with the ion velocity.

All in all, we have seen that the ITTI was growing in our 2D axial-azimuthal simulations when the EDI was suppressed (by averaging azimuthally at each time step). The typical characteristics of this instability were retrieved: mid-range frequency (120 kHz), ion wave-riding mechanism, low-energy ion group in the plume, etc. Moreover, we managed to relate the origin of this instability to the ion sound speed: it seems to grow at the position for which the ions become supersonic.

However, even if the scaling factor α_ϵ used was relatively big, the computational time required for these simulations was quite important and by averaging azimuthally, we were basically retrieving a simple 1D axial simulation. Hence, as it seems that the ITTI is not directly related to azimuthal effects, or presumably, is a "fluid" instability, additional insights could be more easily obtained by using an axial 1D fluid code (along with a perturbation analysis) which could simulate a case in a couple of minutes instead of a couple of days. Even though a 1D fluid code is already available at LPP, the results are still preliminary and hence, they are out of scope of this manuscript.

6.1.4 Evidence of ITTI in the self-consistent axial-azimuthal simulations

Let us now come back to the "real" self-consistent simulations presented in the previous chapter. The presence of these ion transit-time instabilities can be inferred from the axial ion phase-space and the axial profile of axial electric field. They have been displayed in figure 6.7 for the case $\alpha_\epsilon = 16$ and in figure 6.8 for the case $\alpha_\epsilon = 64$. Because this diagnostic is quite heavy in term of file sizes, it has only been run at the end of the simulations and not for the case $\alpha_\epsilon = 4$. Moreover, we can notice in figure 5.8 that the breathing mode oscillations seem to be damped at the very end of the simulation for the case $\alpha_\epsilon = 16$. Hence, to be able to observe the evolution during a BM oscillation, we will analyse in this

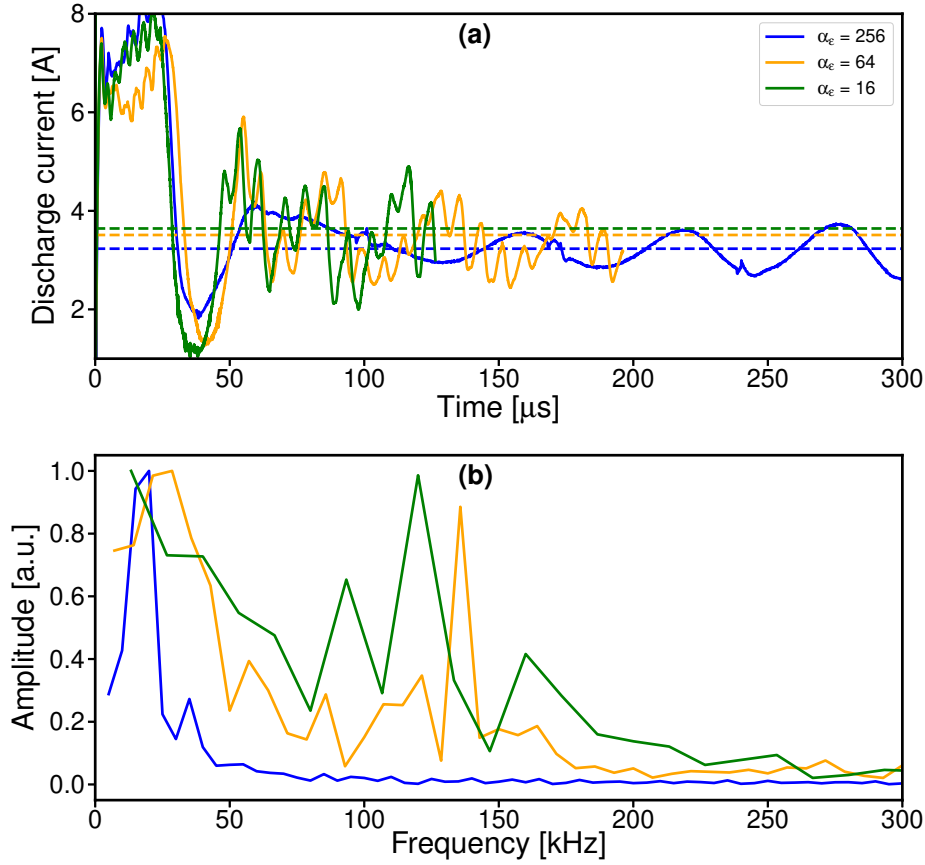


Figure 6.5 – **EDI suppressed**: For different α_ϵ , (a) time evolution of the discharge current (the dashed horizontal lines correspond to the mean value at steady state) and (b) corresponding FFT.

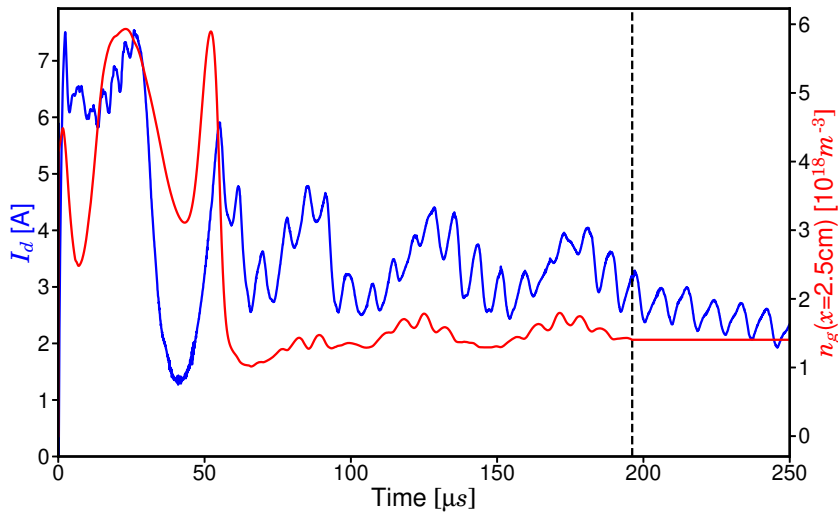


Figure 6.6 – $\alpha_\epsilon=64$ - **EDI suppressed - Frozen neutrals**: Time evolution of discharge current and neutral density at the exit plane. The neutrals have been frozen at the time indicated by the vertical black dashed line.

section the case $\alpha_\epsilon = 16$ without anode ion recombination, which does not affect our conclusion.

First, for both cases, a low-velocity ion group can be found in the plume, along with oscillations of the axial electric field. These oscillations are less pronounced than in the previous section where the EDI was suppressed, and the low-velocity group is also less populated. Hence, in some way, the presence of EDI is damping these transit-time oscillations.

However, if we look at the case $\alpha_\epsilon = 16$, in figure 6.7, we still retrieve a similar behaviour than for the case without EDI of figure 6.3, but less pronounced:

1. First, when the discharge current increases (figure 6.7(a)), we can see that a group of low-velocity ions is separating from the main ion beam. It corresponds to the small density bump near $x = 2$ cm, related to the small well of axial electric field: an upstream peak has been growing just before $x = 2$ cm.
2. For the same ITT oscillation (figure 6.7(b)), we can see that there is some ion wave-riding and a group of low-energy ions in the plume that have been trapped by the negative potential.
3. Later, when the discharge current decreases (figure 6.7(c)), this phenomena seems localized more upstream, in the plume. Indeed, we retrieve the axial electric field well and the ion density bump, near $x = 3$ cm.
4. It is again associated with a wave-riding mechanism and a low-energy group of trapped ions (figure 6.7(d)).

For the case with $\alpha_\epsilon = 64$, displayed in figure 6.8, the behaviour is similar but the axial oscillation on the electric field is more pronounced. It was expected because the EDI is more damped due to the higher scaling factor. Moreover, it is interesting to notice that the axial electric field perturbation seems to grow more upstream for the case $\alpha_\epsilon = 64$ (around $x \approx 1.6$ cm) than for the case $\alpha_\epsilon = 16$ (around $x \approx 1.9$ cm): we found that these positions were corresponding to the ion sonic point, similarly than in the previous section. Finally, we can relate these two figures to the IVDF displayed in the previous chapter (figures 5.15 and 5.16): indeed, the low-energy ion peaks observed in the plume ($x = 3$ cm) correspond to these trapped ions, which form a bigger group when the discharge current decreases.

Even though we have given evidence of the presence of the ITTI in our simulations, this instability is propagating mainly in the axial direction. Hence, it is still not clear if and how it is related to the change of the azimuthal instabilities in the plume region when the discharge current decreases. To get more insights, we will study in the next section the influence of the azimuthal domain length on this phenomena.

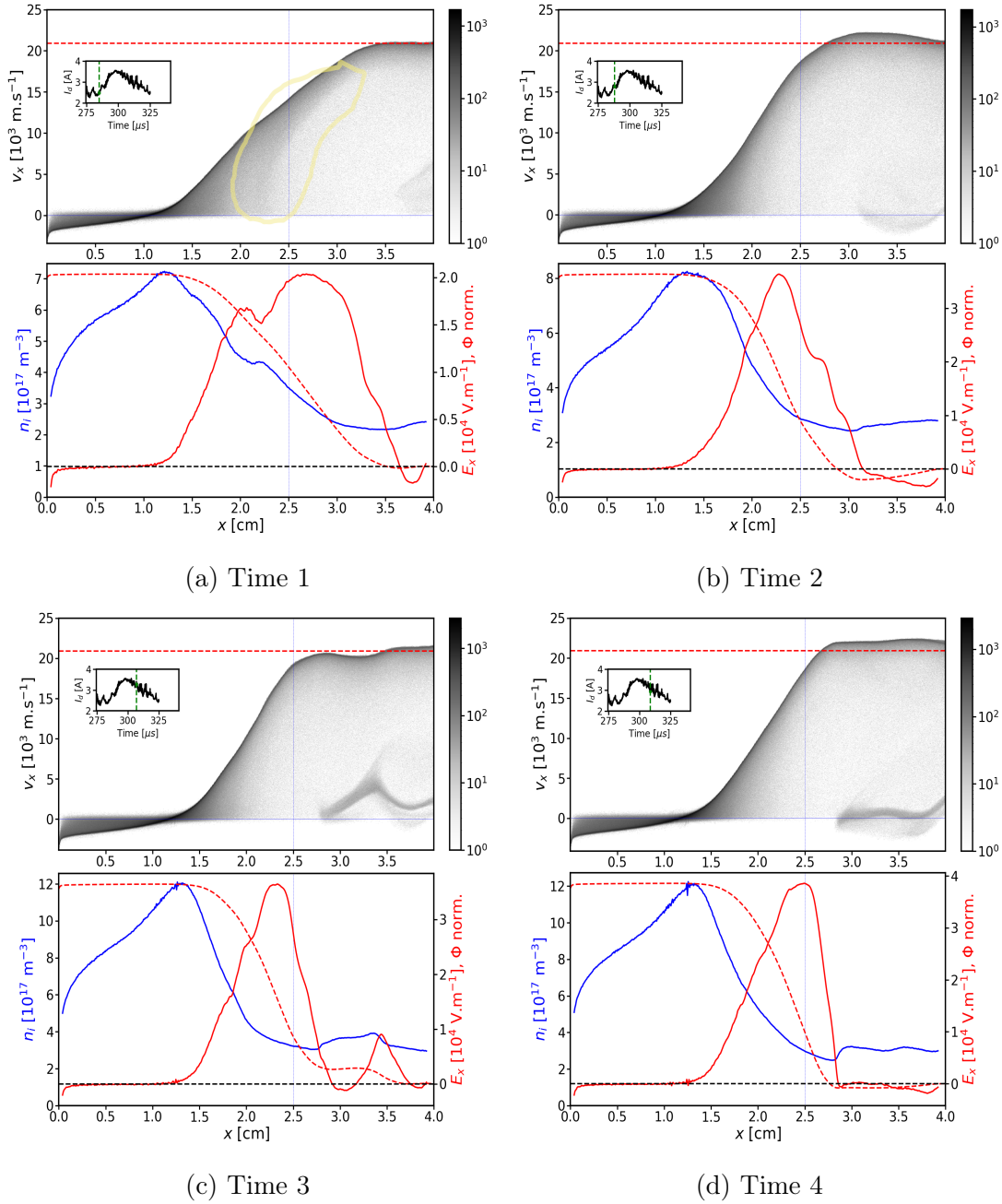


Figure 6.7 – $\alpha_\epsilon=16$, **nominal**: 4 different moments of an ion transit-time oscillation. Top: Axial ion phase-space with $v_{i,max}$ given by the horizontal red dashed line and in inset, time evolution of discharge current with the green dot indicating the corresponding time. The yellow zones indicate the ions that will form the low-velocity group in the plume. Bottom: Corresponding profiles of ion density (blue line), axial electric field (solid red line) and electric potential (dashed red line, normalized).

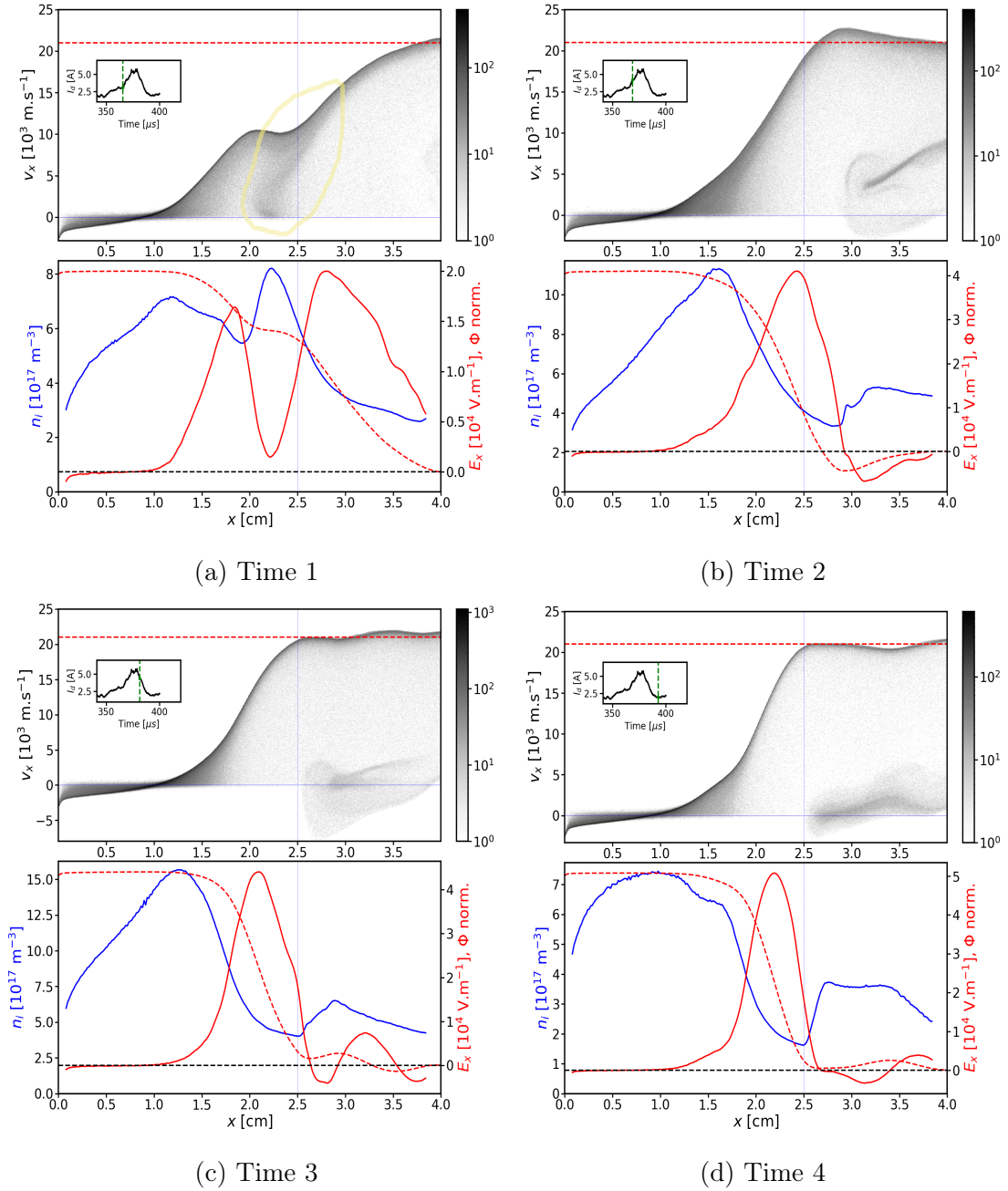


Figure 6.8 – $\alpha_\epsilon=64$, nominal: 4 different moments of an ion transit-time oscillation. Top: Axial ion phase-space with $v_{i,max}$ given by the horizontal red dashed line and in inset, time evolution of discharge current with the green dot indicating the corresponding time. The yellow zones indicate the ions that will form the low-velocity group in the plume. Bottom: Corresponding profiles of ion density (blue line), axial electric field (solid red line) and electric potential (dashed red line, normalized).

6.2 Influence of the azimuthal domain length L_y

We have increased the azimuthal domain length L_y from 1 cm to 2, 4 and 8 cm, for $\alpha_\epsilon = 64$. It has not been decreased to 0.5 cm because not enough EDI wavelengths were then captured and moreover, as the increase of needed computational resources is directly proportional to the one of L_y , we needed to use at least a scaling factor of 64.

Prior to any local analysis, the corresponding time evolutions of the discharge current are displayed in figure 6.9. We can see that the oscillation amplitude is greatly enhanced when L_y is increased, which is related to a wave energy that is also greater when the azimuthal length is higher. Hence, the mean value of the discharge current increases also with L_y . It is important to mention that the case $L_y = 8$ cm may have not reached steady-state yet.

6.2.1 Axial electron transport

Similarly to the analysis performed in the previous chapter, we will look first at the axial electron transport. The azimuthal momentum terms averaged over several BM oscillations are shown in figure 6.10. First, we can see that the classical collision term is almost independent on L_y , and that the friction force for $x \leq 1.5$ cm is almost null, which gives a near-anode axial electron transport rather identical for each case. However, from $x = 1.5$ cm to the cathode, we observe a significant increase of the friction force when L_y is increased, which enhances equally the axial transport. It is coherent with the discharge current evolution (figure 6.9): the mean value of discharge current is higher when L_y is increased because the plasma conductivity is enhanced via the electron-ion friction force. Moreover, the discharge behaviours for $L_y = 1$ cm or $L_y = 2$ cm are very similar.

One can notice that the friction force for the case $L_y = 8$ cm is very noisy in the plume, which is due to the momentum term diagnostic which was not averaged on enough samples when the discharge current was high. We can compare it to the figure 6.11(a) in which the usual grid diagnostic was used, with a slightly lower friction force in the plume for this particular case. We can see in this figure that again, the ion sonic point seems to mark a transition between the small friction force zone upstream and the significant friction-force enhancement with L_y downstream. Moreover, we can notice that this sonic point is shifted towards the anode when L_y is increased, which can also be related to this friction-force enhancement.

The axial profiles of the ratio of the wave energy to the electron thermal energy are displayed in figure 6.11(b). We can see that this ratio increases significantly with L_y , and even though this increase occurs upstream of the ion sonic point, we can probably relate it to the one of the electron-ion friction force. Moreover, the ion-wave trapping saturation limit, computed in the previous chapter (Eq. 4.29) has been displayed and we can notice that for the two cases in which the friction-force is significantly enhanced (i.e. $L_y = 4$ or 8 cm), the wave energy

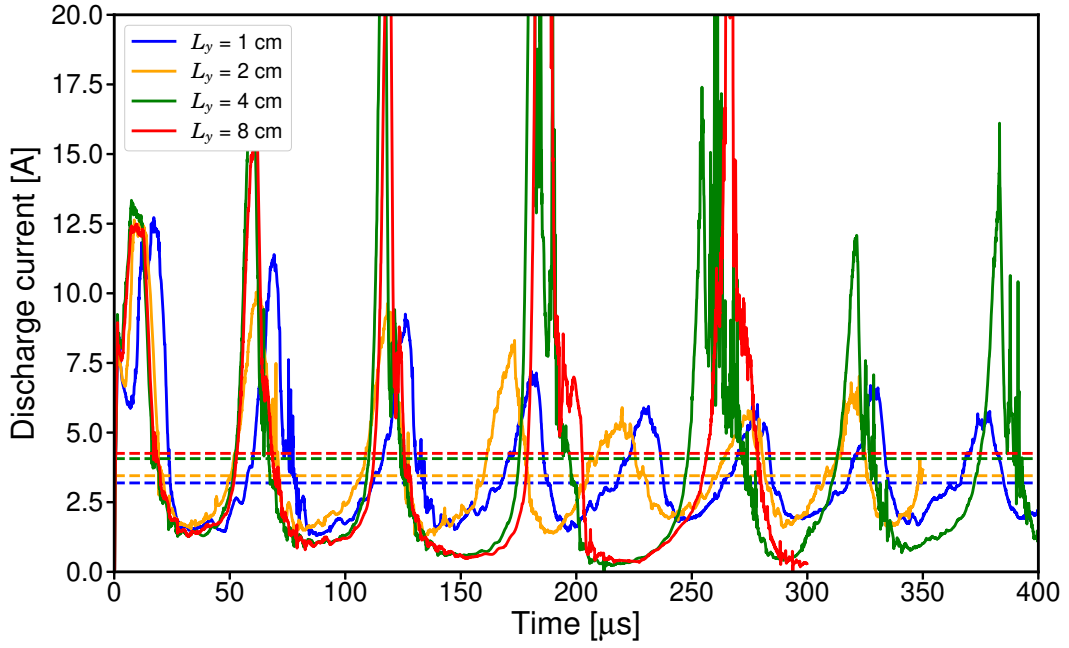


Figure 6.9 – $\alpha_\epsilon = 64$: Time evolution of discharge current for 4 values of azimuthal length L_y . The dashed horizontal lines correspond to the mean value at steady state.

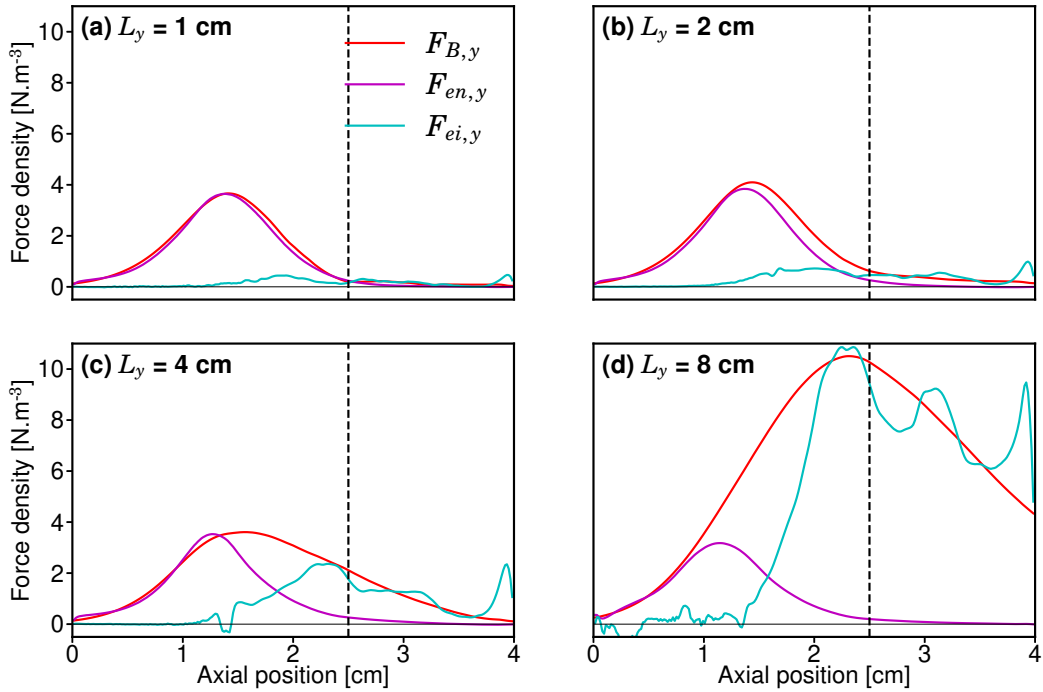


Figure 6.10 – $\alpha_\epsilon = 64$: Azimuthal electron momentum terms averaged over several BM oscillations, for different values of L_y . The red line corresponds to $F_{B,y} = -qn_e Bv_{e,x}$, related to the axial electron transport. The cyan $F_{ei,y}$ line corresponds to the instability-enhanced drag force on the electrons. The magenta line corresponds to the electron-neutral collision term $F_{en,y}$.

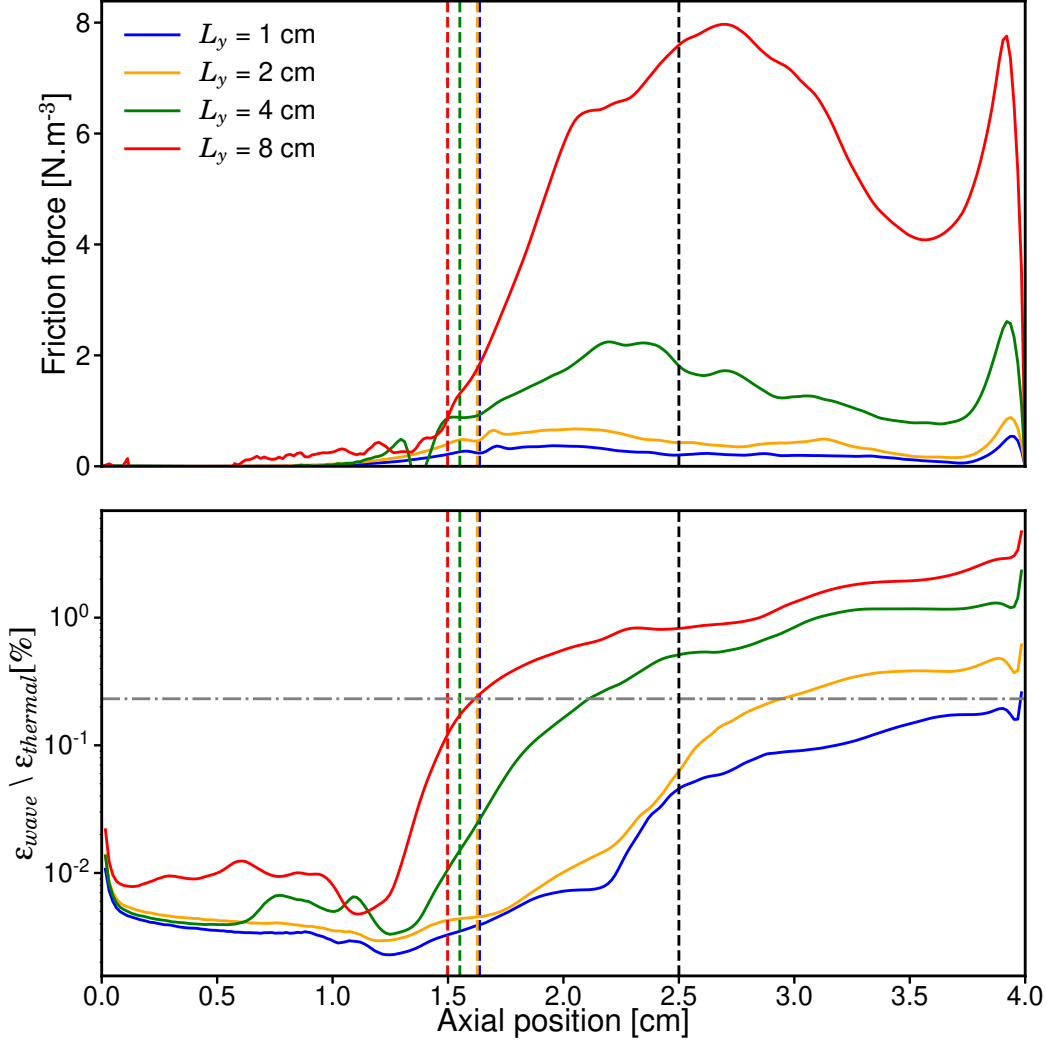


Figure 6.11 – $\alpha_\epsilon = 64$: Averaged profiles over several BM oscillations (and azimuthally), for different L_y , of: (a) Electron-ion friction force. (b) Ratio of the wave energy density to the electron thermal energy density. Horizontal grey dot-dashed line: ion-wave trapping saturation limit (Eq. 4.29). Vertical coloured dashed lines: axial position of ion sonic point ($v_{ix} = c_s$). Black dashed line: position of maximum magnetic field.

ratio $\frac{\epsilon_{wave}}{\epsilon_{th}}$ is higher than this saturation limit which means that the instabilities are behaving differently.

Plasma fluctuations

Similarly to figures 5.17 and 5.18 for the case $\alpha_\epsilon = 4$, we have displayed in figure 6.12 the axial and time evolution of the plasma fluctuations during one BM oscillation $\alpha_\epsilon = 64$ and $L_y = 8$ cm, with specific axial profiles at different moments of a BM oscillation in figure 6.13. First, we can see that again the ion sonic point corresponds to a transition towards an instability which is not convected axially and exhibits high amplitudes when the discharge current decreases. This time, the link with the ITTI can be easily observed on the evolution of the axial electric field which exhibits strong oscillations originating from the sonic point, with an high amplitude when the discharge current decreases.

Moreover, contrary to the case $\alpha_\epsilon = 4$, there are almost no fluctuations between the position of null axial velocity and the sonic point: it seems that the EDI growth is almost negligible there. This behaviour was expected looking at the null friction force in this zone (figure 6.11(a)) and it is mainly a consequence of the high scaling factor ($\alpha_\epsilon = 64$) used.

Finally, one can notice that, as seen already in figure 6.11(b), there is no ion-trapping saturation of $\frac{\langle \delta n_e \rangle}{n_e}$ any more. Additionally, we no longer have the equality $\frac{\langle \delta n_e \rangle}{n_e} \approx \frac{\langle \delta \phi \rangle}{T_e}$ due to a level of potential energy fluctuations increasing significantly in the plume compared to the plasma thermal energy. It was expected because the ITTI is not a kinetic instability and it could mean that the quasi-linear kinetic theory used before is not valid any more in this particular zone.

However, it seems to contredict the azimuthal IVDF displayed in figure 6.14 when I_d decreases: whereas no ion-trapping is present for the cases $L_y = 1$ cm or $L_y = 2$ cm, for higher azimuthal length, we observe a trapping for $x \geq 2$ cm, with a trapped velocity increasing with L_y . This surprising behaviour is not fully understood yet.

To get more insights on this wave energy dependency with L_y , we will study in the next subsection the azimuthal instabilities characteristics.

6.2.2 Azimuthal instabilities

As in the previous chapter, 2D snapshots of the azimuthal electric field for different L_y have been displayed in figures 6.15 (when I_d increases) and 6.17 (when I_d decreases), with again a transition corresponding to the ion sonic point. The corresponding 2D FFT have been calculated at two different axial positions (upstream and downstream of the ion sonic point) and are shown in figures 6.16 and 6.18 respectively, with again a time range of 5 μ s.

Upstream of the sonic point, it is hard to distinguish the azimuthal oscillations because of the colormap scale (as seen above, their amplitude are very small),

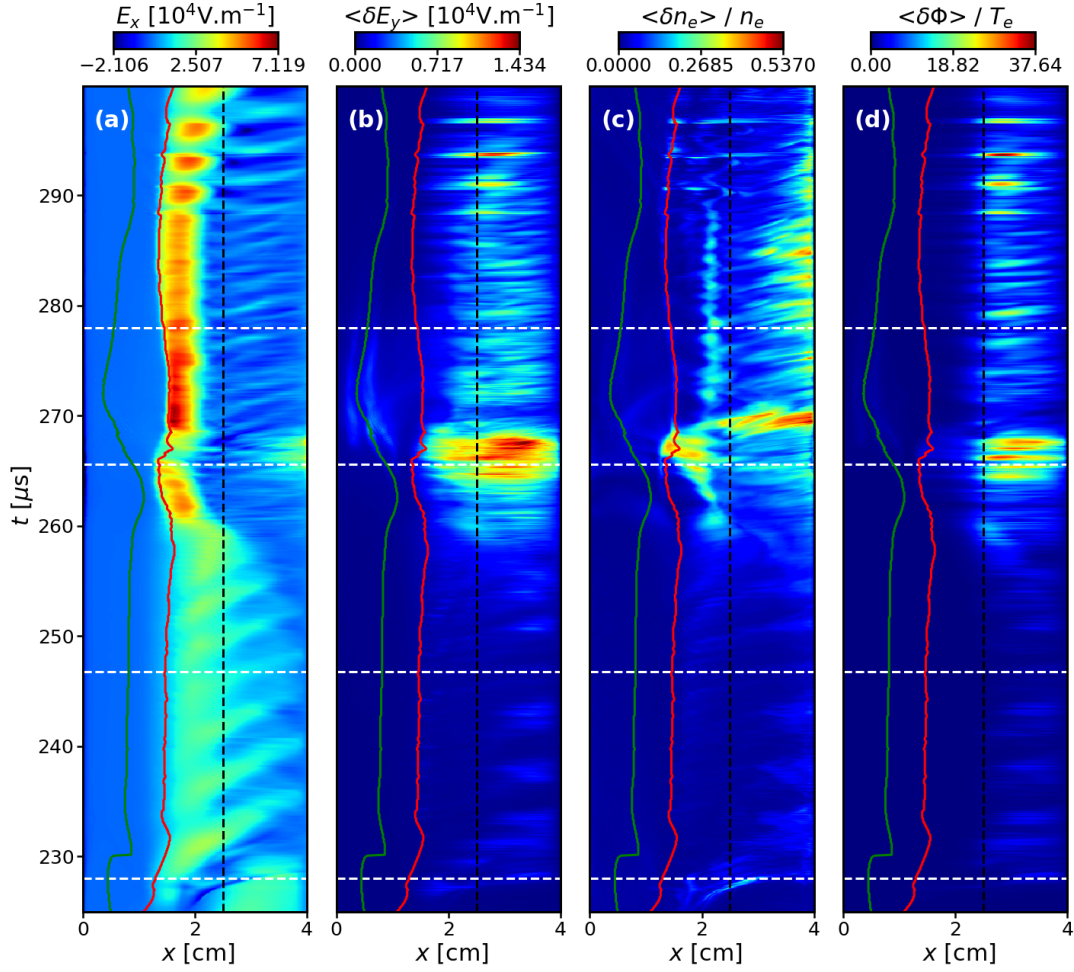


Figure 6.12 – $\alpha_\epsilon = 64$, $L_y = 8$: Time and axial evolution during one BM oscillation of: (a) axial electric field, (b) azimuthal electric field, (c) normalized electron density and (d) normalized plasma potential fluctuations. Green vertical curve: axial position of null ion axial velocity. Red vertical curve: axial position of ion sonic point ($v_{ix} = c_s$). Horizontal white dashed line: moments used to compute figure 6.13 (I_d maximum at $t=266\mu s$). Vertical black dashed lines: axial position of maximum magnetic field.

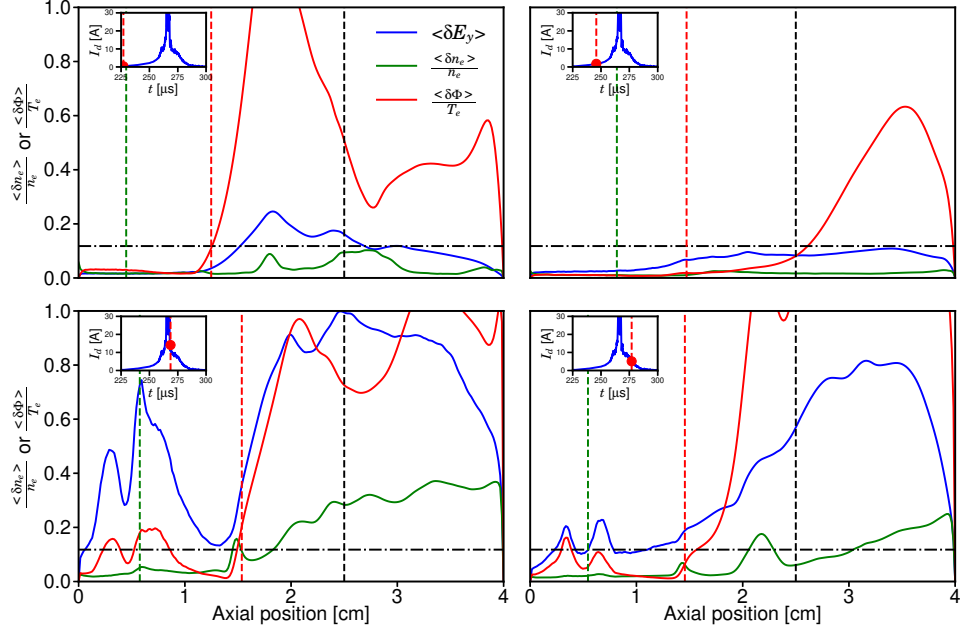


Figure 6.13 – $\alpha_\epsilon = 64$, $L_y = 8$: Axial profiles of the azimuthal electric field (divided by 5×10^3), normalized electron density and normalized plasma potential fluctuations for different moments of a BM oscillation. Vertical green dashed lines: axial position of null ion axial velocity. Vertical red dashed lines: axial position of ion sonic point ($v_{ix} = c_s$). Vertical black dashed lines: Axial position of maximum magnetic field. Horizontal black dashed lines: expected amplitude for a fully-saturated ion-acoustic instability i.e. $\frac{1}{6\sqrt{2}}$. Inset: Time evolution of discharge current, red dot indicating the corresponding time.

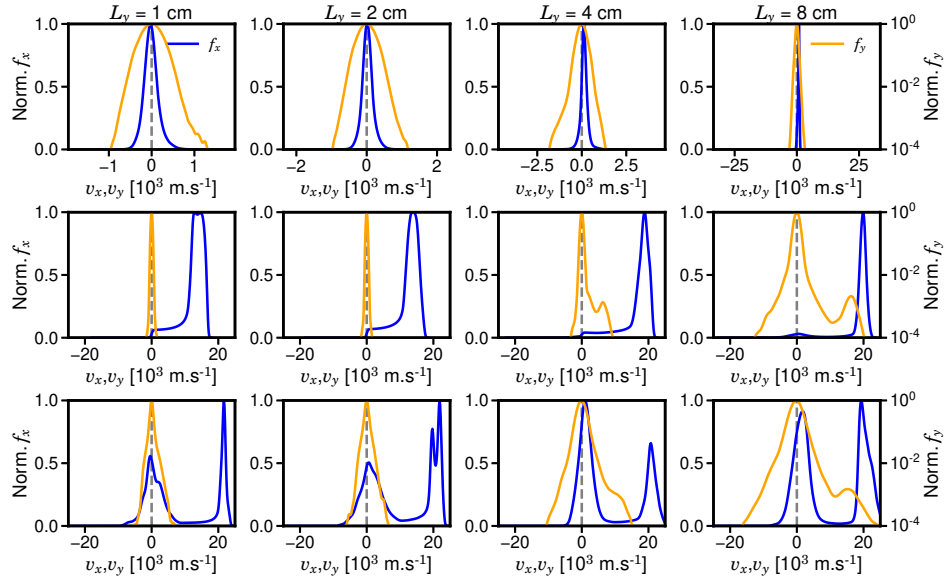


Figure 6.14 – $\alpha_\epsilon = 64$: Axial (blue) and azimuthal (orange) IVDF for 3 axial positions (rows) and for 4 values of L_y (columns) when I_d decreases. Careful, the azimuthal IVDF y-axis has been put in log-scale for the best display.

but the corresponding 2D FFTs (at $x = 1$ cm) show that for all the cases, the dispersion relation is very close to a modified ion-acoustic DR. However, it is more complicated to analyse the behaviour when the ions are supersonic. Indeed, the spectrum tends to be more discrete with a long-wavelength peak which tends to smooth out when I_d increases and gets close to the modified ion-acoustic DR. From the 2D snapshots of E_y , we can see that there is a long-wavelength oscillation which is over-imposed on the usual short-wavelength oscillation and form big "blobs" of azimuthal electric field, which propagate azimuthally and vanish periodically. Its wavelength seems to depend on L_y , with $m = 1$ being the dominant mode. We can also see it on the FFT for which the peak goes toward low-wavenumber when L_y increases. This behaviour is probably related to the previous observations on the increased axial transport (and wave energy), when L_y is increased.

Finally, the Power Spectral Distribution (PSD) for the azimuthal electric field (computed with the function `signal.welch` from the `scipy` package [227]) is shown in figure 6.19 for different axial position with $L_y = 8$ cm. We can see more clearly the transition from short to long wavelengths at $x = 2$ cm and $x = 3$ cm. This phenomena could be related to the "inverse energy cascade" which has recently been observed in other PIC simulations [87, 72]: more energy will then be carried by this long-wavelength structures, explaining the wave energy increase.

All in all, we have seen that, along with the well-known Breathing Mode and Electron Drift Instabilities, another instability was developing in the Hall thruster: the Ion Transit-Time instability. Contrary to what was observed by Coche *et al.* [76], this instability seems to be present throughout the whole BM oscillation (not only when the discharge current is decreasing) but because the EDI is stronger when the discharge current increases, it is more difficult to observe the ITTI during this phase. Moreover, the higher density inside the thruster also enhances the EDI which explains why the effect of the ITTI is more visible in the plume. This behaviour pledges in favour of the theory of Fernandez *et al.* [225] who found that the ITTI growth rate was inversely proportional to the electron mobility ($\propto \mu_e^{-1/2}$): hence, the high mobility inside the thruster and during I_d growth (enhanced by the EDI) could be the one damping this ITTI. This damping of axial modes due to the strong electron mobility was also recently retrieved by Smolyakov *et al.* [228] with 1D fluid and hybrid models. Finally, the EDI in the plume is also strongly affected by the ITTI, probably because the ITTI causes a change of the local plasma parameters.

Even though we managed to highlight the importance of the ion sonic point, the interaction between the ITTI and the EDI is still mostly not understood. To get more insights, we will thicken our analysis in the next section, with additional information from the simplified benchmark case of chapter 3.

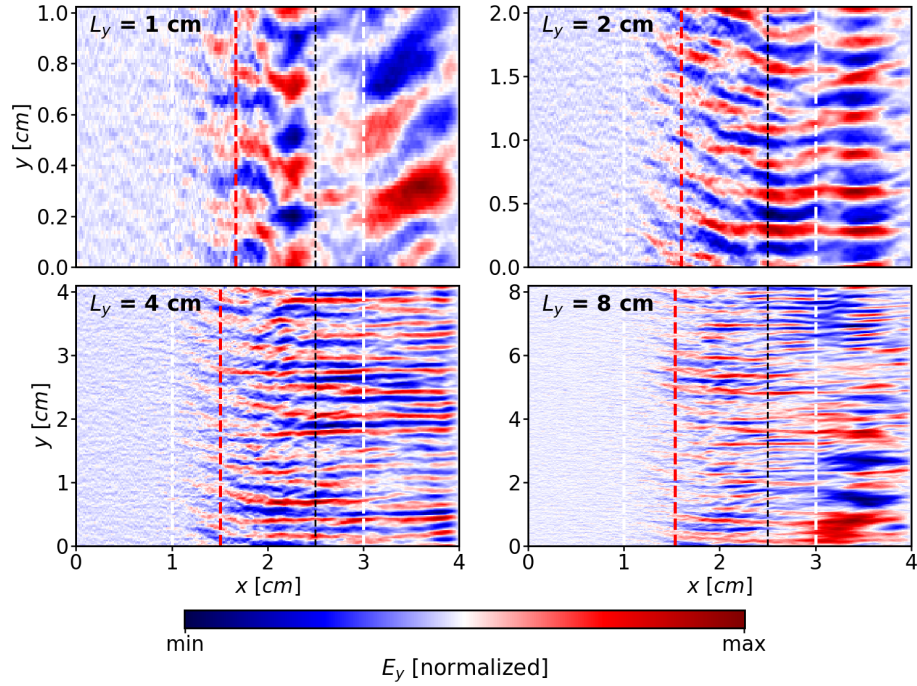


Figure 6.15 – $\alpha_\epsilon = 64$: 2D maps of azimuthal electric field for different L_y , when I_d increases. Red dashed lines: axial position of ion sonic point ($v_{ix} = c_s$). White dashed lines: axial position of FFTs (figure 6.16). Black dashed line: position of maximum magnetic field.

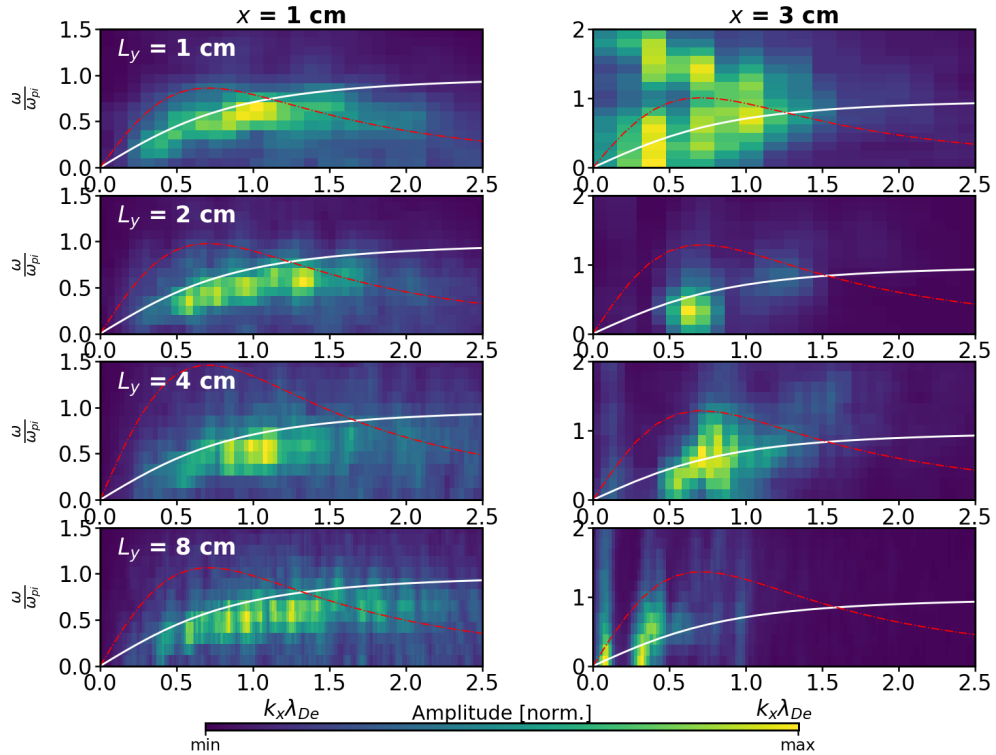


Figure 6.16 – $\alpha_\epsilon = 64$: Corresponding FFT for $x=1$ cm (left column) and $x=3$ cm (right column), when I_d increases. White thick line: ion-acoustic dispersion relation. Red dashed lines: ion-acoustic growth rate rescaled by a constant factor to fit the image. The spectrum has been zoomed to focus on the zone of interest.

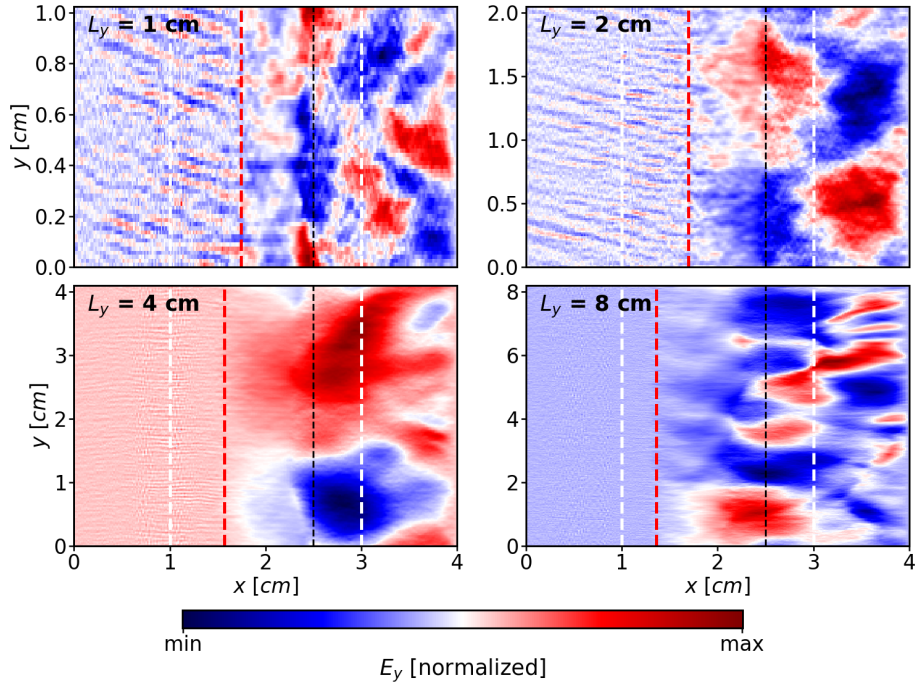


Figure 6.17 – $\alpha_\epsilon = 64$: 2D maps of azimuthal electric field for different L_y , when I_d decreases. Red dashed lines: axial position of ion sonic point ($v_{ix} = c_s$). White dashed lines: axial position of FFTs (figure 6.18). Black dashed line: position of maximum magnetic field.

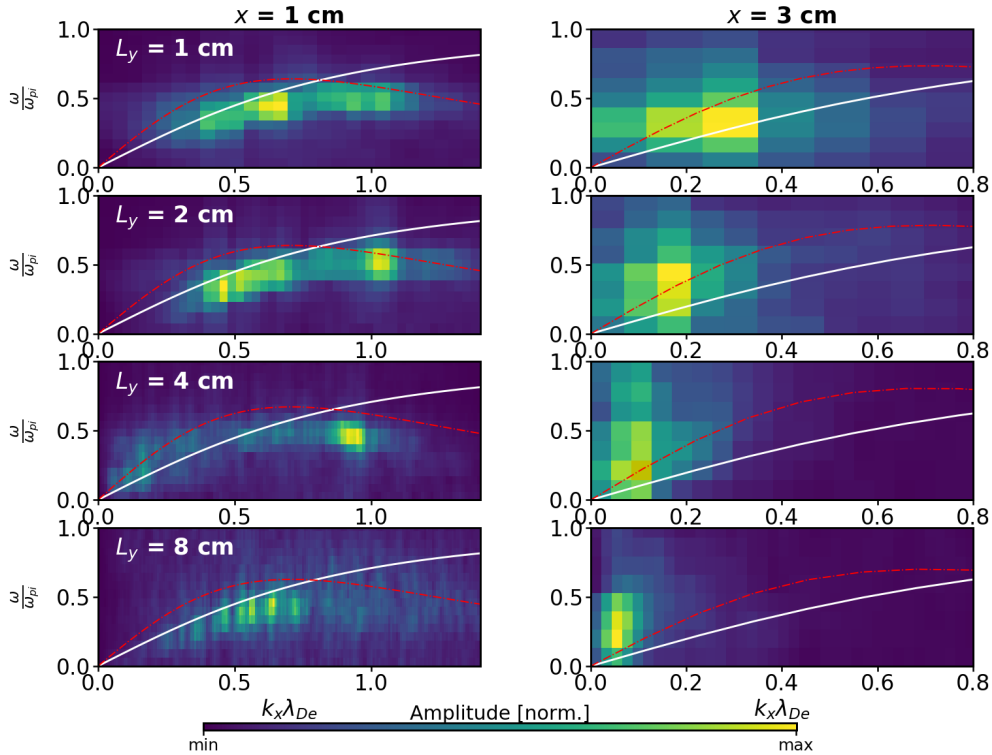


Figure 6.18 – $\alpha_\epsilon = 64$: Corresponding FFT for $x=1$ cm (left column) and $x=3$ cm (right column), when I_d decreases. White thick line: ion-acoustic dispersion relation. Red dashed line: ion-acoustic growth rate rescaled by a constant factor to fit the image. The spectrum has been zoomed to focus on the zone of interest.

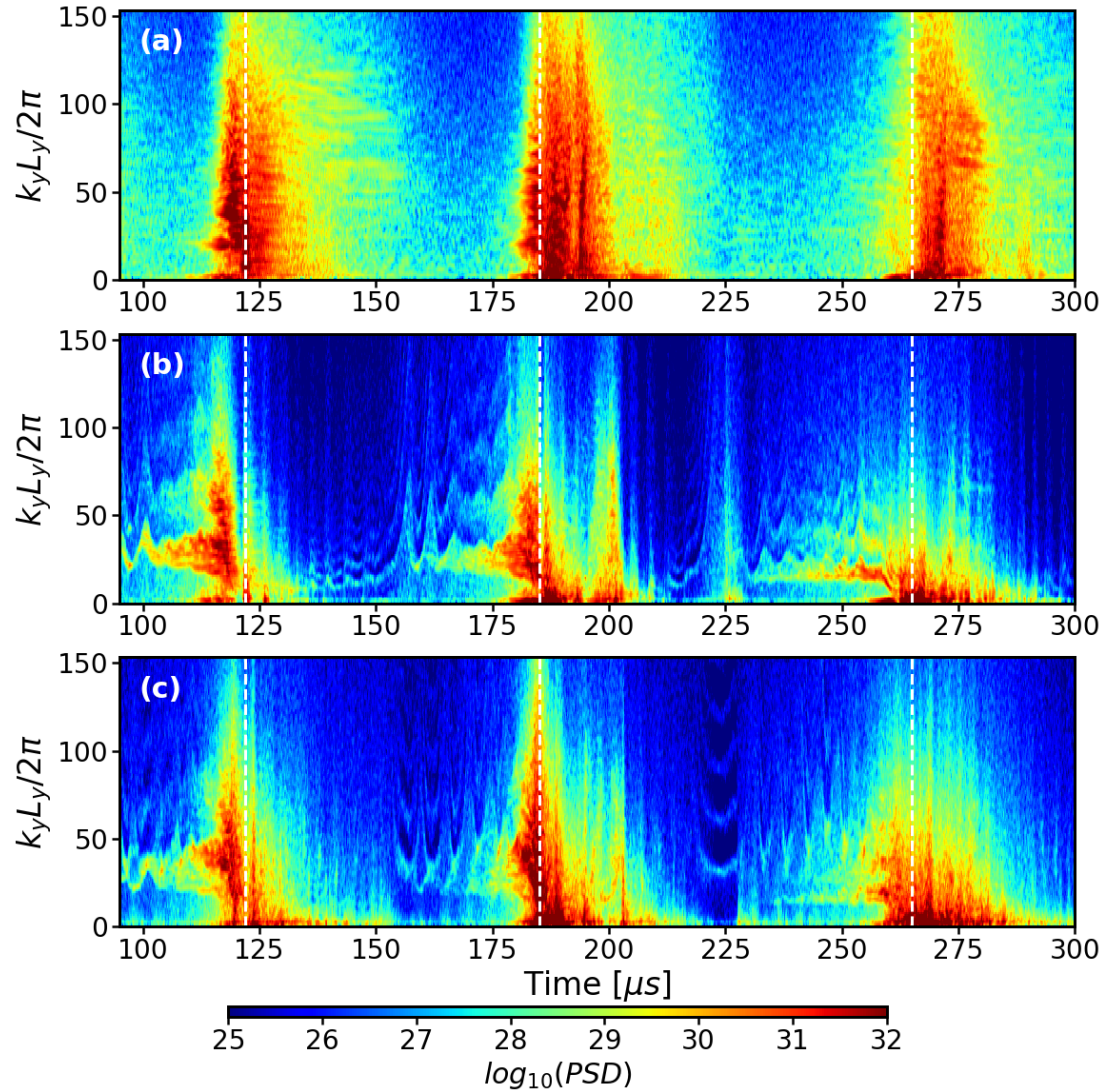


Figure 6.19 – $\alpha_\epsilon = 64$, $L_y = 8$ cm: PSD of azimuthal electric field at (a) $x = 1$ cm, (b) $x = 2$ cm and (c) $x = 3$ cm. The white vertical dashed lines correspond to moments when the discharge current is maximum.

6.3 Interaction between ITTI & EDI

6.3.1 Preliminary analysis on the self-consistent simulations

To decouple these two instabilities, we used Dynamic Mode Decomposition (DMD) [229] on the simulation results. In a few words, DMD is a data-driven method that gives the dominant spatial temporal coherent modes of a signal. The algorithm that we developed, based on the library Antares [230], can then reconstruct the signal with specific modes. We applied this DMD method to the 2D snapshots of azimuthal electric field to find the two modes corresponding to EDI and ITT, identifying them as respectively the small-wavelength azimuthal instability and the long-wavelength axial instability.

However, the process is not as straightforward as expected: the DMD algorithm finds many modes with close frequency values and it is hard to reconstruct specifically the one corresponding to the ion transit-time instability. To alleviate this constraint we can gather all the modes in a chosen range of frequencies. For example, we have displayed in figure 6.20 the different modes for the case $\alpha_\epsilon = 64$ with $L_y = 4$ cm, just after the discharge current maximum. We can see on the bottom row that we captured almost all the original signal and at that particular moment, we retrieve the strange behaviour observed previously in section 6.2: while in the thruster, small-wavelength instability are propagating, in the plume a long-wavelength instability with a mode $m = 1$ appears. Thanks to this DMD analysis, we can see that this small-wavelength instability exhibits a high-frequency behaviour (1-4 MHz), while the long-wavelength one has a mid-range frequency of 100-500 kHz. Hence, we can relate the former to the EDI and the latter to the ITT.

However, this DMD analysis is more qualitative than quantitative. To get more insights, the Power Spectral Density (PSD) of the ion density fluctuations $\delta n_i = n_i - \langle n_i \rangle$ has been computed over several breathing modes oscillations, at different axial positions, for different α_ϵ and $L_y = 1$ cm (figure 6.21) and different L_y and $\alpha_\epsilon = 64$ (figure 6.22).

First, we can see in figure 6.21 that when α_ϵ is decreased, the amplitude of the high-frequency peak is more important and, as expected, the corresponding frequency value is increased. On the contrary, the low-frequency content between 100 and 500 kHz has a smaller amplitude. We retrieve the fact that for all the cases, inside the thruster, the high frequency content dominates, while outside the thruster, the low-frequency content is more important. These plots echo with what has been recently observed experimentally by Brown and Jorns [81], with similar ranges of frequencies inside and outside the thruster.

Then, if we perform the same analysis for different values of azimuthal length, we can see in figure 6.22 that the high frequency content does not seem to depend on L_y , especially inside the thruster. It is comforting because it means that the EDI is not affected by the azimuthal domain length. On the contrary, the low-

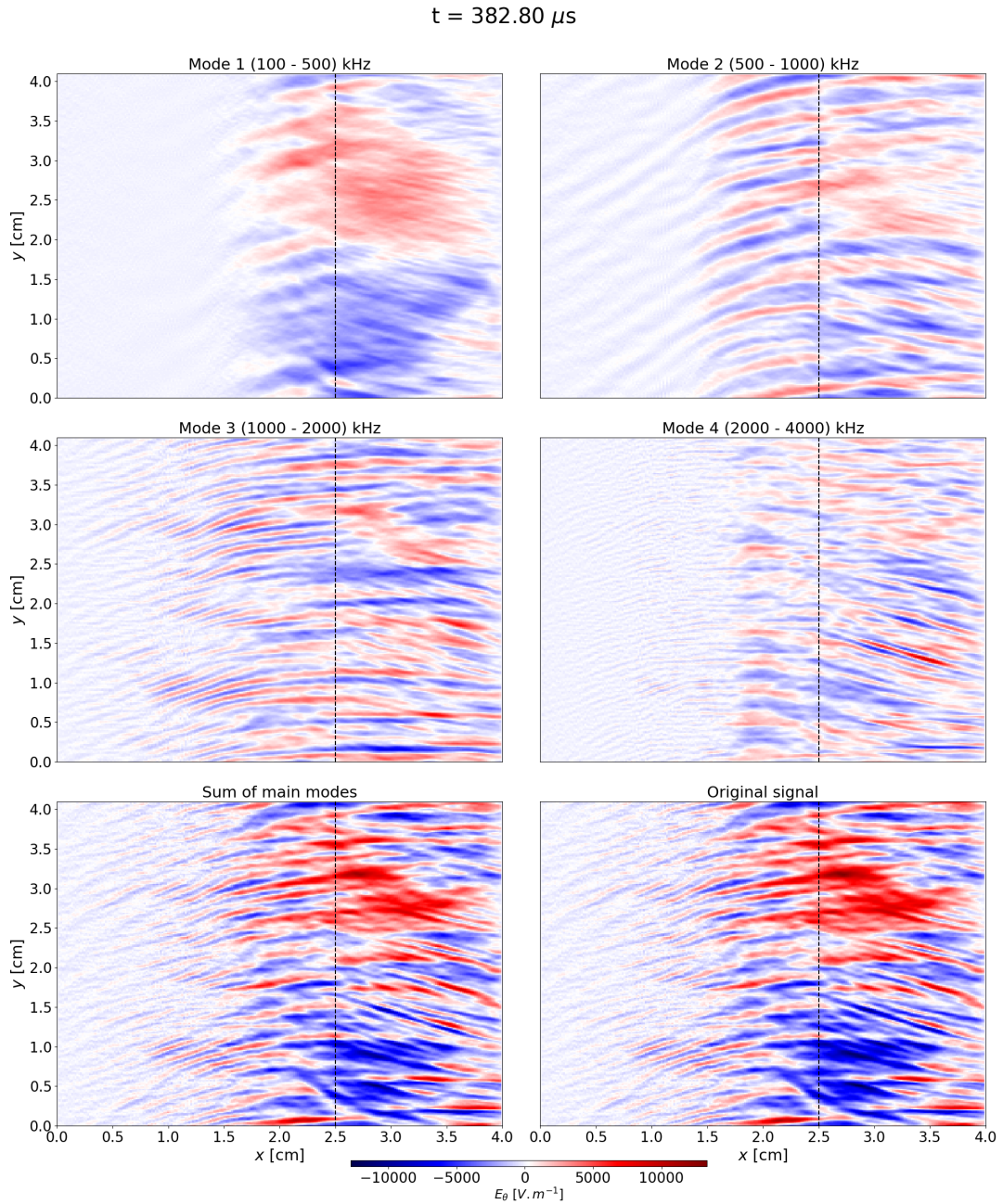


Figure 6.20 – $\alpha_{\epsilon} = 64$, $L_y = 4$ cm: Dynamical Mode Decomposition at a specific time. Mode 1 corresponds to the sum of the modes between 100 and 500 kHz, Mode 2 between 500 kHz and 1 MHz, Mode 3 between 1 and 2 MHz, Mode 4 between 2 and 4 MHz. The sum of all these modes is compared with the original signal on the bottom row. All the images have the same colorbar range.

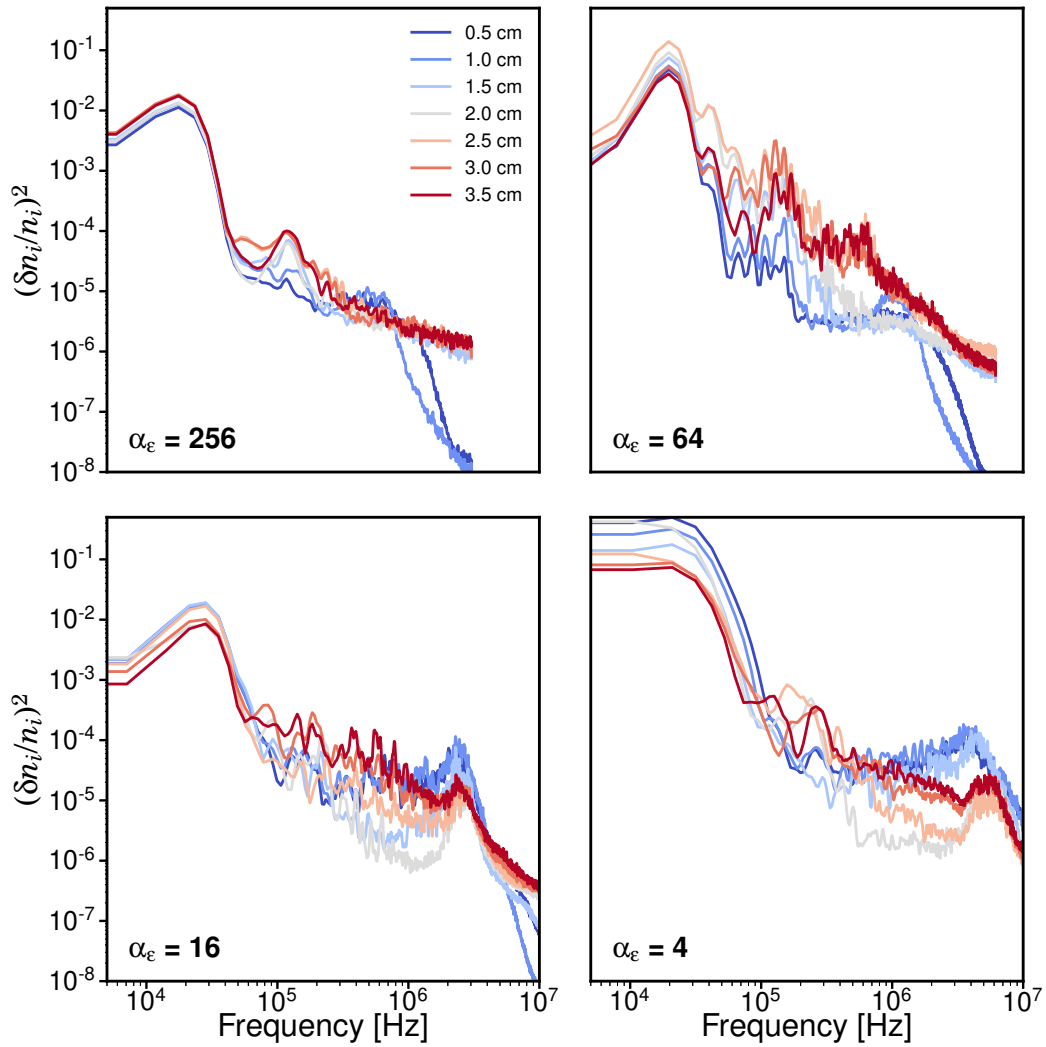


Figure 6.21 – $L_y = 1$ cm: Power Spectral Density of ion density fluctuations normalized by the ion density for different values of α_ϵ , at different axial positions.

frequency content seems to be shifted to higher frequency when L_y is increased, and more importantly, the overall level of fluctuations increases with L_y , which was already observed previously and is still not understood.

All in all, from what we have observed until now, it seems clear that an ITTI is developing inside the HT, characterized by an axial electric field perturbation. This perturbation is then interacting with the EDI which tends to damp it by increasing the electron mobility. However, the mechanism behind this interaction has not been studied theoretically and hence, the assumption that the long-wavelength oscillation of the azimuthal electric field (in the plume) stems from this interaction might be a bit bold. The self-consistent simulation results have been extensively post-treated and the next step would be to develop an analytical theory. However, prior to this heavy work, one last insight can be obtained by using another simulation case: the simplified benchmark case of chapters 3 and 4.

6.3.2 Insights from the simplified benchmark case

Indeed, the azimuthal domain length for the simplified benchmark case was limited to 1.28 cm. To relate with the results for the self-consistent cases, we have taken the more extreme case (with still a reasonable computational time) and we have increased this L_y to 10 cm, keeping the same cell size (8 times more azimuthal cells). The 2D snapshots of azimuthal electric field at steady-state has been displayed in figure 6.23, along with the corresponding FFT (performed on 10 μ s) at two axial positions. We can see that no long-wavelength structure is developing (similarly to the preliminary results of Powis *et al.* [219]) and that the azimuthal instability have a dominant wavelength close to the one predicted by the modified ion-acoustic dispersion relation (equation 4.18). However, whereas the modified ion-acoustic DR fits perfectly the spectrum inside the thruster, it is not the case any more in the plume. Following the work of Tavant [120], we overlapped at this position the modified ion-acoustic DR with the plasma parameters of the axial position $x = 0.5$ cm, which corresponds approximately to the origin of the EDI growth (maximum of plasma density). The good agreement obtained with this shifted DR led us to the conclusion that when the EDI is convected from the position where it has grown, it keeps some of its characteristics. Whereas we observed in this particular case that it was the wave velocity that was conserved, more work is needed to confirm this observation.

Finally, it is important to mention that contrary to what was initially presumed in chapter 4 and [185], the two zones for the azimuthal instabilities are not separated by the maximum of magnetic field but instead, it corresponds again to the position of the ion sonic point (not shown in figure 6.23 as it overlaps almost perfectly). We have also verified that in the case of the nominal benchmark case (figure 3.8), the shifted modified ion-acoustic DR is fitting well the measured spectrum in the plume.

With this simple analysis, we have shown that no long-wavelength structure

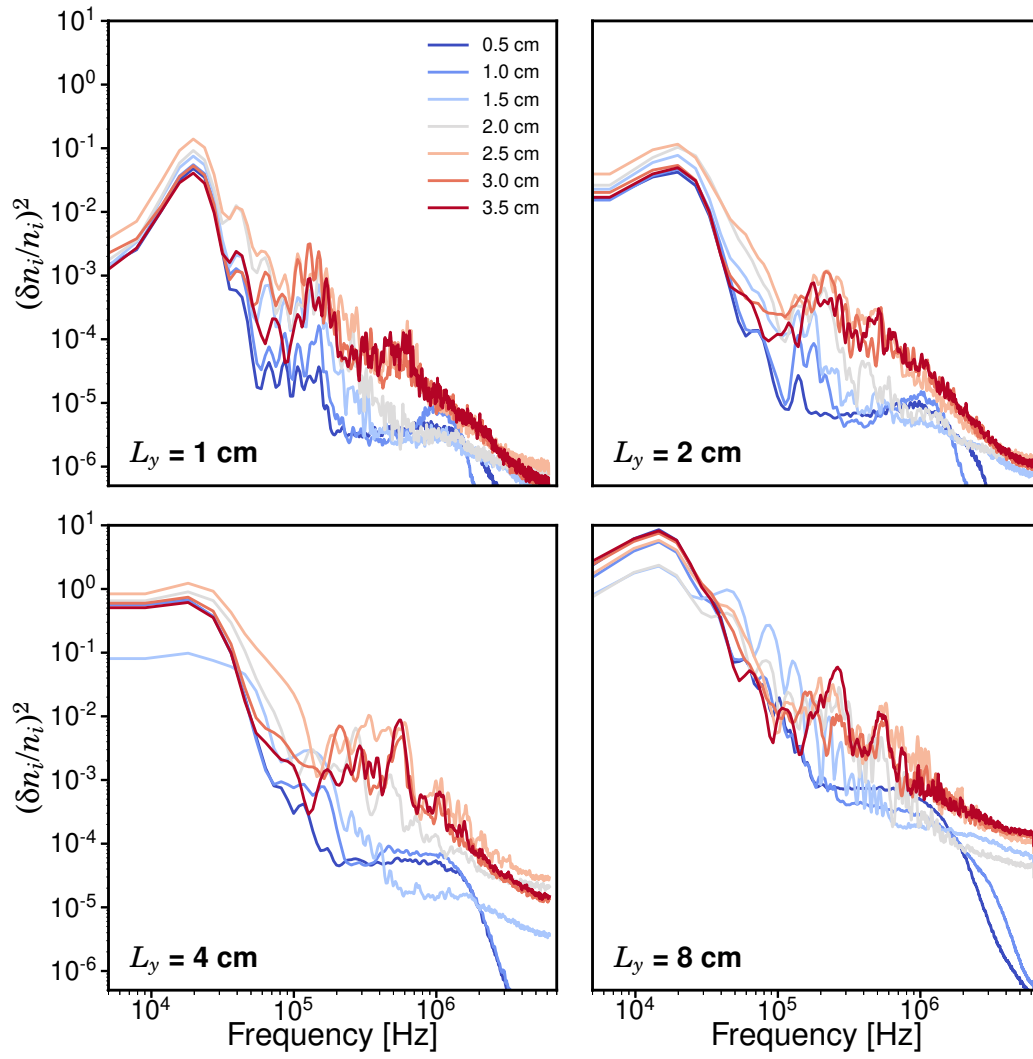


Figure 6.22 – $\alpha_\epsilon=64$: Power Spectral Density of ion density fluctuations normalized by the ion density for different values of L_y , at different axial positions.

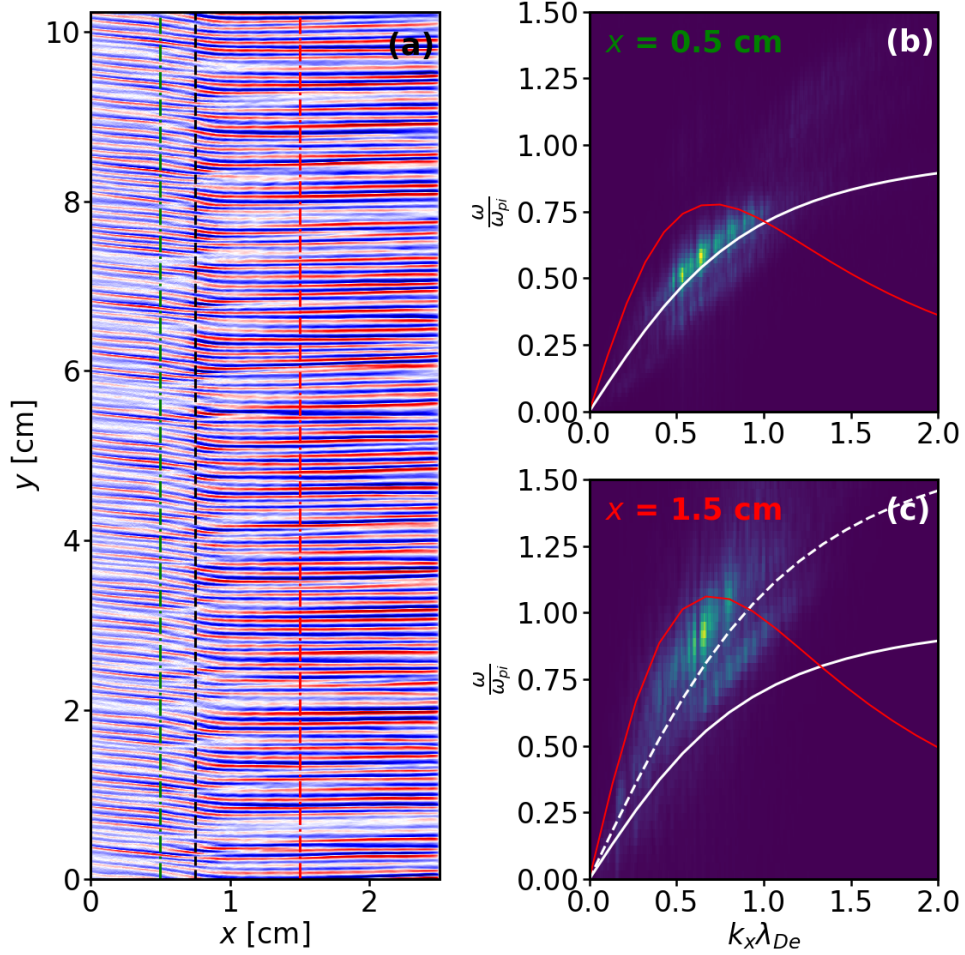


Figure 6.23 – **Benchmark case with $L_y=10$ cm:** (a) 2D maps of azimuthal electric field at $t = 26 \mu s$. The green and red vertical dashed lines indicates the position of the FFT. The black vertical dashed line corresponds to the position of maximum magnetic field. (b) Corresponding 2D FFT at $x=0.5$ cm. (c) Corresponding 2D FFT at $x=1.5$ cm. White thick line: local ion-acoustic dispersion relation. White dashed line: ion-acoustic dispersion relation convected from $x=0.5$ cm. Red dashed line: ion-acoustic growth rate rescaled by a constant factor to fit the image. The spectrum has been zoomed to focus on the zone of interest.

was appearing in the simplified benchmark case, despite the use of a very long azimuthal domain length. Again, we should keep in mind that this case has many limitations but it still gives us an important insight on the azimuthal instabilities behaviour in 2D axial-azimuthal simulations: in absence of BM or ITT oscillations, there is no inverse energy cascade towards long-wavelength structures.

Finally, one can wonder why the ITTI does not seem to grow in this simplified benchmark case. The first hypothesis stems from the imposed ionization source term which is seen to oscillate similarly than the axial electric field during one ITT oscillation in the self-consistent simulations. Having a constant source term could then preclude the on-set of the ITTI. Moreover, another hypothesis relates this absence of ITTI to a different axial position of the ion sonic point. Indeed, we have observed that because of the short distance between the maximum magnetic field and the anode, the ion sonic point was always located downstream of the exit plane, i.e. in a region where the magnetic field gradient was negative. Even though we have still no clue if it is this negative magnetic field gradient which is damping the ITT, it is certain that the stability condition are linked to the sonic behaviour of the ions and the local plasma conditions (maybe the local ion current fraction as presumed in [224]). More work is still in progress to see if we observe an ITTI in simulation cases with an extended discharge channel length (to obtain a sonic point upstream of the magnetic field maximum, similarly to the self-consistent simulations) or an artificially modulated ionization source term.

6.4 Conclusion

The analysis performed in this chapter was motivated by a surprising observation: downstream of the ion sonic point, when the discharge current decreases, a long-wavelength azimuthal instabilities is developing, superimposed on the usual short-wavelength EDI. Recently, many people in the $\mathbf{E} \times \mathbf{B}$ community were convinced that there is an inverse energy cascade towards long wavelength modes in the Hall thruster plume (experimentally [81] and numerically [71, 87, 88, 79]). However, this phenomena was never observed in simulations including the HT axial direction and moreover, it is scarcely understood theoretically. Here, we have found that these long-wavelength modes were appearing at the same time than an axial instability known as the ion-transit time instability.

This ITTI has been poorly studied and hence, we decided to first shed light on this hundreds-kHz instability by removing any azimuthal oscillations. Even though their main characteristics (frequency, low-energy ion population in the plume, ion wave-riding) were retrieved, their origin still remains unclear. They seem to be related to the ion sound speed, as the axial electric field wave is growing at the position where the ions become supersonic. However, more work is still needed, using simpler models, such as 1D axial fluid ones, and perturbation analysis.

Coming back to the self-consistent simulations, we managed to highlight the presence of this ITTI in the simulations presented in the previous chapter. We

studied its interaction with the EDI by first looking at the influence of the azimuthal domain length on these long-wavelength structures. It appeared that while an increase of L_y had almost no effect on the EDI propagating upstream of the sonic point, it was significantly enhancing the wave energy (and hence the friction force and the axial electron transport) in the region where the ions are supersonic. Because of this increase of the wave energy compared to the thermal energy, the quasi-linear kinetic theory was not applicable there any more. Moreover, we found that the wavelength of these large structures was almost proportional to L_y , with $m = 1$ being the dominant mode: it could explain why the cases with $L_y = 1$ cm or $L_y = 2$ cm were quite similar: maybe the wavelength of these large structures is around 8 cm and they were not able to fit in a smaller periodic box. A simulation case with a longer L_y could then be of use to confirm this hypothesis.

The apparition of these long-wavelength instabilities, along with the significant increase of wave energy, pledged in favour of the inverse energy cascade hypothesis. However, from what we have observed in the self-consistent simulations and the fact that no long-wavelength structure was developing for the simplified benchmark case with a long azimuthal domain length, it made us think that these large structures are stemming from the interaction between the EDI and the ITT. The latter is affecting the local plasma parameters in such a way that the EDI is no longer saturated and the wave energy keeps increasing. This was already observed in a 2D fluid framework [88] in which the axial resistive modes were found to destabilize the azimuthal modes, generating large scale structures and enhancing the axial electron transport via an inverse energy cascade. It would be interesting to study to which extent this fluid analysis could apply to our PIC results.

Finally, it is important to mention that these changes of azimuthal domain length were performed for a relatively high scaling factor of $\alpha_\epsilon = 64$. For lower α_ϵ , we have already observed in the previous chapter that, upstream of the ion sonic point throughout the whole BM oscillation, and also downstream when the discharge current is decreasing, the EDI was growing with the "usual" behaviour, well-approximated by quasi-linear kinetic theory. Following previous observations [46, 59, 225], we made the hypothesis that the high electron mobility was damping the ITTI, hence preventing any EDI/ITTI interaction. Hence, it is possible that in "real" cases with no artificial scaling, the EDI growth rate will be strong enough to damp the ITT, even downstream of the ion sonic point in the BM phase of decreasing current, hence reducing this wave energy increase for longer azimuthal domain lengths. This hypothesis requires further investigations (lower α_ϵ with longer L_y) that are very computationally expensive and remain unfortunately out of scope of this work.

Chapter 7

Conclusion

7.1 Summary of the thesis

If we put in perspective the results obtained in this work with the significant number of published papers on Hall Thrusters these last two decades, we can capture a glimpse of the complexity of these devices. Due to the relatively low demand at the early beginning of the 21st century, the main HT manufacturers were able to build thrusters in a narrow range of power, by using try-and-error methods, through long and costly experimental tests. The breakthrough of the New Space industry in the last decade was a game-changer, along with the one of full-electric satellites. A broad range of thruster powers and sizes are now required for a variety of space missions and the HT manufacturers need to find more efficient methods to quickly build efficient thrusters.

This work belongs to this framework of developing numerical models which could help HT designs. As we have seen in chapter 1, even though fluid models are faster and less computationally expensive, they currently use several assumptions that preclude any self-consistent thruster simulations: for example, the plasma/wall interactions are often poorly accounted for, due to the quasi-neutrality assumption, and more importantly, no self-consistent, first principles, model exist for the axial electron "anomalous" transport. Most of the works on HT are trying to palliate the latter issue and understand how to account properly for this anomalous transport. Whereas at first, the plasma/wall interactions were thought to be the main origin for this transport, it appeared that they seem to have a smaller influence compared to the azimuthal instabilities propagating in the thruster, mostly the Electron Drift Instability.

Because these instabilities are kinetic in nature, they can only be studied via Particle-In-Cell codes which are unfortunately quite demanding in term of computational requirements. Despite the significant improvements on the computational hardware (more powerful CPU, GPU, etc.) and the development of efficient parallelisation techniques (MPI, OpenMP, etc.) on large clusters, we are not yet able to simulate in 3D a real-size HT. Hence, we need to settle for only 2 dimensions, with sometimes even additional artificial scaling techniques

which can affect the discharge behaviour. In this work, we chose to simulate the azimuthal direction, to capture these aforementioned instabilities, while also including the axial direction to account for their convection and be able to compute engineering parameters such as the thrust or the specific impulse. A significant part of this work, summarized in chapter 2, is related to the changes made on *LPPic*, a 2D PIC code originally developed to simulate the HT radial-azimuthal directions. The two main changes to account for this axial direction were related to the modelling of the cathode and the dynamics of the neutral atoms. The former was not straight-forward due to the absence of any radial direction and we found that the neutral dynamics was playing a major role in the discharge behaviour. These new models were both extensively verified, either via specific tests, comparisons with other PIC codes (axial-azimuthal benchmark of chapter 3) or even parametric studies (such as the one for the cathode model of section 3.6). Finally, because of the important density gradients in the axial direction, it was also necessary to improve the code performances and develop specific algorithms to speed-up the code.

7.1.1 Importance of code verification

As *LPPic* is used by several users at the same time, for various applications (radial-azimuthal HT simulations, inductively coupled plasmas in GIT, etc.), an efficient collaborative development framework was needed, with the implementation of good coding practices (Git, Continuous Integration, etc.). Even though unitary tests, along with the 1D helium benchmark [156], were regularly performed to verify our results, it quickly appeared that we needed a simulation case closer to a HT configuration to verify *LPPic*. As described in chapter 3, we managed to make 7 independent PIC codes converge on similar results for a previously-defined benchmark simulation case. The purpose was manifold: the most obvious one was to develop a benchmark case which could be used to verify any 2D axial-azimuthal PIC codes of $\mathbf{E} \times \mathbf{B}$ discharges, but additionally, we started a broad collaboration between independent research groups, in the framework of the LANDMARK project. Hence, this first benchmark paved the way to new benchmarks in different configurations (the radial-azimuthal PIC benchmark being the most advanced one) and also to collaborative parametric studies, for which several independent codes can simulate a broad range of simulation cases, hence efficiently providing a huge database to study the HT physics. These collaborative parametric studies are still a work-in-progress but an example on the cathode model was given at the end of chapter 3. Additionally, this test-case has also been recently used to improve the analytical description of ions in fluid models. As this work is out of scope of this manuscript, the reader can refer to the corresponding publication for more information [231].

Nowadays, all this work towards code verification is crucial to increase our confidence in the results given by these more-and-more complex codes. As any code development can take months, or even years, it is compulsory to verify it

before trying to analyse any physical results. The benchmark case can also be used to test the code performance or the influence of specific numerical models. Hence, we hope that this axial-azimuthal benchmark will help improve PIC codes in the $\mathbf{E} \times \mathbf{B}$ community.

7.1.2 Origin of electron anomalous transport

This benchmark activity was not only useful to verify *LPPic* but we also used it to come back to the original purpose of this work: a better understanding of the electron anomalous transport. Indeed, due to its simplicity and relatively small computational requirements, this case was the perfect candidate to stress-test analytical developments. A quasi-linear kinetic theory was previously proposed by Lafleur *et al.* [70, 84] and verified only once on a specific axial-azimuthal self-consistent PIC simulation case, during the increasing part of a breathing mode oscillation [86]. We took this opportunity of using the simplified benchmark case and varying several input parameters to obtain a broad range of discharge behaviours and hence, be able to extensively test this kinetic theory. The results, given in chapter 4, were conclusive and it strengthened our confidence in considering the EDI as the main source of anomalous transport.

However, this work suffered from several limitations due mainly to the absence of collisions and the underlying imposed ionization source term, which were precluding the on-set of important HT instabilities such as the breathing mode or the ion transit-time instabilities. We alleviated these constraints by including a neutral dynamics solver, hence obtaining self-consistent simulations. Unfortunately, the strong plasma density fluctuations due to the BM oscillations are significantly increasing the computational requirements, to such an extent that a real simulation case is currently out-of-reach. We decided to use an artificial scaling technique, increasing the vacuum permittivity, to relax the PIC stability constraints and speed-up the simulations. Thanks to an efficient code parallelisation, we managed to reduce this scaling factor to a small value, hence simulating a case close to reality. Whereas we retrieved several characteristics previously observed in axial-azimuthal PIC simulations, we found that we could distinguish two zones for the azimuthal instabilities, depending on the sonic behaviour of the ions. Upstream of the ion sonic point, the plasma density is high and the EDI growth rate is important: the anomalous electron transport can be well approximated by the aforementioned quasi-linear kinetic theory. However, when the ions become supersonic, another instability is growing and propagating axially: the ITTI. While its growth is damped by the high electron mobility in the BM phase of increasing discharge current, it interacts with the EDI when the discharge current decreases, hence causing the formation of long-wavelength azimuthal structures, superimposed on the usual small-wavelength instabilities. It results in an enhanced anomalous transport in this region, which is currently not captured by the quasi-linear kinetic theory. In addition to these results, we studied the influence of the vacuum permittivity scaling factor in the rest of chapter

5 and we found that, as expected, the main effect of the scaling technique was to damp the EDI, hence reducing the anomalous transport.

The presence of the ITTI led us to a final analysis in chapter 6, with first a model simplification towards 1D axial simulations (by averaging the azimuthal direction) to study more specifically this instability. It appeared that the sonic behaviour of the ions was playing a major role on its on-set, as observed already for the "real" simulation cases. Even though its origin remains unclear, we decided to increase the domain azimuthal length to see how it was affecting the long-wavelength structures. We observed a dependence of their wavelength on this azimuthal domain length, along with a significant increase of the wave energy in the plume (and hence of the anomalous transport). This could be related to recent observations of an inverse energy cascade. Even though we are convinced that this phenomena stems from the interaction between the ITTI and the EDI, as indicated by an analysis on the simplified benchmark case with a long azimuthal domain length, the detailed mechanism is still not fully captured. A similar study on the effect of the azimuthal domain length with smaller scaling factors is needed to see to which extent this ITTI will be damped when the EDI will be stronger (hence increasing the electron mobility) and how it will affect the apparition of the long-wavelength azimuthal instabilities in the HT plume.

7.2 Recommendations and prospects

The initial objective of this PhD project was to take advantage of the highly-parallelised code *LPPic* to simulate the computationally-demanding axial-azimuthal HT configuration and find a way to self-consistently account for the electron anomalous transport in fluid codes. During these last three years, it lead us to different problems, from code development to code verification and finally, analytical analysis of the simulation results. This last task requires a strong theoretical background (especially on plasma wave theory) that was beyond the scope of this work. Even though we managed to collaborate with Lafleur who had developed the quasi-linear kinetic model for the friction-force, this was detrimental to an advanced analysis of the results obtained, particularly on the EDI/ITTI interaction. This could represent the first, and main, prospect for this work: the complexity of the PIC results would deserve a more extensive theoretical analysis, maybe via a collaboration with specialists in plasma wave theory or plasma turbulence.

Several other future works, which appeared relevant throughout the course of this project but were not explored due to a lack of time and/or resources, are detailed in the following.

7.2.1 Improvements of *LPPic*

An important prospect echoes back to the self-consistent simulations of the last two chapters: to be able to simulate HT configurations close to reality, with

no artificial scaling factor and a long azimuthal domain length, the code performances need to be improved. As mentioned earlier, this is a work-in-progress, with the help of the High Level Support Team at the National Computing Center for Higher Education. Several bottlenecks have already been identified and the first developments were promising (change of data structure for better memory management, removing of reverse loops for better efficiency, etc.): we have good hope of soon being able to simulate a case without artificial scaling.

Moreover, as already described in section 2.5, several new features should be added to *LPPic* to account for effects that are expected to play a role in the HT discharge behaviour. As shown by Tavant during his PhD thesis [120], the inclusion of a fake-radial dimension would decrease the plasma density, along with the electron temperature, hence damping the EDI. This should normally reduce the amplitude of plasma density fluctuations during the BM oscillations and hence speed-up the computation. Finally, we have seen that the axial ion dynamics was also playing an important role, via the ITTI. Hence, we think that it is important to account for the doubly-charged ions which represents around 10% of the ions and could also generate additional instabilities.

Finally, while performing self-consistent simulations, it quickly appeared that the neutral dynamics was playing a major role on the discharge behaviour. Even though we solved the full Euler equations, accounting for the variable neutral velocity, more work might be needed to account for the variation of neutral temperature or the recombination of the ions when hitting the "fake" walls. But most importantly, as mentioned before, the RLC circuit used between the power-supply and the thruster to damp the BM oscillations should be accounted for. The inclusion of this circuit to *LPPic* is expected to be quite complicated numerically as we might have to adapt it to the leapfrog scheme [232, 233] but it could also help damping the BM oscillation and speed-up the computation.

7.2.2 Code validation with experiments

Even though this PhD project was mostly focused on numerical simulations, experimental diagnostics on a small HT were also planned initially in order to compare with the simulation results and validate *LPPic*. The goal was to use non-invasive emission spectroscopy measurements, combined with a Collisional Radiative Model (CRM), to obtain an axial profile of electron temperature. Additionally, a Langmuir probe could be used to measure the electron temperature in the plume, and validate this method. But the most interesting zone would be the discharge channel near the exit plane (accessible through a thin slit in the channel walls), where the electron temperature is expected to vary significantly axially, a variation that cannot be captured with an invasive Langmuir probe (known to perturb the plasma and also expected to melt). Whereas such a diagnostic has been recently performed by another research group [234], the main objective was to compare the measured electron temperature axial profile to the one obtained with *LPPic* and hence, validate our code. The CRM is cur-

rently under-development [235] and this whole experimental work will soon be performed.

Moreover, other experimental diagnostics were performed on this small HT such as a Proper Orthogonal Decomposition analysis of high-speed camera imaging, to study the rotating spokes. We managed to find two different operating regimes depending on the cathode heating current, with long-wavelength structures rotating in the plume for one of these regimes. Whereas it is still difficult to relate these large structures to the ones observed numerically with *LPPic*, the influence of the cathode current can be studied numerically by limiting the amount of electrons injected in the simulation domain. Because this manuscript was mainly focused on numerical simulations, we decided not to include these experimental diagnostics and the reader can refer to the corresponding publication for more information [99].

7.2.3 Towards an engineering tool?

As we have seen throughout this work, PIC simulations are quite cumbersome either because of the computational requirements or the complexity of the results. Hence, they are often only used to get insights on the physics, which will later be included in fluid or hybrid simulations. However, engineering parameters such as the thrust or the specific impulse can also be computed with *LPPic*, and 2D axial-azimuthal simulations with a high artificial scaling factor could still give results close to reality (which will be even more improved with the inclusion of a fake-radial dimension and doubly charged ions), while being reasonably fast (a couple of days for a vacuum permittivity scaling factor of 64). One has to determine if a fluid code with an artificial anomalous transport coefficient is more precise than a PIC code with an artificial scaling factor, but this latter option might be of interest for HT manufacturers, especially if the PIC code performances keep being improved.

In any case, simpler numerical models are still needed to study specific parts of the HT physics. We think that the EDI has now been quite extensively studied and more efforts need to be put into the analysis of other instabilities that interact with the EDI and are hence expected to play a role in the anomalous electron transport (such as the BM or the ITTI), but are still not fully-understood. This might represent the next step towards finding a self-consistent model for anomalous transport that could be then included in fluid models.

Appendix A

Sod test case

We consider for this test a cylindrical shock tube, with two zones separated by a diaphragm. The two zones are static, with different conditions of density and pressure, given in figure A.1.

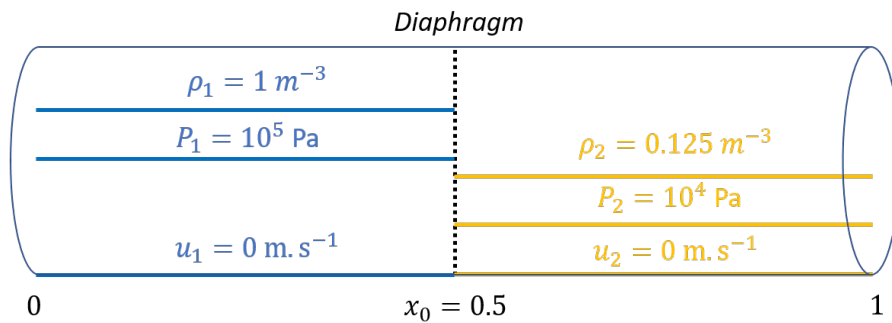


Figure A.1 – Initial conditions of Sod test case, with left state 1 (ρ_1, u_1, P_1) and right state 2 (ρ_2, u_2, P_2). The absciss is in centimeters.

At initial time, the diaphragm is broken, which creates a shock wave in the tube. Sod has derived an analytical solution that we can compare with the one obtained with our Riemann solver, as seen in figure A.2. We can notice that the two profiles are in good agreement but some diffusion is observed near the discontinuities. This diffusion is inherent to first-order Riemann solvers and it is necessary for the scheme to represent discontinuities without introducing new local extrema [236]. More details can be found in the Master's thesis of Tordeux [176].

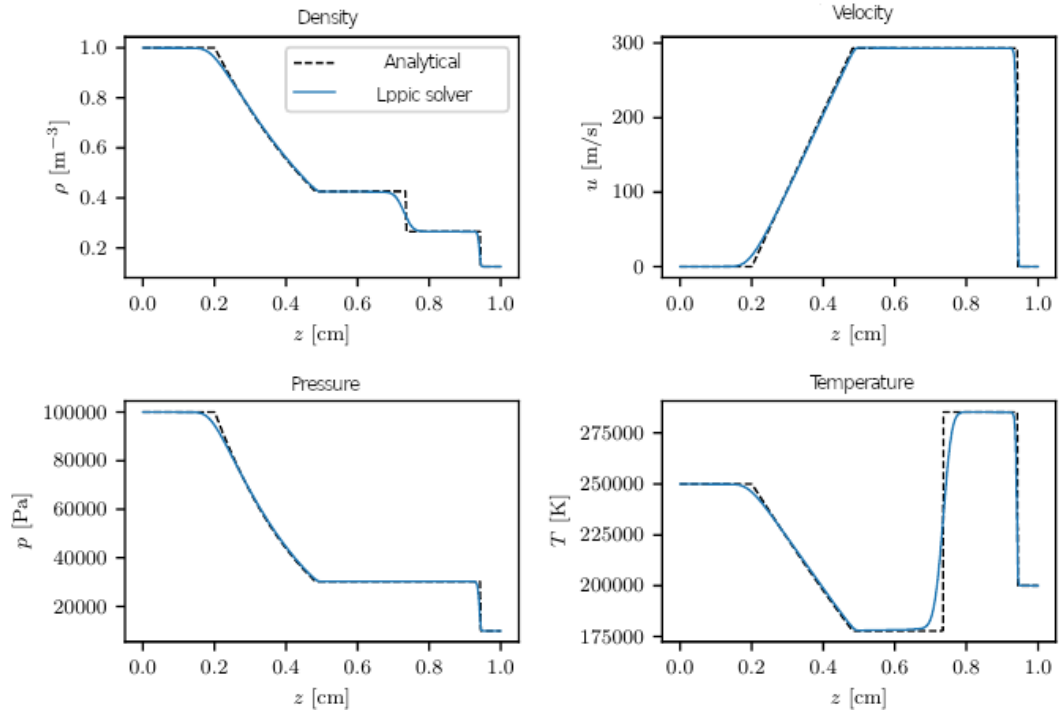


Figure A.2 – Results of Sod test case for $\Delta z = 2 \times 10^{-3}$ cm and $t = 0.8$ ms. Dashed black line: analytical solution. Blue line: LPPic solver. Diaphragm was originally at $z = 0.5$ cm. Adapted from [176].

Bibliography

- [1] K. Tsiolkovsky. Issledovanie mirovykh prostransty reaktivnymi priborami. *Naootchnoye Obozreniye*, 1903.
- [2] <https://spacenews.com/all-electric-satellites-halfway-to-becoming-half-of-all-satellites/>, 2017.
- [3] S. Mazouffre. Electric propulsion for satellites and spacecraft: established technologies and novel approaches. *Plasma Sources Sci. Technol.*, 25(3):033002, 2016.
- [4] L. Johnson, J. Jones, L. Kos, A. Trausch, R. Farris, and G. Woodcock. Benefits of nuclear electric propulsion to outer planets exploration. In *38th AIAA/ASME/SAE/ASEE Joint Propulsion Conference*, 2002.
- [5] E. Y. Choueiri. A critical history of electric propulsion: The first 50 years (1906-1956). *J. Propul. Power*, 20(2):193–203, 2004.
- [6] A. I. Morozov. The conceptual development of stationary plasma thrusters. *Plasma Phys. Rep.*, 29(3):235–250, 2003.
- [7] D. Lev, R. M. Myers, K. M. Lemmer, J. Kolbeck, H. Koizumi, and K. Polzin. The technological and commercial expansion of electric propulsion. *Acta Astronautica*, 159:213 – 227, 2019.
- [8] C Charles. Plasmas for spacecraft propulsion. *J. Phys. D (Appl. Phys.)*, 42(16):163001, 2009.
- [9] C Charles and R W Boswell. Measurement and modelling of a radiofrequency micro-thruster. *Plasma Sources Sci. Technol.*, 21(2):022002, 2012.
- [10] S. Pottinger, V. Lappas, C. Charles, and R. Boswell. Performance characterization of a helicon double layer thruster using direct thrust measurements. *J. Phys. D (Appl. Phys.)*, 44:235201, 2011.
- [11] F Díaz, J. Squire, A. Ilin, G Mccaskill, T.X. Nguyen, D Winter, A Petro, G Goebel, L. Cassady, K Stokke, C Dexter, T. Graves, L Jr, J George, R. Bengtson, B Breizman, V Jacobson, A. Arefiev, A Chan, and T Glover.

- The development of vasismr engine. In *Proceedings of International Conference on Electromagnetics in Advanced Applications (ICEAA99)*, Sept. 13-17, 1999, Torino, Italy, volume 37831, pages 99–102, 1999.
- [12] K.F. Long. *Deep Space Propulsion, A Roadmap to Interstellar Flight*. Springer Science+Business Media, LLC, 2012.
- [13] I. Levchenko, S. Xu, S. Mazouffre, D. Lev, D. Pedrini, D. Goebel, L. Garrigues, F. Taccogna, and K. Bazaka. Perspectives, frontiers, and new horizons for plasma-based space electric propulsion. *Phys. Plasmas*, 27(2):020601, 2020.
- [14] P.A. Czysz and C. Bruno. *Future Spacecraft Propulsion Systems, Enabling Technologies for Space Exploration, 2nd edition*. Praxis Publishing Ltd, 2009.
- [15] R. Dressler, Y.H. Chiu, and D. Levandier. Propellant alternatives for ion and hall effect thrusters. In *38th Aerospace Sciences Meeting and Exhibit*, 2000.
- [16] V. Croes, A. Tavant, R. Lucken, R. Martorelli, T. Lafleur, A. Bourdon, and P. Chabert. The effect of alternative propellants on the electron drift instability in hall-effect thrusters: Insight from 2d particle-in-cell simulations. *Phys. Plasmas*, 25:063522, 2018.
- [17] R.G. Jahn. *Physics of electric propulsion*. Dover Publications, Inc., 2006.
- [18] D.M. Goebel and I. Katz. *Fundamentals of Electric Propulsion: Ion and Hall Thrusters*. Wiley, Ney Jersey, 2008.
- [19] A. Bouchoule, A. Cadiou, A. Héron, M. Dudeck, and M. Lyszyk. An overview of the french research program on plasma thrusters for space applications. *Contrib. Plasma Phys.*, 41(6):573–588, 2001.
- [20] P.J. Wilbur, V.K. Rawlin, and J. R. Beattie. Ion thruster development trends and status in the united states. *J. Propul. Power*, 14(5):708–715, 1998.
- [21] P. Chabert, J. Arancibia Monreal, J. Bredin, L. Popelier, and A. Aanesland. Global model of a gridded-ion thruster powered by a radiofrequency inductive coil. *Phys. Plasmas*, 19(7):073512, 2012.
- [22] J.P. Boeuf. Tutorial : Physics and modeling of hall thrusters. *J. Appl. Phys.*, 121:011101, 2017.
- [23] A. Morozov and V. Savelyev. Fundamentals of stationary plasma thruster theory. *Rev. Plasma Phys.*, 21, 2000.

- [24] A Bouchoule, J-P Boeuf, A Heron, and O Duchemin. Physical investigations and developments of hall plasma thrusters. *Plasma Phys. Control. Fusion*, 46(12B):B407–B421, 2004.
- [25] J.C. Adam, J-P. Boeuf, N. Dubuit, M. Dudeck, L. Garrigues, D. Gresillon, A. Heron, G.J.M. Hagelaar, V. Kulaev, N. Lemoine, S. Mazouffre, J. Perez Luna, V. Pisarev, and S Tsikata. Physics, simulation and diagnostics of hall effect thrusters. *Plasma Phys. Control. Fusion*, 50:124041, 2008.
- [26] V V Zhurin, H R Kaufman, and R S Robinson. Physics of closed drift thrusters. *Plasma Sources Sci. Technol.*, 8(1):R1–R20, 1999.
- [27] R. Betzendahl. The 2014 rare gases market report. *Cryogas International*, 52, 2014.
- [28] N. Gascon, M. Dudeck, and S. Barral. Wall material effects in stationary plasma thrusters. i. parametric studies of an spt-100. *Phys. Plasmas*, 10(10):4123–4136, 2003.
- [29] S. Barral, K. Makowski, and Z. Peradzyński. Wall material effects in stationary plasma thrusters. ii. near-wall and in-wall conductivity. *Phys. Plasmas* 10, 4137, 2003.
- [30] I.G. Mikellides, R.R. Hofer, I. Katz, and D.M. Goebel. Magnetic shielding of hall thrusters at high discharge voltages. *J. Appl. Phys.*, 116(5):053302, 2014.
- [31] S.E Cusson, B.A. Jorns, and A.D. Gallimore. Non-invasive in situ measurement of the near-wall ion kinetic energy in a magnetically shielded hall thruster. *Plasma Sources Sci. Technol.*, 28(10):105012, 2019.
- [32] K.G. Xu and M.L.R. Walker. Effect of external cathode azimuthal position on hall-effect thruster plume and diagnostics. *J. Propul. Power*, 30(2):506–513, 2014.
- [33] Takeshi M., Tomohiro K., Makoto A., Kazuya O., Masahiro S., Yuki M., and Hiroki K. Influences of cathode position on operations and thrust performance of side by side hall thruster system. *Vacuum*, 167:524 – 529, 2019.
- [34] V. Kim. Main physical features and processes determining the performance of stationary plasma thrusters. *J. Propul. Power*, 14(5):736–743, 1998.
- [35] P. Chabert and N. Braithwaite. *Physics of Radio-Frequency Plasmas*. Cambridge University Press, 2011.
- [36] P.M. Bellan. *Fundamentals of Plasma Physics*. Cambridge University Press, 2006.

- [37] T.H. Stix. *Waves in plasmas*. AIP-Press, 1992.
- [38] E. Choueiri. Plasma oscillations in hall thrusters. *Phys. Plasmas*, 8:1411, 2001.
- [39] A. Smolyakov, O Chapurin, Frias P.W., O Koshkarov, I. Romadanov, T. Tang, M. Umansky, Y Raitses, I. Kaganovich, and V Lakhin. Fluid theory and simulations of instabilities, turbulent transport and coherent structures in partially-magnetized plasmas of $\mathbf{E} \times \mathbf{B}$ discharges. *Plasma Phys. Control. Fusion*, 59:014041, 2017.
- [40] T. Lafleur. Electron drift instabilities in exb plasmas: kinetic theory and pic simulations. In *ExB Plasmas for Space and Industrial Applications, Toulouse, France*, 2017.
- [41] Tilinin G. High-frequency plasma waves in a hall accelerator with an extended acceleration zone. *Sov. Phys. Tech. Phys.*, 22:974, 1977.
- [42] E. Chesta, C. M. Lam, N. B. Meezan, D. P. Schmidt, and M. A. Cappelli. A characterization of plasma fluctuations within a hall discharge. *IEEE Trans. Plasma Sci.*, 29(4):582–591, 2001.
- [43] R. B. Lobbia. *A Time-resolved Investigation of the Hall Thruster Breathing Mode*. PhD thesis, The University of Michigan, 2010.
- [44] S. Barral and J. Miedzik. Numerical investigation of closed-loop control for hall accelerators. *J. Appl. Phys.*, 109(1):013302, 2011.
- [45] Wei L., Wang C., Ning Z., Liu W., Zhang C., and Yu D. Experimental study on the role of a resistor in the filter of hall thrusters. *Phys. Plasmas*, 18(6):063508, 2011.
- [46] J. M. Fife. *Hybrid-PIC modeling and electrostatic probe survey of Hall thrusters*. PhD thesis, (Massachusetts Institute of Technology, 1998.
- [47] V. Volterra. Variations and fluctuations of the number of individuals in animal species living together. *Animal Ecology*, 1931.
- [48] S. Barral and E. Ahedo. Low-frequency model of breathing oscillations in hall discharges. *Phys. Rev. E*, 79:046401, 2009.
- [49] J. P. Boeuf and L. Garrigues. Low frequency oscillations in a stationary plasma thruster. *J. Appl. Phys.*, 84(7):3541–3554, 1998.
- [50] S. Barral and E. Ahedo. On the origin of low frequency oscillations in hall thrusters. *AIP Conference Proceedings*, 993(1):439–442, 2008.
- [51] K. Hara, M.J. Sekerak, I.D. Boyd, and A.D. Gallimore. Perturbation analysis of ionization oscillations in hall effect thrusters. *Phys. Plasmas*, 21(12):122103, 2014.

- [52] K. Hara, M.J. Sekerak, I.D. Boyd, and A.D. Gallimore. Mode transition of a hall thruster discharge plasma. *J. Appl. Phys.* 115, 203304, 2014.
- [53] I Romadanov, Y Raitses, and A Smolyakov. Hall thruster operation with externally driven breathing mode oscillations. *Plasma Sources Sci. Technol.*, 27(9):094006, 2018.
- [54] S. Chable and F. Rogier. Numerical investigation and modeling of stationary plasma thruster low frequency oscillations. *Phys. Plasmas*, 12(3):033504, 2005.
- [55] Y.B. Esipchuck, A. I. Morozov, G. N. Tilinin, and A. V. Trofimov. Plasma oscillations in closed-drift accelerators with an extended acceleration zone. *Sov. Phys. Tech. Phys.*, 18:928, 1974.
- [56] J. Vaudolon and S. Mazouffre. “investigation of the ion transit time instability in a hall thruster combining time-resolved lif spectroscopy and analytical calculations,. In *Joint Conference of 30th International Symposium on Space Technology and Science, 34th International Electric Propulsion Conference and 6th Nano-Satellite Symposium*. IEPC-2015-90259/ISTS-2015-b-90259, 2015.
- [57] J. Vaudolon and S. Mazouffre. Observation of high-frequency ion instabilities in a cross-field plasma. *Plasma Sources Sci. Technol.*, 24(3):032003, 2015.
- [58] G. J. M. Hagelaar, J. Bareilles, L. Garrigues, and J.-P. Boeuf. Role of anomalous electron transport in a stationary plasma thruster simulation. *J. Appl. Phys.*, 93(1):67–75, 2003.
- [59] J. Bareilles, G. J. M. Hagelaar, L. Garrigues, C. Boniface, J. P. Boeuf, and N. Gascon. Critical assessment of a two-dimensional hybrid hall thruster model: Comparisons with experiments. *Phys. Plasmas*, 11(6):3035–3046, 2004.
- [60] D. W. Forslund, R. L. Morse, and C. W. Nielson. Electron cyclotron drift instability. *Phys. Rev. Lett.*, 25(18):1266, 1970.
- [61] D. Forslund, C. Nielson, R. Morse, and J. Fu. Electron-cyclotron drift instability and turbulence. *Phys. Fluids*, 15(7):1303, 1972.
- [62] S.P. Gary and J. J. Sanderson. Longitudinal waves in a perpendicular collisionless plasma shock: I. cold ions. *J. Plasma Phys.*, 4(4):739–751, 1970.
- [63] M Lampe, W. Manheimer, J B. McBride, J H. Orens, R Shanny, and R.N. Sudan. Nonlinear development of the beam-cyclotron instability. *Phys. Rev. Lett.*, 26:1221–1225, 1971.

- [64] M. Lampe, W.M. Manheimer, J. B. McBride, and J. H. Orens. Anomalous resistance due to cross-field electron-ion streaming instabilities. *Phys. Fluids*, 15(12):2356–2362, 1972.
- [65] D. Biskamp and R. Chodura. Nonlinear electron-cyclotron drift instability. *Nucl. Fusion*, 12(4):485, 1972.
- [66] J. C. Adam, A. Heron, and G. Laval. Study of stationary plasma thrusters using two-dimensional fully kinetic simulations. *Phys. Plasmas*, 11(1):295–305, 2004.
- [67] S. Tsikata, N. Lemoine, V. Pisarev, and D. M. Grésillon. Dispersion relations of electron density fluctuations in a hall thruster plasma, observed by collective light scattering. *Phys. Plasmas*, 16(3):033506, 2009.
- [68] S. Tsikata, C. Honoré, D. Grésillon, and N. Lemoine. Collective light scattering for the study of fluctuations in magnetized plasmas: The hall thruster case study. *Contrib. Plasma Phys.*, 51(2-3):119–125, 2011.
- [69] S. Tsikata, C. Honoré, and D. Grésillon. Collective thomson scattering for studying plasma instabilities in electric thrusters. *Journal of Instrumentation*, 8(10):C10012–C10012, 2013.
- [70] T. Lafleur, S. D. Baalrud, and P. Chabert. Theory for the anomalous electron transport in Hall effect thrusters. i. insights from particle-in-cell simulations. *Phys. Plasmas*, 23(5):053502, 2016.
- [71] S. Janhunen, A. Smolyakov, O. Chapurin, D. Sydorenko, I. Kaganovich, and Y. Raitses. Nonlinear structures and anomalous transport in partially magnetized plasmas. *Phys. Plasmas*, 25:011608, 2018.
- [72] Z. Asadi, F. Taccogna, and M. Sharifian. Numerical study of electron cyclotron drift instability: Application to hall thruster. *Front. Phys.*, 7:140, 2019.
- [73] A. Smolyakov, T. Zintel, L. Couedel, D. Sydorenko, A. Umnov, E. Sorokina, and N. Marusov. Anomalous electron transport in one-dimensional electron cyclotron drift turbulence. *Plasma Phys. Rep.*, 46:496–505, 2020.
- [74] A. Héron and J. C. Adam. Anomalous conductivity in hall thrusters: Effects of the non-linear coupling of the electron-cyclotron drift instability with secondary electron emission of the walls. *Phys. Plasmas*, 20(8):082313, 2013.
- [75] J.P. Boeuf. Rotating structures in low temperature magnetized plasmas—insight from particle simulations. *Front. Phys.*, 2:74, 2014.
- [76] P. Coche and L. Garrigues. A two-dimensional (azimuthal-axial) particle-in-cell model of a hall thruster. *Phys. Plasmas*, 21:023503, 2014.

- [77] V. Croes, T. Lafleur, Z. Bonaventura, A. Bourdon, and P. Chabert. 2d particle-in-cell simulations of the electron drift instability and associated anomalous electron transport in hall-effect thrusters. *Plasma Sources Sci. Technol.*, 26:034001, 2017.
- [78] F. Taccogna, P. Minelli, Z. Asadi, and G. Bogopolsky. Numerical studies of the ExB electron drift instability in hall thrusters. *Plasma Sources Sci. Technol.*, 28(6):064002, 2019.
- [79] M. Sengupta and A. Smolyakov. Mode transitions in non linear evolution of the electron drift instability in a 2d annular exb system. *Phys. Plasmas*, 27(2):022309, 2020.
- [80] A. Lazurenko, G. Coduti, S. Mazouffre, and G. Bonhomme. Dispersion relation of high-frequency plasma oscillations in hall thrusters. *Phys. Plasmas*, 15(3):034502, 2008.
- [81] Z.A. Brown and B.A. Jorns. Spatial evolution of small wavelength fluctuations in a hall thruster. *Phys. Plasmas*, 26(11):113504, 2019.
- [82] A. Ducrocq, J. C. Adam, A. Heron, and G. Laval. High-frequency electron drift instability in the cross-field configuration of Hall thrusters. *Phys. Plasmas*, 13(10):102111, 2006.
- [83] J. Cavalier, N. Lemoine, G. Bonhomme, S. Tsikata, C. Honore, and D. Gressillon. Hall thruster plasma fluctuations identified as the e x b electron drift instability: Modeling and fitting on experimental data. *Phys. Plasmas*, 20(8):082107, 2013.
- [84] T. Lafleur, S. D. Baalrud, and P. Chabert. Theory for the anomalous electron transport in hall effect thrusters. ii. kinetic model. *Phys. Plasmas*, 23(5):053503, 2016.
- [85] T. Lafleur, S. D. Baalrud, and P. Chabert. Characteristics and transport effects of the electron drift instability in hall-effect thrusters. *Plasma Sources Sci. Technol.*, 26(2):024008, 2017.
- [86] T. Lafleur, R. Martorelli, P. Chabert, and A. Bourdon. Anomalous electron transport in hall-effect thrusters: Comparison between quasi-linear kinetic theory and particle-in-cell simulations. *Phys. Plasmas*, 25(6):061202, 2018.
- [87] S. Janhunen, A. Smolyakov, D. Sydorenko, M. Jimenez, I. Kaganovich, and Y. Raitses. Evolution of the electron cyclotron drift instability in two-dimensions. *Phys. Plasmas*, 25(8):082308, 2018.
- [88] O. Koshkarov, A. Smolyakov, Y. Raitses, and I. Kaganovich. Self-organization, structures, and anomalous transport in turbulent partially magnetized plasmas with crossed electric and magnetic fields. *Phys. Rev. Lett.*, 122:185001, 2019.

- [89] F. Taccogna and P. Minelli. Three-dimensional particle-in-cell model of hall thruster: The discharge channel. *Phys. Plasmas*, 25(6):061208, 2018.
- [90] G. S. Janes and R. S. Lowder. Anomalous electron diffusion and ion acceleration in a low density plasma. *Phys. Fluids*, 9:1115, 1966.
- [91] M.S. McDonald and A.D. Gallimore. Parametric investigation of the rotating spoke instability in hall thrusters. In *32nd International Electric Propulsion Conference*. Paper 242, 2011.
- [92] A. Powis, J. Carlsson, I. Kaganovich, Y. Raitses, and A. Smolyakov. Scaling of spoke rotation frequency within a penning discharge. *Phys. Plasmas*, 25:072110, 2018.
- [93] J. P. Boeuf and B. Chaudhury. Rotating instability in low-temperature magnetized plasmas. *Phys. Rev. Lett.*, 111:155005, 2013.
- [94] R. Kawashima, K. Hara, and K. Komurasaki. Numerical analysis of azimuthal rotating spokes in a crossed-field discharge plasma. *Plasma Sources Sci. Technol.*, 27, 2017.
- [95] K Matyash, R Schneider, S Mazouffre, S Tsikata, and L Grimaud. Rotating spoke instabilities in a wall-less hall thruster: simulations. *Plasma Sources Sci. Technol.*, 28(4):044002, 2019.
- [96] M. E. Griswold, C. L. Ellison, Y. Raitses, and N. J. Fisch. Feedback control of an azimuthal oscillation in the exb discharge of hall thrusters. *Phys. Plasmas*, 19(5):053506, 2012.
- [97] J. B. Parker, Y. Raitses, and N. J. Fisch. Transition in electron transport in a cylindrical hall thruster. *Appl. Phys. Lett.*, 97(9):091501, 2010.
- [98] A. M. Kapulkin A. I. Morozov, Y. Epsinchuck. *Sov. Phys. Tech. Phys.*, 17:482, 1972.
- [99] V. Désangles, S. Shcherbanev, T. Charoy, N. Clément, C. Deltel, P. Richard, S. Vincent, P. Chabert, and A. Bourdon. A fast camera analysis of plasma instabilities in hall effect thrusters using a pod method under different operating regimes. *Atmosphere*, 11:518, 2020.
- [100] K. Dannenmayer and S. Mazouffre. Elementary scaling relations for hall effect thrusters. *J. Propul. Power*, 27(1):236–245, 2011.
- [101] Kim V.P., Hrdlichko D.P., Merkurev D.V., Popov G.A., Shilov E.A., Zakharchenko V.S, Korkunov M.V., and Lesnevsky V.A. Investigation of the possibility to develop a competitive low power stationary plasma thruster. In *36th International Electric Propulsion Conference*, 2019.

- [102] C. Berbieri T. Misuri, F. Battista and E. A. De Marco. High power hall thrusters design options. In *30th International Electric Propulsion Conference, Florence (311)*, 2007.
- [103] N.B. Meezan, W.A. Hargus Jr, and M.A. Cappelli. Anomalous electron mobility in a coaxial hall discharge plasma. *Phys. Rev. E*, 63:026410, 2001.
- [104] D. Sydorenko, A. Smolyakov, I. Kaganovich, and Y. Raitses. Kinetic simulation of secondary electron emission effects in hall thrusters. *Phys. Plasmas*, 13(1):014501, 2006.
- [105] Y. Raitses, I. D. Kaganovich, A. Khrabrov, D. Sydorenko, N. J. Fisch, and A. Smolyakov. Effect of secondary electron emission on electron cross-field current in $e \times b$ discharges. *IEEE Trans. Plasma Sci.*, 39(4):995–1006, 2011.
- [106] D. Sydorenko, A. Smolyakov, I. Kaganovich, and Y. Raitses. Plasma-sheath instability in hall thrusters due to periodic modulation of the energy of secondary electrons in cyclotron motion. *Phys. Plasmas*, 15(5):053506, 2008.
- [107] F. Taccogna, S. Longo, M. Capitelli, and R. Schneider. Anomalous transport induced by sheath instability in hall effect thrusters. *Appl. Phys. Lett.*, 94(25):251502, 2009.
- [108] E. Ahedo, J. M. Gallardo, and M. Martinez-Sanchez. Effects of the radial plasma-wall interaction on the hall thruster discharge. *Phys. Plasmas*, 10(8):3397–3409, 2003.
- [109] A. Tavant, V. Croes, R. Lucken, T. Lafleur, A. Bourdon, and P. Chabert. The effects of secondary electron emission on plasma sheath characteristics and electron transport in an $\mathbf{e} \times \mathbf{b}$ discharge via kinetic simulations. *Plasma Sources Sci. Technol.*, 27:12, 2018.
- [110] A. Ducrocq. *Rôle des instabilités électroniques de dérive dans le transport électronique du propulseur à effet Hall*. Phd thesis, Ecole polytechnique, 2006.
- [111] T. Lafleur and P. Chabert. The role of instability-enhanced friction on ‘anomalous’ electron and ion transport in hall-effect thrusters. *Plasma Sources Sci. Technol.*, 27:015003, 2018.
- [112] W. Frias, A.I. Smolyakov, I.D. Kaganovich, and Y. Raitses. Long wavelength gradient drift instability in hall plasma devices. i. fluid theory. *Phys. Plasmas*, 19(7):072112, 2012.
- [113] V. P. Lakhin, V. I. Ilgisonis, A. I. Smolyakov, E. A. Sorokina, and N. A. Marusov. Effects of finite electron temperature on gradient drift instabilities in partially magnetized plasmas. *Phys. Plasmas*, 25(1):012106, 2018.

- [114] N A Marusov, E A Sorokina, V P Lakhin, V I Ilgisonis, and A I Smolyakov. Gradient-drift instability applied to hall thrusters. *Plasma Sources Sci. Technol.*, 28(1):015002, 2019.
- [115] S. Cho, K. Komurasaki, and Y. Arakawa. Kinetic particle simulation of discharge and wall erosion of a hall thruster. *Phys. Plasmas*, 20(6):063501, 2013.
- [116] J. Liu, H. Li, Y. Hu, X. Liu, Y. Ding, L. Wei, D. Yu, and X. Wang. Particle-in-cell simulation of the effect of curved magnetic field on wall bombardment and erosion in a hall thruster. *Contrib. Plasma Phys.*, 59(8):e201800001, 2019.
- [117] Ioannis G. Mikellides, Ira Katz, Richard R. Hofer, and Dan M. Goebel. Magnetic shielding of a laboratory hall thruster. i. theory and validation. *J. Appl. Phys.*, 115(4):043303, 2014.
- [118] J. Vaudolon, S. Mazouffre, C. Hénaux, D. Harribey, and A. Rossi. Optimization of a wall-less hall thruster. *Appl. Phys. Lett.*, 107(17):174103, 2015.
- [119] V. Croes. *Modélisation bidimensionnelle de la décharge plasma dans un propulseur de Hall*. PhD thesis, Université Paris-Saclay, France, 2018.
- [120] A. Tavant. *Plasma-wall interaction and electron transport in Hall Effect Thrusters*. PhD thesis, Université Paris-Saclay, France, 2019.
- [121] M.L.R. Brown, N.P.; Walker. Review of plasma-induced hall thruster erosion. *Appl. Sci.*, 10:3775, 2020.
- [122] K. Hara. An overview of discharge plasma modeling for hall effect thrusters. *Plasma Sources Sci. Technol.*, 28:044001, 2019.
- [123] F. Taccogna and L. Garrigues. Latest progress in hall thrusters plasma modelling. *Rev. Mod. Plasma Phys.*, 3(1):12, 2019.
- [124] M. Keidar, I.D. Boyd, and I.I. Beilis. Modeling of a high-power thruster with anode layer. *Phys. Plasmas*, 11(4):1715–1722, 2004.
- [125] I.G. Mikellides and I. Katz. Numerical simulations of hall-effect plasma accelerators on a magnetic-field-aligned mesh. *Phys. Rev. E*, 86:046703, 2012.
- [126] E. Ahedo. Presheath/sheath model with secondary electron emission from two parallel walls. *Phys. Plasmas*, 9(10):4340–4347, 2002.
- [127] V. Joncquieres, F. Pechereau, A. Alvarez Laguna, A. Bourdon, O. Vermorel, and B. Cuenot. A 10-moment fluid numerical solver of plasma with sheaths in a hall effect thruster. In *Joint Propulsion Conference, AIAA 2018-4905, July 9-11, 2018 Cincinnati, Ohio*, 2018.

- [128] V. Jonquieres. *Modélisation et simulation numérique des moteurs à effet Hall*. PhD thesis, Institut National Polytechnique de Toulouse, France, 2019.
- [129] A. Alvarez-Laguna, T. Magin, M. Massot, A. Bourdon, and P. Chabert. Plasma-sheath transition in multi-fluid models with inertial terms under low pressure conditions: Comparison with the classical and kinetic theory. *Plasma Sources Sci. Technol.*, dec 2019.
- [130] A. Alvarez Laguna, T. Pichard, T. Magin, P. Chabert, A. Bourdon, and M. Massot. An asymptotic preserving well-balanced scheme for the isothermal fluid equations in low-temperature plasmas at low-pressure. *J. Comp. Phys.*, 419:109634, 2020.
- [131] F. I. Parra, E. Ahedo, J. M. Fife, and M. Martínez-Sánchez. A two-dimensional hybrid model of the hall thruster discharge. *Journal of Applied Physics*, 100(2):023304, 2006.
- [132] I.G. Mikellides, B. Jorns, I. Katz, and A. Lopez Ortega. Hall2de simulations with a first-principles electron transport model based on the electron cyclotron drift instability. In *52nd AIAA/SAE/ASEE Joint Propulsion Conference*. American Institute of Aeronautics and Astronautics, 2016, 2016.
- [133] R. Martorelli, T. Laffleur, A. Bourdon, and P. Chabert. Comparison between ad-hoc and instability-induced electron anomalous transport in a 1d fluid simulation of hall-effect thruster. *Phys. Plasmas*, 26(8):083502, 2019.
- [134] B. Jorns. Predictive, data-driven model for the anomalous electron collision frequency in a hall effect thruster. *Plasma Sources Sci. Technol.*, 27(10):104007, 2018.
- [135] C.K. Birdsall and A.B. Langdon. *Plasma physics via computer simulation*, chapter 16. Institute of Physics, 1991.
- [136] F. Taccogna, S. Longo, and M. Capitelli. Plasma sheaths in hall discharge. *Phys. Plasmas*, 12(9):093506, 2005.
- [137] D. Y. Sydorenko. *Particle-in-cell simulations of electron dynamics in low pressure discharges with magnetic fields*. PhD thesis, University of Saskatchewan, Canada, 2006.
- [138] A. Tavant, R. Lucken, A. Bourdon, and P. Chabert. Non-isothermal sheath model for low pressure plasmas. *Plasma Sources Sci. Technol.*, 28(7):075007, 2019.
- [139] J.J. Jr. Szabo. *Fully Kinetic Numerical Modeling of a Plasma Thruster*. PhD thesis, Massachusetts Institute of Technology, 2001.

- [140] J-P. Boeuf and L. Garrigues. Exb electron drift instability in hall thrusters: Particle-in-cell simulations vs. theory. *Phys. Plasmas.*, 25:061204, 2018.
- [141] I. Katz, V.H. Chaplin, and A. Lopez Ortega. Particle-in-cell simulations of hall thruster acceleration and near plume regions. *Phys. Plasmas*, 25(12):123504, 2018.
- [142] T. Chernyshev, E. Son, and O. Gorshkov. 2d3v kinetic simulation of hall effect thruster, including azimuthal waves and diamagnetic effect. *J. Phys. D (Appl. Phys.)*, 52(44):444002, 2019.
- [143] M. Hirakawa and Y. Arakawa. Particle simulation of plasma phenomena in hall thrusters. In *24th International Electric Propulsion Conference (164)*, 1995.
- [144] K. Matyash, R. Schneider, S. Mazouffre, S. Tsikata, Y. Raitses, and A. D'Allo. 3d simulation of the rotating spoke in a hall thruster. In *33rd International Electric Propulsion Conference*, 2013.
- [145] K. Hara and K. Hanquist. Test cases for grid-based direct kinetic modeling of plasma flows. *Plasma Sources Sci. Technol.*, 27(6):065004, 2018.
- [146] A.L. Raisanen, K. Hara, and I.D. Boyd. Two-dimensional hybrid-direct kinetic simulation of a hall thruster discharge plasma. *Phys. Plasmas*, 26(12):123515, 2019.
- [147] K. Hara, I.D. Boyd, and V.I. Kolobov. One-dimensional hybrid-direct kinetic simulation of the discharge plasma in a hall thruster. *Phys. Plasmas*, 19(11):113508, 2012.
- [148] B. Jorns. Two equation closure model for plasma turbulence in a hall effect thruster (paper 129). In *36th International Electric Propulsion Conference, Vienna*, 2019.
- [149] M.M. Turner. Kinetic properties of particle-in-cell simulations compromised by monte carlo collisions. *Phys. Plasmas*, 13:033506, 2006.
- [150] J-P. Boris and Ramy A Shanny. Relativistic plasma simulation-optimization of a hybrid code. In *Proc. 4th Conf. on Numerical Simulation of Plasmas*, pp 3-67. Naval Research Laboratory, Washington DC, 1970.
- [151] V. Vahedi and M. Surendra. A monte carlo collision model for the particle-in-cell method: applications to argon and oxygen discharges. *Comput. Phys. Commun.*, 87:179–198, 1995.
- [152] R.D. Falgout and Ulrike Meier Yang. hypre: A library of high performance preconditioners. In *Computational Science — ICCS 2002*, pages 632–641. Springer Berlin Heidelberg, 2002.

- [153] A. V. Phelps. *Compilation of atomic and molecular data*. see www.lxcat.net/Phelps, 2016.
- [154] Cross sections extracted from program magboltz, version 7.1 june 2004.
- [155] D. Sydorenko, A. Smolyakov, I. Kaganovich, and Y. Raitses. Modification of electron velocity distribution in bounded plasmas by secondary electron emission. *IEEE Trans. Plasma Sci.*, 34(3):815–824, 2006.
- [156] M.M. Turner, A. Derzsi, Z. Donkó, D. Eremin, S.J. Kelly, T. Lafleur, and T. Mussenbrock. Simulation benchmarks for low-pressure plasmas: Capacitive discharges. *Phys. Plasmas*, 20:013507, 2013.
- [157] R. Lucken. *Theory and simulation of low-pressure plasma transport phenomena : Application to the PEGASES Thruster*. PhD thesis, Université Paris-Saclay, France, 2019.
- [158] J. M. Haas and A. D. Gallimore. Considerations on the role of the hall current in a laboratory-model thruster. *IEEE Trans. Plasma Sci.*, 30(2):687–697, 2002.
- [159] P.Y. Peterson, A.D. Gallimore, and J.M. Haas. An experimental investigation of the internal magnetic field topography of an operating hall thruster. *Phys. Plasmas*, 9(10):4354–4362, 2002.
- [160] C. K. Birdsall. Particle-in-cell charged-particle simulations, plus monte carlo collisions with neutral atoms, pic-mcc. *IEEE Trans. Plasma Sci.*, 19(2):65–85, 1991.
- [161] K.J Bowers. Accelerating a particle-in-cell simulation using a hybrid counting sort. *J. Comp. Phys.*, 173(2):393 – 411, 2001.
- [162] A. Beck, J. Derouillat, M. Lobet, A. Farjallah, F. Massimo, I. Zemzemi, F. Perez, T. Vinci, and M. Grech. Adaptive simd optimizations in particle-in-cell codes with fine-grain particle sorting. *Comput. Phys. Commun.*, 244:246 – 263, 2019.
- [163] J. C. Adam, A. G. Serveniere, and A. B. Langdon. Electron sub-cycling in particle simulation of plasma. *J. Comp. Phys.*, 47:229–244, 1982.
- [164] M. Hirakawa and Y. Arakawa. Numerical simulation of plasma particle behavior in a hall thruster. In *32nd Joint Propulsion Conference and Exhibit*, 1995.
- [165] J. Szabo, N. Warner, M. Martinez-Sanchez, and O. Batishchev. Full particle-in-cell simulation methodology for axisymmetric hall effect thrusters. *J. Propul. Power*, 30(1):197–208, 2014.

- [166] F. Taccogna, S. Longo, M. Capitelli, and R. Schneider. Self-similarity in hall plasma discharges: Applications to particle models. *Phys. Plasmas*, 12(5):053502, 2005.
- [167] J. Teunissen and U. Ebert. Controlling the weights of simulation particles: adaptive particle management using k-d trees. *J. Comput. Phys.*, 259:318 – 330, 2014.
- [168] P.T. Luu, T. Tückmantel, and A. Pukhov. Voronoi particle merging algorithm for pic codes. *Comput. Phys. Commun.*, 202:165 – 174, 2016.
- [169] S Mazouffre, G Bourgeois, L Garrigues, and E Pawelec. A comprehensive study on the atom flow in the cross-field discharge of a hall thruster. *J. Phys. D (Appl. Phys.)*, 44(10):105203, 2011.
- [170] A. Harten, P.D. Lax, and B. Van Leer. On upstream differencing and godunov-type schemes for hyperbolic conservation laws. *SIAM Review*, 25(1):35–61, 1983.
- [171] E. F. Toro, M. Spruce, and W. Speares. Restoration of the contact surface in the HLL-Riemann solver. *Shock Waves*, 4(1):25–34, 1994.
- [172] E.F. Toro. *Riemann solvers and numerical methods for fluid dynamics : a practical introduction*. Springer-Verlag Berlin Heidelberg, 2013.
- [173] A. Leroux. *Modélisation d’écoulements supersoniques hors-équilibre chimique et thermique*. PhD thesis, Université de Rouen, France, 1997.
- [174] F. Dubois. Partial riemann problem, boundary conditions, and gas dynamics. *Absorbing Boundaries and Layers, Domain Decomposition Methods: Applications to Large Scale Computations*, pages 16–77, 2001.
- [175] G.A. Sod. A survey of several finite difference methods for systems of nonlinear hyperbolic conservation laws. *J. Comput. Phys.*, 27(1):1 – 31, 1978.
- [176] D. Tordeux. Modélisation de la dynamique des neutres dans un code pic d’un plasma froid magnétisé : application à la propulsion électrique. Master’s thesis, Ecole Polytechnique, 2018.
- [177] G. Sary, L. Garrigues, and J.P. Boeuf. Hollow cathode modeling: I. A coupled plasma thermal two-dimensional model. *Plasma Sources Sci. Technol.*, 26(5):055007, 2017.
- [178] K. Kubota, Y. Oshio, H. Watanabe, S. Cho, and I. Funaki. Numerical Simulation of Hollow Cathode with Hybrid-PIC Coupled with Growth Model of Ion Acoustic Turbulence. In *2018 Joint Propulsion Conference*, Cincinnati, Ohio, 2018. American Institute of Aeronautics and Astronautics.

- [179] K. Hara and C. Treece. Ion kinetics and nonlinear saturation of current-driven instabilities relevant to hollow cathode plasmas. *Plasma Sources Sci. Technol.*, 28(5):055013, 2019.
- [180] S. Cho, H. Watanabe, K. Kubota, and I. Funaki. The Effects of Cathode Boundary Condition on Particle Simulation of a SPT-100-like Hall Thruster. In *52nd AIAA/SAE/ASEE Joint Propulsion Conference*. American Institute of Aeronautics and Astronautics, 2016.
- [181] W.B. Li, H. Li, Y.J. Ding, L.Q. Wei, Q. Gao, F. Wu, Y. Lv, and D.R Yu. Study on the influence of change in axial position of cathode on the ignition process of a hall thruster. *Vacuum*, 167:234 – 243, 2019.
- [182] R.R. Hofer K.K. Jameson, D.M. Goebel and R.M. Watkins. Cathode coupling in hall thrusters. In *in 30th International Electric Propulsion Conference*, 2007.
- [183] K.L. Cartwright, J.P. Verboncoeur, and C.K. Birdsall. Loading and injection of maxwellian distributions in particle simulations. *J. Comput. Phys.* 162, 483–513, 2000.
- [184] L. Garrigues, G. Fubiani, and J. P. Boeuf. Appropriate use of the particle in-cell method in low temperature plasmas: Application to the simulation of negative ion extraction. *J. Appl. Phys.*, 120:213303, 2016.
- [185] T Charoy, J P Boeuf, A Bourdon, J A Carlsson, P Chabert, B Cuenot, D Eremin, L Garrigues, K Hara, I D Kaganovich, A T Powis, A Smolyakov, D Sydorenko, A Tavant, O Vermorel, and W Villafana. 2d axial-azimuthal particle-in-cell benchmark for low-temperature partially magnetized plasmas. *Plasma Sources Sci. Technol.*, 28(10):105010, 2019.
- [186] S.-W. Kim and A. D. Gallimore. Plume study of a 1.35 kw spt-100 using an exb probe. *AIAA-99-2423*, 1999.
- [187] I. Katz, R. R. Hofer, and D. M. Goebel. Ion current in hall thrusters. *IEEE Trans. Plasma Sci.*, 36(5):2015–2024, 2008.
- [188] S. Tsikata, J. Cavalier, A. Héron, C. Honoré, N. Lemoine, D. Grésillon, and D. Coulette. An axially propagating two-stream instability in the hall thruster plasma. *Phys. Plasmas*, 21(7):072116, 2014.
- [189] L K Jha, Santosh Kumar, O P Roy, and P Kumar. Single and double ionization of kr and xe by electron impact. *Physica Scripta*, 77(1):015304, 2007.
- [190] E. W. Bell, Djuric N., and G. H. Dunn. Electron-impact ionization of In+ and Xe+. *Phys. Rev. A*, 48:4286–4291, 1993.

- [191] K. Nanbu. Probability theory of electron-molecule, ion-molecule, molecule-molecule, and coulomb collisions for particle modeling of materials processing plasmas and cases. *IEEE Trans. Plasma Sci.*, 28(3):971–990, 2000.
- [192] LANDMARK project. <https://www.landmark-plasma.com/>, 2018.
- [193] A. Anders. Tutorial: Reactive high power impulse magnetron sputtering (r-hipims). *J. Appl. Phys.*, 121(17):171101, 2017.
- [194] J. T. Gudmundsson, N. Brenning, D. Lundin, and U. Helmersson. High power impulse magnetron sputtering discharge. *J. Plasma Phys. A*, 30(3):030801, 2012.
- [195] M.M. Turner. Verification of particle-in-cell simulations with monte carlo collisions. *Plasma Sources Sci. Technol.*, 25:054007, 2016.
- [196] M. Surendra. Radiofrequency discharge benchmark model comparison. *Plasma Sources Sci. Technol.*, 4:56, 1995.
- [197] J. Carlsson, A. Khrabrov, I. Kaganovich, T. Sommerer, and D. Keating. Validation and benchmarking of two particle-in-cell codes for a glow discharge. *Plasma Sources Sci. Technol.*, 26:014003, 2017.
- [198] B. Bagheri, J. Teunissen, U. Ebert, M.M. Becker, S. Chen, O. Ducasse, O. Eichwald, D. Loffhagen, A. Luque, D. Mihailova, J.M. Plewa, J. van Dijk, and M. Yousfi. Comparison of six simulation codes for positive streamers in air. *Plasma Sources Sci. Technol.*, 27:095002, 2018.
- [199] H. Okuda and C.K. Birdsall. Collisions in a plasma of finite size particles. *Phys. Fluids*, 13:2123, 1970.
- [200] T. Charoy, T. Lafleur, A. Tavant, P. Chabert, and A. Bourdon. A comparison between kinetic theory and particle-in-cell simulations of anomalous electron transport in $E \times B$ plasma discharges. *Phys. Plasmas*, 27(6):063510, 2020.
- [201] A.A. Litvak, Y. Raitses, and N.J. Fisch. Experimental studies of high-frequency azimuthal waves in hall thrusters. *Phys. Plasmas*, 11(4):1701–1705, 2004.
- [202] A. Lazurenko, V. Vial, M. Prioul, and A. Bouchoule. Experimental investigation of high-frequency drifting perturbations in hall thrusters. *Phys. Plasmas*, 12(1):013501–013501–9, 2005.
- [203] B. Vincent, S. Tsikata, S. Mazouffre, T. Minea, and J. Fils. A compact new incoherent thomson scattering diagnostic for low-temperature plasma studies. *Plasma Sources Sci. Technol.*, 27(5):055002, 2018.

- [204] I.G. Mikellides and A. Lopez Ortega. Challenges in the development and verification of first-principles models in hall-effect thruster simulations that are based on anomalous resistivity and generalized ohm's law. *Plasma Sources Sci. Technol.*, 28:014003, 2019.
- [205] R.C. Davidson and N.A. Krall. Anomalous transport in high-temperature plasmas with applications to solenoidal fusion systems. *Nucl. Fusion*, 17(6):1313–1372, 1977.
- [206] A. Lenard. On bogoliubov's kinetic equation for a spatially homogeneous plasma. *Ann. Phys.*, 10(3):390 – 400, 1960.
- [207] R. Balescu. Irreversible processes in ionized gases. *Phys. Fluids*, 3(1):52–63, 1960.
- [208] F. F. Chen. *Introduction to Plasma Physics and Controlled Fusion: Plasma Physics, 2nd ed.* Plenum, New York, 1984.
- [209] A. Lazurenko, T. Dudok de Wit, C. Cavoit, V. Krasnoselskikh, A. Bouchoule, and M. Dudeck. Determination of the electron anomalous mobility through measurements of turbulent magnetic field in hall thrusters. *Phys. Plasmas*, 14(3):033504, 2007.
- [210] E. Velikhov A. A. Vedenov and R. Z. Sagdeev. In *International Conference on Plasma Physics and Controlled Thermonuclear Fusion*. Paper 199, 1961.
- [211] A A Vedenov. Quasi-linear plasma theory (theory of a weakly turbulent plasma). *Journal of Nuclear Energy. Part C, Plasma Physics, Accelerators, Thermonuclear Research*, 5(3):169–186, 1963.
- [212] R. C. Davidson. *Methods in Nonlinear Plasma Theory*. Academic Press, New York and London, 1972.
- [213] S. D. Baalrud, C. C. Hegna, and J. D. Callen. Instability-enhanced collisional friction can determine the bohm criterion in multiple-ion-species plasmas. *Phys. Rev. Lett.*, 103:205002, 2009.
- [214] S. D. Baalrud. *Kinetic theory of instability-enhanced collective interactions in plasma*. Phd thesis, University of Wisconsin-Madison, 2010.
- [215] S. Tsikata and K. Hara. Plasma instabilities in cross-field configuration: an analysis of the relevance of different modes for electron transport. In *36th International Electric Propulsion Conference, Vienna*. Paper A758, 2019.
- [216] W.M. Manheimer and J.P. Boris. Self-consistent theory of a collisionless resistive shock. *Phys. Rev. Lett.*, 28:659–662, 1972.

- [217] T. Charoy, T. Lafleur, A. Tavant, A. Bourdon, and P. Chabert. Oscillation analysis in hall thrusters with 2d (axial-azimuthal) particle-in-cell simulations. In *36th International Electric Propulsion Conference, Vienna*. Paper A487, 2019.
- [218] I. Katz, A. Lopez Ortega, B.A. Jorns, and I.G. Mikellides. Growth and saturation of ion acoustic waves in hall thrusters. *52nd AIAA/SAE/ASEE Joint Propulsion Conference*, 2016.
- [219] J.A. Carlsson, I.D. Kaganovich, E. Rodriguez, Y. Raitses, and A. Smolyakov. Scaling of spoke rotation frequency within a penning discharge and code development updates. In *36th International Electric Propulsion Conference, Vienna*. Paper A816, 2019.
- [220] P. Coche. *Modélisation cinétique d'un propulseur à effet Hall*. PhD thesis, Université Toulouse 3 Paul Sabatier, 2013.
- [221] L.V. Borodachev and D.O. Kolomiets. Calculation of particle dynamics in the nonradiative model of plasma. *Math Models Comput Simul*, 3:357–364, 2011.
- [222] S. Barral, J. Miedzik, and E. Ahedo. *A Model for the Active Control of Low Frequency Oscillations in Hall Thrusters*.
- [223] Y.B. Esipchuk and G. N. Tilinin. Drift instability in a hall-current plasma accelerator. *Sov. Phys. Tech. Phys.*, 21:417, 1976.
- [224] S. Barral, K. Makowski, Z. Peradzyński, and M. Dudeck. Transit-time instability in hall thrusters. *Phys. Plasmas*, 12(7):073504, 2005.
- [225] E. Fernandez, M. K. Scharfe, C. A. Thomas, N. Gascon, and M. A. Cappelli. Growth of resistive instabilities in exb plasma discharge simulations. *Phys. Plasmas*, 15(1):012102, 2008.
- [226] O. Koshkarov, A. I. Smolyakov, I. V. Romadanov, O. Chapurin, M. V. Umansky, Y. Raitses, and I. D. Kaganovich. Current flow instability and nonlinear structures in dissipative two-fluid plasmas. *Phys. Plasmas*, 25(1):011604, 2018.
- [227] <https://docs.scipy.org/doc/scipy-0.14.0/reference/generated/scipy.signal.welch.html> (signal.welch scipy function).
- [228] A. Smolyakov, O. Chapurin, I. Romadanov, Y. Raitses, I. Kaganovich, G. Hagelarr, and JP. Boeuf. Theory and modelling of axial mode oscillations in hall thruster. In *AIAA Propulsion and Energy Forum, Indianapolis*, 2019.
- [229] P.J. Schmid. Dynamic mode decomposition of numerical and experimental data. *Journal of Fluid Mechanics*, 656:5–28, 2010.

- [230] Antares Development Team. Antares Documentation Release 1.15.0, 2012–2020.
- [231] S. Boccelli, T. Charoy, A. Alvarez Laguna, P. Chabert, A. Bourdon, and T. E. Magin. Collisionless ion modeling in hall thrusters: Analytical axial velocity distribution function and heat flux closures. *Phys. Plasmas*, 27(7):073506, 2020.
- [232] J.P. Verboncoeur, M.V. Alves, V. Vahedi, and C.K. Birdsall. Simultaneous potential and circuit solution for 1d bounded plasma particle simulation codes. *J. Comp. Phys.*, 104(2):321 – 328, 1993.
- [233] V. Vahedi and G. DiPeso. Simultaneous potential and circuit solution for two-dimensional bounded plasma simulation codes. *J. Comp. Phys.*, 131(1):149 – 163, 1997.
- [234] X.M Zhu, Y.F Wang, Y. Wang, D.R. Yu, O. Zatsarinny, K. Bartschat, T. Vaskov, and U. Czarnetzki. A xenon collisional-radiative model applicable to electric propulsion devices: II. kinetics of the 6s, 6p, and 5d states of atoms and ions in hall thrusters. *Plasma Sources Sci. Technol.*, 28(10):105005, oct 2019.
- [235] T. Ben Slimane. A xenon collisional radiative model for electric propulsion application. Master’s thesis, Ecole Polytechnique, KTH Royal Institute of Technology, 2020.
- [236] R.J. Leveque. *Finite Volume Methods for Hyperbolic Problems*. Cambridge Texts in Applied Mathematics. Cambridge University Press, 2002.

Titre : Étude numérique du transport des électrons dans un propulseur à effet Hall

Mots clés : Propulsion électrique, propulseur de Hall, simulation PIC, benchmark, instabilités

Résumé : Ces dernières années, le nombre de satellites en orbite autour de la Terre a augmenté de manière exponentielle. Grâce à leur faible consommation en carburant, de plus en plus de propulseurs électriques sont utilisés à bord de ces satellites, notamment le propulseur de Hall qui est l'un des plus efficaces. De la diversité des applications découle le besoin d'avoir des propulseurs de taille et puissance variables. Cependant, la physique des propulseurs de Hall est encore méconnue et les nouveaux designs se font de manière empirique, avec un développement long et coûteux, pour un résultat final limité. Pour pallier ce problème, des codes de simulation peuvent être utilisés mais une meilleure compréhension des phénomènes clés est alors nécessaire, plus particulièrement du transport anormal des électrons qui doit être pris en compte de manière auto-consistante pour pouvoir capturer totalement le comportement de la décharge.

Ce transport étant relié à l'instabilité azimuthale de dérive électronique, un code 2D particulière existant a été amélioré pour pouvoir simuler cette direction azimuthale mais aussi la direction axiale. Avant d'analyser le comportement de la décharge, ce code a été vérifié sur un cas de benchmark, avec 6 autres

codes particuliers développés par différents groupes de recherches internationaux. Ce cas simplifié a été ensuite utilisé pour vérifier de manière intensive un développement analytique pour estimer la force de friction électron-ion, qui est le témoin de la contribution des instabilités azimuthales sur le transport anormal. Puis, la dynamique des neutres a été rajoutée pour capturer de manière auto-consistante le comportement de la décharge. Une technique artificielle de loi d'échelle a été adoptée, avec une augmentation de la permittivité du vide, pour alléger les contraintes de stabilité du code particulière et accélérer les simulations. Grâce à une parallélisation du code efficace, ce facteur artificiel a été réduit de manière significative, se rapprochant ainsi d'un cas proche de la réalité. La force de friction électron-ion a été observée comme étant celle qui contribuait le plus au transport anormal durant les oscillation basse-fréquence du mode de respiration. Pour finir, l'interaction complexe entre le mode de respiration, l'instabilité de transit des ions et l'instabilité de dérive électronique a aussi été étudiée, avec la formation de structures azimuthales à grande longueur d'onde, associées à un plus grand transport anormal.

Title : Numerical study of electron transport in Hall Thrusters

Keywords : Electric propulsion, Hall thruster, PIC simulation, benchmark, instabilities

Abstract : In the last decade, the number of satellites orbiting around Earth has grown exponentially. Thanks to their low propellant consumption, more and more electric thrusters are now used aboard these satellites, with the Hall thrusters being one of the most efficient. From the diversity of applications stems the need of widening the thruster power capabilities. However, due to a lack of knowledge on Hall thruster physics, this scaling is currently done empirically, which limits the efficiency of the newly developed thrusters and increases the development time and cost. To overcome this issue, numerical models can be used but a deeper understanding on key phenomena is still needed, more specifically on the electron anomalous transport which should be self-consistently accounted for to properly capture the discharge behaviour.

As this transport is related to the azimuthal electron drift instability, an existing 2D Particle-In-Cell code was further developed to simulate this azimuthal direction along with the axial direction in which the ions are accelerated, producing the thrust. Prior to analyse the discharge behaviour, this code has been verified

on a benchmark case, with 6 other PIC codes developed in different international research groups. This simplified case was later used to stress-test previous analytical developments to approximate the instability-enhanced electron-ion friction force which represents the contribution of the azimuthal instabilities to the anomalous transport. Then, the neutral dynamics has been included to capture the full self-consistent behaviour of the discharge. We used an artificial scaling technique, increasing the vacuum permittivity, to relax the PIC stability constraints and speed-up the simulations. Thanks to an efficient code parallelisation, we managed to reduce this scaling factor to a small value, hence simulating a case close to reality. The electron-ion friction force was found to be the main contributor to the anomalous transport throughout the whole low-frequency breathing mode oscillations. Finally, the complex interaction between the breathing mode, the ion-transit time instabilities and the azimuthal electron drift instabilities has been studied, with the formation of long-wavelength structures associated with an enhanced anomalous transport.